Radar Near-Field Sensing For Biomedical Applications

by

Omid Bagheri

A thesis
presented to the University of Waterloo
in fulfillment of the
thesis requirement for the degree of
Doctor of Philosophy
in
Electrical and Computer Engineering

Waterloo, Ontario, Canada, 2025

© Omid Bagheri 2025

Examining Committee Membership

The following served on the Examining Committee for this thesis. The decision of the Examining Committee is by majority vote.

External Examiner	**Prof. Manos M. Tentzeris** Professor, Electrical & Computer Engineering, Georgia Institute of Technology, USA
Supervisor	**Prof. George Shaker** Adjunct Associate Professor, Department of Electrical and Computer Engineering, University of Waterloo
Supervisor	**Prof. Omar M. Ramahi** Professor, Department of Electrical and Computer Engineering, University of Waterloo
Internal Member	**Prof. Hamed Majedi** Professor, Department of Electrical and Computer Engineering, University of Waterloo
Internal Member	**Prof. Lan Wei** Associate Professor, Department of Electrical and Computer Engineering, University of Waterloo
Internal-external Member	**Prof. Veronika Magdanz** Assistant Professor, Department of Systems Design Engineering, University of Waterloo

Author's Declaration

I hereby declare that I am the sole author of this thesis. This is a true copy of the thesis, including any required final revisions, as accepted by my examiners.

I understand that my thesis may be made electronically available to the public.

Abstract

Biomedical sensing technologies are essential for real-time health monitoring and disease management. Among their applications, blood glucose monitoring is of particular importance due to the global prevalence of diabetes that demands early detection and continuous management. Although clinically approved invasive methods exist, they are often inconvenient and unsuitable for continuous monitoring. Despite extensive research, non-invasive glucose monitoring, whether through wearables or smartwatches, remains an unsolved challenge, with no commercially or clinically validated solutions available.

Radar-based biomedical sensing offers a promising non-invasive, continuous monitoring approach with tissue penetration capabilities. However, challenges such as suboptimal antenna design, near-field limitations, air-skin impedance mismatch, and poor depth resolution persist. A key objective in improving radar sensing performance is to maximize the transmitted power density from the radar's transmit (TX) antenna into the target medium while simultaneously enhancing the reflected power received by the receive (RX) antenna. This dual enhancement significantly improves the radar's signal-to-noise ratio (SNR). Integrating advanced lenses and metasurfaces addresses these limitations, enabling efficient, practical deployment without major redesigns.

This research introduces the development and implementation of novel radar-based methodologies tailored for biomedical sensing applications. Through innovative system design, advanced signal processing, and rigorous experimental validation, the proposed solutions address key challenges in on-body sensing. The first contribution focuses on advanced lens designs, such as dielectric rod arrays and modified gradient-index (GRIN) Luneburg lenses, aimed at enhancing radar-based external health monitoring at 10 GHz.

The second contribution advances metasurface technologies for internal biomarker monitoring, enabling compact, skin-contact wearable systems with enhanced sensitivity and spatial resolution, with a specific emphasis on non-invasive blood glucose detection. Operating in the 58–63 GHz millimeter-wave band, the proposed metasurface-enhanced radar system integrates the BGT60TR13C sensor from Infineon Technologies with a planar, phase-synthesized metasurface for near-field focusing within the skin dermis layer, achieving over 11-fold improvement in SNR by enhancing both transmitted and reflected power. Four progressively objectives are presented, each expanding upon the foundation of the previous stage: single-band, single-focus metasurface, a preliminary design serving as proof of concept; metasurface-enhanced multi-radar fusion for distributed sensing; dual-band, dual-focus metasurface for depth-selective monitoring; and a multi-band, multi-focus non-interleaved metasurface for combined spatial and depth resolution. These innovations have the potential to revolutionize non-invasive, continuous health monitoring.

Acknowledgments

I would like to express my deepest gratitude to my supervisors, Professor George Shaker and Professor Omar M. Ramahi, for their invaluable guidance, continuous encouragement, and unwavering support throughout the course of this research. Their insights and expertise have been instrumental in shaping the direction and quality of this work.

This research was financially and technically supported by several organizations, whose contributions were vital to the realization of this work. I would like to acknowledge: the Natural Sciences and Engineering Research Council of Canada (NSERC) and Mitacs for their financial support; CMC Microsystems for providing software and simulation resources; the Research Institute for Aging (RIA) in Waterloo, Ontario, Canada for offering facilities and experimental environments for measurements and clinical testing; Ansys for their software support; Infineon Technologies for supplying high-quality mm-wave radars essential for our experiments and evaluations; Fortify for consultation support and 3D-printing fabrication of the Luneburg lens; Google for initially defining this project and expressing interest in advancing non-invasive glucose monitoring capabilities in wearable devices; and the Royal Military College of Canada, especially Professor Yahia Antar, for their support and interest in this research.

I also wish to acknowledge the strong institutional support provided by the University of Waterloo, the Faculty of Engineering, and the Wireless Sensors and Devices Lab, whose coverage of fabrication costs and provision of fully equipped measurement laboratories created an outstanding research environment.

Finally, I am deeply indebted to my family for their unwavering love, patience, and encouragement throughout my academic journey. Their support has been a constant source of inspiration, without which this accomplishment would not have been possible.






















Table of Contents

Examining Committee Membership ii

Author's Declaration iii

Abstract iv

Acknowledgments v

List of Figures x

List of Tables xxi

1 Introduction 1

1.1 Motivation 1

1.2 Objectives 4

1.3 Thesis Outline 6

2 Literature Review 8

2.1 Overview of Radar Sensing Technologies 10

2.1.1 Radar Applications in Modern Wireless Systems 11

2.1.2 Radar Applications in Biomedical Sensing and Imaging 13

2.1.3 Limitations of Radar in Biomedical Contexts 18

2.2 Radar Near-Field Sensing . . . 21
2.2.1 Microwave Near-Field Antenna Technologies . . . 22
2.2.2 Near-Field Antennas in Biomedical Applications . . . 27
2.2.3 Limitations of Existing Near-Field Antennas . . . 32
2.3 Metasurface Near-Field Focusing Approaches . . . 34
2.3.1 Metasurface Theory and Principles . . . 34
2.3.2 Metasurfaces in Near-Field Antenna Design . . . 41
2.4 Summary and Gaps in Literature . . . 43

3 Radar Sensing and Power-Focusing Enhancement Techniques 46
3.1 Problem Statement and Objectives . . . 47
3.2 3D-Printed Dielectric Rod Lens . . . 49
3.2.1 Dielectric Rod Lens Design . . . 51
3.2.2 Simulation Results . . . 55
3.2.3 Fabrication and Measurement Process . . . 58
3.3 Spherical Dielectric GRIN Luneburg Lens . . . 60
3.3.1 Radar Antennas Employing a Modified Dielectric GRIN Luneburg Lens . . . 64
3.3.2 Modified GRIN Luneburg Lens for Radar Integration . . . 65
3.3.3 Modified GRIN Luneburg Lens Manufacturing . . . 71
3.3.4 Radar Module Integrated with GRIN MLL: Measurement Results . . . 78
3.4 Summary and Key Takeaways . . . 82

4 Radar Near-Field Sensing Using Metasurface for Biomedical Applications 84
4.1 Objective 1: Radar Near-Field Sensing Using Single-Band Single-Focus Metasurface . . . 88
4.1.1 Near-Field-Focused Metasurface Design in Skin Medium . . . 88
4.1.2 Metasurface As an Impedance Matching Medium . . . 93

4.1.3 Planar Metasurface Unitcell Design in Skin Medium 96
4.1.4 Planar Metasurface Array Design 101
4.1.5 Simulation Results: Radar System Integrated With and Without Metasurface 106
4.1.6 Sensitivity Analysis in Near-Field Bio-Sensing Design 112
4.1.7 Fabrication Setup and Measurement Results 117
4.2 Objective 2: Multi-Focus Distributed Sensing Using Metasurface-Enhanced Multi-Radar Fusion 122
4.2.1 Synchronized Multi-Radar Signal Processing 124
4.2.2 Experimental Results with the Multi-Radar Fusion System 126
4.3 Objective 3: Radar Near-Field Sensing Using Dual-Band, Dual-Focus Metasurface 128
4.3.1 Dual-Band, Dual Near-Field Focus Metasurface 131
4.3.2 Dual-Band Unitcell and Array Design 131
4.3.3 Radar Module Integrated with The Dual-Band Dual-Focus Metasurface 137
4.3.4 Sensitivity Analysis in Dual-Band Metasurface 140
4.3.5 Fabrication Process and Measurement Results 146
4.4 Objective 4: Frequency-Scanning Multi-Focus Radar Sensing Using Multi-Band Metasurface 154
4.4.1 Multi-Radar System for Distributed Human Skin Scanning 156
4.4.2 Multi-Band Non-Interleaved Metasurface Design for Multi-Focus Bio-Sensing 158
4.4.3 Fabrication Process and Measurement Results 173

5 Conclusion and Future Works **179**
5.1 Conclusions 179
5.2 Initial Evaluation and Pre-Clinical Validation in Human Subjects 189
5.3 Future Works 192
5.3.1 Reconfigurable Metasurface for Multi-Focus Sensing 192

5.3.2 Near-Field Scanning System for Enhanced Bio-Sensing at Low Frequencies . . . 194
5.3.3 GRIN Planar Luneburg Lens for Near-Field Focusing in Biomedical Sensing . . . 201
5.3.4 Non-Invasive Bio-Sensing Using Metasurface-Enhanced Radar and Optical Spectroscopy Fusion . . . 202

References **204**

APPENDICES **236**

A Radar Signal Processing **237**

A.1 Radar Signal Processing . . . 237
A.2 Synchronized Multi-Radar System . . . 240

List of Figures

2.1 (a) Illustration of the general principle of radar performance in two configurations: (a) monostatic radar, where the TX and RX are co-located, and (b) bistatic radar, where the TX and RX are spatially separated, forming a bistatic angle β at the target [11]. 11

2.2 Commonly used off-the-shelf radar modules for various applications [12-14]. 12

2.3 (a) General conceptual illustration of the portable radar driven sensor for measuring the glucose level non-invasively from the fingertip by sending electromagnetic waves of small wavelength into the blood vessels [27] (b) A multiplexed electrochemical system for continuous monitoring of a panel of analytes in sweat, integrated into a smart wristband for fitness monitoring [28] (c) a bedroom with a radar attached to a ceiling on the bed for human vital sign tracking [31] (d) The radar experimental setup for glucose detection in blood test tubes [39] (e) a millimeter-wave arterial sensing device mounted on wrist and a tonometer placed on radial artery of a subject [42]. 14

2.4 (a) Electromagnetic wavefronts in the near-field and far-field regions of a radar TX/RX antenna, where the far-field exhibits planar wavefronts and the near-field exhibits more complex, typically spherical propagation. (b) Illustration of electromagnetic field interactions in a multiple-source (array) antenna configuration, showing constructive interference in the far-field and disordered field behavior in the near-field due to mutual coupling and reactive effects [66]. 22

2.5 convergence of equiphase surfaces generated by electromagnetic sources located on a planar aperture and directed towards a focal point, F, within the antenna's radiative NF region. L, corresponds to the antenna aperture size, and R_F represents the focal distance [72]. 23

2.6 Basic geometrical configurations of different NFF planar lens antennas: (a) reflectarray, and (b) transmitarray [82-85] 26
2.7 Schematic representations of breast, antenna and tumor showing signal scattering in a normal breast and a breast with a tumor [119] 31
2.8 Scheme of the freestanding array of metallic patches of zero thickness under oblique incidence [126]. 36
2.9 simulation model and E-field intensity on the focal plane at 5.8 GHz for Near-field focused metasurface of 500×500 mm with 20×20 elements [103] . 43

3.1 The dimensions of full prototype and PCB layout of the HB100 radar module with TX/RX sections. 51
3.2 The full structure and design parameters of the dielectric rod lens integrated with HB100 radar module: (a) top view and (b) side view. 54
3.3 Magnitude and direction of the electric field distribution on the dielectric rod lens with appropriate excitation mode coupled from the array patch antenna. 56
3.4 The 2D E-plane and H-plane realized gain pattern for the RX/TX antenna with and without using dielectric rod lens at 10.52 GHz. 57
3.5 The realized gain variation versus frequency for the RX/TX antenna with and without integrating dielectric rod lens, (b) The investigation of reflection coefficient and mutual coupling for TX/RX antenna integrated with dielectric rod lens. 57
3.6 An HB100 radar antenna fabricated prototype mounted on a bicycle integrated with and without the dielectric rod lens. 58
3.7 A flowchart outlining the main steps of the design, simulation, and manufacturing procedure necessary for integrating the dielectric rod lens with the radar module for detection range enhancement. 59
3.8 Ray tracing for GRIN Luneburg lens feeding scenarios: (a) Single center-fed, (b) Dual-beam symmetric feeds, (c) Single offset-fed, (d) Dual-beam asymmetric feeds. 61
3.9 (a) Layout of the X-band Doppler off-the-shelf radar module with bistatic TX and RX antennas on the same plane, utilized for bicycle collision applications; (b) Integration of the conventional GRIN Luneburg lens with the radar, illustrating beam tilting issue using the ray tracing method; (c) Integration of the GRIN modified Luneburg lens, demonstrating focused radiation directed towards the boresight. 62

3.10 (a) Cross-section of the conventional GRIN Luneburg (CLL) lens showing its permittivity distribution profile; (b) E-field propagation from the radar TX/RX antennas in the presence of the CLL; (c) 2D gain pattern for TX/RX antenna at 10.4 GHz when the radar is integrated with the CLL. 66

3.11 (a) permittivity distribution profile of the Modified GRIN Luneburg lens (MLL) in different planes; (b) E-field propagation from the radar TX/RX antennas in the presence of the MLL; (c) 2D gain pattern for TX/RX antenna radiation at 10.4 GHz when the radar is integrated with the MLL. . 69

3.12 (a) Permittivity distribution profile of the updated GRIN MLL with overlapped rods; (b) Electric field propagation from the radar TX/RX antennas in the presence of the MLL with overlapped rods; (c) 2D realized gain pattern for TX/RX antenna radiation at 10.4 GHz when the radar is integrated with the MLL updated with overlapped rods. 74

3.13 (a) Simulation analysis of the S-parameters for the radar module integrated with the updated GRIN MLL, including S(TX-TX) and S(RX-RX), and investigation of the power received from TX to RX when a corner reflector is placed in front of the radar radiation, comparing cases with and without the lens, (b) Beam angle and realized gain variations of the radar antenna integrated with the MLL as a function of frequency. 75

3.14 (a) Prototype of the MLL uniformly fabricated using Fortify 3D-printing, with a 2D cross-section showing the implementation of overlapped rods designed within the lens; (b) 3D-printed fixture for holding the corner reflector and HB100 radar module, powered by a DC power supply, and positioned at an appropriate location and distance attached to the MLL. 78

3.15 In-lab measurement setup illustrating the radar system as the transmitter and an X-band horn antenna as the receiver, positioned at different distances: (a) radar without the MLL integrated; (b) radar integrated with the MLL. 79

3.16 Comparative analysis of the power transmitted by the radar with/without the MLL and received by the X-band horn antenna placed at distances of (a) 10λ, (b) 15λ, and (c) 20λ. (d) Comparative analysis of the power received by the radar with/without the MLL in the presence of corner reflector . . . 80

3.17 Measurement and simulation results of the reconstructed radar radiation pattern for cases with and without the MLL integrated. 82

4.1 (a) A wearable device equipped with radar technology positioned near a human hand; (b) Incorporating a metasurface structure between the radar antennas and the hand to enhance the near-field energy coupling and Signal-to-Noise Ratio (SNR). 87

4.2 Power transferred and efficiency investigation in the near-field focusing using metasurface [103]. 89

4.3 Investigation of the path gain versus radar range variations for the near-field in comparison to the far-field. 91

4.4 A conventional FPC resonator antenna featuring a partially reflective surface (PRS) creating an air-filled cavity between the PRS and the ground plane, fed by a source antenna [197] 92

4.5 The transferred and received power in the radar system in the presence of the metasurface loaded by the skin model 94

4.6 The free-space wave impedance variations in the near-field region of the radar. 95

4.7 (a) Analysis of transferred and received power between transmitter (TX) and receiver (RX) antennas in the metasurface-enhanced radar system loaded by skin model. (b) Investigation of the radar system performance using impedance analysis for each medium, comparing the radar system without a metasurface to (c) the radar system with integrated metasurface. 96

4.8 Comparative analysis of transmissive metasurface unitcells designed in free-space and human body skin medium. (a) Unitcell dimensions designed for radiation in free space, (b) Simulation representing the Floquet port analysis of the unitcell designed for free-space, (c) Unitcell designed for radiation in human body skin medium, (d) Simulation illustrating the Floquet port analysis of the unitcell in the presence of the human body skin modelled as a dielectric slab. The design parameter values are: W_F=2.5, t_F=1.25, L_F=1.32, S_F=0.2, W_S=1.1, L_S=0.65, S_S=0.2, t_{SF}=3 (all in mm). 97

4.9 Reflection coefficient analysis of the unitcells: designed in free-space medium in contact with and without the human skin model, and designed in the skin medium in contact with the human skin model. 98

4.10 The imaginary part variations of the wave impedances versus frequency for the skin model and the designed metasurface. 98

4.11 Investigation of unitcell required phase shift to design a near-field focused transmitarray metasurface to be placed at $\lambda/2$ distance from the feed based on the number of the elements in x and y directions. (a) 3×3 elements (b) 5×5 elements (c) 7×7 elements (d) 9×9 elements. 103

4.12 Simulated transmission coefficients (S21 magnitude and phase) of the two-layered crossed-dipole unitcell in presence of skin layer. (a) magnitude (Mag) and phase analysis for various metallic branches lengths at center frequency, D_S=L_S+W_S/2; (b) magnitude and phase analysis for various incident angles at center frequency; (c) magnitude investigation across different frequencies within the desired bandwidth; (d) phase investigation across different frequencies within the desired bandwidth. 106

4.13 Radar-Metasurface integration for near-field power density measurement using a human skin model phantom. (a) The Infineon BGT60TR13C radar chipset with highlighted transmitter (TX) and receiver (RX) antennas and the designed phase-corrected transmitarray metasurface (b) radar integrated with the metasurface contacting the proposed phantom, a beaker filled with pure water, in replace with human skin model. 108

4.14 (a) The required phase shift compensation of the 7×7 array when TX radar source is in the offset, and (b) The phase difference between the case when source is placed in offset with the case source is placed at the center of the 7×7 array. 109

4.15 Simulated 2D contour plots of radar system transmitter antenna near-field radiation inside the phantom model at 60 GHz, illustrating on a plane positioned 2 mm above the metasurface. (a) radiated electric field (E-Field) intensity of radar system without metasurface (b) radiated electric field intensity of radar system integrated with the metasurface; (c) radiated near field (NF) power density of radar system without metasurface (d) radiated near field power density of radar system integrated with the metasurface. . 110

4.16 The S-parameter analysis, simulated reflection and coupling magnitude of the radar system transmitter (TX) and receiver (RX3) antennas integrated with and without the metasurface in presence of the phantom model. . . . 111

4.17 (a) The metasurface array's scale relative to a wearable device, like a smartwatch worn on a human wrist, showcasing the substantial difference in dimensions; (b) The transmission coefficient analysis of the metasurface unitcell under different air gap conditions between the metasurface and the human skin model 113

4.18 Analyzing the transmission coefficient of the metasurface unitcell in response to variations in the permittivity of the human skin model. 116

4.19 Impact of varying air gap distances between the metasurface and radar antennas' surfaces on power distribution above the metasurface, illustrated for distances of (a) 0.4 λ, (b) 0.6 λ. 117

4.20 (a) fabricated prototype showcasing the integration process of a radar system with a transmitarray metasurface, utilizing a 3D-printed dielectric housing for enhanced design precision; (b) measurement setup required for measuring near-field power density inside the phantom. 118

4.21 Measurement results of metasurface-enhanced radar signal transmission and reflection in presence of the proposed phantom. (a) The measured near-field power density incident by Infineon radar transmitter (TX) antenna inside the beaker-filled with pure water in the presence or absence of the designed transmissive metasurface. (b) The investigation of the measured power reflected from the beaker filled with pure water received by the third receiver radar antenna (RX3) over a period in the presence or absence of the designed transmissive metasurface for different concentration levels of glucose. 119

4.22 Multi-Radar Sensor Fusion System for Distributed Full-Body or Site-Specific Sensing 123

4.23 (a) Multi-radar system configuration consisting of three Infineon 60 GHz BGT60TR13C radar modules enhanced with metasurfaces, applied to a human skin phantom model with varying glucose concentration levels (GCL). (b) Real-time visualization of the system's data capture. 125

4.24 Received power measurements representing radar SNR for phantoms with varying glucose concentration levels. 127

4.25 The mm-wave radar module integrated with a dual-band metasurface, generating dual near-field focus points within human skin, with the goal of incorporating this functionality into wearable devices. 130

4.26 Configuration of the mm-wave Infineon radar module antennas alongside the designed dual-band, dual-focus metasurface, incorporating crossed-dipole and square loop slot elements within the unitcell design. 132

4.27 S-parameters analysis of the dual-band mm-wave unitcell featuring interleaved slot elements. 133

4.28 Simulated S11 parameter to investigate independence between two frequency bands: (a) Through changing UC-PBG slot length, (b) Through changing crossed-dipole slot length. 134

4.29 Phase synthesis analysis of the metasurface array with 7×7 unitcells, showing phase shift compensation required for (a) focusing at boresight at 59 GHz, and (b) focusing at boresight at 61 GHz, (a) focusing at +20 degrees at 59 GHz, and (b) focusing at -20 degrees at 61 GHz. 136

4.30 Simulated transmission phase shift of three-layer unitcell (a) For lower frequency band, (b) For upper frequency band 137

4.31 S-parameters analysis of the radar received power from TX to RX2, with and without the dual-band metasurface. 138

4.32 2D contour plots of near-field power density 2 mm inside the skin model for the dual-band metasurface-enhanced radar system's TX antenna at (a) 58.5 GHz, (b) 59 GHz, (c) 60 GHz, (d) 61 GHz, (e) 62 GHz, and (f) 63 GHz . . 139

4.33 S-parameters analysis comparing the responses of the dual-band unitcell to frequency-dependent variations in human skin properties, highlighting the impact of dielectric changes at each operational band. 141

4.34 S-parameter analysis comparing the responses of the dual-band unitcell under varying metallic layer thicknesses, highlighting deviations from the ideal (zero-thickness) case. 142

4.35 Illustration of wave interaction with the surface of a transmit array antenna: (a) without distortion, (b) with distortion, and (c) Vector representation of phase error caused by surface distortion. 143

4.36 Prototype fabrication process of the triple-layer dual-band metasurface, consisting of 0.1 mm thick metallic sheets, assembled using a 3D-printed square frame with a 0.5 mm interlayer spacing. The final assembled structure is shown applied to a human hand for scale comparison, illustrating the compact form factor suitable for wearable biomedical applications. 147

4.37 Measurement setup for validating transmitted power enhancement at dual frequencies and dual focal depths within the phantom using a dual-band metasurface-enhanced radar system. 149

4.38 Screenshots of the spectrum analyzer display showing the dual-band response of transmitted power at two symmetrical off-axis locations within the phantom; (a) Shows distinct frequency peaks and corresponding power levels at 59 GHz and 62 GHz. (b) Illustrates the spectral isolation and independence between the two bands, confirming effective dual-band, dual-focus performance with minimal cross-band interference. 150

4.39 Measurement results of the transmitted power density within the phantom for the radar system integrated with and without the dual-band metasurface, demonstrating both dual-band operation and the enhancement in focused power delivery at target locations. 151

4.40 Metasurface-enhanced multi-radar near-field system. 155

4.41 Configuration of the metasurface-enhanced multi-radar near-field scanning system, designed as a wearable wristband for easy and continuous real-time glucose monitoring on the human body. 158

4.42 General configuration of the mm-wave Infineon radar system with one transmitter and three receiver antennas, incorporating a metasurface in direct contact with a skin model and optimized for specific frequencies within the radar's frequency range from 58 to 63 GHz. 160

4.43 Investigation of the reflection coefficient (S11) for the proposed unitcells at their respective frequencies. 161

4.44 Phase shift differences required for mapping the 7×7 metasurface array using the designed metasurface between 58 and 63 GHz: (a) when the feed is aligned with the center of the array, and (b) when the feed is located at a 20 degrees offset, (c) (b) when the feed is located at a 40 degrees offset. . 163

4.45 (a) The multi-bio-sensing radar system integrated with a multi-band non-interleaved metasurface, (b) Enhancement of power density within the human skin model, investigated across various penetration depths and operational frequencies. 164

4.46 New metasurface unitcell design composed of three layers: two crossed-dipole microstrip structures on the top and bottom layers, with a UC-PBG layer integrated in the middle to enhance phase compensation and resonance control. 166

4.47 Reflection coefficient (S11) analysis of the newly designed metasurface unitcell composed of three layers, demonstrating that the inclusion of the UC-PBG layer enhances the quality factor and sharpens the resonance response. 167

4.48 Required phase distribution for the 9 × 9 metasurface array, synthesized using near-field focusing equations to achieve dual focal points at 2.5 mm above and 2 mm below the metasurface. 168
4.49 Simulated transmission coefficients (S21 magnitude and phase) of the three-layer unitcell across the starting and ending frequency points within the desired bandwidth. 168
4.50 Simulated 2D contour plots of the radar system TX antenna's radiated near-field power density within the phantom model, evaluated on a plane positioned 2 mm above the multi-band non-interleaved metasurface, at 58 GHz 170
4.51 Simulated 2D contour plots of the radar system TX antenna's radiated near-field power density within the phantom model, evaluated on a plane positioned 2 mm above the multi-band non-interleaved metasurface, at 59 GHz 170
4.52 Simulated 2D contour plots of the radar system TX antenna's radiated near-field power density within the phantom model, evaluated on a plane positioned 2 mm above the multi-band non-interleaved metasurface, at 61 GHz 171
4.53 Simulated 2D contour plots of the radar system TX antenna's radiated near-field power density within the phantom model, evaluated on a plane positioned 2 mm above the multi-band non-interleaved metasurface, at 62 GHz 171
4.54 S-parameter analysis showing the simulated reflection and coupling magnitudes of the radar system transmitter (TX) and receiver (RX3) antennas, integrated with and without the metasurface in the presence of the phantom model: (a) at 58 GHz, (b) at 59 GHz, (c) at 61 GHz, and (d) at 62 GHz. . 172
4.55 Fabricated multi-band non-interleaved metasurface on a single panel, separated circular metasurfaces after dispatching, and individual circular metasurface element ready for integration. 174
4.56 Measurement setup for evaluating near-field transmitted power density inside the phantom at different frequencies, using the fabricated multi-band non-interleaved metasurfaces integrated with the radar system. 174
4.57 S-parameter analysis showing the simulated reflection and coupling magnitudes of the radar system transmitter (TX) and receiver (RX3) antennas, integrated with and without the metasurface in the presence of the phantom model: (a) at 58 GHz, (b) at 59 GHz, (c) at 61 GHz, and (d) at 62 GHz. . 175
4.58 Signal-to-noise ratio analysis for varying glucose concentration levels, comparing the performance of single-band single-focus, dual-band dual-focus, and multi-band multi-focus non-interleaved metasurface designs. 177

5.1 Advancements in blood glucose sensing with metasurfaces: (a) Single-focu;, (b) Dual-focus with dual-band capability for dual-depth sensing (Depth Sensing); (c) Multi-focus radar sensing enhanced with identical near-field focus metasurfaces (Spatial Sensing); (d) Multi-focus non-interleaved metasurfaces for distributed sensing via multi-radar fusion (Spatial+Depth Sensing). 183

5.2 Developed radar-based bio-sensor systems for non-invasive glucose monitoring, showcasing the evolution from single-band single-focus design to advanced multi-band multi-focus sensing. 187

5.3 Measurement setup showing the mm-wave radar module integrated with a single-focus metasurface. The system is connected to a data acquisition interface, with real-time data captured using a Python script. 190

5.4 Initial radar measurement results from human subjects using the single-focus metasurface-integrated mm-wave radar module. The plots illustrate the variations in radar signal response over time, reflecting individual physiological differences in glucose absorption and skin interaction; (a) subject 1, evaluation on right and left hand finger; (b) subject 2; and (c) subject 3. 191

5.5 (a) Beam steering in a phased-array antenna system for far-field target detection; (b) Electronic focus steering using a reconfigurable metasurface for near-field energy localization within human body skin. 193

5.6 The near-field scanning system setup for bio-sensing 195

5.7 The measurement setup for the near-field scanning approach 196

5.8 Simulation setup for the scanning approach, TX and RX antennas; with Scanning surface at 5 cm above the TX. 197

5.9 Dielectric skin phantom model used for near-field radar measurements. The Pyrex container is filled with a water-glycerin mixture (55% glycerin by volume), emulating human skin electrical properties. 198

5.10 Near electric field pattern captured by scanning the RX antenna at different permittivity values deviating from the baseline human skin permittivity at 2.4 GHz, illustrating the radar's ability to detect dielectric abnormalities in biological tissue. 199

5.11 Comparing the scanned near-field electric field patterns by subtracting them from the baseline scenario facilitates the identification of abnormalities or glucose-induced permittivity variations within the body. 200

5.12 Near-field scanning scenario involving a 1×1 cm cube embedded within a dielectric slab beneath the dipole antenna. The bar chart results illustrate the system's capability to detect permittivity variations within the cube, demonstrating the sensitivity of near-field sensing to localized dielectric anomalies. 200

5.13 Multi-technology fusion setup integrating a metasurface-enhanced mm-wave radar and an optical sensor for high-accuracy, non-invasive glucose monitoring at the earlobe. 203

A.1 (a) A simple block diagram of radar before signal processing where both transmitter and receiver are at the same place. (b) The signal processing chain for power calculation 237

A.2 Block diagram of radar signal processing: (a) non-averaging fusion mode, (b) averaging fusion mode. 242

List of Tables

3.1 Design parameters of the dielectric rod lens 55

3.2 Results comparison between the presented MLL and previously designed lenses for radar integration in the literature. 82

3.3 Comparison of 3D Lenses and Planar Metasurfaces for Bio-sensing Radar . 83

4.1 Variations in the dielectric properties of the human body's skin model in response to different frequencies within the radar range of 58 to 63 GHz. . 160

4.2 Comparison of Simulated and Measured Focused Transmitted Power Inside the Skin for Multi-Radar Sensing with Multi-Band Multi-Focus Non-Interleaved Metasurface 176

5.1 Comparative Analysis of Low-Frequency and Mm-Wave Radar Sensing for Biomedical Applications 180

5.2 Radar-Based Biomedical Sensing Challenges and the Corresponding Solutions Presented in This Thesis 188

A.1 The designed signal parameters 240

Chapter 1

Introduction

Radar technology provides a high level of resolution and accuracy in identifying delicate variations within biological tissues and fluids. The detailed precision of radar signals enables in-depth sensing and comprehensive characterization of biological structures, thereby facilitating precise diagnosis and ongoing monitoring of medical conditions. This capability to identify and distinguish minor irregularities or deviations from the standard serves a crucial role in the early detection of diseases and contributes significantly to planning treatments and interventions. This thesis focuses on employing near-field radar sensing in the realm of biomedical applications, discussing its potential advantages, advancements, and applications that contribute to enhancing healthcare and medical diagnostics.

In this chapter, we delve into the motivation behind our research, focusing on the challenges of utilizing radar technology for internal physiological sensing. Unlike conventional biomedical sensing methods that monitor external vital signs such as heart rate or respiration through skin movement, our work targets the detection of internal biomarkers, such as glucose levels, offering a non-invasive window into the body's physiological state. We present clear objectives that guide the proposed steps and address the complexities of integrating radar systems into advanced biomedical applications. This targeted approach establishes a strong foundation for exploring the transformative potential of radar in non-invasive internal health monitoring.

1.1 Motivation

Radar-based biomedical sensing systems offer a promising avenue for non-invasive, contactless, and continuous monitoring of physiological parameters, addressing the growing

demand for long-term health observation with minimal patient discomfort. Unlike traditional methods that require physical contact, often involving cumbersome electrodes or wearable sensors, radar systems enable passive sensing, significantly enhancing patient comfort and compliance. The motivation for using such contactless systems lies in their potential to reduce costs, extend device lifespan, and provide reliable sensing over prolonged periods. Applications span from post-operative recovery tracking to evaluating lifestyle impacts such as diet, exercise, and substance intake on sleep and overall health.

However, while conventional biomedical radar systems have largely focused on external vital signs, such as respiration and heart rate, through the detection of mechanical movements at the skin surface, this thesis targets a more challenging and underexplored domain: non-invasive detection of internal physiological markers, such as blood glucose levels. This shift introduces critical challenges, particularly in terms of antenna design, electromagnetic wave penetration, and interaction with the heterogeneous dielectric properties of human tissues.

In striving to achieve precise and high-quality sensing for biomedical applications through radar technology, a significant obstacle arises in the form of near-field-focused antennas. Merely designing an antenna is insufficient to adequately penetrate the human body and deliver effective sensing capabilities. The primary challenge lies in the limited capabilities of these antennas to efficiently access and capture data from the body's intricate and varied internal structures. This hinders their ability to provide accurate and in-depth sensing, emphasizing the need for a more sophisticated approach that surpasses the limitations of antenna design to enhance penetration and improve overall sensing performance within biomedical applications.

Radar systems operating at millimeter-wave frequencies, especially frequency-modulated continuous wave (FMCW) radars, have garnered attention for their high resolution and sensitivity to dielectric property variations. These features are crucial for detecting subtle physiological changes, such as variations in glucose concentration or the presence of anomalies like tumors. Their compact size makes them especially suitable for integration into wearable systems, such as smartwatches or biomedical rings. Nonetheless, their limited penetration depth remains a bottleneck for deep tissue sensing. In contrast, lower-frequency radar systems offer superior tissue penetration at the expense of spatial resolution, necessitating a careful trade-off based on the sensing application.

In bio-sensing scenarios, the effectiveness of radar hardware is evaluated by utilizing the near-field sensing capabilities of the antenna when it is placed in immediate proximity to the human body. Focusing energy at specific internal locations can significantly enhance signal fidelity and sensing accuracy. This requires not only effective spatial control of the

electric field but also meticulous consideration of impedance matching, power delivery, and interaction with complex tissue dielectric profiles. An effective technique involves harnessing the radiated power of the transmitter antenna to focus the electric field at a specific location near the radar surface. This process enables the system to capture reflected signals carrying relevant information from the target, consequently enhancing the near-field sensing capabilities. Such an approach significantly improves the system's capacity to detect and gather information when the radar is closely situated to the human body.

The literature reveals a considerable gap in the development of radar antennas optimized for internal biomedical sensing. Initially, there is a shortage of research focusing on millimeter-wave, hindering progress in developing applicable technologies for biomedical use. In addition, many existing designs for near-field sensing are hampered by bulky geometries, high-profile structures, and lossy feeding networks, rendering them impractical for real-time or wearable healthcare applications.

Moreover, the conventional practice of defining the far-field by placing the focal point distant from the antenna limits the ability to focus very close to the aperture, imposing a substantial constraint on targeting specific areas in biomedical contexts. In the domain of near-field antenna design, it is essential to emphasize that far-field design parameters should not be uniformly applied. While considerations like radiation pattern, antenna gain, directivity, and sidelobe level are crucial in most applications, their interpretation differs in the context of near-field antennas. The primary aim of near-field antenna design is to optimize the performance and characteristics of the antenna in close proximity to the radiating source, typically within a wavelength or less. Therefore, the focus shifts towards achieving efficient power transfer, minimizing near-field distortions, and tailoring the antenna's features to meet the specific requirements of short-range communication systems. Employing far-field design parameters without adjustments in the near-field context can result in suboptimal performance and potentially nullify the advantages of using near-field antennas.

Furthermore, the oversight regarding impedance matching in the near-field significantly restricts the practical application of these antennas for direct contact with the human body, a crucial element in their integration into medical devices. In medical microwave sensing, antennas are positioned close to the body to capture faint echoes from internal organs, often overshadowed by strong reflections from the skin. Considering the antennas' close proximity to the body, it becomes imperative to carefully address the characteristics of near-field antennas. Challenges arise when attempting to integrate these antenna structures with compact devices like radars or sensors, limiting their feasibility in real-time health monitoring applications. Despite common use of optimization techniques to achieve near-

field focus, a notable gap exists due to the lack of comprehensive theories in near-field studies, particularly concerning impedance and electric field behavior. This shortfall has contributed to the absence of any widely adopted commercial or clinical device for non-invasive glucose monitoring using radar, despite substantial research efforts. Attempts have included sensing through interstitial fluid and sweat, yet the realization of a reliable, fully contactless blood glucose sensor remains elusive.

The development of antennas for bio-sensing devices, meant for in-body applications, presents considerable challenges due to various crucial factors involved in their design. These factors encompass antenna size, bandwidth, patient safety, and diverse security considerations. The complex dielectric properties of human tissues and the need for wide bandwidth pose significant limitations in these applications. Even with recent progress in diagnosing diseases like lung conditions, persistent limitations exist that need addressing, such as low spatial resolution and the necessity for real-time monitoring in appropriate clinical settings. These challenges underline the complexity and ongoing hurdles in the development of effective bio-sensing devices for a range of medical applications.

Tackling these challenges is pivotal for creating effective, efficient, and practical antenna solutions in biomedical applications. Recent advances in metasurfaces, which enable dynamic manipulation of electromagnetic waves, offer a powerful solution. When integrated with radar platforms, metasurfaces can enhance field control, improve sensitivity, and increase resolution. This synergy promises a new generation of bio-radar systems capable of non-invasive, accurate, and reliable internal sensing, contributing to the next frontier in personalized healthcare technologies.

1.2 Objectives

Radar systems have increasingly demonstrated their suitability for a wide range of biomedical applications due to their ability to operate reliably in complex environments and penetrate various non-metallic materials including biological tissues, without requiring direct contact. This unique capability allows healthcare professionals to gather vital physiological information in real-time, supporting early diagnosis, continuous monitoring, and timely intervention. Compared to conventional imaging and sensing systems, radar offers a cost-effective, portable, and non-invasive solution suitable for integration into wearable or handheld platforms. These features are particularly appealing for applications such as blood glucose monitoring, fall detection, tumor localization, and sleep apnea diagnosis.

However, realizing the full potential of radar sensing in biomedical applications, especially for internal and non-invasive monitoring of biomarkers like glucose, demands sig-

nificant innovation at the hardware level, most critically in the design and integration of near-field sensing antennas. Near-field operation is essential for biomedical radar systems operating in close proximity to human skin or tissue. Yet, challenges such as limited penetration depth at high frequencies, air-to-skin impedance mismatches, and inefficient field focusing severely limit the efficacy of off-the-shelf radar modules.

Recent advancements in metasurfaces, subwavelength structures capable of manipulating electromagnetic waves with high precision, offer a powerful means to overcome these limitations. Metasurface-enhanced radar antennas enable the design of compact, low-profile systems with superior near-field focusing, resolution, and sensitivity. When properly designed, metasurfaces act as impedance-matching interfaces between the radar antenna and the biological tissue, maximizing the absorbed power and enhancing backscattered signal levels without disturbing the system's matching network. These advantages can be harnessed to boost signal-to-noise ratio (SNR) and sensing accuracy in radar-based biomedical applications.

This thesis proposes a comprehensive investigation into the use of metasurface-enabled radar systems for non-invasive physiological monitoring, with a focus on glucose sensing and deep-tissue anomaly detection. The thesis aims to address both the theoretical and practical challenges of designing effective near-field radar sensors for the human body, bridging the gap between existing radar technology and clinical deployment. The specific objectives of the thesis are as follows:

Objective 1: Radar Near-Field Sensing Using Single-Band Single-Focus Metasurface

Design and validate a compact, passive, transmissive metasurface engineered using phase-synthesized unit cells to focus the radar's electric field at a specific depth within the skin. This metasurface is optimized for integration with the Infineon BGT60TR13C radar module and targets improved impedance matching at the air–skin interface, thereby increasing the absorbed Poynting power density and reflected signal strength.

Objective 2: Synchronized Multi-Radar Fusion Sensing Using Single-Band, Multi-Focus Metasurface for Real-Time Distributed Monitoring

Develop and implement a synchronized multi-radar sensing system in which multiple radar modules, each equipped with identical near-field metasurfaces, monitor physiological signals from various body locations simultaneously. This distributed architecture compensates for biological variability across body sites and enhances the robustness of glucose monitoring. Data fusion and synchronization techniques are employed to integrate readings in real-time.

Objective 3: Radar Near-Field Sensing Using Dual-Band, Independently Tunable Dual-Focus Metasurface

Advance the system to a dual-band configuration that enables independent control of two spatially distinct focal points using frequency-selective metasurface layers. This design addresses the limitations of single-point sensing by enabling multi-depth interrogation, useful for layered tissue analysis or simultaneous monitoring of multiple biomarkers.

Objective 4: Frequency-Scanning Multi-Radar Fusion Sensing Using Multi-Band, Multi-Focus, Non-Interleaved Metasurface

Introduce a multi-band, non-interleaved metasurface design where discrete zones are optimized for different operating frequencies. This enables depth-tunable sensing by utilizing the frequency-dependent penetration characteristics of millimeter-wave signals. Each frequency zone functions as an independent matching network for a specific depth layer in tissue.

Overall, this thesis systematically explores the design, simulation, and experimental validation of metasurface-enhanced radar systems for biomedical sensing. By integrating advanced electromagnetic structures with commercially available radar modules, the proposed solutions address long-standing limitations in penetration, resolution, and system integration for non-invasive internal sensing. The outcomes of this research aim to inform future clinical technologies and lay the groundwork for practical, wearable, and contactless radar-based biosensors capable of reliable real-time health monitoring.

1.3 Thesis Outline

This thesis is structured into five chapters, each building upon the previous to develop and evaluate a comprehensive radar-based sensing system for biomedical applications, particularly focused on non-invasive internal monitoring.

Chapter 2 presents a detailed literature review covering the foundational aspects of near-field sensing technologies and radar applications in biomedical contexts. It begins by introducing key principles of near-field microwave antennas, followed by an exploration of their specific biomedical applications. The chapter then transitions into a focused discussion on metasurface-based near-field focusing approaches, which form the theoretical basis for the proposed solutions in this thesis. In the second part of the chapter, various radar sensing technologies are reviewed, with emphasis on their roles in modern wireless communication networks and their emerging use in medical sensing and imaging. The

chapter concludes by identifying the primary challenges in designing radar antennas for bio-sensing, particularly within the near-field regime.

Chapter 3 focuses on the fundamentals of radar sensing and introduces various power-focusing enhancement techniques relevant to biomedical applications. It begins by outlining the principles of radar operation, contrasting far-field and near-field sensing, and discussing their implications in target monitoring. The chapter then presents three enhancement strategies aimed at improving near-field energy delivery: a 3D-printed dielectric rod lens, a spherical GRIN Luneburg lens, and planar metasurfaces. These techniques are evaluated in terms of their efficiency, complexity, and suitability for integration with compact radar systems. This chapter establishes the motivation for adopting planar metasurfaces as a practical and effective solution for radar-based bio-sensing.

Chapter 4 constitutes the core of this thesis and details the design, development, and validation of several metasurface-integrated radar systems tailored for biomedical sensing. It encompasses four objectives, begins by introducing a single-frequency near-field-focused metasurface and its integration with a radar module in direct contact with a human skin model. The subsections address the unitcell design, full-array construction, simulation results, fabrication process, signal processing techniques, and measurement verification. Building on this foundation, the chapter explores a synchronized multi-radar fusion system for distributed sensing across multiple skin sites, followed by the development of a dual-band metasurface capable of independently focusing energy at two distinct depths. Additionally, a frequency-scanning radar architecture incorporating a non-interleaved multi-band metasurface is introduced to enable depth-selective sensing. Throughout these sections, both simulation and experimental results are presented to validate the performance improvements and biomedical sensing enhancements achieved through the proposed metasurface designs.

Chapter 5 concludes the thesis by summarizing the major findings, emphasizing the contributions made toward advancing radar-based near-field biomedical sensing. It highlights how the integration of metasurfaces has improved power delivery, field focusing, and signal-to-noise ratio across various configurations. The chapter also discusses potential future research directions, clinical trials, integration with wearable technologies, and adaptation to other physiological monitoring targets.

Chapter 2

Literature Review

Radar sensing has gained significant attention in recent years due to its versatility, contactless nature, and ability to function effectively in challenging environments [1]. These characteristics make it especially attractive for biomedical applications, where non-invasive monitoring and reliability are of critical importance. Radar systems are capable of penetrating various materials, including biological tissues, without requiring physical contact, enabling the collection of real-time physiological information while ensuring user comfort and system longevity. As a result, radar sensing is increasingly being explored for diverse medical applications such as respiration and heart rate monitoring [2], sleep analysis [3], fall detection [4], and non-invasive blood glucose monitoring [5].

Despite these advantages, the application of radar to internal physiological sensing remains complex. In biomedical contexts, especially when the radar is positioned in close proximity to the human body, the operating conditions shift from the far-field to the near-field regime. Under these conditions, conventional radar and antenna design principles no longer apply. Challenges such as air-to-skin impedance mismatch, rapid decay of evanescent fields, and poor field penetration limit the effectiveness of radar systems in detecting subsurface physiological changes. These limitations underscore the need for advanced electromagnetic structures and antenna design strategies that can overcome the inherent difficulties associated with near-field biomedical sensing.

Exploring the engineering of the near-field (NF) in radiating systems has therefore attracted increasing interest, particularly due to its wide array of practical applications across multiple domains. These include near-field radiometry [6], which is crucial for measuring electromagnetic emissions from electronic devices, deep tissue hyperthermia [7], where localized energy deposition is essential for therapeutic treatment, and wireless power

transfer to biomedical implants [8], which ensures continuous and non-invasive powering of embedded devices. These examples illustrate the broad utility of near-field engineering beyond traditional wireless communication, particularly within biomedical systems.

Antenna near-field sensing plays a pivotal role in advancing biomedical applications by facilitating non-invasive diagnostics, medical imaging, and therapeutic interventions. This technology enables precise and detailed medical imaging which assists in early disease detection and the study of soft tissues and organs. Near-field sensors are crucial for wireless communication in implantable medical devices, promoting remote monitoring and improving patient care. They also aid in research by providing insights into the electromagnetic properties of biological tissues and cells. Additionally, near-field sensing supports the development of minimally invasive procedures for cancer treatment and drug delivery, offering safer and more effective options for patients. These applications underscore the significance of antenna near-field sensing in the ever-evolving landscape of biomedical research and healthcare [9].

In essence, the primary objective of near-field engineering is to control and shape the electromagnetic field distribution in the immediate vicinity of an antenna. This involves tailoring the field to achieve desired characteristics either in free space or within surrounding materials such as biological tissues. Applications range from enhancing signal propagation and maximizing energy absorption to directing electromagnetic energy for therapeutic or diagnostic purposes. Near-field engineering thus holds significant potential to transform the way electromagnetic energy is utilized, particularly in advanced biomedical systems. However, unlike the far-field regime, where radiated fields are well-behaved and design methodologies are well-established, the near-field region, typically defined within a few wavelengths of the antenna, is characterized by highly complex, reactive, and non-radiative field components. These complexities make accurate modeling and optimization more difficult and contribute to the lack of standardized design frameworks, thereby posing a considerable challenge for practical implementation in precision applications.

There are many existing technologies available today for health and activity monitoring that can track physiological parameters and support healthcare applications [10]. However, most of these are either contact-based or limited in their sensing depth and accuracy. In response, radar sensing and near-field antenna technologies—especially those enhanced by emerging concepts such as metasurfaces, offer promising avenues for addressing the unmet needs in biomedical sensing.

In this chapter, we present an extensive review of the existing literature related to radar sensing and near-field antenna design, with a particular focus on their integration into biomedical applications. We begin by examining radar technologies and their potential in

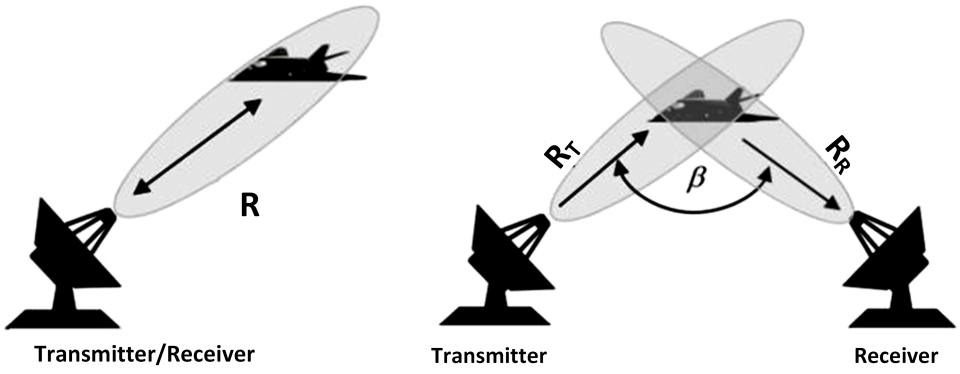
healthcare, followed by a focused discussion on near-field sensing principles, and conclude with a review of metasurface-based solutions for near-field enhancement in radar-based biomedical sensing.

2.1 Overview of Radar Sensing Technologies

Radar is a mature and widely adopted technology that utilizes electromagnetic waves to detect and characterize objects based on the reflection of transmitted signals. Originally developed for military and aviation applications, radar has evolved to serve a broad range of domains including automotive safety systems, remote sensing, environmental monitoring, gesture recognition, and healthcare. The core operating principle of radar involves the transmission of modulated electromagnetic waves, typically in the radio or microwave frequency range, which reflect off a target and return to the receiver. By analyzing parameters such as time delay, frequency shift (Doppler), and amplitude, radar systems can extract information about the target's distance, velocity, motion, and material properties.

Monostatic and bistatic radar systems represent two fundamental configurations used for target detection and range measurement [11]. In a monostatic radar, the transmitter and receiver are co-located or share the same antenna, meaning that the radar transmits a signal and listens for its echo from the same position, as shown in Fig. 2.1a. This setup simplifies the system architecture and signal processing, making monostatic radars widely used in applications such as automotive sensing, weather monitoring, and biomedical diagnostics. In contrast, a bistatic radar separates the transmitter and receiver by a finite distance, forming a spatial baseline between the two, as shown in Fig. 2.1b. This configuration offers advantages in terms of reduced susceptibility to detection, enhanced spatial resolution, and the ability to capture scattered signals from different angles. However, bistatic systems require more complex synchronization and geometry management, as the signal path and processing depend on the positions of both the transmitter and receiver relative to the target. In biomedical sensing contexts, monostatic configurations are more commonly adopted due to their compactness and ease of integration, although bistatic approaches are being explored for specialized applications that benefit from angular diversity or distributed sensing.

Radar sensing technologies have undergone remarkable advancements over the past several decades, evolving from bulky, military-grade systems into compact, high-resolution sensors suitable for a wide range of commercial and scientific applications. These advancements have been driven by innovations in microwave engineering, signal processing, semiconductor fabrication, and antenna design.



(a) (b)

Figure 2.1: (a) Illustration of the general principle of radar performance in two configurations: (a) monostatic radar, where the TX and RX are co-located, and (b) bistatic radar, where the TX and RX are spatially separated, forming a bistatic angle β at the target [11].

Off-the-shelf radar modules offer numerous benefits that have significantly accelerated the adoption and development of radar-based solutions across various fields. These pre-designed, cost-effective platforms provide ease of integration, compact form factors, and reliable performance, making them ideal for both research and commercial applications. As illustrated in Fig. 2.2, various off-the-shelf radar modules have been widely adopted across multiple domains. For instance, the Texas Instruments AWR1843BOOST radar module, operating at 79 GHz, has been widely used in automotive systems for applications such as object detection and adaptive cruise control [12]. The HB100 radar module, operating at 10 GHz, has found utility in through-the-wall sensing, safety monitoring, and collision warning systems [13]. Similarly, the Infineon BGT60TR13C radar, operating at 60 GHz, is commonly employed in biomedical and human-machine interaction applications, including cardio-respiratory health monitoring, eye tracking, gesture recognition, and in-car driver monitoring [14, 15]. These modules exemplify the versatility and accessibility of commercial radar systems, enabling rapid prototyping and deployment in diverse sensing environments.

2.1.1 Radar Applications in Modern Wireless Systems

Radar technology has evolved from its origins in military and defense systems into a vital component of modern wireless systems, finding broad adoption in automotive, industrial,

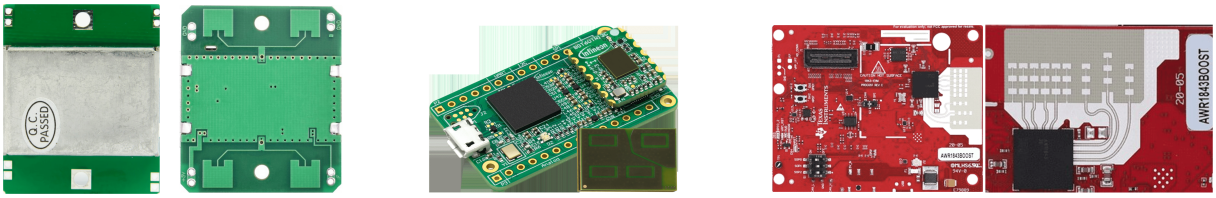


Figure 2.2: Commonly used off-the-shelf radar modules for various applications [12-14].

healthcare, and consumer applications. In particular, automotive radar has seen rapid integration into advanced driver-assistance systems (ADAS), supporting functions such as adaptive cruise control, blind-spot detection, emergency braking, and lane-keeping assistance [16]. These systems typically operate in the 24 GHz and 77–81 GHz bands, offering reliable performance under varying weather and lighting conditions, which makes them essential for both semi-autonomous and fully autonomous vehicles [17].

Beyond the road, radar technology is also shaping the future of urban air mobility. Drones are being increasingly adopted for package delivery, including urgent medical supplies like blood and vaccines. Companies such as Alphabet's Wing have deployed radar-enabled drone delivery services in several countries, while Wisk, a subsidiary of the same parent company, is developing autonomous air taxis aimed at reducing urban congestion [18].

In the consumer electronics and smart living sectors, radar plays a critical role in enabling wireless indoor sensing for gesture recognition, presence detection, and occupancy monitoring. These applications are central to smart homes, human–computer interaction, and energy-efficient building automation [19]. Compact radar modules offer the ability to detect fine-grained human motions—such as hand and finger gestures—even through obstacles and without the need for line-of-sight, unlike traditional optical systems [20]. Google's Soli radar, operating in the 60 GHz ISM band with a 7 GHz bandwidth, exemplifies this trend. It provides a range resolution of approximately 2 cm and is integrated into mobile devices to translate subtle gestures into computer commands using machine learning [21].

Radar also plays a key role in human sensing and healthcare, where its non-contact nature allows for monitoring vital signs such as respiration and heartbeat through clothing, bedding, or even in complete darkness. Advanced techniques, including continuous-wave Doppler radar and phase-modulated MIMO systems, allow for simultaneous tracking of multiple subjects—capabilities particularly valuable in epidemic scenarios such as COVID-19, where contactless monitoring is essential [22].

In the industrial domain, radar is widely used for short-range high-precision measurements. Millimeter-wave (mm-wave) radar sensors, due to their compact size and ability to operate under extreme environmental conditions, dust, heat, and low visibility, are ideal for applications such as tank level gauging, vibration monitoring, metal micromachining, and production engineering [23, 24]. Radar applications are typically dictated by frequency allocation and operational constraints. For instance, frequencies beyond 100 GHz face significant atmospheric losses, making them suitable mainly for short-range tasks such as high-precision vibration detection, security imaging, and gesture recognition [25].

In wireless communication systems, radar technologies are being explored within the emerging framework of Joint Radar-Communication (JRC) or Integrated Sensing and Communication (ISAC). These approaches leverage shared waveforms and hardware to perform both sensing and data transmission simultaneously, offering spectrum and hardware efficiency. ISAC is considered a foundational enabler for future wireless generations such as 6G, where situational awareness, spatial intelligence, and environmental adaptability are key performance indicators [26].

These diverse and evolving applications underscore radar's growing role as a versatile sensing modality in wireless systems, offering high resolution, robustness, and adaptability that complement and enhance existing wireless technologies.

2.1.2 Radar Applications in Biomedical Sensing and Imaging

Radar systems have recently been used in many bio-sensing applications to extract specific bio-signals pertaining to the target individual's health. They can be successfully applied to contactlessly characterize a number of biomedical parameters, detect emergencies, and provide excellent long-term care benefits [22]. Over the last decade, several prototypes have been developed that demonstrate the potential of using AI-powered radar systems for non-invasive glucose sensing (Fig. 2.3a) [27], wearable sweat monitoring (Fig. 2.3b) [28, 29], multi-person vital sign tracking (Fig. 2.3c) [22, 30, 31], gait monitoring [32], fall detection [32], human eye activity monitoring [33], and imaging [34]. Compact radars are also often used in wearable technology, such as smartwatches, for routine human health monitoring [35, 36]. Radar system development for industrial and biomedical microwave applications has recently accelerated due to an increase in interest in millimetre (mm)-wave communication for near-field sensing using low-profile and low-cost antennas providing sufficient energy penetration into the body [37]. Recently published papers in peer-reviewed journals demonstrate the utility of some compact mm-wave off-the-shelf short-range radar modules in biomedical applications such as blood glucose concentration level detection [38],

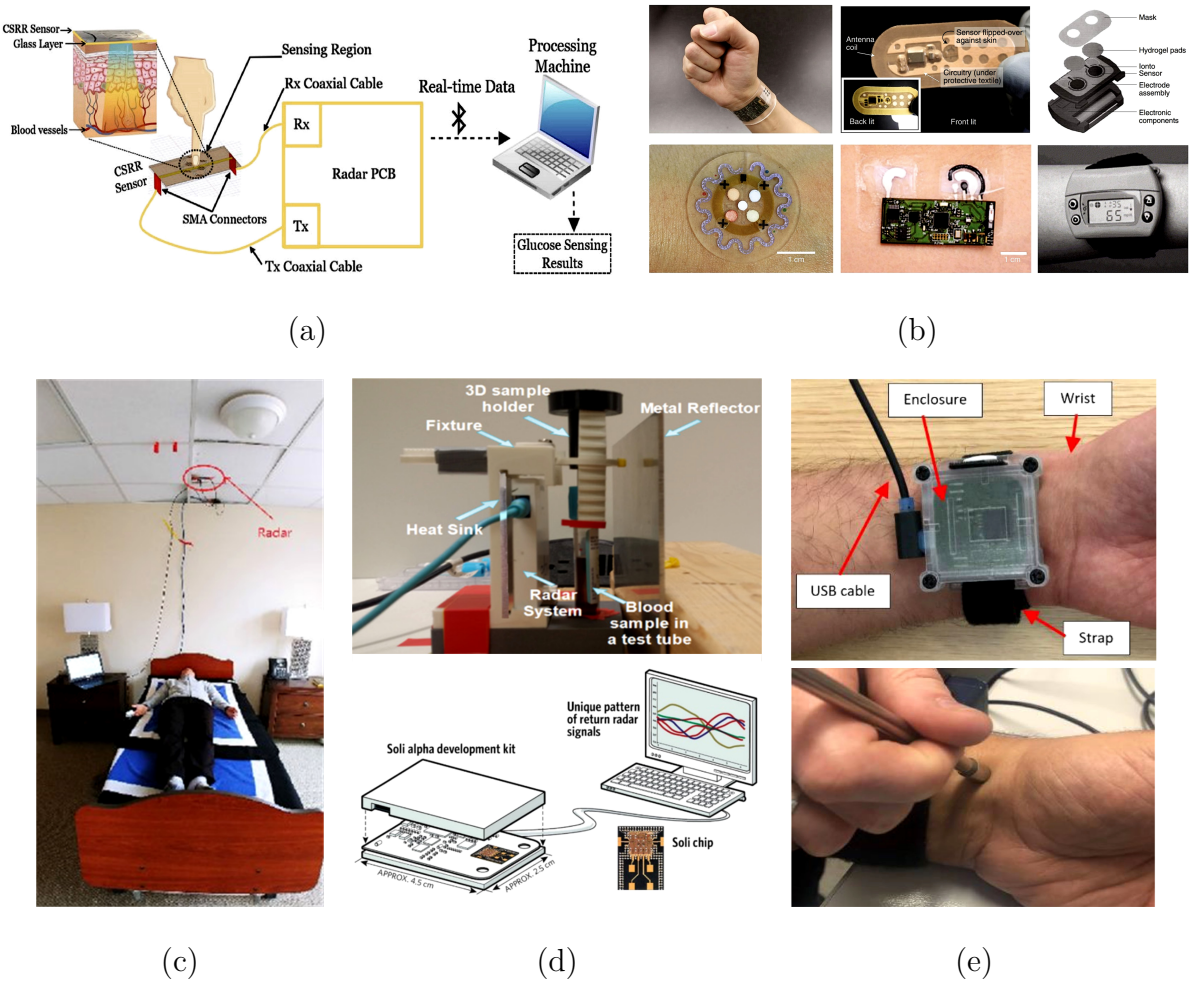


Figure 2.3: (a) General conceptual illustration of the portable radar driven sensor for measuring the glucose level non-invasively from the fingertip by sending electromagnetic waves of small wavelength into the blood vessels [27] (b) A multiplexed electrochemical system for continuous monitoring of a panel of analytes in sweat, integrated into a smart wristband for fitness monitoring [28] (c) a bedroom with a radar attached to a ceiling on the bed for human vital sign tracking [31] (d) The radar experimental setup for glucose detection in blood test tubes [39] (e) a millimeter-wave arterial sensing device mounted on wrist and a tonometer placed on radial artery of a subject [42].

differentiating blood samples from disparate glucose concentrations (Fig. 2.3d) [39], breast cancer detection [40], skin cancer detection [41], arterial pulse waveforms measurements for blood pressure tracking (Fig. 2.3e) [42], and continuous extraction of cardiorespiratory displacement waveforms with high precision [43].

Non-contact cardiopulmonary monitoring is emerging as a promising technological solution for monitoring vital signs during sleep, home healthcare, infant monitoring, post-surgery care, and search and rescue operations. Over the past years, radar-based non-contact physiological sensing has notably advanced, transitioning from laboratory experimental demonstrations to real-world applications across various fields, as highlighted in [44]. This progress potentially paves the way for the creation of a non-contact, inconspicuous, and long-term respiration sensing device. Cardiopulmonary monitoring typically occurs within a hospital setting, using sensors that need to be attached to the body, such as electrocardiogram (ECG) electrodes. Early detection and identification of respiratory irregularities through continuous monitoring are crucial in reducing mortality rates. During the COVID-19 pandemic, there has been a notable recognition within the scientific community regarding the significance of non-contact respiratory sensing. Numerous publications, as highlighted in [45], have emphasized the importance of non-contact methods for respiratory monitoring during this health crisis.

The traditional method of assessing cardiopulmonary functions is mostly contacted sensor-based where sensors need to be attached to the human subject. In hospital settings, ECG is the gold standard to monitor the heart rate of patients. Although there is no equivalent gold standard for respiratory monitoring. Respiratory rate is one of the critical vital signs but not measured frequently. But based on respiratory rate physiological instability of human subjects can be assessed. In hospital settings, different vital signs such as blood pressure, pulse rate, and arterial oxygen saturation can be monitored frequently by healthcare professionals (nurses) with different sensors. Although the respiratory rate is measured by visual inspection with a nurse counting the chest movement [10].

Non-invasive and discreet forms of respiratory monitoring devices hold significant potential in modern healthcare. For instance, monitoring vital signs in burn victim patients presents challenges due to insufficient available skin for electrode placement. A non-contact, wireless system for monitoring heart and breathing has the potential to alleviate the distress experienced by neonates and burn victims [10]. An effective Doppler radar-based non-contact and inconspicuous respiratory monitoring system has demonstrated its ability to identify various sleep apnea events in a clinical study [46]. Therefore, combining Doppler radar with other methods could render it non-contact and discreet, potentially reducing patient discomfort [47]. Furthermore, a portable sleep monitoring device based on radar might aid in early diagnosis of Obstructive Sleep Apnea [47].

Doppler radar has already demonstrated its effectiveness in monitoring human gait, as indicated in [48]. Furthermore, it has been employed for fall detection with remarkable accuracy, distinguishing between routine activities and instances of falls, as noted in [49]. The application of Doppler radar systems holds promise in elderly healthcare monitoring, potentially eliminating the need to attach sensors to the body. In this domain, Frequency-Modulated Continuous Wave (FMCW) radar has demonstrated its applicability by detecting both the target's position and chest micro-motions due to breathing, as referenced in [50]. Moreover, a proposal by [51] introduced an Ultra-Wideband (UWB) system-on-chip radar sensor capable of monitoring breathing rates, detecting respiration activity from sub-centimeter chest movements. Additionally, [22] showcased a radar-based sensor capable of multi-person tracking and monitoring vital signs (such as heartbeat and respiration) for more than one subject in a practical setting. Furthermore, [52] presented an assessment of a non-contact Doppler radar-based system, showcasing its efficacy in detecting vital signs, as well as an individual's presence and activities within an RF shielded room.

Characterized by elevated blood glucose levels, diabetes is a prevalent and chronic condition that underscores the crucial need for early detection and diagnosis. Despite the availability of invasive techniques, the increasing focus on non-invasive glucose measurement, offering additional benefits without causing inconvenience to the human body, drives ongoing research and the exploration of new possibilities [53].

Selecting an optimal operational frequency for glucose monitoring remains a challenge due to the trade-offs between tissue penetration, spatial resolution, and the need for a compact structure suitable for wearable devices.

At low frequencies, [27] introduces a design of a portable planar microwave sensor operating within the ISM band 2.4–2.5 GHz, enabling non-invasive blood glucose level monitoring. [54] proposes an alternative glucose monitoring approach using an antenna sensor operating at 4.2 GHz positioned on the pancreas to capture dielectric radiation signals. A noninvasive glucose sensing method using 3–10 GHz UWB microwave signals and STFT-based time-frequency analysis demonstrated detection of blood glucose levels through a simulated earlobe, with energy features and S21 parameters showing sensitivity down to 50 mg/dL increments [55]. The sensor presented in [56] operates at two resonance frequencies (5.5 GHz and 8.5 GHz) and utilizes the principle that changes in glucose concentration alter the dielectric permittivity of fingertip tissues, resulting in measurable shifts in resonance frequency across a glucose range of 89–262 mg/dL. A triple-pole CSRR-based microwave biosensor presented in [57] with sensitivity of up to 6.2 dB/(mg/mL) for non-invasive glucose detection over 70–120 mg/dL, using harmonic resonance amplitude variations in the 4.5 GHz range. Although a theoretical correlation exists between

permittivity and glucose levels, the changes in permittivity due to glucose are subtle, resulting in minute and often undetectable shifts in S-parameter magnitudes. Furthermore, S-parameters are highly sensitive to body movements and environmental electromagnetic interference, making them unstable for consistent glucose monitoring [53]. A noninvasive and continuous blood glucose monitoring system using radar-based microwave imaging is presented in [58]. Instead of utilizing frequency-tuned electromagnetic sensors, this approach employs ultra-wideband (UWB) radar to generate high-resolution images of tissues influenced by glucose concentration changes. The system uses Gaussian pulses spanning a 0–5 GHz bandwidth and demonstrates sensitivity across a glucose concentration range of 0.2 to 5 mg/mL.

On the other hand, millimeter-wave radar sensing has been identified as a promising non-invasive approach for blood glucose monitoring, utilizing changes in tissue permittivity and resonant frequency to detect glucose concentration variations with real-time capability [59]. An approach for monitoring glucose levels, outlined in [38] and [39], utilizes a robust low-power mm-wave radar system to detect various glucose concentration levels in artificial blood samples and differentiate between them. A preliminary dielectric spectroscopy study (300 MHz–67 GHz) revealed that the 50–67 GHz band offers optimal sensitivity to glucose-induced dielectric variations, providing a favorable trade-off between tissue penetration depth and detection sensitivity [39]. A 60 GHz FMCW mm-wave radar system was employed to detect glucose-induced variations in tissue dielectric properties by analyzing S-parameters of backscattered signals, which were further processed using machine learning algorithms to classify glucose concentrations ranging from 1.0 to 2.0 mg/mL with a resolution of 0.25 mg/mL [60]. The [61] introduces GlucoRadar, a contactless and non-invasive glucose sensing platform that integrates a 60 GHz FMCW radar with a compact convolutional neural network (CNN) for classification tasks. Operating in the far-field at a sensing distance of 4.8 cm, the system is designed to classify glucose concentrations in aqueous solutions across a physiologically relevant range of 50–200 mg/dL, with a resolution of 10 mg/dL. A multimodal sensing system combining 40-GHz millimeter-wave and near-infrared signals with skin temperature and pressure inputs is employed in [62] to enhance glucose prediction accuracy in a non-invasive approach for real-time blood glucose monitoring.

These recent works emphasize the growing need for the development of high-sensitivity mm-wave radar system for continuous monitoring of blood glucose levels. Nonetheless, monitoring blood glucose non-invasively remains challenging, with no reliable commercial or clinical device developed from various explored techniques [54].

The concept of near-field sensing improvement of a radar system including transmitter/receiver (TX/RX) antennas implies a significant increase in the near-field power density

radiated by TX into the body without disturbing antenna impedance matching while improving radar sensing by providing more received power reflected from the body into the RX antenna, representing the signal-to-noise ratio (SNR) enhancement of the radar system. It is therefore extremely challenging to develop a compact, wireless mm-wave radar for biomedical applications meeting the proposed requirements for high near-field sensing, high levels of integration, and low manufacturing costs.

2.1.3 Limitations of Radar in Biomedical Contexts

While radar technology offers several compelling advantages for biomedical applications, such as contactless operation, the ability to penetrate dielectric materials, and suitability for continuous real-time monitoring, it also presents numerous challenges that limit its effectiveness and broader clinical adoption.

One of the primary limitations of radar in biomedical applications lies in the limited penetration of electromagnetic waves through biological tissue. Although radar waves can traverse non-metallic materials, their interaction with human tissue is significantly constrained by high dielectric losses and dispersion [63]. The radar signal is often rapidly absorbed or scattered by skin, fat, muscle, and other heterogeneous layers, resulting in substantial attenuation and reduced sensing depth. This poses a significant challenge for accurately detecting physiological parameters located beneath the skin surface. Furthermore, different biomedical targets require specific trade-offs between penetration depth and spatial resolution, depending on the frequency band employed. For instance, mm-wave radar systems, typically operating in the 60–100 GHz range, offer high spatial resolution due to their short wavelengths, making them ideal for detecting fine dielectric changes near the skin, such as those related to non-invasive glucose monitoring. However, their limited penetration renders them unsuitable for deep-tissue applications. In contrast, low-frequency radar systems are better suited for deeper tissue sensing, such as tumor or cancer detection, though they suffer from lower resolution and require larger antenna structures [64]. As such, the selection of the operational frequency band is a critical design consideration that must be aligned with the specific biomedical use case, carefully balancing penetration, resolution, and system-level constraints to ensure optimal performance.

Another major challenge is the air–skin impedance mismatch, which results in strong reflections at the skin surface and reduced signal transmission into the body. These reflections dominate the received signal, often masking weaker echoes originating from subsurface structures or physiological activity [65]. To overcome this, specialized antenna designs and impedance matching techniques are required, often involving conformal or skin-contact antennas, which can compromise the radar's non-contact advantage.

Radar sensing in biomedical contexts inherently requires operation in the near-field region, primarily due to the proximity of the radar sensor to the human body and the shallow depth of many physiological targets. Unlike conventional far-field radar systems, which assume uniform wavefront propagation and rely on angular resolution at large distances, biomedical radar must operate within a few wavelengths of the body, where wave behavior is dominated by evanescent and reactive field components. These components decay exponentially with distance and do not radiate energy in the classical sense, making them particularly sensitive to local dielectric properties, a valuable trait when attempting to detect subtle physiological changes in tissues or fluids [66]. However, operating in the near-field introduces substantial technical challenges. The electromagnetic field distribution becomes highly non-uniform and complex, invalidating far-field assumptions such as plane wave propagation or simple beam steering. As a result, traditional antenna parameters like gain, directivity, and sidelobe level lose their intuitive meaning and must be reinterpreted within the near-field framework. Accurate sensing in this regime demands precise control of the antenna's spatial field distribution, careful consideration of the antenna, tissue interface, and often, direct contact or conformal placement to minimize mismatch and maximize energy coupling. In these scenarios, the signal reflected from the target of interest is often buried under stronger reflections from the skin or clothing, and the radar system must be engineered to focus electromagnetic energy precisely at or just beneath the skin to enhance sensitivity. This necessitates near-field field shaping and energy focusing techniques, such as the use of metamaterials, metasurfaces, or lens structures.

Additionally, motion artifacts and physiological variability present significant barriers to robust radar-based health monitoring. Even minor voluntary or involuntary body movements, such as posture shifts, tremors, or talking, can introduce artifacts that interfere with the accurate detection of vital signs like heart rate, respiration, or glucose-induced dielectric changes [67]. Furthermore, intra- and inter-subject variability caused by differences in skin thickness, hydration levels, age, and anatomical structures, can reduce the repeatability and generalizability of radar-based measurements across individuals [68].

From a system-level perspective, signal processing and noise rejection are additional hurdles. Biomedical radar signals are often weak and buried under clutter or environmental interference. Extracting meaningful physiological information from such signals requires advanced algorithms for filtering, feature extraction, and classification, many of which are still in experimental stages and not yet optimized for real-time clinical use [30].

Moreover, regulatory and safety considerations impose stringent constraints on the transmit power levels of radar systems, especially in wearable or continuous biomedical monitoring applications. To ensure human safety and minimize adverse biological effects from prolonged exposure to electromagnetic fields, radar devices must comply with inter-

national standards such as those established by the International Commission on Non-Ionizing Radiation Protection (ICNIRP) and the Institute of Electrical and Electronics Engineers (IEEE) [69]. One of the key metrics used to assess human exposure to EM radiation is the Specific Absorption Rate (SAR), which quantifies the rate at which the human body absorbs energy from the electromagnetic field, typically expressed in watts per kilogram (W/kg). In North America, regulatory agencies such as the Federal Communications Commission (FCC) and Health Canada have adopted SAR limits aligned with IEEE and ICNIRP recommendations. The FCC mandates a maximum localized SAR of 1.6 W/kg averaged over 1 gram of tissue, particularly for devices used in close proximity to the body, such as wearable sensors and handheld electronics. These constraints are even more critical for radar systems operating at millimeter-wave frequencies, where energy absorption by the skin is more pronounced due to the shallow penetration depth of high-frequency waves. To comply with these exposure limits, biomedical radar systems must operate at low effective isotropic radiated power (EIRP) levels, often well below 10 dBm. While this ensures safe operation, it simultaneously restricts signal strength, penetration depth, and signal-to-noise ratio (SNR), particularly in non-contact configurations or when sensing subsurface physiological signals.

Finally, despite significant academic progress, a lack of clinical validation and standardization continues to hinder the translation of radar-based biomedical systems into real-world healthcare settings. Few radar-based sensing devices have been approved for medical use, and there is limited availability of standardized testing protocols, reference models, or large-scale validation studies [70]. As a result, many proposed solutions remain confined to laboratory environments without crossing the threshold into routine clinical practice.

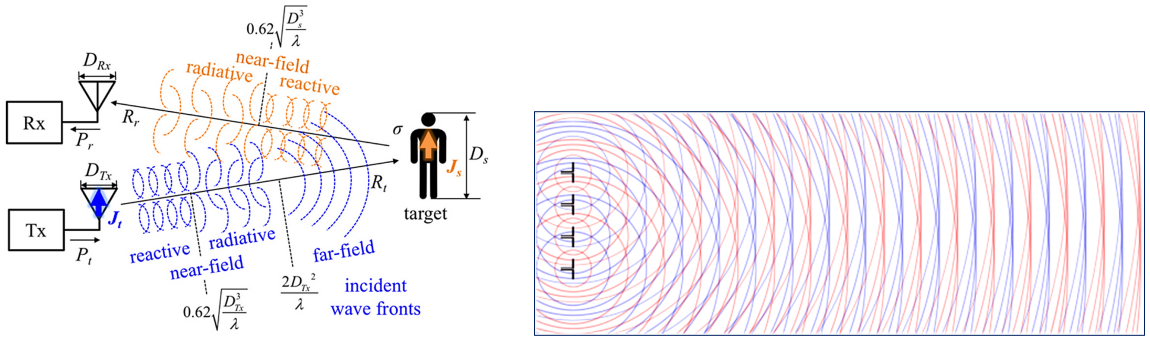
In summary, radar technology offers significant promise for biomedical sensing due to its non-contact, real-time, and adaptable nature. However, its broader adoption in clinical and wearable applications remains constrained by several key limitations. Overcoming these challenges demands an interdisciplinary approach that combines advances in hardware design, electromagnetic field control, and intelligent signal processing. Among these, one of the most critical aspects is the ability to manage electromagnetic behavior in close proximity to the human body, highlighting the importance of near-field sensing as a foundational enabler for effective radar-based biomedical systems. The following section explores this concept in detail, examining the principles, challenges, and technological approaches associated with near-field radar sensing.

2.2 Radar Near-Field Sensing

The rapid advancement of wireless communication technologies using radar systems has created a pressing need for highly efficient antenna systems that can enhance signal reception, transmission, and overall system performance. With the proliferation of wireless devices, high-data-rate applications, and the expansion of the Internet of Things (IoT), optimizing antenna functionality has become a critical focus. One promising technique to meet these demands is antenna near-field focusing, which involves concentrating electromagnetic energy within a confined region close to the antenna surface. By shaping the near-field distribution, this approach offers several advantages, including improved spatial resolution, increased signal strength, and enhanced communication reliability. Near-field focusing is particularly valuable in environments where precise energy delivery and localized sensing are essential, laying the groundwork for innovative applications in both communication and biomedical systems.

Generally, the electromagnetic (EM) field radiated from radar transmitter (TX) and receiver (RX) antennas can be categorized into two distinct regions: the near-field and far-field regions [66]. These regions exhibit markedly different wave propagation characteristics. As illustrated in Fig. 2.4a, the EM wavefront in the far-field region can be approximated as planar, which simplifies system analysis and antenna modeling. In contrast, EM propagation in the near-field region is more complex and typically requires spherical wavefront models to accurately describe field behavior. The boundary between these two regions is commonly defined by the Rayleigh distance, given by $2D^2/\lambda$, where D is the antenna aperture and λ is the wavelength [71]. The interaction of near- and far-field components becomes even more critical when multiple antenna elements are positioned in close proximity, as in array antenna configurations. This interaction is demonstrated in Fig. 2.4b, where the electric fields in the far-field region constructively combine in a well-ordered manner, while the near-field region exhibits a more chaotic and non-uniform behavior due to complex mutual coupling and reactive field interactions.

This section explores various aspects of antenna near-field focusing reported in the literature, including its principles, techniques, applications, and associated challenges, with a focus on advancing the understanding and implementation of this technology for modern communication systems and highlighting the potential of antenna near-field focusing in the field of biomedical, emphasizing its role in enhancing imaging resolution, targeted treatments, and non-invasive monitoring.



(a) (b)

Figure 2.4: (a) Electromagnetic wavefronts in the near-field and far-field regions of a radar TX/RX antenna, where the far-field exhibits planar wavefronts and the near-field exhibits more complex, typically spherical propagation. (b) Illustration of electromagnetic field interactions in a multiple-source (array) antenna configuration, showing constructive interference in the far-field and disordered field behavior in the near-field due to mutual coupling and reactive effects [66].

2.2.1 Microwave Near-Field Antenna Technologies

Historically, from the first-generation (1G) to fifth-generation (5G) wireless systems, the near-field region was relatively small, typically limited to a few meters or less, because of the use of lower frequencies and compact antenna arrays. As a result, most communication systems were efficiently designed under the far-field assumption [66]. However, in emerging 6G networks, characterized by extremely large-scale antenna arrays (ELAA) and tremendously high operating frequencies, the near-field region can extend to hundreds of meters, making traditional far-field approximations increasingly inaccurate. In biomedical sensing applications, similar considerations apply. Due to the close proximity of the radar antennas to the human body, signal interaction predominantly occurs within the near-field region. Therefore, accurate modeling and optimization of radar-based biomedical systems require near-field electromagnetic analysis to ensure proper field focusing, energy coupling, and signal interpretation in highly localized sensing environments.

Similar to far-field (FF) focusing, which is based on the principle of directivity in uni-directional antennas, near-field focusing (NFF) aims to concentrate electromagnetic energy at a specific point within the antenna's near-field region. This results in a localized increase in electromagnetic power density within a limited spatial region near the antenna

aperture. The fundamental concept behind NFF is to manipulate the phase distribution of the radiated fields, either by controlling the excitation phases of array elements, adjusting surface currents, or shaping the aperture field, so that the emitted waves constructively interfere at the desired focal point. Using a ray-optics approximation, it can be shown that the phase profile across the aperture must compensate for the varying path lengths between each point on the antenna or array surface and the focal point. This ensures that the wavefronts arriving at the focal point are in phase, thereby forming spherical equiphase surfaces that converge at the targeted location, as illustrated in Fig. 2.5 [72]. Such near-field focusing techniques are particularly beneficial in applications requiring spatial selectivity and enhanced resolution in the immediate vicinity of the antenna, such as biomedical sensing and high-precision localization.

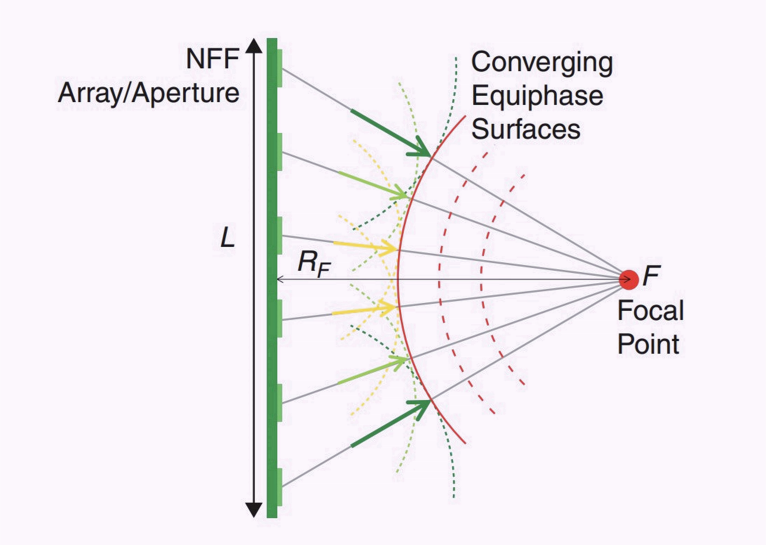


Figure 2.5: convergence of equiphase surfaces generated by electromagnetic sources located on a planar aperture and directed towards a focal point, F, within the antenna's radiative NF region. L, corresponds to the antenna aperture size, and R_F represents the focal distance [72].

NFF techniques have shown promising advantages in a variety of practical applications where conventional far-field antenna designs fall short. For example, in certain radio-frequency identification (RFID) systems, the tagged object is located so close to the reader that it lies within the reader antenna's near-field region. In such cases, an NFF-enabled RFID reader antenna offers improved performance and read accuracy compared to a traditional FF-focused design [72]. Similarly, in non-contact, non-destructive microwave mate-

rial inspection, near-field focusing can significantly enhance sensor sensitivity, particularly when detecting small spatial variations in material properties or testing compact samples [73]. NFF arrays also find utility in microwave radiometry for temperature sensing, where concentrated energy enhances measurement resolution and accuracy [6]. Moreover, multi-focus NFF antennas are being explored for multipoint wireless charging of mobile electronic devices and in simultaneous wireless information systems, where they can serve as smart antennas that dynamically focus energy and data streams to multiple targets [72].

To address the growing demand for highly directive and compact NF solutions, a wide range of antenna technologies and array configurations have been proposed and studied. Many of these designs are adapted from traditional far-field focused antenna architectures, including rectangular and circular arrays of printed antennas, arrays of dielectric resonator antennas, reflectarrays, transmitarrays, and lens antennas. Each of these configurations offers specific advantages and trade-offs depending on the intended near-field application [74]. In the design of near-field focused antennas, it is common practice to evaluate performance using conventional FF parameters, such as radiation pattern, antenna gain, directivity, and sidelobe level. These parameters remain important, as they help assess the antenna's ability to minimize unwanted radiation into the far-field region, which is critical in many NF applications. In short-range and confined environments, reducing far-field radiation is especially beneficial, it helps prevent interference with nearby wireless systems, mitigates multipath propagation effects, and limits unnecessary electromagnetic exposure to surrounding personnel.

Some existing options comprise pyramidal or conical horn antennas with a dielectric lens in front of the antenna aperture, ellipsoidal reflector antennas, and leaky-wave (LW) antennas [75]. In the following, NFF antennas made by slotted waveguide antennas [76], radial line slot antennas, and arrays of open-ended waveguides have also been proposed. Indeed, when compared with printed antenna technology, waveguide antennas show a better efficiency and a higher power handling. More recently, NFF antennas using dielectric resonator antennas [77], [78] and the surface-integrated waveguide technology [79], [80] have also been investigated. However, these options are typically bulky and heavy, particularly when employed in the microwave frequency range, making them less suitable for integration into compact devices and often less efficient for various applications, including biomedical ones. As a result, alternative technologies that facilitate the development of planar NFF microwave antennas are more preferable. Many of these alternatives involve the use of array antennas, where the phase of each element's current is adjusted to achieve constructive interference, effectively focusing all field contributions at the desired focal point [74].

Numerous planar and linear microstrip arrays have been specifically developed and tested for wireless communication at frequencies spanning 2.4 GHz, 5.8 GHz, and within

the X-band range [72]. Compared to traditional unfocused microstrip arrays, NFF arrays primarily necessitate an adjustment in the microstrip feeding network for their operation. The NFF array serves to enhance the field amplitude within the antenna's near-field region while concurrently diminishing the far-field radiation in comparison to the corresponding FF-focused array. In the context of the millimeter-wave near-field focused array antenna operating at 35 GHz described in [81], its radiated power is concentrated at a near-field point, generating a focal spot approximately 15 mm wide and 150 mm deep.

Near-field-focused planar array structures face a multitude of challenges that hinder their effective implementation in various applications. Their complex design, high profile, high cost, and dependency on lossy feeding networks collectively pose significant obstacles in their practical usage. One of the primary limitations lies in their inability to provide near-field focus in close proximity to the antenna array surface due to the high mutual coupling between the elements. This shortfall limits their precision and effectiveness, hindering the ability to target specific areas or tissues with accuracy in biomedical applications or other contexts requiring precise near-field focus. The cumulative impact of these issues compromises the overall efficiency and practicality of these planar array structures, underscoring the pressing need for innovative solutions to address these shortcomings and enhance their usability in diverse real-world applications.

Fresnel zone plate lens antennas [73], [74], reflectarrays (Fig. 2.6a) [82], [83], [84], and transmitarrays (Fig. 2.6b) [85] have also been considered to implement NFF planar lens antennas, which can be considered as devices that are able to shape the phase-front of the electromagnetic field radiated by a conventional feed antenna. They are proposed as alternatives to avoid the complexity and losses introduced by the feeding network of electrically large NFF microstrip arrays. However, it is important to note that spillover can significantly reduce their efficiency. Similar to conventional Far-Field focused reflectarrays and transmitarrays, these devices achieve the necessary phase adjustment by modifying one or more geometric parameters within the unit cell of the quasi-periodic surface.

Transmitarrays and reflectarrays achieve the required phase modification by suitably adjusting one or more geometric characteristics within each unit cell of the quasi-periodic surface used for transmitting or reflecting. In the conjugate-phase method [72], the phase of excitation for each element in the array is configured to compensate the phase delay caused by the path between the array element and the specified focal point. This adjustment aims to ensure that all contributions synchronize constructively at the focal point. When the focal distance is considerably larger than the size of the antenna, the phase adjustments can be approximated by a quadratic phase profile (referred to as the Fresnel approximation). Actually, due to the field spreading factor, the peak of the radiated power density does not occur at the focal point where all field contributions sum in phase (focal shift) [72].

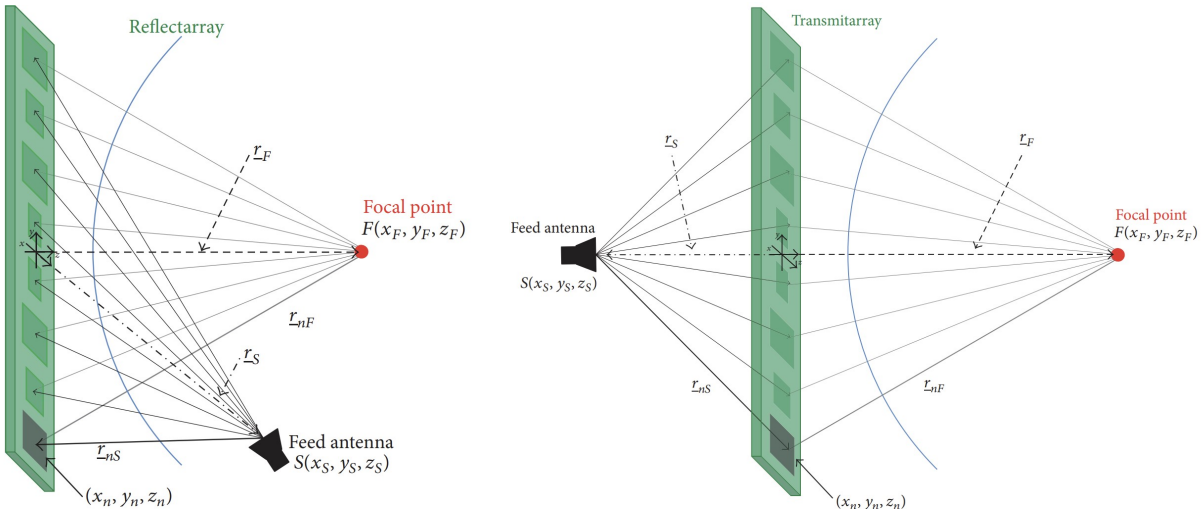


Figure 2.6: Basic geometrical configurations of different NFF planar lens antennas: (a) reflectarray, and (b) transmitarray [82-85]

Reflectarrays combine the promising features of reflector and array antennas into the realization of high-gain FF-focused antennas. In NFF reflectarrays, the required phase of the reflection coefficient at the nth element, for focusing at the focal point F, can be calculated by using a ray-optics approximation. By considering the geometrical parameters shown in Fig. 2.6a, it follows that each cell of the quasi-periodic surface has to introduce a phase shift of the reflection coefficient given by [74],

$$\varphi_n = \frac{2\pi \left(r_{nS} - r_S + r_{nF} - r_F\right)}{\lambda} \tag{2.1}$$

where r_{nS} and r_{nF} are the distances of the nth array element from the feeder phase center S(x_S, y_S, z_S) and the focal point F(x_F, y_F, z_F), respectively. Moreover, r_S and r_F are the distances of the array center from the feeder phase center and the focal point, respectively.

In [84], a Near-Field Focusing reflectarray specifically designed for RFID systems operating at 2.4 GHz is presented and assessed. This circular reflectarray measures 80 cm in diameter and enables the attainment of a focal spot size of approximately 20 cm on a transverse plane, located at a distance of 90 cm from the center of the reflectarray. For higher frequencies, an NFF reflectarray designed for operation at 8 GHz was created and

prototyped to exhibit efficacy in H3N2 virus sanitization [86]. This reflectarray measures around 16 cm, with both the feed horn and the designated focal point situated at a distance of 16 cm from the reflectarray surface.

In Near-Field Focusing transmitarrays, the phase compensation applied at the n-th array element for focusing at the focal point FF is similar to equation 2.1, utilizing the geometrical parameters depicted in Fig. 2.6b. Unlike a reflectarray, a transmitarray does not necessitate an offset feed arrangement to evade blockage effects; the feed can be positioned directly in front of the array without incurring blockage losses. In [87], a simple model for analyzing an NFF transmitarray is presented, utilizing an array-based approach capable of addressing the spillover effect at 10 GHz. An 18x18 NFF transmitarray, focused at 6.5 cm from the antenna aperture, demonstrates a spot size of 1.7 cm and a side lobe level of approximately -13 dB at the focal plane.

In conclusion, this section has provided a comprehensive overview of the existing literature on near-field-focused antenna technologies. Through this review, the strengths and limitations of these NFF antennas have been explored and discussed. The examination underscores the intricate characteristics of these technologies, offering insight into their strengths and weaknesses across diverse applications. Understanding the intricacies of NFF antennas is crucial for further advancements in this field, paving the way for innovative solutions that leverage strengths while addressing the identified challenges. Furthermore, in the next section, the application of NFF antennas specifically in the biomedical context is presented, offering deeper insights into their potential uses and challenges within this critical domain. This exploration will illuminate the specific considerations and opportunities for employing NFF antennas in biomedical applications, contributing to the ongoing evolution of this technology for healthcare and diagnostic purposes.

2.2.2 Near-Field Antennas in Biomedical Applications

In addition to its pivotal role in enhancing traditional communication systems, antenna near-field focusing has garnered significant attention for its potential applications in the realm of biomedicine. The intersection of antenna technology and biomedical engineering presents a promising frontier for developing innovative solutions that can revolutionize healthcare diagnostics and therapeutics. Antenna near-field focusing, when tailored and adapted to the unique requirements of biomedical applications, holds the promise of improving imaging resolution, enabling precise targeted treatments, and facilitating non-invasive monitoring within the human body.

The utilization of antenna near-field focusing in biomedical applications requires a com-

prehensive understanding of both antenna engineering and biomedical principles. Leveraging the principles of near-field focusing enables the customization of electromagnetic fields to precisely interact with biological tissues in a controlled and targeted manner. This approach creates prospects for non-invasive imaging methods like microwave and millimeter-wave imaging, crucial for precise diagnostics that demand improved resolution and depth penetration.

Due to the lack of widely accepted near-field performance metrics to assist in antenna selection and design, it is a common practice to initially utilize only far-field characteristics in the preliminary stages. Criteria fall on phase center and radiation pattern stability, unidirectional beam [88], and phase linearity across the bandwidth [89]. Other factors that do not necessarily depend on the observation distance but are affected by the near-field obstacles are required as well, such as impedance bandwidth [90]. The band falls typically within the 1–10 GHz interval, as a compromise between opposing requirements: highest possible body penetration depth, highest possible image resolution, and smallest antenna size. Frequently used antennas include bowties [91], planar dipole [92] and monopole [93], slot-based [94], Vivaldi [95], and horn [96] antennas.

Different types of antennas, such as high-profile reflectors or aperture antennas are frequently used to provide high sensing in the near-field region for biomedical applications [97]. The quadratic phase for near-field focusing on reflector antennas can be obtained, as stated in [97], by defocusing the feed away from the focal point. The structure produced by this method, however, is bulky and unsuitable for low-profile and compact applications. Planar antennas with a low profile and easy-to-fabricate features present an alternative option [84]. [98] describes a near-field sensing system for glucose level monitoring that uses two facing microstrip patch antennas, TX and RX, operating at 60 GHz. However, the single microstrip planar antenna essentially provides low field intensity in the near-field region. A near-field focused microstrip array antenna at 2.45 GHz reported in [99] to maximize the power transmission efficiency between two antennas. However, a large number of array elements are necessary to achieve high focused power in the near-field region resulting in a high-profile structure with a complex feeding network design, high fabrication cost and loss.

Space-fed planar array antennas, such as reflectarrays and transmitarrays, offer an alternative by removing the intricate and expensive feeding networks, resulting in higher efficiency by modifying the phase front of the radiated fields from the feed [100]. A design of an optically transparent reflectarray antenna at 5.8 GHz and a bi-layer resonant wires transmitarray antenna at 157 MHz for power transfer enhancement in near-field are reported in [101] and [102], respectively. Near-field multi-focus reflectarray and transmitarray apertures illuminated by numerous horn antennas are also shown in [103] and [104]

with a distance of 9.6 λ at 5.8 GHz and 9.3 λ at 28 GHz, respectively. In [105] a folded transmitarray structure fed by a horn antenna at a spacing of 2.2 λ is proposed to concentrate power in both the near and far field at 2.45 GHz. Since the feed is not in the near-field radiation zone, the feeding blockage has no impact on the radiation of the transmitarrays in comparison to the reflectarrays [106]. In the literature on near-field focusing, existing transmitarray antenna designs do not possess the capacity to seamlessly integrate with a low-profile radar system operating at mm-Wave frequencies. This limitation is attributed to their conspicuous high-profile structures, along with their reliance on a bulky feed antenna positioned at a considerable distance from the aperture.

Focusing techniques have been applied in biomedical engineering to improve spatial resolution in imaging systems or to increase the temperature in size-limited spot regions. In microwave hypothermia applicators, for instance, the deposited power density must be maximized in a limited spot area around the diseased tissue without overheating the surrounding healthy tissues [107], [108], [109], [110]. Further applications could exist in communication/tracking systems for wireless endoscopic capsules or in antennas for remote monitoring of vital signs [111].

In recent years, the endoscopic evaluation of disease activity has become a crucial clinical practice, playing a substantial role in medical diagnosis, prognosis, and monitoring. These techniques predominantly rely on non-invasive approaches to diagnose endoscopic diseases such as gastrointestinal tract diseases, tumors, infections, and more. However, these applications face critical limitations due to various factors, including the size of the capsule, low data transmission rates, and inefficient antenna propagation. Hence, the development of an antenna with superior performance parameters is imperative to address these challenges and enhance the efficacy of these diagnostic tools. Wireless endoscopy has garnered significant attention as it provides a non-invasive method for diagnosing and treating patients. This technology offers a means of conducting endoscopic procedures without the need for invasive techniques [112]. In endoscopic systems, the antenna plays a crucial role in gathering image data used to examine gastrointestinal-related diseases and transmitting this information to external interfaced units. However, designing antennas specifically intended for in-body applications remains a significant challenge for researchers worldwide. Several critical factors, including antenna size, bandwidth, patient safety, and various security considerations, must be carefully considered in the design process. These complexities contribute to the challenge researchers face in developing antennas suitable for in-body medical applications [112]. Certainly, the intricate dielectric properties of human tissues pose a significant challenge, particularly the necessity for wide bandwidth in such medical applications. In a recent study introduced in [113], a microstrip antenna design capable of delivering ultra-wideband performance suitable for endoscopic applications is

presented. This antenna is specifically engineered to operate within the ISM 2.4–2.4835 GHz frequency band, addressing the need for broader frequency coverage essential in medical imaging and diagnostic procedures.

Monitoring blood glucose levels non-invasively has posed a considerable challenge. Few devices offer truly non-invasive, accurate, and reliable measurements. Various non-invasive techniques have been explored, including Bioimpedance spectroscopy, Electromagnetic sensing, Near Infrared (NIR) spectroscopy, Optical coherence tomography, and Ultrasound. However, none of these methods has yet led to the development of a reliable commercial or clinical glucose monitoring device, as mentioned in [114]. Additionally, efforts have been directed towards non-invasive epidermal blood glucose monitoring from interstitial fluids and sweat. While some devices exist, their reliability still needs to be rigorously tested against gold standard clinical methods in extensive trials, as highlighted in [115]. Consequently, the development of a completely contactless method for monitoring blood glucose levels remains relatively rare.

In a recent study discussed in [116], a novel technique was proposed to measure blood glucose levels utilizing temperature readings from the eardrum and the inner surface of the head obtained by a contactless thermometer. The method capitalizes on the correlation between temperature elevation and the increase in blood glucose levels that follows food intake. The researchers developed an empirical equation to account for these relationships in order to estimate blood glucose levels based on eardrum temperature. Evaluation through Standard Clark error grid analysis revealed that the technique demonstrated an average accuracy range of approximately 87.5% in estimating blood glucose levels, as reported in [116]. The current focus on contactless techniques for physiological monitoring predominantly revolves around video-based or radar-based methods. However, changes in blood glucose levels do not typically produce significant alterations detectable by video-based approaches. Similarly, there is a lack of evidence supporting the measurable detection of blood glucose changes using radar technology. The method based on eardrum temperature for contactless blood glucose monitoring shows promise; however, its suitability for daily blood glucose monitoring can only be confirmed after a comprehensive large-scale clinical trial to assess its efficacy and reliability.

In medical microwave imaging (MMWI), the antennas usually operate at close distance from the body and are required to pick up weak echoes from the inside that are masked by high skin reflection. The near-field antenna behavior strongly determines how the received signals affect the effectiveness of the imaging algorithms. In the context of medical microwave imaging, it is common to assume conventional far-field radiation behaviors for antennas, as indicated in [90]. Antennas are pivotal in both stages of the imaging process, particularly due to their close proximity to the body for link budget considerations. The

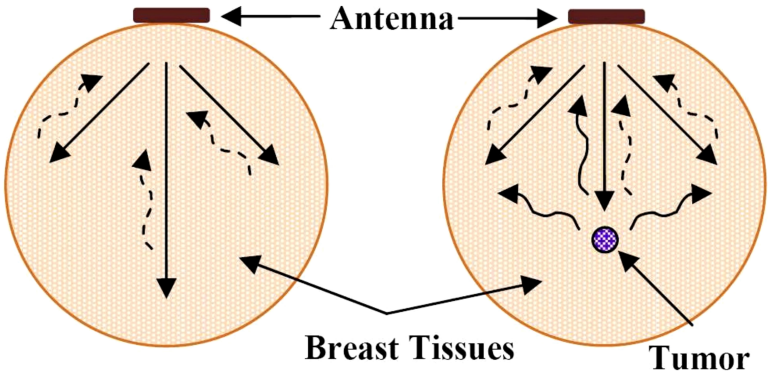


Figure 2.7: Schematic representations of breast, antenna and tumor showing signal scattering in a normal breast and a breast with a tumor [119]

weak signals scattered by tumors face additional attenuation due to body penetration loss, while SAR limitations restrict the maximum incident power. The antennas' extremely close proximity to the body necessitates a meticulous consideration of antenna characteristics that are usually overlooked in the postprocessing of imaging signals [90].

Microwave breast imaging (MBI) employs lower-power, longer-wavelength signals (as compared to X-ray mammography) to gather information about breast tissues, offering a potentially safer and more accurate method for routine breast scanning. However, a significant challenge in this technology has been the substantial reflection of signals from the skin of the breast. Many techniques to reducing the signal reflection at the breast skin have been employed [117], [118]. Most of the approaches use an intermediate solution between the antenna and the breast, but no significant success has been achieved thus far. [119] presents a method to reducing the effect of signal reflection from the breast skin by placing the antenna in-contact with the breast skin. The described method involves treating the skin as a layer of the antenna substrate operating at 2.54 GHz, and the influence of the antenna's contact with the skin is integrated into the antenna's design. Consequently, this design enables the placement of the antenna directly on the breast skin. This approach aims to decrease the signal scattering from the skin, directing more of the transmitted signal towards the tumor. This enhancement potentially increases the sensitivity of tumor detection, as illustrated in the provided Fig. 2.7.

Further advancements in microwave antenna design for biomedical applications are crucial to establish highly efficient devices capable of enabling real-time health monitoring. The existing efforts, although commendable, face a notable challenge due to their limited efficiency, largely attributed to the inadequate consideration of near-field aspects in antenna

design. The optimization of antennas for medical purposes demands a more comprehensive integration of near-field principles [120].

2.2.3 Limitations of Existing Near-Field Antennas

Despite the increasing use of antennas in biomedical sensing, several technical challenges hinder their effectiveness and integration into practical healthcare systems. One of the most critical issues is the inappropriate selection of the operational frequency band. Millimeter-wave systems provide high spatial resolution but suffer from limited penetration, making them ideal for shallow sensing tasks like glucose monitoring, whereas low-frequency systems enable deeper penetration for applications such as tumor detection but sacrifice resolution. Therefore, frequency selection must be carefully aligned with the specific biomedical application to ensure optimal performance.

Additionally, many conventional antenna structures are physically complex, high-profile, and costly to fabricate, particularly due to the use of lossy feeding networks and multilayer designs. These characteristics make them unsuitable for compact, low-cost, and wearable implementations. Solutions to this include adopting simplified, low-profile, feedless designs that minimize fabrication cost while maintaining near-field performance.

A common design limitation is the continued reliance on traditional far-field antenna principles, which fail to account for the complex electromagnetic interactions that occur when the antenna operates in close proximity to the human body. In such cases, near-field theory must be applied to accurately model and design antennas capable of focusing energy in localized tissue regions.

Impedance mismatch between the near-field antenna and the human body presents another major constraint. Biological tissues exhibit high losses and heterogeneous dielectric properties, often leading to significant reflection losses at the interface. This mismatch can be mitigated by incorporating intermediary matching layers, such as metamaterial or metasurface interfaces, which help bridge the impedance gap and enhance coupling efficiency.

Furthermore, many existing designs fail to concentrate electromagnetic power precisely at the intended sensing location. Poor spatial focusing reduces sensitivity and signal-to-noise ratio (SNR). This can be addressed by designing antennas or metasurfaces that direct near-field energy to specific targeted regions within the body, thus enhancing localized sensing performance.

Beyond these core challenges, additional factors further limit existing near-field antenna performance in biomedical scenarios. One such issue is the lack of adaptivity in dynamic

environments. The human body is continuously changing due to motion, posture, and physiological variability, but many antennas are statically designed. This motivates the use of reconfigurable or tunable metasurfaces that can dynamically adjust the focal point and impedance matching in real time.

Another significant limitation is the low spatial resolution in multi-layer tissue environments, where traditional antennas struggle to distinguish subtle dielectric changes between adjacent tissue layers. Multi-frequency or dual-band near-field antennas can be used to probe at multiple depths, offering layered insights and improved diagnostic capability. When multiple antennas are arranged in close proximity, mutual coupling often distorts field uniformity and affects performance, especially in multi-radar or distributed sensing systems. Incorporating decoupling structures or metamaterial isolators can effectively mitigate this problem and preserve signal fidelity.

There is also a lack of standardized testing procedures and benchmarking for evaluating antenna performance in biomedical contexts. This hinders fair comparison and clinical translation. The development of standardized tissue-mimicking phantoms and public datasets can help unify validation efforts across different research groups.

To help mitigate some of these design and implementation barriers, many researchers have turned to commercially available radar modules, which offer compact, integrated, and user-friendly platforms. These radars typically consolidate the TX/RX antennas, frequency generation, signal processing, power management, and communication interfaces into a single device. Available in various frequency bands, such as 24 GHz, 60 GHz, and 77–79 GHz, they offer flexibility and accessibility for a wide range of biomedical sensing tasks. Their plug-and-play nature and low-cost production make them attractive for rapid prototyping and continuous health monitoring. Furthermore, they eliminate the need for costly external equipment like vector network analyzers and significantly simplify the system development pipeline.

However, the integrated antennas in these commercial radar systems inherit the same fundamental limitations as conventional near-field antennas, namely poor impedance matching with biological tissues, lack of spatial field control, and inability to dynamically focus or steer the energy. These limitations restrict their sensing precision, especially in contactless or shallow-depth biomedical applications.

To overcome these issues without modifying the internal radar hardware, metasurfaces have emerged as a powerful external augmentation strategy. These ultra-thin, subwavelength-engineered structures can be precisely designed to reshape and focus electromagnetic energy, acting as a lens or matching interface between the radar and the human body. When integrated with commercial radar systems, metasurfaces enable enhanced near-field fo-

cusing, multi-point sensing, frequency-selective behavior, and improved SNR—all while preserving the radar's compact form and ease of use. Therefore, metasurfaces represent a critical innovation that bridges the gap between affordable, commercially viable radar platforms and the high-performance demands of biomedical sensing applications.

2.3 Metasurface Near-Field Focusing Approaches

In recent years, metasurfaces open a whole new paradigm in physics and engineering by enabling new microwave properties not achievable using conventional antennas and microwave devices [121]. A metasurface with hundreds or thousands of periodic subwavelength elements can be fabricated with a simple and low-cost PCB process, especially when produced in large quantities. By tailoring the properties of each element of the metasurface, one can spatially control the phase of scattered waves and consequently mold the wavefronts [122]. Based on this concept, it is easier to realize near-field focusing. Owing to the properties of manipulating waves flexibly, metasurface of microwave near-field focusing is a promising technique for high-efficiency Wireless Power Transfer as well as biomedical sensing.

2.3.1 Metasurface Theory and Principles

Metasurface antennas represent an emerging class of advanced electromagnetic devices engineered to precisely manipulate and control the behavior of electromagnetic (EM) waves. These antennas typically consist of two-dimensional arrays of subwavelength-sized resonant elements, periodically arranged on a planar surface. The strategic design of these elements enables wavefront shaping, polarization control, and frequency-selective manipulation, offering compact, high-performance solutions for modern communication and sensing applications. When integrated with radar systems, metasurface-enhanced radar architectures provide numerous advantages over traditional designs, including higher spatial resolution, enhanced sensitivity, and improved target localization. These capabilities are particularly significant in biomedical applications, where precise energy focusing, compact design, and high sensitivity are required for non-invasive physiological monitoring and imaging.

Metasurfaces, broadly classified as planar metamaterials with subwavelength thickness, are inherently compatible with modern fabrication methods such as lithography, inkjet printing, and nano-imprinting techniques. Both metamaterials and metasurfaces are rapidly growing fields of research due to their ability to achieve spatially varying EM responses in terms of phase, amplitude, and polarization. By engineering the geometry and

arrangement of their constituent unit cells, metasurfaces can realize diverse functionalities such as beam deflection, absorption, lensing, and filtering.

In terms of their functional operation, metasurfaces can be categorized based on their electromagnetic response mechanisms. These include frequency-selective surfaces (FSSs), high-impedance surfaces, perfect absorbers, and reflective/transmissive phase gradient surfaces, among others. As defined in [123], FSSs are a subclass of metasurfaces distinguished by their use of periodic resonant elements that produce sharp frequency-dependent reflection or transmission characteristics. This targeted spectral behaviour makes FSSs a practical choice for applications that need spatial filtering or precise control of specific frequency bands, without requiring the broader design complexity found in more general-purpose metasurfaces.

From the perspective of antenna and microwave engineering, FSSs are typically realized using planar and periodic arrays of metallic elements—such as patches, strips, or slots—deposited on a dielectric substrate. These elements are usually electrically thin (negligible thickness compared to the wavelength) but large relative to the metal's skin depth, allowing them to be accurately modeled as perfectly conducting, resonant scatterers. This approximation is also applicable to complementary FSS structures, such as slot-type (aperture) arrays. However, aperture-type FSSs become less effective when the cavity area approaches the size of the unit cell, limiting their design flexibility [124].

The geometry and arrangement of FSS unit cells strongly influence their spectral characteristics. Traditional FSS designs have employed square or hexagonal wire mesh structures, commonly referred to as capacitive grids. These configurations function as spatial filters, allowing EM waves at certain resonant frequencies to pass while blocking or reflecting others. This behavior emerges when the frequency of the incident plane wave matches the natural resonance of the unit cell. As a result, FSSs can selectively transmit or reject EM waves, and are best identified as two-dimensional spatial filters [123].

One notable characteristic of traditional FSSs is the presence of side lobes in both transmitted and reflected fields. These side lobes arise from the resonant size of the array elements and the periodic spacing between them, often resulting in grating lobes when the periodicity is not deeply subwavelength. However, in contrast to classical FSSs, modern metasurfaces are composed of unit cells that are much smaller than the operating wavelength, effectively suppressing grating lobes and producing smoother frequency responses [125].

The field of frequency-selective surfaces has been extensively studied for over six decades, and numerous microwave and optical FSS structures have been proposed and realized [123]. These structures have evolved to support diverse applications ranging from stealth

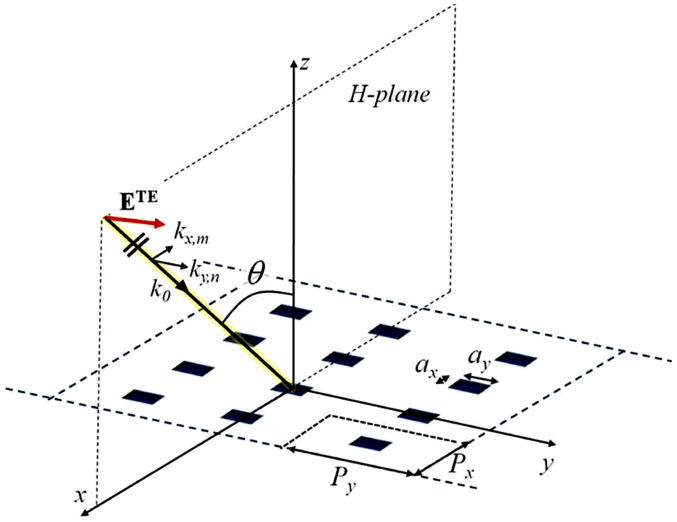


Figure 2.8: Scheme of the freestanding array of metallic patches of zero thickness under oblique incidence [126].

and shielding to bandpass filtering, antenna radomes, and near-field focusing systems. In the context of metasurface antennas, FSS-based designs offer a cost-effective, planar, and lightweight platform to achieve frequency-selective beam control in compact radar and sensing systems.

In order to present the basic principles of FSS design, it is considered a freestanding periodic surface built from the periodic arrangement of conducting zero-thickness metallic patches as shown in Fig. 2.8. The array extends along the x-axis and y-axes, with periodicieties P_x and P_y, respectively. The periodic surface is located at z=0 and a plane wave impinges on this surface from the direction defined by θ. As can be seen in Fig. 2.8, the plane of the incident is xz, and the wave is TE-polarized (its electric field is directed along the y-axis). Therefore, in the scanned H-plane, the impinging field is always parallel to the metallic patches, having a strong interaction with them. Due to periodicity, Floquet (space) harmonics are excited by the incident plane wave as it reaches the array [126]. These scattered waves can be either TE or TM polarized. The wavenumbers in the x- and y-axes associated with the space harmonics are given by,

$$k_{x,m} = k_0 \sin\theta + \frac{2m\,\pi}{P_x} \quad , \quad k_{y,n} = \frac{2n\,\pi}{P_y} \tag{2.2}$$

where $m, n = 0, \pm 1, \pm 2, \ldots$, and $k_0 = \frac{2\pi f}{c}$ is the free-space wavenumber, with f being the

frequency and c the speed of light in vacuum. Each excited space harmonic is defined by a pair of integers mn with the following associated complex wavenumber along the z-direction:

$$k_{z,mn}^{(\varepsilon_r)} = \begin{cases} \beta_{mn} = \sqrt{k_0^2\varepsilon_r - k_{x,m}^2 - k_{y,n}^2} & f \geq f_{c,mn}^{(\varepsilon_r)} \\ -j\alpha_{mn} = -j\sqrt{k_{x,m}^2 + k_{y,n}^2 - k_0^2\varepsilon_r} & f < f_{c,mn}^{(\varepsilon_r)} \end{cases} \tag{2.3}$$

where $f_{c,mn}^{(\varepsilon_r)}$ is the cutoff frequency of the mnth harmonic, namely, the frequency that satisfies,

$$\gamma_{mn}^2 = k_{x,m}^2 + k_{y,n}^2 - k_0^2\varepsilon_r = 0 \tag{2.4}$$

and that can be expressed as,

$$f_{c,mn}^{(\varepsilon_r)} = \frac{1}{\varepsilon_r - \sin^2\theta} \times \left\{ \frac{mc}{P_x}\sin\theta + \sqrt{\varepsilon_r\left[\left(\frac{mc}{P_x}\right)^2 + \left(\frac{nc}{P_y}\right)^2\right] - \left(\frac{nc}{P_y}\sin\theta\right)^2} \right\} \tag{2.5}$$

The above cutoff frequency is determined by the array periodicities (P_x and P_y), the angle of incidence (θ), and the medium dielectric constant (ε_r), but it is independent of the patch dimensions. For convenience, the cutoff frequency is here formulated in the presence of a homogeneous dielectric medium with permittivity ε_r. This fact is represented by the superscript (ε_r), although free space is assumed in the present section ($\varepsilon_r = 1$), which will be denoted by the superscript (1). Note that, for the case of normal incidence ($\theta = 0°$), 2.5 reduces to the well-known expression of the modal cutoff frequencies in a rectangular waveguide of dimensions $P_x \times P_y$.

At a given frequency, as 2.3 reveals, $k_{z,mn}^{(1)}$ can be purely imaginary or real, defining evanescent (slow) or grating (fast) waves, respectively [124]. Specifically, each harmonic is an evanescent wave that decays along the z-direction below its cutoff frequency $f_{c,mn}^{(1)}$. Above this frequency, $k_{z,mn}^{(1)}$ is no longer imaginary and the associated harmonic becomes a grating (plane) wave that propagates along a direction parallel to the vector $\mathbf{k}_{mn} = k_{x,m}\hat{\mathbf{x}} + k_{y,n}\hat{\mathbf{y}} + k_{z,mn}^{(1)}\hat{\mathbf{z}}$.

In this analysis, the incident plane wave in Fig. 2.8 corresponds to the dominant $mn = 00$ Floquet harmonic. This wave propagates at any given frequency along the

direction defined by θ (note that $k_{z,00}^{(\varepsilon_r)}$ is always real). In most microwave engineering and antenna applications, the working frequencies are within the so-called *no grating lobes regime* [124]; only the dominant Floquet harmonic is propagating while the remaining harmonics are evanescent. In general, each Floquet harmonic can be either TE or TM polarized, and has the following associated characteristic impedance [124]:

$$Z_{TE,mn}^{(\varepsilon_r)}(\omega) = \frac{j\omega\mu_0}{\gamma_{mn}} \quad , \quad Z_{TM,mn}^{(\varepsilon_r)}(\omega) = -\frac{j\gamma_{mn}}{\omega\varepsilon_0\varepsilon_r} \tag{2.6}$$

The above expressions tell that, depending on the propagative or evanescent nature of the harmonic, its associated impedance is real or purely imaginary. In particular, inductive/capacitive impedances correspond to TE/TM evanescent waves [124]. Due to the assumed impinging TE polarization and plane of incidence, the unit cell of the problem under consideration can be seen as a transmission line formed by two parallel-to-xz-plane electric walls separated by a distance P_y and two parallel-to-yz-plane Floquet walls separated by a distance P_x (see Fig. 2.8). It should be noted that the set of excited Floquet harmonics corresponds to the modal solutions of this transmission line. TM_{m0} harmonics do not satisfy the specified boundary conditions and are not excited in the structure under consideration.

The methodology previously used in [126] of the TE incidence case can equally be applied when the exciting plane wave is TM-polarized or it impinges in other planes. In practice, partially reflecting sheet arrays are normally illuminated by a single central feed, with the feeding element oriented so that the excited polarized electric field has a strong interaction with the dipoles. Therefore, the characterization of the periodic array under TM polarization becomes relevant when the scan plane of incidence is yz (E-plane). An equivalent network can also be proposed for TE polarization in E-plane or TM in H-plane, although these cases are less relevant from a practical point of view. Thus, in this section, the incidence of a TM-polarized plane wave in the E-plane of a array is modeled [126],

$$k_{x,m} = \frac{2m\pi}{P_x} \ , \ k_{y,n} = k_0 \sin\theta + \frac{2n\pi}{P_y} \tag{2.7}$$

The cutoff frequencies associated with higher order harmonics can be computed as,

$$f_{c,mn}^{(\varepsilon_r)} = \frac{1}{\varepsilon_r - \sin^2\theta} \times \left\{ \frac{nc}{P_y}\sin\theta + \sqrt{\varepsilon_r \left[\left(\frac{nc}{P_y}\right)^2 + \left(\frac{mc}{P_x}\right)^2 \right] - \left(\frac{mc}{P_x}\sin\theta\right)^2} \right\} \tag{2.8}$$

The periodic problem under consideration can be reduced to a single unit cell problem with magnetic walls parallel to the yz-plane and Floquet walls (periodic boundary conditions) parallel to the xz-plane. Therefore, TE_{0n} harmonics do not satisfy the boundary conditions, and are not excited by the TM polarized impinging wave.

In the analysis of periodic structures such as frequency-selective surfaces, three fundamental operating regimes can be identified based on the relationship between the structural periodicity and the operating wavelength [126]. At long wavelengths, where the periodicity D of the FSS is much smaller than the wavelength, the structure operates in what is known as the quasi-static regime. In this regime, the periodic surface can be effectively treated as a homogenized medium, and its electromagnetic behavior can be accurately modeled using effective medium approximations. As the frequency increases and the wavelength becomes comparable to the periodicity, the structure enters an intermediate regime in which the FSS elements may become electrically resonant. Here, circuit-based models can still be applied to describe the surface, typically using lumped-element representations. However, due to the complexity of the resonance phenomena, the lumped parameters can no longer be determined analytically and must instead be extracted through full-wave simulations and inverse modeling techniques. When the D approaches the guided wavelength λ_g, the FSS behavior becomes increasingly nonlinear. In this regime, multiple Floquet harmonics can propagate simultaneously, leading to intricate modal interactions. Traditional circuit models become inadequate, and a full multi-mode network approach is required to accurately represent the electromagnetic response of the structure, even for simple resonant elements.

While the conventional Floquet analysis in FSSs primarily focuses on propagating harmonics observable in the far-field, the electromagnetic behavior in the near-field region is governed by a different spectral composition, where evanescent Floquet modes contribute significantly to the local field characteristics. As described in (2.3), each Floquet harmonic is associated with a longitudinal wave number $k_{z,mn}^{(\varepsilon_r)}$. When the operating frequency is below the cutoff frequency $f_{c,mn}^{(\varepsilon_r)}$ of the mn-th harmonic, the wave number becomes purely imaginary, and the mode is classified as evanescent. In conventional microwave applications, the analysis often assumes the *no-grating-lobe regime* [124], where only the $(m, n) = (0, 0)$ fundamental harmonic is propagating, and all higher-order modes are evanescent and neglected in the far-field.

However, in near-field applications, especially those involving sensing at distances on the order of a wavelength or less, these evanescent harmonics cannot be ignored. They exhibit exponential decay in the direction normal to the array and contribute substantially to the field distribution in close proximity to the structure. The total field, therefore, must

be expanded as a superposition of both propagating and evanescent harmonics:

$$\mathbf{E}(x,y,z) = \sum_{m,n} \mathbf{E}_{mn}(0)\, e^{-j(k_{x,m}x + k_{y,n}y)}\, e^{-jk_{z,mn}^{(\varepsilon_r)} z} \tag{2.9}$$

Here, the exponential term along z may describe either oscillatory (for propagating modes) or decaying (for evanescent modes) behavior, depending on the real or imaginary nature of $k_{z,mn}^{(\varepsilon_r)}$. In particular, evanescent harmonics dominate power delivery and field localization in metasurface-based biomedical sensing systems, where the radar operates in close contact with the body. These harmonics are crucial for achieving subwavelength resolution, enhanced local field intensities, and impedance matching to lossy, dispersive biological tissues.

The radiating near-field region, also known as the Fresnel region, represents an intermediate electromagnetic zone that exists between the reactive near-field, which lies very close to the radiating surface, and the far-field, where planar wavefront assumptions and angular uniformity dominate. Unlike the reactive near-field, which is characterized by stored, non-radiative energy, the radiating near-field contains a combination of radiative and reactive components. This region is distinguished by non-uniform phase fronts, curved wavefronts, and spatially varying amplitude and phase distributions across the aperture. In this zone, the total electromagnetic field is formed by the superposition of multiple components, propagating Floquet harmonics with real-valued longitudinal wave numbers, responsible for carrying energy away from the structure; evanescent Floquet harmonics with imaginary wave numbers, which decay exponentially and contribute to field shaping in the immediate vicinity of the structure; and reactive fields, which store energy locally and influence impedance behavior near the source. The field strength and direction in the radiating near-field depend strongly on both the radial distance from the source and the angular position, making its analysis significantly more complex than the far-field, where fields depend only on angular direction and are typically uniform in amplitude and phase.

This region is particularly important in applications requiring beam shaping and energy focusing, such as near-field metasurface design for biomedical radar sensing. In such systems, the target medium, often human skin or internal tissue, frequently lies within the radiating near-field of the metasurface. This proximity is crucial, as it allows radiating near-field modes to deliver real power into lossy biological media, enabling deeper tissue penetration and improved signal sensitivity. Unlike purely reactive or evanescent fields, which are confined close to the source and do not radiate power, radiating near-field modes enable energy transmission to the target while maintaining the ability to shape the

spatial field profile. Therefore, near-field beamforming and subwavelength focusing are achievable primarily by manipulating field interactions within this region.

2.3.2 Metasurfaces in Near-Field Antenna Design

To get around the current limitations of bio-electronic interfaces, metasurfaces with subwavelength structures can be engineered to control electromagnetic fields around the human body [127]. Integrated metamaterials [128] and superstrate structures with reflective or transmissive functionality are utilized in near-field sensing by invoking the arrays' mechanism and taking advantage of the compact feeding antennas' design compatibility to offer suitable features in the near-field region [120]. Particularly, an engineered superstrate with two layers of perforated aluminium sheets is used in [129] as a near-field manipulator to adjust the electromagnetic radiation pattern of a horn antenna by modifying its near-field components in the frequency range of 10 GHz to 12 GHz. [130] reports a transmissive programmable metasurface for high-resolution far-field and near-field detection. Each metasurface unit cell is made up of five microstrip layers with an airgap in between, and a programmable phase shifter is used to adjust the phase shift for various focusing points at 5.75 GHz. These approaches are not suitable for mm-wave frequency bands, and the proposed structures have a complex design, high profile, and high manufacturing costs.

As suggested in [131], placing an appropriate solid or liquid media between the radar antenna and the tissue reduces antenna mismatching. To mitigate impedance mismatch, however, a number of media layers are required, resulting in a high-profile structure that poses integration difficulties, and applying liquid onto a person's skin can evoke discomfort. Metamaterials and metasurfaces, which are more practical and easier to integrate with radars, can also be used to improve antenna matching in the presence of tissue [132–135]. [36] presents a bow-tie antenna design that makes use of metasurfaces as an impedance-matching layer between the biological tissue and the antenna to enhance radiating performance when close to the human body at 2.56 GHz. However, creating a metasurface with the intention of enhancing antenna matching close to the human body is insufficient to deliver a highly near-field focused power directed towards the body, and to significantly enhance the near-field sensing capabilities of the radar. Based on our extensive review of the literature, we have observed that none of the metasurfaces documented so far possesses a suitable structure that combines low profile and high integration capability, particularly to accommodate mm-wave frequencies. This deficiency hinders their integration with radar sensors, thereby limiting their potential for enabling high-precision sensing in near-field biomedical applications.

Specifically in biomedical applications, utilizing metasurface offers several advantages: i) Miniaturization: Metasurface antennas can be designed to be extremely compact, allowing for minimally invasive or even implantable sensing devices. This is crucial for biomedical applications where size constraints are important, such as implantable medical devices or wearable sensors [136]. ii) Beamforming and Reconfigurability: Metasurface antennas can be engineered to focus or steer electromagnetic waves with high efficiency. Recently, designing reconfigurable focusing apertures using metasurfaces has been demonstrated with promising results [137]. In the context of biomedical sensing, this can enable more precise targeting of specific tissues or regions of interest, improving the accuracy of measurements and reducing interference from surrounding tissues. iii) Multifunctionality: Metasurfaces can be tailored to operate over a wide range of frequencies, from microwave to terahertz and beyond [138]. This adaptability is valuable for diverse biomedical sensing modalities, such as microwave imaging, terahertz spectroscopy, and even multi-modal sensing applications. iv) Improved Signal-to-Noise Ratio: Metasurface antennas can enhance signal quality and reduce interference from the surrounding environment. This is particularly important in biomedical sensing applications where weak signals need to be detected with high sensitivity [139]. v) Enhanced Resolution: Metasurface antennas can provide superior spatial resolution compared to traditional antennas, which is essential for applications like medical imaging, such as microwave breast imaging or terahertz spectroscopy for tissue analysis [140]. vi) Versatility: Metasurface antennas can be designed to work with various sensing techniques, including radar-based sensing, near-field communication, and passive sensing, making them suitable for a wide range of biomedical applications, from disease detection to physiological monitoring [141]. vii) Frequency Selectivity: Metasurfaces can be engineered to have sharp frequency response characteristics, allowing for precise sensing within specific frequency bands. This is useful for differentiating between different biological tissues or detecting specific biomarkers [120]. viii) Integration with Electronics: Metasurface antennas can be integrated with electronic components for data processing and communication. This integration is essential for real-time monitoring, data storage, and transmission in biomedical sensing systems [139]. While metasurface antennas hold great promise for biomedical sensing, there are still several challenges to overcome, including issues related to biocompatibility, power requirements, and long-term stability.

[103] presents a new design of near-field focused metasurface for high-efficiency wireless power transfer with multifocus characteristics. A general synthesis procedure is outlined to design metasurfaces with desired multiple foci in the near-field zone. Different feeding and focusing designs of the printed tridipole metasurfaces 20×20 elements are designed at 5.8 GHz as shown in Fig. 2.9.

A near field (NF) focused lens antenna fabricated by the 3D printing method for wireless

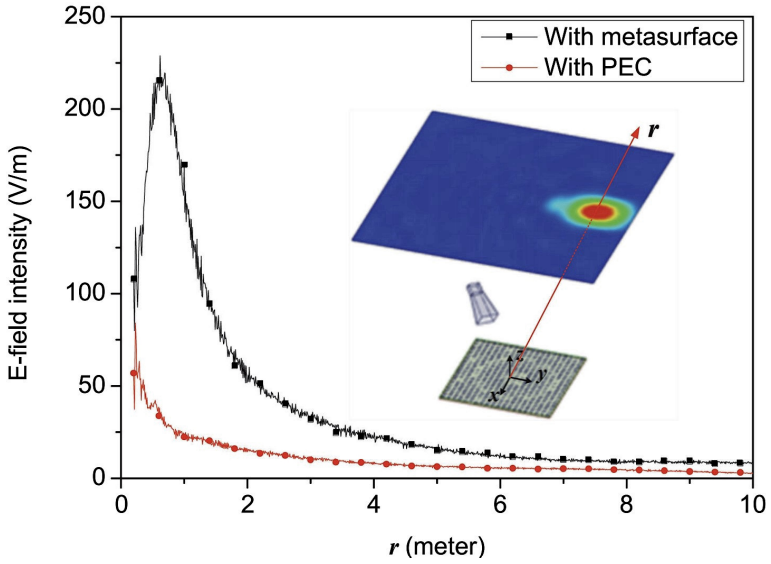


Figure 2.9: simulation model and E-field intensity on the focal plane at 5.8 GHz for Near-field focused metasurface of 500×500 mm with 20×20 elements [103]

power transmission (WPT) systems are proposed in [142]. The lens antenna operating at 35 GHz, is employed as the transmitting antenna to focus the electromagnetic power and reduce the diffraction loss during power transmission in free space. The aperture size is $100.8 \times 100.8\ mm^2$, with a designed focused length of 300 mm.

The integration of metasurfaces with traditional antennas presents a multitude of advantages in near-field across various applications. However, especially within the realm of biomedical sensing, this approach remains largely unexplored and significantly underreported. Combining metasurfaces with conventional antennas offers potential benefits such as enhanced performance, increased sensitivity and resolution, and the ability to manipulate electromagnetic waves in innovative ways.

2.4 Summary and Gaps in Literature

This chapter provides a comprehensive overview of the latest advancements in near-field sensing technology specifically tailored for biomedical applications. The research conducted in this field has been categorized into two main areas: near-field-focused antennas and near-field radar sensing for biomedical applications. The chapter delves into these categories,

highlighting the current progress, innovations, and the challenges that researchers are facing in these specialized areas of research.

In the hardware design of a radar system, both the radar chipset architecture and the design of the accompanying antenna are essential considerations. In bio-sensing applications, the radar hardware's performance is assessed by leveraging the near-field sensing capabilities of the antenna when positioned in close proximity to the human body. One effective method involves using the transmitter antenna's radiated power to concentrate the electric field at a particular location near the radar surface. By doing so, the system can receive reflected signals carrying information from the target, enhancing near-field sensing capabilities. This approach improves the system's ability to detect and gather information when the radar is placed in close proximity to the target, such as the human body in bio-sensing applications.

The review of literature in the field of biomedical applications highlights several critical challenges in the development of millimeter-wave (mm-wave) and low-frequency antennas. First, the scarcity of works pertaining to these frequencies limits the advancement of applicable technologies in the biomedical domain. For instance, planar array antennas operating in the near-field suffer from several issues, including complex designs, high profiles, and lossy feeding networks, leading to inefficiencies and impracticalities in real-world applications. Moreover, the conventional approach of defining the far-field by placing the focal point far from the antenna restricts the ability to focus very close to the aperture, presenting a significant limitation in targeting specific areas in biomedical scenarios. In the realm of near-field antenna design, it is crucial to emphasize that the far-field design parameters should not be indiscriminately applied. While radiation pattern, antenna gain, directivity, and sidelobe level are indeed important considerations in most applications, they should be interpreted differently in the context of near-field antennas. The primary objective of near-field antenna design is to optimize the performance and characteristics of the antenna in close proximity to the radiating source, typically within a wavelength or less. Therefore, the emphasis shifts towards achieving efficient power transfer, minimizing near-field distortions, and tailoring the antenna's characteristics to meet the specific needs of short-range communication systems. Applying far-field design parameters without modification in the near-field context can lead to less-than-ideal performance and potentially negate the benefits of using near-field antennas.

Furthermore, the absence of attention to impedance matching in the near-field significantly limits the practical use of these antennas for direct contact with the human body, a critical aspect in integrating them into medical devices. In medical microwave imaging, antennas are positioned in close proximity to the body to capture faint echoes from the internal organs, which are often obscured by strong reflections from the skin. Given

the antennas' extremely close proximity to the body, it is vital to carefully consider the characteristics of near-field antennas. The challenge arises when attempting to integrate these antenna structures with compact devices like radars or sensors, impeding their practicality in real-time health monitoring applications. Although optimization techniques are commonly utilized to achieve focus in the near-field, there is a lack of comprehensive near-field theories, particularly concerning impedance and electric field behavior, representing a significant gap in this area of research. Most existing reviews primarily concentrate on near-field antennas with larger sizes and focal points located beyond the free-space wavelength. As a result, these studies are unsuitable for compact and lightweight integration into devices meant for real-time health monitoring, a crucial necessity in practical biomedical applications.

Designing antennas for bio-sensing devices poses significant challenges due to various crucial factors involved in their design. These factors include antenna size, bandwidth, patient safety, and diverse security considerations. The intricate dielectric properties of human tissues and the necessity for broad bandwidth present critical limitations in such applications. Although efforts have been made in blood glucose monitoring, none of the methods developed have resulted in a reliable commercial or clinical glucose monitoring device. Moreover, attempts have focused on non-invasive epidermal blood glucose monitoring from interstitial fluids and sweat. Consequently, the creation of a completely contactless method for monitoring blood glucose levels remains relatively uncommon. Even with recent advancements in Electrical Impedance Tomography (EIT) for disease diagnosis, such as lung conditions, there are persisting limitations that need to be addressed, like low spatial resolution and the requirement for real-time monitoring in suitable clinical settings.

Addressing these challenges is crucial for the development of effective, efficient, and practical antenna solutions for biomedical uses. Metasurfaces are designed to manipulate electromagnetic waves upon interaction, enabling precise management of wavefront shaping, polarization, and other characteristics. Combining metasurfaces with radar technology results in radar systems that are significantly improved, offering greater resolution, heightened sensitivity, and improved capabilities in detecting targets. This integration contributes to progress in biomedical applications.

Chapter 3

Radar Sensing and Power-Focusing Enhancement Techniques

Radar systems have gained increasing importance in modern sensing applications due to their ability to operate across diverse environments and frequency bands, offering robust performance in both far-field and near-field scenarios. A key aspect of enhancing radar effectiveness, particularly in applications requiring high-resolution target detection or localized energy delivery, is the capability to concentrate electromagnetic power in a specific direction or region. This chapter presents a series of radar sensing configurations and power-focusing enhancement techniques developed as part of this thesis, aimed at improving field concentration through the use of passive structures and phase-engineered surfaces.

Three-dimensional dielectric lens structures, including dielectric rod arrays and gradient-index (GRIN) Luneburg lens designs, are presented, alongside the motivation for transitioning to two-dimensional planar metasurfaces. These structures are designed to manipulate the spatial phase profile of incident radar waves, enabling improved directivity, beam shaping, and localized power enhancement. Each design is evaluated through full-wave electromagnetic simulations, and corresponding prototypes have been fabricated and experimentally validated. The results demonstrate substantial improvements in spatial control and energy efficiency, providing the basis for high-performance, compact radar systems applicable across a variety of sensing and communication scenarios.

Although the primary focus of this thesis is on near-field radar sensing for biomedical applications, the techniques introduced in this chapter serve as an essential foundation. The lens-based systems presented here are optimized for far-field applications and general-purpose radar enhancement; however, the underlying principles of wavefront con-

trol and power focusing directly inform the metasurface-based near-field sensing strategies developed in subsequent chapters. Notably, all implementations in this work are based on bistatic radar modules, where separate transmit and receive antennas allow for more flexible integration of passive focusing elements. While lens integration in bistatic configurations has been explored in some studies, challenges related to alignment, coupling efficiency, and form factor remain, especially for compact or body-conformal systems. These early contributions, therefore, establish the groundwork for transitioning from traditional lens designs to advanced metasurface solutions that offer low-profile, near-field performance tailored to biomedical environments.

3.1 Problem Statement and Objectives

The rapid evolution of radar sensing in wireless communication technologies has generated significant interest in radar systems that offer a high level of integration, cost-effective fabrication processes, wide-angle scanning capabilities, and enhanced detection ranges [143].

To address these requirements, radar-on-chip modules have been developed and are now commercially available, offering compact designs and cost-effective solutions across a broad spectrum of applications. These include contactless sleep sensing systems [144], non-invasive blood glucose monitoring [39], in-body cardiovascular dynamics measurement [145], human respiration monitoring [146], gait analysis and in-home activity tracking [147, 148], multi-gesture recognition [149], autonomous driving and intelligent transportation systems [150], human-vehicle detection [151], road user detection for autonomous vehicles [152], and surveillance applications [153].

Continuous-wave radars are commonly utilized to measure the velocity of a mobile entity at a specific distance based on Doppler shifts. The X-band HB100 Doppler radar module, known for its popularity, accuracy, and affordability, finds extensive utilization in a range of applications such as automatic door startup, car/house intrusion alarm systems, collision warning systems, and traffic monitoring [154]. A limitation of this radar system is its restricted detection range, as it is capable of detecting vehicles up to a maximum distance of approximately 7 m [155].

Although current radar modules demonstrate suitability for many of these use cases, they often lack tailored designs for specific scenarios that demand broader coverage, enhanced angular resolution, or customized field-of-view characteristics. Most of the radar module designs include the radar chipsets and the transmitter/receiver antennas which are implemented in a printed circuit board (PCB), using on-chip or on-PCB antennas. In the

context of such systems, it is imperative for the antenna to possess a compact form factor to facilitate seamless integration while simultaneously delivering high gain to ensure an extended detection range and high efficiency to prevent power loss. Conventionally, this necessitates distinct antenna design to achieve a varying antenna gain or pattern that typically entails a complete overhaul of the integrated antennas and subsequent remanufacturing of the radar module, leading to substantial associated expenses.

Numerous methodologies have been proposed to enhance the gain of PCB antennas employed in radar modules, including planar arrays for continuous-wave radar [156] and vivaldi antennas for handheld through-wall radar [157]. In these traditional methods, achieving enhanced radar-on-chip performance requires dedicated antenna designs, which often necessitate a complete redesign and re-manufacturing of the radar module. This process results in significant costs, making it a challenging approach for applications demanding tailored performance.

Alternatively, add-on lens and metasurface structures offer straightforward design and fabrication processes, enabling seamless integration with radar systems to instantly enhance their antenna performance [158]. The benefits associated with the utilization of lens antennas include the straightforwardness of the design, increased resilience to variations in production parameters, enhanced efficiency due to reduced mutual coupling, and the often sufficient usage of a single element, such as a patch or slot antenna, positioned at the focal point of the lens as a feeder. These structures are utilized in a variety of applications, including radar antenna RCS reduction [159], polarization conversion for radar sensing applications [160], enhancement of radar antenna directivity, extension of detection range, improvement of signal-to-noise ratio [161], enhancing radar imaging in extreme cold environments [162], and enhanced beamforming with high spatial resolution [163]. Superstrate designs incorporating Fabry-Perot resonators and metamaterial theory present promising approaches in different applications for gain enhancement [164]. In [165], a dielectric parallel-plate metamaterial waveguide including nine dielectric FR-4 plates with $\lambda/4$ airgap is placed above the transmitter and receiver of an HB100 radar antenna separately. The overall gain enhancement of 5.5 dB is obtained for the transmitter and receiver antenna. In [166], an array of patch antennas covered by a flat high-refractive-index metamaterial provided 3.4 dB gain improvement. In [167], a hyperbolic lens antenna is designed and fabricated for an mm-wave MIMO radar operating at 77 GHz, providing more than 12 dB gain improvement. However, the relatively large dimension of the lens antennas is challenging at lower frequency bands. To place a lens closer to the feeder for a low-profile design, the thickness of the lens should be increased, leading to a heavy and high-profile structure causing multiple reflections between the feeder and lens surface. On the other hand, using a thinner lens far away from the feeder causes too much spillover with a very-

high-profile design [167]. Therefore, these gain enhancement methods necessitate intricate and costly designs, as well as high-profile structures; otherwise, they offer only marginal improvements in gain, rendering them unsuitable for long-range detection radars.

Furthermore, most studies in the literature focus on lenses designed for integration with monostatic radar systems, where a single antenna serves as both the TX and RX. However, such lenses are unsuitable for scenarios where TX and RX antennas are positioned on a PCB board, as they can introduce beam tilting errors. The research gap lies in enhancing the performance of a bistatic in-package radar configuration where the TX and RX antennas are co-located and share a single lens structure. This approach eliminates the need for multi-lens configurations, thereby reducing fabrication costs and design complexity, while simultaneously delivering improved performance for both the TX and RX antennas. [168] presents metamaterial lenses designed to enhance 77 GHz bistatic radar systems for long-range detection in automotive radar applications. Rectangular cylindrical lenses with focal lengths ranging from 7.7λ to 15.4λ and dimensions of $30.8\lambda \times 15.4\lambda, \text{mm}^2$ were developed and implemented, offering significant improvements in beam collimation and directionality. However, the design exhibits a high-profile and bulky structure, which limit its practicality in compact systems. In [169], three lens antennas for a 122 GHz FMCW radar are evaluated. A double plano-hyperbolic lens (DPHL-T) achieves a 19 dB gain but suffers from bulkiness and back-reflection. A single-surface variant (DPHL-O) offers 11.8 dB gain with even higher reflection and lower performance. A Fresnel-zoned lens (DFZL) provides 10.6 dB gain with minimal reflection but limited applicability due to lower gain. All designs are bulky and rely on CNC machining fabrication method. Alternatively, a 3D-printed hyperbolic lens for a 79 GHz MIMO radar system achieves 14 dB gain [161], yet its large physical size remains a limitation, especially at lower frequencies.

In overall, lens structures explored in the literature face several limitations, including high-profile configurations, complex designs, large focal point distances, and significant challenges in manufacturing and integration within bistatic radar modules.

3.2 3D-Printed Dielectric Rod Lens

Given some attractive attributes such as lightweight, low-profile, and being cost-effective to fabricate, dielectric rods, commonly referred to as end-fired surface-wave antennas, are gaining popularity in a wide range of applications [170], such as directivity enhancement of printed antennas for high-data-rate wireless communications [171], high-gain omnidirectional antenna [172], and aperture efficiency improvement of the space-fed antennas [106].

[171] introduces a V-band antenna consisting of a patch-fed dielectric rod. The dielectric rod, fabricated using Teflon through a CNC machine, is positioned on top of the patch to produce complex mode excitations. To convert the mode from the patch and eliminate undesired modes during radiation, an additional design incorporating a metallic cylindrical waveguide is implemented at the base. The additional height of the circular waveguide is set to 1.42λ, resulting in a total length of 6.71λ while yielding a 16 dB gain at 61 GHz. In [173], three arrays of multiple dielectric rods with airgaps in between are designed by high-permittivity material ($\epsilon_r = 9.8$) placed in parallel to a patch antenna. This design provides an EBG-type superstrate to enhance directivity up to 8 dB compared to an isolated patch antenna. In [172], a lens consisting of 16 periodic aluminium rods attached to the aluminium plates is proposed to enhance the gain of an omnidirectional cylindrical radiator at 920 MHz, providing an overall gain of 19.47 dB. However, The dielectric rod structures discussed in these studies employ intricate design methodologies, expensive fabrication processes involving high-permittivity dielectric materials or complex metal shaping, and face difficulties when it comes to integrating them with the primary feeder.

Recently, the adoption of 3D-printing, a cost-effective and straightforward manufacturing technique, has gained prominence for fabricating dielectric rods. This method enables the uniform fabrication of arbitrary rod structures according to specific requirements. As reported in [174], the 3D-printing-based manufacturing process is an efficient solution for designing high-performance dielectric lens antennas.

In [175], we presented a design strategy to alter the radiation characteristics of modular radar printed circuit boards without the need for expensive retooling and remanufacturing is presented in this section [175]. To this end, a compact radar module including microstrip array antennas integrated with a dielectric rod lens is considered for a demonstration of an X-band radar antenna gain improvement leading to radar detection sensing enhancement. Using travelling wave theory, the proposed lens is designed to target the excitation of HE_{11} mode to achieve gain improvement without disturbing reflection coefficients. Using a low-cost rapid-manufacturing 3D-printing technology, two pairs of the 3D-printed dielectric rods integrated with a dielectric housing are designed and fabricated uniformly for a commercially available off-the-shelf radar module. The radar integration with the dielectric rod lens leads to a low-cost and easy-to-fabricate long-range radar system. Compared with the radar without the rods, the design system achieved a measured 6.6 dB gain improvement of the transmitter and receiver antennas which causes doubling the detection range for both elevation and azimuth directions at 10.525 GHz.

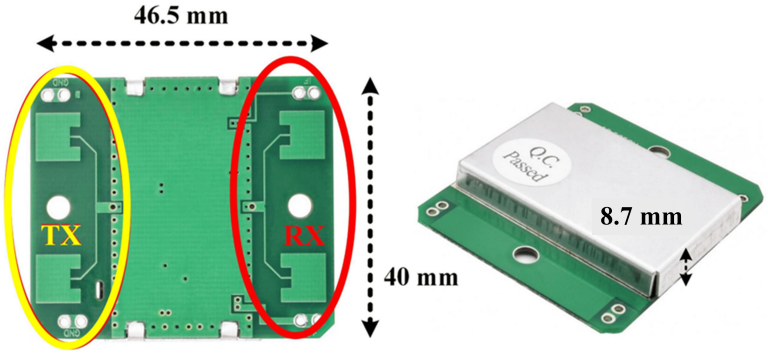


Figure 3.1: The dimensions of full prototype and PCB layout of the HB100 radar module with TX/RX sections.

3.2.1 Dielectric Rod Lens Design

This section focuses on designing the configuration of a 2×2 dielectric rod array as an integrated lens aiming to enhance the gain of the HB100 radar module. The Doppler effect is harnessed by a radar system to detect alterations in the velocity of objects at a specific range by bouncing a microwave signal off a desired target. The X-band HB100 Doppler radar, one of the popular, accurate, and affordable modules, is widely employed in various applications such as automatic door startup, car and house intrusion alarms, collision warning, and traffic monitoring.

The structure of the selected radar is shown in Fig. 3.1. As seen, the radar PCB consists of two pairs of 1×2 arrays of a rectangular microstrip patch antenna as a transmitter and a receiver antenna. The total rectangular dimension is 40×46.5 mm, printed on the FR-4 substrate with a thickness of 0.8 mm. Based on the simulation, the proposed antennas provide 6.5 dB realized gain separately. According to the datasheet, the radar has a detection range coverage of 20 m. However, this detection range works properly for a vehicle at a close range of about 7 m at the center frequency of 10.525 GHz.

The dielectric rod, which belongs to the category of travelling surface wave antennas, functions as a dielectric waveguide, leading to the emission of radiation at points of discontinuity. The hybrid HE_{11} mode, a proper combination of TE and TM modes, is the dominant mode exhibited by the dielectric rod which generates equiphase electric fields with no cut-off frequency. The dielectric constant of the rod structure imposes limitations. It can be shown that matching the dielectric rod with low-permittivity materials requires a large dimension and complicated design. Given that low-cost materials commonly employed in 3D-printing machines typically exhibit low permittivity, ($\epsilon_r = 2.5$ in the X-band),

a compromise must be established between the maximum feasible size and the subsequent enhancement in gain. The gain of the rod is influenced by its length, emphasizing the importance of this parameter. Additionally, the mode conversion process is significantly affected by the shape and dimensions of the rod's cross-section.

The utilization of a dielectric rod with a circular cross-section offers several advantages, including a symmetric radiation pattern, wider bandwidth, low cross-polarization, and a simple design that allows for greater flexibility. To ensure a seamless and efficient transition from patch radiation to the HE_{11} mode, as well as from the HE_{11} mode to a plane wave, careful consideration must be given to the diameter of the rod's cross-section. The fundamental HE_{11} mode can be excited in a circular dielectric rod by considering a rod diameter of at least 0.58 λ_d (λ_d is the wavelength in a dielectric rod). Therefore, a proper diameter-to-wavelength ratio guarantees the HE_{11} mode excitation. Considering the mutual coupling between the radar antennas, the bottom cross-section diameter is approximately considered 0.78 λ_d (Rl = 14 mm) to match the highest radiated power from the patch in free space to the surface wave. On the other hand, the field profile of the HE_{11} mode is extended by reducing the rod diameter at the radiation end that should be tapered in the dielectric rod body.

The introduction of longitudinal tapering in the rod enhances the radiation characteristics by facilitating radiation along the entire length of the taper, resulting in improved performance. The nontapered cylindrical dielectric rod propagates with the sum of the radiation from discontinuities which provides low gain and high side-lobe levels due to the interference between the ends and free space. Conversely, in tapered rods, power is leaked through the tapered profile, and the radiated power comprises the cumulative effect of radiation originating from the leaky wave structure. Therefore, it is crucial for the tapering process to be conducted gradually in order to mitigate higher-order coupling effects and minimize fabrication complexities. In light of this, various types of tapered profiles are investigated, revealing negligible discrepancies among the outcomes. Consequently, a linear taper is favoured for its ease of fabrication and minimal errors when employing a 3D-printing machine.

Upon choosing the appropriate tapering profile, the top cross-section, denoted as Rs, needs to be optimized in order to achieve improved matching with free space. The sensitivity analysis yields an optimal value for each design parameter, ensuring an appropriate and suitable amount for their respective contributions. It can be shown that the top cross-section with a diameter of 0.45 λ_d (Rs = 8 mm) connected to the bottom cross-section through a smooth linear tapering provides an optimized structure with enhanced performance and suitability as a lens for the patch antenna.

In [176], a direct relationship between the gain and the length of the antenna integrated with the tapered dielectric rod is derived:

$$G_{max} = 10\frac{h}{\lambda} \tag{3.1}$$

Using (3.1), one can find the optimum gain of the tapered rod in terms of length. Alternatively, in order to achieve a double detection range for both the transmitter and receiver antenna independently, it is necessary to determine the desired gain improvement and subsequently determine the optimal length of the dielectric rod. To obtain the desired gain improvement, the common radar equation is used. The intensity of the received power P_{RX} is calculated as,

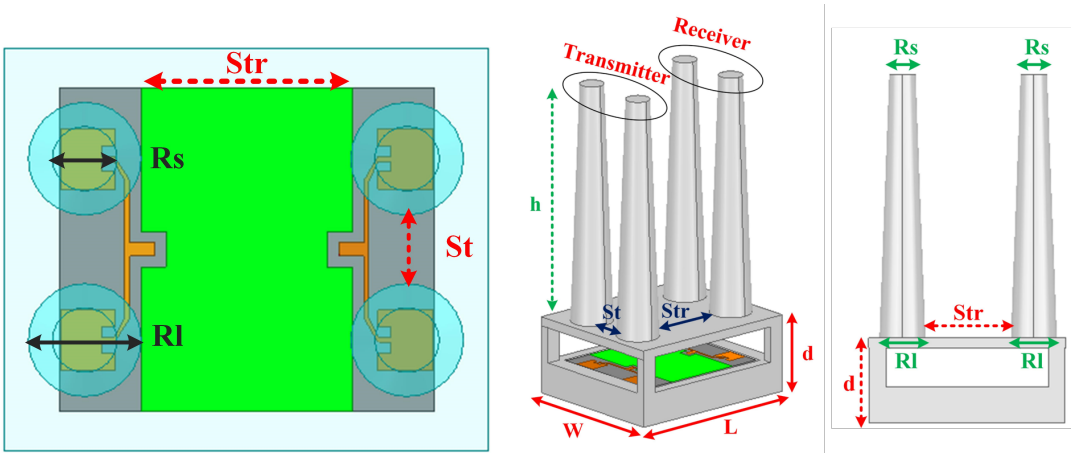
$$P_{RX} = \frac{\sigma\lambda^2 P_{TX} G_{TX} G_{RX}}{(4\pi)^3 R^4} \tag{3.2}$$

where P_{TX} is the transmitter power, R is the detection range, λ is the wavelength of the transmitted signal, σ is the radar cross-section, and G_{RX} and G_{TX} are the gain of the receiver and transmitter antenna, respectively. Regarding the proposed measurement setup used in [175], P_{TX}, λ, and σ remain constant across all angles. In this case, R, G_{RX} and G_{TX} are the effective ones in (3.2). Assuming a stable received power P_{RX}, it can be shown that,

$$K = \frac{G_{TX} G_{RX}}{R^4} \Rightarrow R = (\frac{G_{TX} G_{RX}}{K})^{\frac{1}{4}} \tag{3.3}$$

where K is a constant at all angles.

The (3.3) clearly demonstrates that a 6 dB gain improvement at both the transmitter and receiver antennas corresponds to a fourfold increase in their respective gains, resulting in the doubling of the detection range. By conducting a full-wave simulation, it was determined that the individual gain of the TX/RX antenna in the HB100 radar module is 6.7 dB. Thus, achieving a gain of 12.7 dB should be adequate to fulfil the specified requirement. Based on this analysis, the minimum length of the tapered dielectric rod antenna can be determined using (3.1), resulting in a value of h= 1.8λ. According to theoretical considerations, increasing the length of h leads to greater gain enhancement of the radar antenna. However, there exists a limitation on how much the length can be increased, which is dependent on the operating frequency. Furthermore, extending the taper length results in the emergence of higher side lobes and higher-order modes,



(a) (b)

Figure 3.2: The full structure and design parameters of the dielectric rod lens integrated with HB100 radar module: (a) top view and (b) side view.

which can introduce detrimental effects on the radiation characteristics of the antenna. To mitigate the detrimental effects and strike a balance between achieving the desired gain and maintaining structural compactness, this work proposes an optimized length for the dielectric rod of 2λ, corresponding to 60 mm. The structure of the dielectric rod lens integrated with the radar module is presented in Fig. 3.2.

The design of the lens is intricately linked to the specific application, as well as the dimensions and shape of the radar system being considered. The structure of the desired X-band HB100 radar module, as shown in Fig. 3.1, includes two pairs of 1×2 microstrip patch arrays as a receiver and a transmitter. Consequently, an effective approach to modeling a lens involves employing four identical tapered dielectric rods positioned at the center of each patch, as illustrated in Fig. 3.2a, which are positioned at an appropriate distance above each microstrip patch antenna.

In order to avoid unexpected modes and effectively mitigate their impact through supplementary design measures, a compact and low-profile lens based on the principles of Fabry-Perot (FP) theory is introduced. Following FP theory, it is determined that a 0.5λ air gap between the patch antenna and the lens is adequate to stimulate the dielectric rod and enhance the gain of the patch antenna [175], as shown in Fig. 3.2b. This specific gap distance is considered to maximize power reception from the patch radiation and facilitate optimal excitation of surface waves. To achieve this, dielectric housing is utilized as a

foundation to maintain the rods at the desired distance from the radar chipset's surface. The integrated structure is fabricated uniformly using a 3D-printing machine, ensuring consistent performance throughout.

The compact lens is formed by integrating the four dielectric rods with a dielectric housing, which encompasses the proposed HB100 radar module. This configuration results in a compact lens with overall dimensions measuring 50×60×60 mm. The values of the design parameters are presented in Table 3.1. The parameter S_t is the distance between two patches in the transmitter or receiver section, while the parameter S_{tr} shows the distance between the TX and the RX patches. Sufficient space is maintained between the dielectric rods to ensure low mutual coupling, with a separation distance between the two TX/RX arrays set at $3\lambda/2$.

Table 3.1: Design parameters of the dielectric rod lens

Parameter	**Description**	**Value (mm)**
W	Width of the dielectric housing	50
L	Length of the dielectric housing	60
Str	Distance between TX and RX antennas	26
Sr	Distance between RX elements	8.5
St	Distance between TX elements	8.5
h	Height of dielectric rod	60
Rl	Diameter of the bottom cross-section	14
Rs	Diameter of the top cross-section	8
d	Height of dielectric housing	14.8

3.2.2 Simulation Results

In this section, the dielectric rod lens provided in the study is modeled through established full-wave simulation tools. These simulations entail utilizing the physical dimensions outlined in design Section, which are subsequently optimized to achieve advantageous results. The results of these simulations are graphically represented in Fig. 3.3 to 3.6, illustrating aspects such as the distribution of the electric field on the dielectric rod, E-, and H-plane gain patterns, gain variations concerning frequency changes, and the lens's impedance matching characteristics.

By utilizing a dielectric rod as a lens, the radiation of the patch antenna couples a portion of the input power into a surface wave, producing a hybrid mode, which travels along

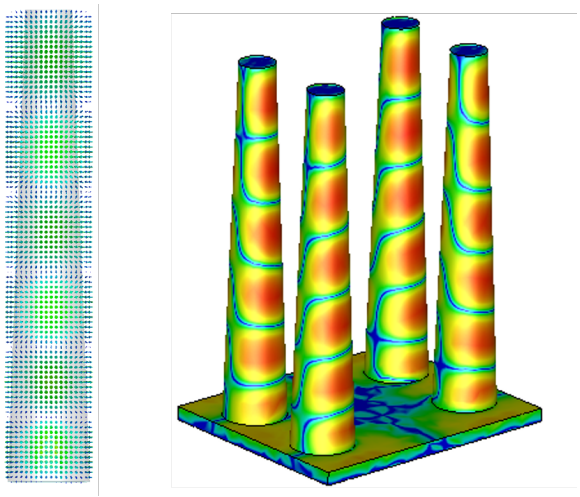


Figure 3.3: Magnitude and direction of the electric field distribution on the dielectric rod lens with appropriate excitation mode coupled from the array patch antenna.

the rod structure and subsequently radiates into the surrounding free space. The presence of the excited HE_{11} mode, characterized by a zero cut-off frequency, results in an equiphase electric field configuration. This arrangement contributes to the enhancement of gain by concentrating the radiation field. To confirm the successful radiation of the HE_{11} mode within the designed dielectric rod, an investigation is conducted into the field distribution within the proposed rod. As depicted in Fig. 3.3, the electromagnetic fields predominantly concentrate within the dielectric material, while the antenna exhibits radiation in the direction of the rod. The analysis of the electric field further indicates that employing a tapering profile for the dielectric rods results in a gradual and seamless increase in radiation, reaching its maximum intensity at the end of the structure.

The dielectric rod lens is constructed using ABS, a material compatible with 3D-printing machines, offering both structural stability and desirable radiation specifications. Using the X-band waveguide approach in the measurement process, ABS material was measured to have a permittivity of 2.53 and loss tangent of 0.004. By conducting a full-wave simulation, the 2D radiation pattern of the radar transmitter microstrip antenna is obtained and compared with and without the presence of the dielectric rod lens, as shown in Fig. 3.4. It is evident that the dielectric rod lens enhances the realized gain of the TX/RX antenna by approximately 6.6 dB in both the E-plane and H-plane patterns. In accordance with the reciprocity theorem, the functionality of an antenna remains consistent, irrespective of whether it is employed as a transmitter or receiver. The placement symmetry observed in

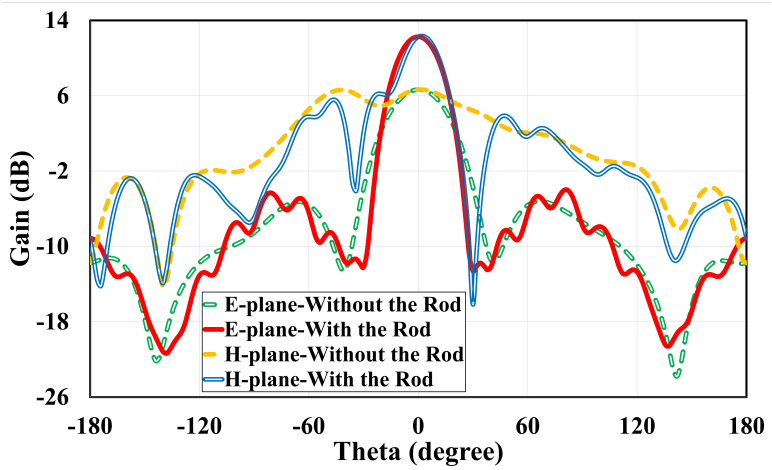
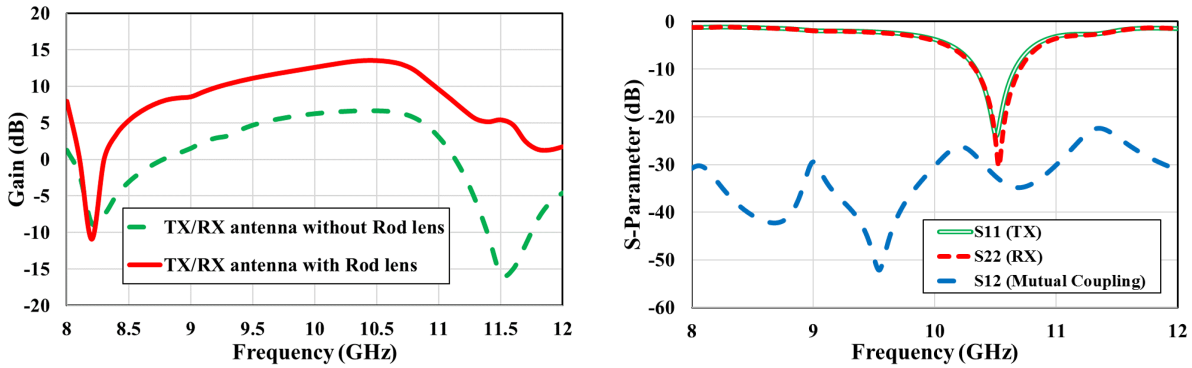


Figure 3.4: The 2D E-plane and H-plane realized gain pattern for the RX/TX antenna with and without using dielectric rod lens at 10.52 GHz.



(a) (b)

Figure 3.5: The realized gain variation versus frequency for the RX/TX antenna with and without integrating dielectric rod lens, (b) The investigation of reflection coefficient and mutual coupling for TX/RX antenna integrated with dielectric rod lens.

radar antennas leads to an identical radiation pattern for both the TX and RX antennas.

The gain variation versus frequency for the radar antenna integrated with and without the dielectric rod lens is investigated in Fig. 3.5a. Since the dielectric rod is known as a travelling wave antenna, it can provide a wide gain bandwidth for the feeder antenna.

Hence, it is evident that despite the dielectric rod lens being excited by the patch radiation at a cut-off frequency of 10.525 GHz, the gain enhancement is attained within the frequency range of 8.2 to 12 GHz. In addition, Fig. 3.5a shows that the maximum gain for the TX/RX antenna without the lens is 6.7 dB while the dielectric rod lens increases it to 13.3 dB.

The reflection coefficient as well as mutual coupling for both transmitter and receiver antennas integrated with and without dielectric lens are investigated and shown in Fig. 3.5b. The results indicate that the designed dielectric rod lens has no substantial impact on the primary performance of the patch antennas.

3.2.3 Fabrication and Measurement Process

A prototype of the fabricated HB100 radar chipset antenna integrated with and without the tapered dielectric rod lens is presented in Fig. 3.6. To evaluate the effectiveness of the proposed system in enhancing radar range detection, the designed structure is mounted on the rear of a bicycle, allowing for practical measurement and assessment with an overall dimension of 50×60×74.8 mm.

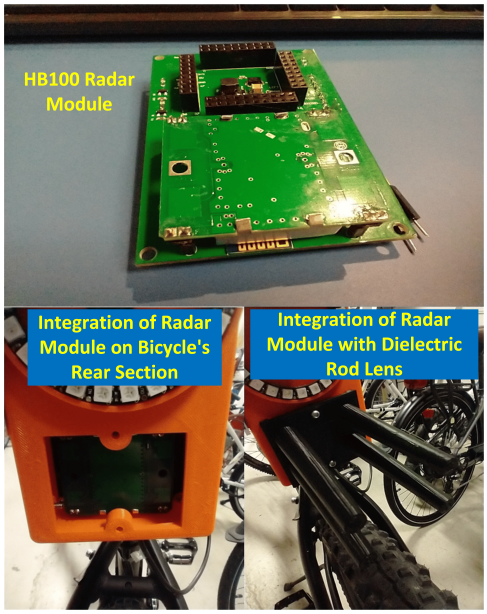


Figure 3.6: An HB100 radar antenna fabricated prototype mounted on a bicycle integrated with and without the dielectric rod lens.

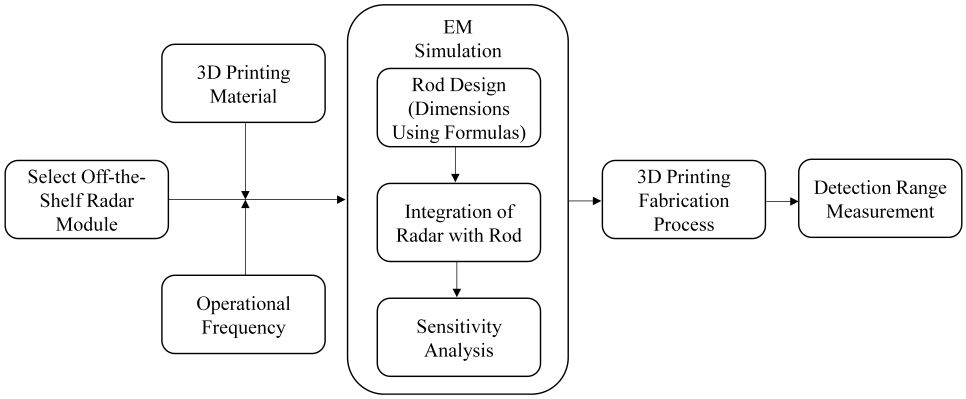


Figure 3.7: A flowchart outlining the main steps of the design, simulation, and manufacturing procedure necessary for integrating the dielectric rod lens with the radar module for detection range enhancement.

According to (3.3), it is evident that a 6 dB gain improvement at both transmitter and receiver antennas means that the TX and RX antennas' gains increase four times leading to the double detection range, separately. Hence, in the proposed system, a gain improvement of 6.6 dB for both the TX and RX antennas is deemed satisfactory to fulfil this requirement. Measurement results confirm that the HB100 radar integrated with the dielectric rod lens located at the back of a bicycle (Fig. 3.6) increases the detection range twice for TX and RX antennas, separately.

A sensitivity analysis was conducted to assess the impact of key design parameters on the gain performance of the dielectric rod lens. It was observed that variations in the diameters of the rod cross-sections (R_s and R_l) significantly affect gain. Specifically, increasing R_s by more than 1 mm or decreasing it by more than 2 mm results in a gain reduction of up to 1 dB, while variations in R_l beyond ± 1.5 mm cause a gradual gain loss of up to 1.8 dB. The spacing between the lens and the ground plane (d) is also critical; deviations greater than ± 2 mm can activate higher-order modes and degrade gain by up to 3 dB due to impedance mismatches. In terms of rod height (h), increasing the length by up to 20 mm or decreasing it by less than 5 mm produces negligible impact; however, further deviation leads to degraded gain and side lobe growth. The distance between rods, particularly Str, plays a key role in minimizing mutual coupling. Adjustments within ± 1.5 mm are safe, but larger changes can reduce gain by more than 2 dB. Similarly, increasing St or Sr by 5 mm or reducing them by 3 mm leads to gain reductions of up to 1 dB. Lastly, material properties are also influential: for dielectric constants between 2.0 and 2.8, gain remains stable, but a shift to 3.0 or 1.8 results in losses of 1 dB and 1.2 dB, respectively.

The complete process, encompassing the main steps such as design, simulation, and fabrication, is visually outlined in a flowchart, as depicted in Fig. 3.7, that is essential for the comprehension of the technique.

3.3 Spherical Dielectric GRIN Luneburg Lens

Gradient-index (GRIN) lenses have been studied using geometric optics, transformation optics, and metamaterials. The Luneburg Lens (LL) is a spherically symmetric GRIN lens with a radially varying refractive index. Various techniques exist to enhance Luneburg lens antenna performance. However, previous studies typically used a single-feed antenna for symmetric illumination of the Luneburg lens (Fig. 3.8a). Other research focused on multi-beam lenses, employing multiple feed antennas to rotate the sphere and align maximum radiation with the lens (Fig. 3.8b). [177] explored optimizing crossover levels between beams and more compact feeding arrangements. Modifications to the lens profile for beam shaping were also suggested, [178], though these often reduced directivity due to beam broadening.

In bistatic radar configurations, inspired by single-antenna gain enhancement techniques, separate lens structures are often proposed and designed specifically for the TX and RX antennas. Utilizing a commercial radar module with co-located transmitter (TX) and receiver (RX) antennas on a planar microstrip surface introduces unique challenges due to its offset-fed design (Fig. 3.8c) and dual independent sources. This setup requires significant modifications to the conventional symmetrically fed Luneburg lens design, typically with a horn antenna. In this configuration, the microstrip antennas direct radiation predominantly towards either the upper or lower hemisphere of the lens (Fig. 3.8d), differing from the symmetrical dual-feed multibeam Luneburg lenses. Here, both TX and RX antennas must project radiation directly forward (boresight), maintaining alignment at $\theta = 0$. In that case, using radar as the feed mechanism, makes the RX and TX antennas strategically offset relative to the lens. This offset causes beam tilting issues for both antennas, which is suboptimal for radar communication systems. In addition, for optimal performance, the feed's phase center should align with the lens's focal point [106].

Fig. 3.9a illustrates a bistatic Doppler X-band HB100 radar module, primarily used in bicycle collision applications. These continuous-wave radars are popular due to their affordability and accuracy but suffer from a limited detection range [175]. To address this limitation, we introduced a 3D-printed lens in the previous section, featuring an array of four dielectric rods with total dimensions of $1.75\lambda \times 2.1\lambda \times 2.5\lambda$, each mounted on separate TX and RX microstrip patch antennas. This design enables seamless integration

with the radar module and effectively doubles its detection range [175]. Achieving higher antenna gain enhancement through the integration of a single lens with the radar module enhances the detection range and significantly improves the radar's effectiveness and overall performance, while also reducing fabrication costs.

The GRIN Luneburg lens, designed as a symmetric structure made from a dielectric material with gradient refractive indices, functions as a polarization-independent system, efficiently converts spherical waves from the feed into quasi-plane waves, resulting in high-gain beam radiation [179]. A 3D-printed flat Luneburg lens designed for the Ku-Band achieved a maximum gain of 19.1 dB. [180] reported a high-gain, 3D-printed planar GRIN lens that, paired with a conical horn, delivered broadband gains of 16 to 24 dB across the Ku-band. Similarly, a planar wavefront transformation lens using gradient-index metamaterials enhanced gain by 6.5 dB at 10 GHz [181]. However, flat Luneburg lenses face challenges compared to spherical designs, particularly in terms of higher edge diffraction losses, which result from the sharp edges of the planar geometry, leading to reduced effi-

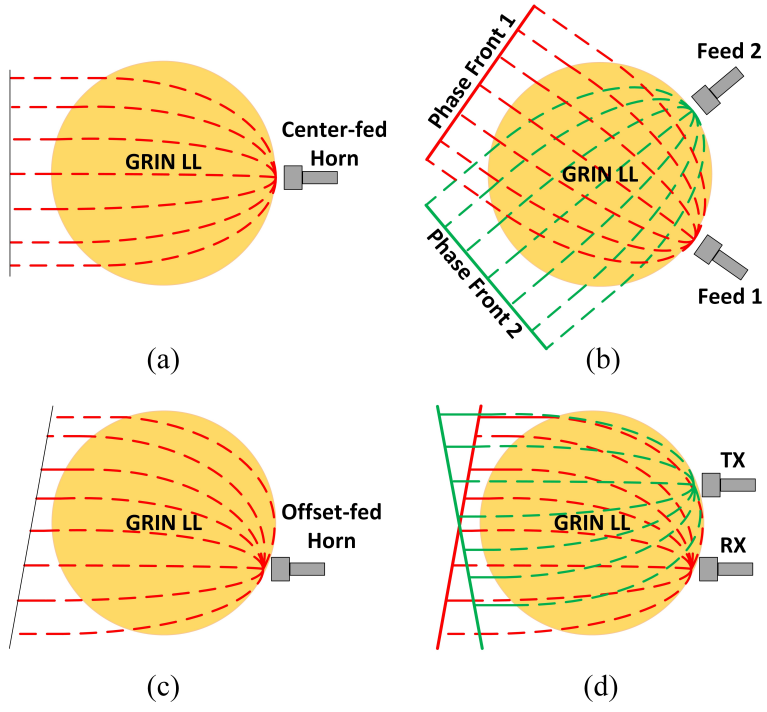


Figure 3.8: Ray tracing for GRIN Luneburg lens feeding scenarios: (a) Single center-fed, (b) Dual-beam symmetric feeds, (c) Single offset-fed, (d) Dual-beam asymmetric feeds.

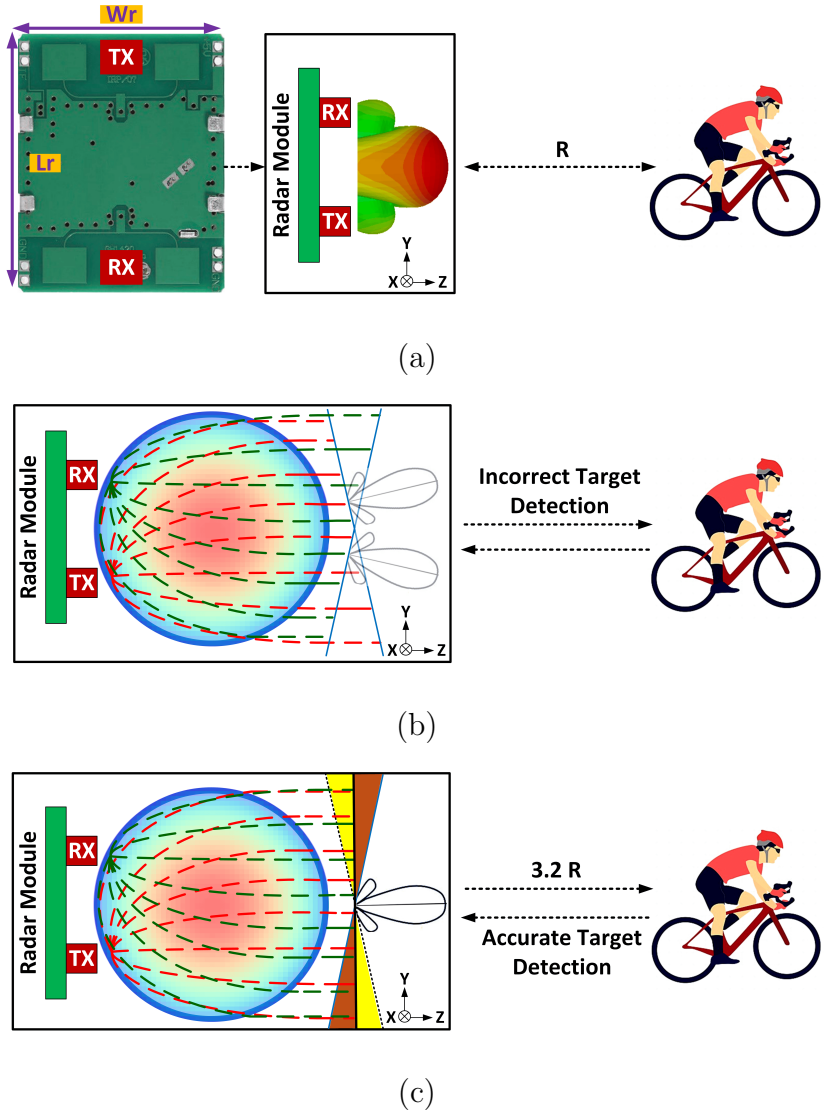


Figure 3.9: (a) Layout of the X-band Doppler off-the-shelf radar module with bistatic TX and RX antennas on the same plane, utilized for bicycle collision applications; (b) Integration of the conventional GRIN Luneburg lens with the radar, illustrating beam tilting issue using the ray tracing method; (c) Integration of the GRIN modified Luneburg lens, demonstrating focused radiation directed towards the boresight.

ciency and pattern distortion. They also exhibit increased side lobe levels (SLL), as the planar structure often produces uneven beam shaping, impacting directivity. Additionally, achieving the necessary GRIN profile in a flat configuration can be complex, limiting their versatility.

There is increasing interest in developing spherical GRIN Luneburg lenses that can be easily manufactured using a single material. However, their curved surfaces and the implementation of gradient indices within the lens pose significant fabrication challenges [182]. Advancements in 3D printing technology, have enabled practical and cost-effective implementations of uniform spherical Luneburg lenses according to specific requirements [183]. Studies have focused on approximating the permittivity distribution of GRIN lens by employing a lens design with constant dielectric permittivity, combined with the concept of effective permittivity areas [184]. However, this approach causes several disadvantages compared to traditional GRIN designs. One major drawback is the reduced focusing accuracy, as the smooth and continuous permittivity variation in GRIN lenses ensures precise wavefront reconstruction, which is compromised in the stepped approximation, leading to wave distortions. Furthermore, increased scattering and reflection losses arise due to abrupt transitions between regions of constant permittivity, degrading efficiency and gain. Finally, the approximated design often requires a larger physical size to achieve comparable performance to a traditional GRIN lens, making it less suitable for compact in-package applications.

In [185], we introduced a design methodology to enhance the radiation efficiency of compact modular bistatic radar systems by employing an advanced spherical dielectric gradient-index (GRIN) Luneburg lens with tunable refractive index gradients. The proposed design utilizes computationally optimized dual-beam masks, implemented as two exponentially tapered rods, to modify the conventional permittivity distribution of the Luneburg lens. This approach enables the use of a single lens for both transmitter (TX) and receiver (RX) radar microstrip antennas while addressing beam tilting issues. To validate the design, a prototype of the GRIN modified Luneburg lens (MLL) was manufactured using a cost-effective and uniform 3D-printing technique and seamlessly integrated with a commercially available X-band radar module. Experimental evaluation was conducted in a laboratory setting, measuring transmitted power using a standard X-band horn antenna connected to a spectrum analyzer and strategically positioned within the radar's radiation field at various aperture-to-aperture distances. Received power measurements were also recorded at the radar RX antenna, demonstrating significant improvements in both transmitted and received power. These enhancements collectively contribute to a substantial increase in the radar's signal-to-noise ratio (SNR) for high-gain communication systems. The MLL-enhanced radar module achieves a realized gain of 17.1 dB at 10.4 GHz, result-

ing in a 3.2-fold extension of the radar's detection range in both elevation and azimuth directions. Additionally, the integration of the GRIN MLL leads to a 10 dB enhancement in received power, corresponding to a 10-fold improvement in SNR when operating along the boresight. These findings validate the effectiveness and robustness of the proposed design in radar sensing enhancement.

To the best of the authors' knowledge, this is the first design of a GRIN Luneburg lens specifically tailored for integration with an in-package radar module, aiming to enhance radar sensing by improving the signal-to-noise ratio. While traditional designs typically employ single or multi-feed antennas for symmetric illumination, our work investigated the integration of a commercial radar module with bistatic communication and co-located TX/RX antennas-on-chip. This offset-fed dual-source configuration introduces unique challenges, requiring substantial modifications to the conventional symmetrically fed Luneburg lens. As shown in Fig. 3.8b, the microstrip antennas in this setup primarily direct radiation toward the upper or lower hemisphere of the lens, reducing efficiency for target detection. To achieve optimal performance, both TX and RX antennas must align and radiate directly forward along the boresight ($\theta = 0$).

3.3.1 Radar Antennas Employing a Modified Dielectric GRIN Luneburg Lens

GRIN Luneburg lenses, symmetrically fed by a single source, produce isotropic radiation through their spherical design, ensuring uniform phase distribution across the lens. Characterized by a spatially varying refractive index as defined by (3.4), traditional GRIN Luneburg lenses provide functional alternatives to conventional dielectric lenses,

$$n^2(r) = \varepsilon_r \mu_r = 2 - \left(\frac{r}{R}\right)^2 \qquad (\mu_r = 1) \tag{3.4}$$

where $r^2 = x^2 + y^2 + z^2$ defines the radial position within the spherical medium, ranging from 0 to R, with (x, y, z) representing the spatial coordinates and R denoting the external radius of the lens [186].

Fig. 3.9b shows ray tracing within a GRIN Luneburg lens with conventional permittivity distribution profile, integrated with radar TX/RX antennas. As shown, the offset placement of the antennas introduces a phase shift deviation from the optimal lens phase distribution, governed by the gradient permittivity profile inside the lens. This phase discrepancy results in two distinct phase fronts on the radiation side of the lens, leading to a

beam-tilting issue. In such cases, while the GRIN Luneburg lens enhances the gain of the radar antennas, the radiation patterns of the TX and RX antennas are not aligned along the boresight, ultimately reducing the SNR and limiting the radar's detection range.

Therefore, as depicted in Fig. 3.9c, a modified phase distribution, achieved by altering the permittivity profile within the conventional Luneburg lens, is required to address the beam-tilting issue. The yellow region represents the required compensation phase distribution for the TX antenna, while the brown region corresponds to the RX antenna. This modification not only corrects the beam misalignment but also enhances the gain of the radar TX/RX antennas.

In a bistatic radar system with co-located TX and RX, the antennas are positioned in close proximity but do not share the same aperture, unlike in monostatic radar. This configuration introduces variations in SNR calculation compared to monostatic systems. Since the TX and RX antennas are identical and positioned on the same plane, the SNR indicated by the radar received power can be expressed as (3.2) [175].

According to (3.2), the enhancement of the SNR in radar systems is significantly influenced by improvements in TX and RX antenna gains. Higher antenna gains increase the power density of the transmitted signal toward the target, thereby maximizing the energy intercepted and re-radiated by the target based on its radar RCS. Simultaneously, improved RX antenna gains enhance the efficiency of capturing the reflected signal, ensuring minimal loss of the target's scattered energy. This synergistic effect leads to a substantial increase in both transmitted and reflected power, directly improving the SNR and enabling more accurate target detection and characterization in radar sensing.

3.3.2 Modified GRIN Luneburg Lens for Radar Integration

This section examines the integration of the proposed bistatic radar system with the GRIN Luneburg lens, designed with a diameter of $5\lambda_0$, as shown in Fig. 3.10a. The radar module is positioned with an approximate 2 cm offset for each TX/RX array antenna relative to the center of the Luneburg lens, maintaining a 0.16λ gap between the antennas and the lens. Full-wave electromagnetic simulations are conducted to generate the radiation patterns for the TX and RX antennas. The permittivity profile of the conventional GRIN Luneburg Lens (CLL), which features a symmetrical permittivity distribution as illustrated in Fig. 3.10a, varies according to (3.4), starting from $\varepsilon_r = 2$ at the center of the sphere and gradually decreasing to $\varepsilon_r = 1$ at its outer layer.

Fig. 3.10b illustrates the 2D cutting-plane of the electric field radiation for the TX and RX antennas separately, in the presence of the CLL. As shown, the generated electric

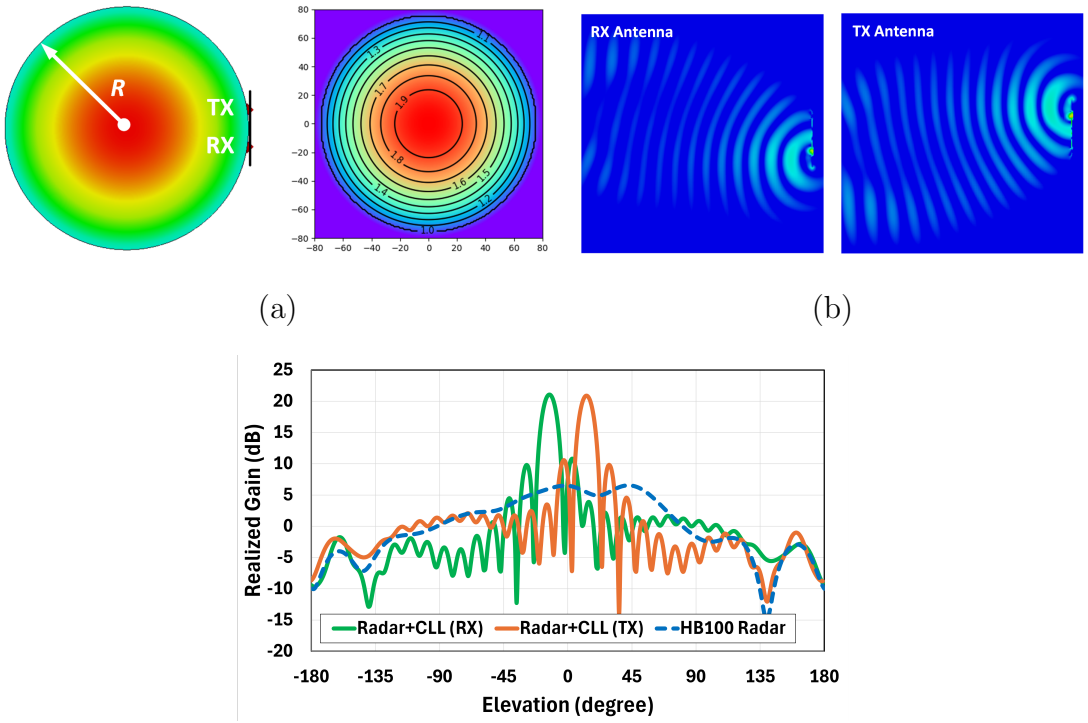


Figure 3.10: (a) Cross-section of the conventional GRIN Luneburg (CLL) lens showing its permittivity distribution profile; (b) E-field propagation from the radar TX/RX antennas in the presence of the CLL; (c) 2D gain pattern for TX/RX antenna at 10.4 GHz when the radar is integrated with the CLL.

fields produce equi-phase radiation on the radiation side of the CLL, resulting in high-gain capability; however, this comes at the cost of phase front rotation. As a result, integrating this lens with a radar module featuring offset TX and RX antennas poses significant design challenges and reduces performance. This E-field distribution generates the far-field radiation pattern for both antennas. As shown in the 2D radiation pattern in Fig. 3.10c, compared to the HB100 radar gain pattern, the integration of the CLL significantly enhances the realized gain of both TX/RX antennas, reaching 21 dB at 10.4 GHz, albeit with a 13° maximum beam tilting.

We address the beam tilting issue in TX and RX antennas by introducing a configurable Modified GRIN Luneburg lens (MLL). The design incorporates dual-beam masks,

implemented as two exponentially tapered rods, to adjust the permittivity distribution of the conventional Luneburg lens, as formulated in (3.5),

$$\varepsilon_r(x,y,z) = \max\{1\ ,\ 2-(\tfrac{r}{R})^2 + f_{\text{inc}} \cdot \sum_{i=1}^{2} \psi\left(e^{\frac{d_z}{\alpha}} \cdot r_t - \sqrt{(x-x_i)^2+(y-y_i)^2}\right)\} \tag{3.5}$$

where R is the radius of the Luneburg lens, α is the parameter controlling the exponential decay along the z-direction, r_t is the radius of the rods, $(x_i,\ y_i)$ are the coordinates of the TX/RX antenna defining the position of the rods' center, f_{inc} is the increment factor for the permittivity inside the rod, and $\psi(\gamma)$ is the Heaviside function defined as,

$$\psi(\gamma) = \begin{cases} 1 & \text{for} \quad \gamma > 0 \\ 0 & \text{for} \quad \gamma \leq 0 \end{cases} \tag{3.6}$$

To achieve optimal performance, the phase center of the radar's TX and RX antennas must align with the lens's focal point [106], which dictates the placement of the rods within the Luneburg lens, d_z. A notable benefit of the GRIN Luneburg lens is that its focal point is located on the outer spherical surface, enabling direct integration with the feeding antenna and eliminating unused space from the lens focal point to the antenna phase center.

In the HB100 radar configuration shown in Fig. 3.10a, the TX and RX antennas share the same x and z coordinates but are symmetrically positioned along the y axis. The two tapered rods are positioned at the phase center of the microstrip array antennas, extending along the full diameter of the sphere in the x-z and y-z planes, as shown in Fig. 3.11a across various Cartesian planes. In the formulation of (3.5), the rods are assumed to be located at coordinates $(x_i,\ y_i,\ z_i)$, where (i) denotes the antenna type (i=1 for TX and i=2 for RX).

The parameters in (3.5) define the permittivity profile of the Luneburg lens with rods positioned near the TX and RX antennas. The exponential decay parameter α governs how the influence of the rods diminishes along the z-axis. Additionally, a variable rod radius r_{tube}, which varies with z through an exponential taper, adds complexity to the rod structure. The increment factor f_{inc} gradually scales the permittivity increase within the rods as described in the equation. However, considering the practicalities of 3D-printing technology for fabrication, discretizing the rod permittivity within the LL is more feasible. To balance fabrication ease and performance, three fixed permittivity values can be assigned to the rod regions. In this case, the Heaviside function $\psi(\gamma)$ in (3.5) functionally defines the masks $(\text{mask}_1, \text{mask}_2, \text{mask}_3)$, which identify the regions where the permittivity is modified due to the presence of the rods,

$$\varepsilon_r(x,y,z) = \max\left\{1, 2 - \frac{r^2}{R^2} + \sum_{i=1}^{2} \psi_i(x,y,z)\right\} \tag{3.7}$$

where $\psi_i(x,y,z)$ accounts for the contributions of rods centered at (x_i, y_i) for each beam, and is defined as:

$$\psi_i(x,y,z) = \begin{cases} \varepsilon_{r1}, & \text{if } z \in [-R, -0.45R] \text{ and} \\ & (x-x_i)^2 + (y-y_i)^2 < r_{\text{tube}}^2, \\ \varepsilon_{r2}, & \text{if } z \in [-0.45R, 0.68R] \text{ and} \\ & (x-x_i)^2 + (y-y_i)^2 < r_{\text{tube}}^2, \\ \varepsilon_{r3}, & \text{if } z \in [0.68R, R] \text{ and} \\ & (x-x_i)^2 + (y-y_i)^2 < r_{\text{tube}}^2, \\ 0, & \text{otherwise.} \end{cases} \tag{3.8}$$

where $r_{\text{tube}}(z)$ is the dynamic radius of the rods, defined as:

$$r_{\text{tube}}(z) = e^{\frac{z}{\alpha}} \cdot r_t \tag{3.9}$$

The base permittivity profile, $2 - r^2/R^2$, represents the classical Luneburg lens permittivity distribution without the rod modifications. The rod contributions are modeled using the Heaviside-like function $\psi_i(x,y,z)$, which segments the lens into three distinct z-regions, each associated with a specific permittivity value (ε_{r1}, ε_{r2}, ε_{r3}). The regions are defined as follows:

- $[-R, -0.45R]$: First region with permittivity ε_{r1}.
- $[-0.45R, 0.68R]$: Second region with permittivity ε_{r2}.
- $[0.68R, R]$: Third region with permittivity ε_{r3}.

The function $\psi_i(x,y,z)$ determines whether a given point (x,y,z) falls within the rod's influence in each region. The dynamic rod radius $r_{\text{tube}}(z)$ ensures the influence of rods varies along the z-axis, reflecting the exponential tapering effect. Algorithm 1 outlines the process for assigning the values of the 3-mask dielectric rods within the Luneburg lens.

The rods are initially designed using the Python code outlined in Algorithm 1, generating dielectric distribution data as an ASCII file that maps permittivity values to specific

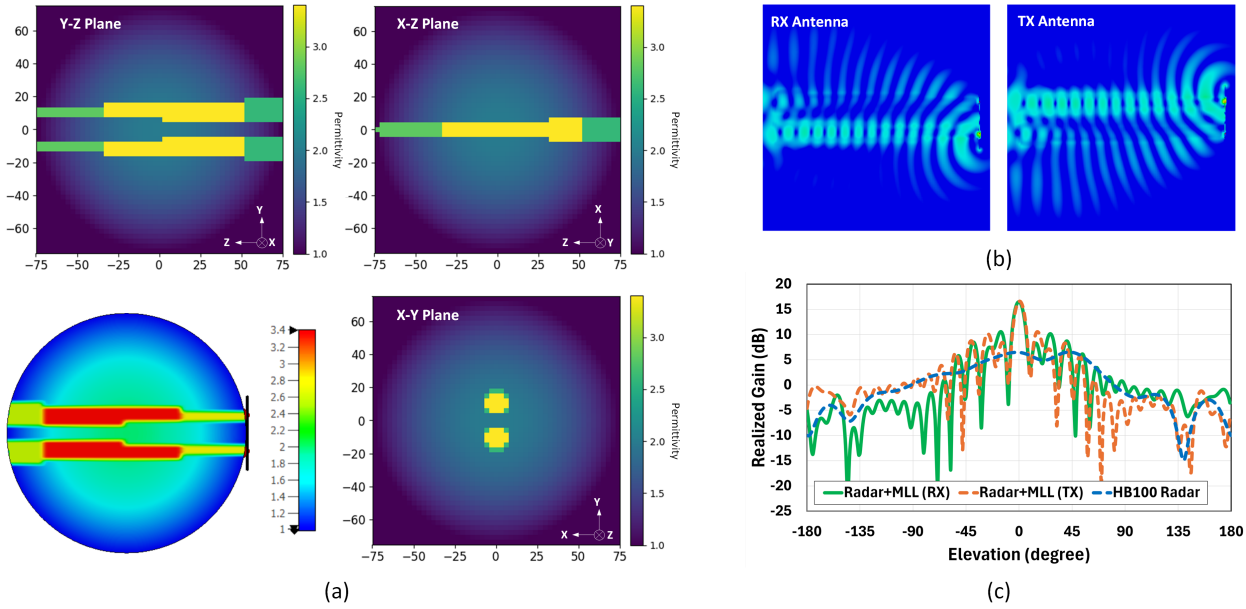


Figure 3.11: (a) permittivity distribution profile of the Modified GRIN Luneburg lens (MLL) in different planes; (b) E-field propagation from the radar TX/RX antennas in the presence of the MLL; (c) 2D gain pattern for TX/RX antenna radiation at 10.4 GHz when the radar is integrated with the MLL.

spatial points. This data is then applied to a sphere fed by the radar in a full-wave simulation environment. The Space Map-based material model used here is a unique material definition that can be customized in Studio using dedicated VBA commands and simulated with the T-solver. This material model is particularly advantageous for designing Gradient Refractive Index (GRIN) lenses, as it allows precise spatial definition of material properties. Advances in additive manufacturing and materials have further enhanced the feasibility of 3D printing GRIN dielectric lenses, unlocking new opportunities for creating custom components.

In (3.5), the initially optimized parameters, considering the offset feed and the distance between the TX and RX antennas, are determined as: $R = 75$ mm, $\alpha = 160$, $r_t = 5$ mm, and $f_{inc} = 1.5$. These parameters correspond to the rods' permittivity values of $\epsilon(\text{mask}_1) = 2.8$, $\epsilon(\text{mask}_2) = 3.4$, and $\epsilon(\text{mask}_3) = 2.6$. These parameters ensure high gain and low side-lobe levels by enhancing the electric field intensity along the rods, as shown in Fig. 3.11b, and confining the electric field distribution to the boresight direction. This targeted field alignment effectively mitigates the beam tilting issue for both TX and RX

Algorithm 1 Dual-Beam Luneburg Lens Design

Input:

R: Radius of the Luneburg lens

r_{step}: Step size for grid discretization

centers $= [\text{center}_1, \text{center}_2]$: Rod centers

r_t: Base radius of the rod tubes

Output:

ϵ: Modified 3D permittivity matrix with dual beams

ASCII file: Fabrication data for manufacturing

Grid Generation:

Discretize x, y, z over the spherical domain using r_{step}

Compute Base Permittivity:

$$\epsilon = 2 - \frac{x^2 + y^2 + z^2}{R^2}$$

Modify Permittivity for Dual Beams:

for each center in centers **do**

Compute $d_z = z - \text{center}[0]$

$r_{\text{tube}} = \exp(d_z/\alpha) \cdot r_t$

Define masks for three segments:

mask1: $z \in [-R, -0.45R]$ and $(x - \text{center}[2])^2 + (y - \text{center}[1])^2 < r_{\text{tube}}^2$

mask2: $z \in [-0.45R, 0.68R]$ and same condition

mask3: $z \in [0.68R, R]$ and same condition

Update ϵ values:

$\epsilon[\text{mask1}] = 2.8$

$\epsilon[\text{mask2}] = 3.4$

$\epsilon[\text{mask3}] = 2.6$

end for

Ensure all $\epsilon \geq 1$

Save Data:

Flatten (x, y, z, ϵ) into a 2D array for ASCII export

Generate 2D plots for XY, XZ, and YZ planes

antennas, resulting in improved radiation performance.

An analysis of the realized gain radiation pattern, depicted in Fig. 3.11c, reveals a well-shaped pattern with peak directivity consistently maintained at $\theta = 0°$, indicating the system's ability to focus energy effectively in the desired direction. This design minimizes phase distortions and ensures uniform wave propagation, critical for maintaining

optimal radar performance. Additionally, a comparison of radiation patterns at 10.4 GHz highlights that the modified GRIN Luneburg lens significantly enhances the gain of the HB100 radar module's TX and RX antennas, achieving 16.6 dB with a peak at $\theta = 0°$. This improvement underscores the lens's ability to enhance radar performance, even under offset-fed conditions. However, it should be noted that this design achieves a 4.4 dB lower gain improvement compared to the conventional ε_r distribution, as illustrated in Fig. 3.10c.

3.3.3 Modified GRIN Luneburg Lens Manufacturing

For transitioning from lab to manufacturing, equipment, processes, and materials must mature to ensure high reliability and throughput while minimizing variability and cost. Traditional manufacturing methods for GRIN lenses often rely on multi-part assembly or complex subtractive manufacturing processes, which are both time-intensive and costly [187]. In contrast, additive manufacturing offers significant design and production flexibility, drastically simplifying the creation of GRIN media. For this study, Fortify's digital light processing (DLP) additive manufacturing platform is employed, enabling efficient and precise fabrication [188]. However, each manufacturing approach comes with its own set of advantages and drawbacks.

The Fortify Flux Core DLP 3D printer is considered for the manufacturing of the designed spherical GRIN MLL, utilizing Rogers Corporation's Radix™ 3D-printable resin dielectric material, with a relative permittivity of 2.8, that offers low dielectric loss with loss tangent of 0.0043 and the ability to print an entire lens layer in a single exposure [189].

Utilizing the output of the Algorithm 1, the simulations are converted to a 3D printable structure featuring a Gyroid shaped unitcell. The unitcell size of artificial dielectrics determines the maximum operating frequency and also drives cost. In this study, the length of the cubic gyroid unitcell at each side, d, is considered as equal as 3 mm, which is the smallest value considering practical manufacturing constraints of Fortify technology to minimize the phase error loss in the permittivity profile within the lens and it is optimal for a maximum operational frequency of 30 GHz, as reported in [190]. In this manufacturing setup, the effective permittivity is controlled using gyroid unitcells by calculating the air fraction for each region of the lens design, while maintaining a constant cubic unitcell size and varying the wall thickness of the unitcell. The relationship between the air volume fraction of the unitcell geometry and the effective permittivity is determined using a Reverse Claussius-Mossotti model [189],

$$V_{\text{air}} = \frac{(\varepsilon_{\text{eff}} - \varepsilon_r) \times (1 + 2\varepsilon_r)}{(\varepsilon_{\text{eff}} + 2\varepsilon_r) \times (1 - \varepsilon_r)} \tag{3.10}$$

where ε_{eff} is the effective permittivity of the gyroid lattice region, V_{air} is the volume fraction of air, and ε_r is the permittivity of the solid dielectric material, resin, used to form the lattice. Considering the ε_{eff} value from the output of the Algorithm 1, and $\varepsilon_{r,\text{resin}} = 2.8$, (3.10) represent the relationship between the required effective permittivity and the relative air fraction which results the calculated wall thickness of the gyroid unitcell.

The lens designed for this study is a 75 mm radius spherical lens with a Luneburg style and permittivity distribution ranging from 1 to 3.4, as shown in Fig. 3.11a. In the manufacturing process, as r approaches R, the relative permittivity approaches 1. However, to maintain structural integrity, the side walls within the unitcell must remain greater than µm which results in a minimum effective permittivity of 1.15. Therefore, the Luneburg lens permittivity profile should be printed such that all radii for which the nominal permittivity is less than 1.15 would maintain that value in the periphery [190]. In that case, a consequence of adapting this lens to be manufacturable is that the focal point of the lens is no longer on the surface. This aspect of a Luneburg lens system prevents the maximization of the antenna's aperture efficiency.

Furthermore, to maximize lens efficiency in this work, a gyroid unitcell size of 3 mm is selected as the smallest feasible option. However, this choice imposes fabrication constraints, including reduced flexibility due to drilling limitations and unitcell wall thickness restrictions. As a result, it can be shown that the maximum achievable effective permittivity is limited to 2.4, which falls short of the proposed MLL design's requirement of 3.4 for the rods. Consequently, the permittivity range in the modified GRIN Luneburg lens, including the rods depicted in Fig. 3a, should be adjusted from (1,3.4) to (1.2,2.4) to accommodate these manufacturing limitations.

To address this issue, we proposes the concept of overlapping two rods to ensure uniformity, which improves wavefront alignment and still resolves the beam tilting problem with less demanding permittivity requirements. This modification involves adjusting the design parameters, including the center positions of the rods, the base radius of the rod tubes, the lengths of the three discrete rod masks, and their relevant permittivity values. These parameters are optimized to maintain the permittivity within the range of $1.15 < \varepsilon < 2.4$, as outlined in Algorithm 2.

Fig. 3.12a illustrates the updated design of the overlapped rods within the conventional GRIN Luneburg lens. The overlap creates an effective permittivity region that blends the properties of both rods, minimizing phase distortions and abrupt changes while enabling

Algorithm 2 Dual-Beam Luneburg Lens Design (Adjusted for Fabrication)

Input:

$R \leftarrow$ Radius of the Luneburg lens

$r_{\text{step}} \leftarrow$ Step size for grid discretization

$\text{centers} = [\text{center}_1, \text{center}_2] \leftarrow$ New rod centers

$r_t \leftarrow$ New base radius of the rod tubes

Output:

$\epsilon \leftarrow$ Modified 3D permittivity matrix with dual beams

ASCII file: Fabrication data for manufacturing

Grid Generation:

Discretize x, y, z over the spherical domain with r_{step}

Compute Base Permittivity Profile:

$\epsilon \leftarrow 2 - \frac{x^2+y^2+z^2}{R^2}$

Modify Permittivity for Dual-Beam Formation:

for each center in $[\text{center}_1, \text{center}_2]$ **do**

$d_z \leftarrow z - \text{center}[0]$

$r_{\text{tube}} \leftarrow e^{d_z/\alpha} \cdot r_t$

Define masks:

$\text{mask}_1 \leftarrow z \in [-R, -0.25R]$ and $(x - \text{center}[2])^2 + (y - \text{center}[1])^2 < r_{\text{tube}}^2$

$\text{mask}_2 \leftarrow z \in [-0.25R, 0.88R]$ and $(x - \text{center}[2])^2 + (y - \text{center}[1])^2 < r_{\text{tube}}^2$

$\text{mask}_3 \leftarrow z \in [0.88R, R]$ and $(x - \text{center}[2])^2 + (y - \text{center}[1])^2 < r_{\text{tube}}^2$

Update ϵ values:

$\epsilon[\text{mask}_1] \leftarrow 1.97$

$\epsilon[\text{mask}_2] \leftarrow 2.4$

$\epsilon[\text{mask}_3] \leftarrow 1.83$

end for

Ensure $\epsilon \geq 1.15$

Save Data:

ASCII file $\leftarrow$ Flatten(x, y, z, ϵ) into a 2D array

Generate 2D plots for the X-Y, X-Z, and Y-Z planes

a smoother transition and gradual blending of permittivity. This results in smoother wavefront propagation and reduced distortion, as depicted in Fig. 3.12b.

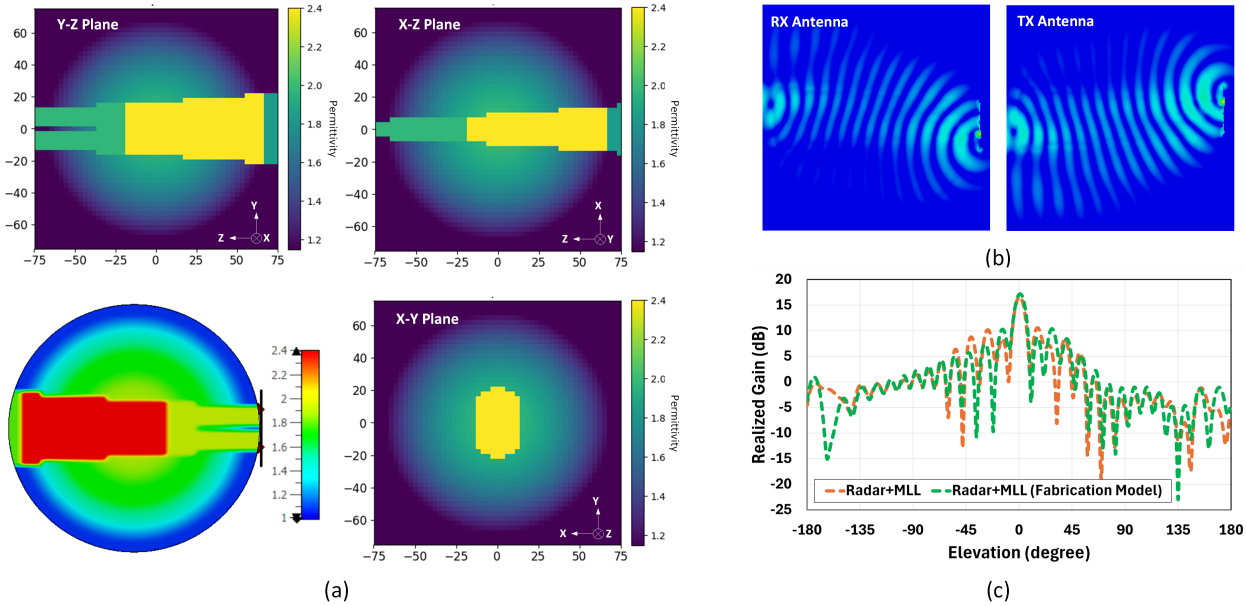
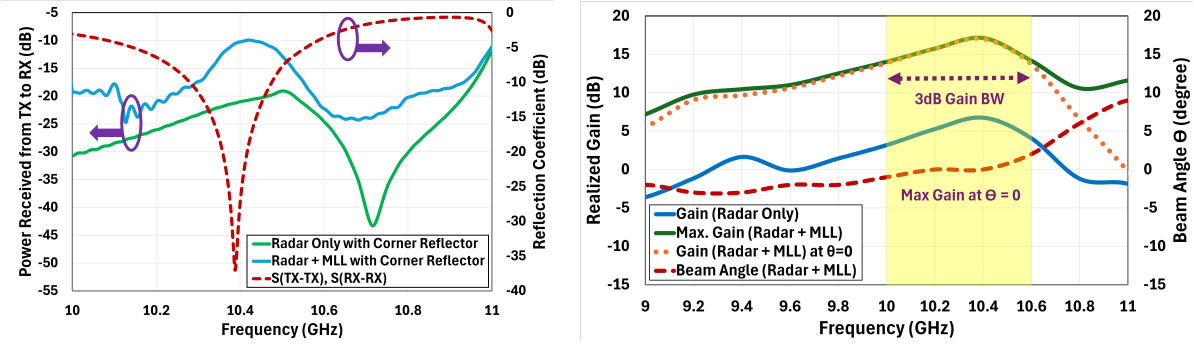


Figure 3.12: (a) Permittivity distribution profile of the updated GRIN MLL with overlapped rods; (b) Electric field propagation from the radar TX/RX antennas in the presence of the MLL with overlapped rods; (c) 2D realized gain pattern for TX/RX antenna radiation at 10.4 GHz when the radar is integrated with the MLL updated with overlapped rods.

The new design version of the GRIN modified Luneburg lens with overlapped rods is integrated with the HB100 radar module to evaluate its efficiency. Fig. 3.12c compares the realized gain pattern of the initial design with the modified lens to the second design featuring overlapped rods optimized for fabrication. The results indicate that the radiation patterns are similar, with both radiating in the boresight direction. Moreover, the new design achieves a higher maximum gain of 17.2 dB at $\theta = 0°$ for both TX and RX antennas, resulting in a 3.2-times improvement in radar detection range, as calculated using (3.2).

Additionally, it is noteworthy that the designed modified Luneburg lens can be directly attached to the radar module, and as demonstrated in Fig. 3.13a, this integration does not disturb the reflection coefficient of the TX/RX antennas. This figure also compares the transmitted power from the TX antenna to the RX antenna, S(TX-RX), for the radar module integrated with and without the MLL, when placed in front of a corner reflector acting as a perfect electric conductor object. The results in Fig. 3.13b demonstrate that integrating the GRIN MLL increases the reflected power from the object by 10 dB, resulting



(a) (b)

Figure 3.13: (a) Simulation analysis of the S-parameters for the radar module integrated with the updated GRIN MLL, including S(TX-TX) and S(RX-RX), and investigation of the power received from TX to RX when a corner reflector is placed in front of the radar radiation, comparing cases with and without the lens, (b) Beam angle and realized gain variations of the radar antenna integrated with the MLL as a function of frequency.

in a 10-times improvement in the radar signal-to-noise ratio, as calculated using (3.2).

To investigate the efficiency, an analytical model can be formulated to establish a correlation between the diameter of a Luneburg lens and the resultant gain enhancement, drawing upon fundamental antenna theory and optimization methodologies. Within the framework of aperture lens theory, the approximate realized gain for a conventional Luneburg lens antenna can be expressed as:

$$G \approx \varepsilon \left(\frac{\pi D}{\lambda}\right)^2 \tag{3.11}$$

where G represents the realized gain of the antenna, influenced by several factors including the aperture efficiency (ϵ), the diameter of the Luneburg lens ($D = 2R$), and the wavelength (λ) of the operating frequency.

Utilizing (3.11) and considering a lens diameter of 15 cm at a design frequency of 10.4 GHz under ideal conditions with 100% efficiency, the theoretical maximum gain that can be provided by the conventional lens is 24.2 dB. In practical simulations, a gain of 23.1 dB was observed for the conventional Luneburg lens when utilizing a single horn antenna as the feed. When integrated with the radar system, the realized gain is measured as 21 dB, with a beam tilting of 13 degrees, causing misalignment from the boresight direction.

This misalignment reduces effective power transfer, degrading the overall system performance. By addressing the beam tilting issue, we improved the alignment of both TX and RX antennas to the boresight direction, ensuring optimal focusing. As a result, while the gain decreased due to additional modifications, the final realized gain reached 17.2 dB. Thus, while solving the beam tilting issue results in a 3.8 dB gain reduction compared to the beam-tilted radar configuration (21 dB to 17.2 dB), this modification significantly enhances radar sensing capability, as the received power is now maximized along the intended direction, improving SNR stability and detection accuracy across the operational range. This trade-off is necessary to maintain boresight beam alignment, thereby improving the radar's sensing accuracy and ensuring optimal SNR at the detection range.

For the designed modified Luneburg lens (MLL), the relationship between gain and lens diameter can be elucidated through a curve-fitting approach. This method involved using a variety of simulated data points, which represented the realized gain across different lens diameters. This analytical technique enabled the derivation of the following relationship for the gain enhancement factor:

$$K = (55.21D^3 - 26.498D^2 + 4.2089D - 0.2162) \times 10^4$$

$$G_{\text{Enhancement}}(dB) = 10\log\left(\frac{K}{G_{\text{feed}}(\text{linear})}\right) \tag{3.12}$$

In the 3D printing dielectric fabrication process, it is crucial to assess the sensitivity of gain performance and main lobe direction to the permittivity distribution within the GRIN MLL, particularly when using rods with varying permittivity values. Analysis indicates that the gain of the TX and RX antennas remains consistent at $\theta = 0^\circ$ provided the permittivity variation in the rods does not exceed 10%. However, when the variation exceeds 13%, the gain decreases by 0.6 dB, accompanied by a 1-degree shift in the main lobe direction.

Another aspect of the investigation focuses on the discretization approach, which balances electromagnetic functionality and manufacturing feasibility. In this study, a step size of $0.1\lambda_0$, equivalent to a unitcell size of 3 mm, is used to ensure a relatively uniform permittivity distribution across the sphere and to minimize phase error loss. It is observed that deviations from this step size of up to 5% result in a 0.5 dB reduction in gain enhancement, while maintaining a constant lens diameter.

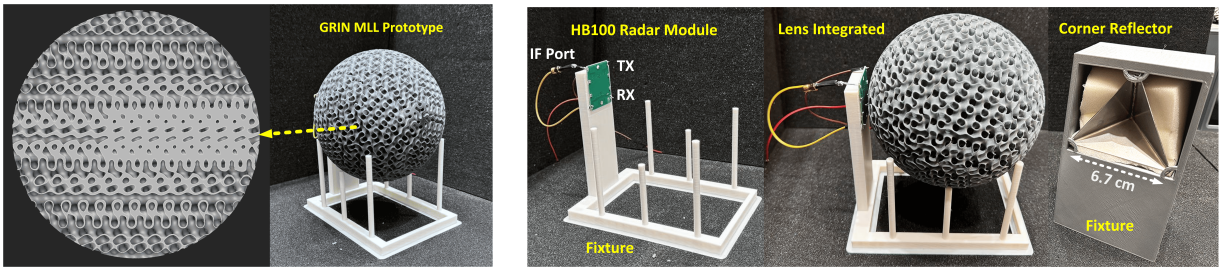
While the proposed MLL demonstrates significant advantages in beam focusing and gain enhancement, it is crucial to acknowledge its limitations compared to alternative solutions

such as planar lenses and metasurfaces. A primary drawback is its volume and size, as the three-dimensional spherical structure of the Luneburg lens makes it inherently bulkier than planar lenses, which are more easily integrated into compact radar systems. It may limit its feasibility in conformal or lightweight designs such as UAV-mounted or wearable radar systems. Fabrication complexity is another important consideration. The GRIN profile of the Luneburg lens requires precise permittivity variation, which is traditionally difficult to achieve using standard dielectric materials. While modern 3D printing technologies provide a viable solution, they introduce constraints in material selection and fabrication precision.

Beam squinting presents another limitation in broadband applications, as the GRIN structure inherently introduces chromatic aberration and phase dispersion due to the frequency-dependent nature of the refractive index. This results in shifts in the focal point and beam direction across different frequencies, affecting the beam's stability. The degree of this shift is influenced by the dispersion properties of the material, as the relative permittivity (ϵ_r) varies with frequency, affecting wave propagation through the GRIN medium. Consequently, in broadband applications, the Luneburg lens is more susceptible to beam misalignment compared to planar lenses, which can incorporate phase compensation techniques to mitigate these effects.

To evaluate this phenomenon, simulations were conducted to analyze the realized gain of the radar system with and without the MLL, focusing on beam angle variations across the 9–11 GHz frequency range. As shown in Fig. 3.13b, while the integration of the MLL continuously enhances the radar's gain, the beam angle shifts with increasing or decreasing frequency. The results indicate that beam angle variation between 9 GHz and 10.75 GHz remains within 5 degrees, with the ideal boresight ($\theta = 0$) occurring at 10.4 GHz. Considering a 5-degree beam variation as the acceptable limit, the 3-dB gain bandwidth of the radar integrated with the MLL extends from 10 GHz to 10.6 GHz.

Despite these limitations, the GRIN Luneburg lens remains a highly promising solution due to its high gain, simple design, and exceptional flexibility in beam direction manipulation, which are particularly advantageous in radar applications requiring efficient energy focusing. Furthermore, advancements in 3D printing technology have significantly improved the feasibility of GRIN structures, making their fabrication more accessible and scalable.



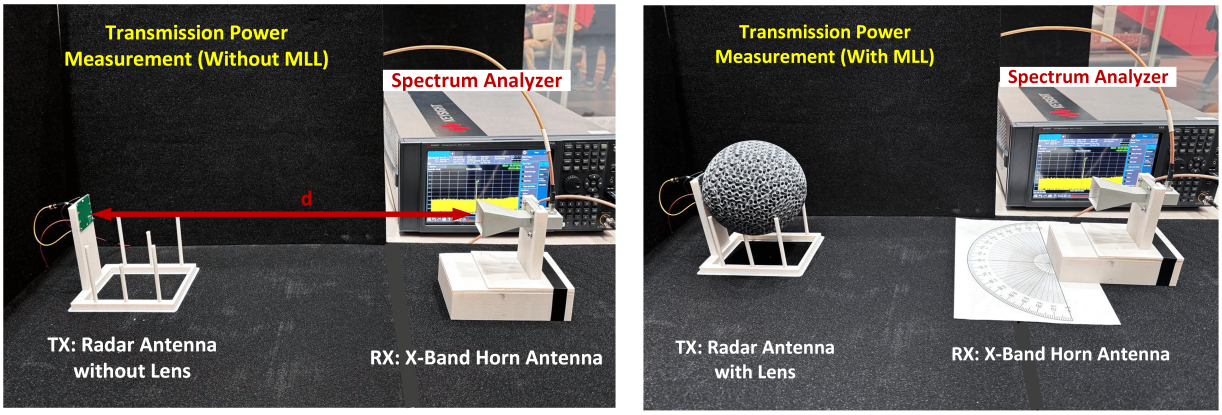
(a) (b)

Figure 3.14: (a) Prototype of the MLL uniformly fabricated using Fortify 3D-printing, with a 2D cross-section showing the implementation of overlapped rods designed within the lens; (b) 3D-printed fixture for holding the corner reflector and HB100 radar module, powered by a DC power supply, and positioned at an appropriate location and distance attached to the MLL.

3.3.4 Radar Module Integrated with GRIN MLL: Measurement Results

In this section, the performance of the Updated GRIN modified Luneburg Lens is evaluated. The section concludes with in-lab measurements of transmitted and reflected power, providing an analysis of the gain enhancement capabilities of the GRIN MLL.

To evaluate the performance of the proposed setup, an X-band HB100 radar module was utilized to illuminate the modified GRIN Luneburg lens. The measurement setup is illustrated in Fig. 3.14. Fig. 3.14a shows the fabricated prototype of the 3D-printed spherical modified GRIN Luneburg lens, along with a 2D cross-section of its structure to demonstrate how the modified rods are designed and implemented within the sphere. As shown in Fig. 3.14b, a 3D-printed dielectric fixture was designed to securely position the GRIN MLL in front of the radar, ensuring that the rods are aligned with the radar's TX/RX antennas at an appropriate distance. The radar is in direct contact with the lens, and due to the spherical nature of the lens and antennas' offset, the distance from the antennas to the lens surface reaches 1.8 mm. The radar operates with a +5 volt DC power supply for optimal performance. The intermediate frequency (IF) port of the radar is subsequently employed to quantify the enhancement in reflected power from a corner reflector, characterized by three flat surfaces each measuring 6.7 cm in side length. This measurement is conducted by connecting the IF port to a spectrum analyzer, which records the signals received by the radar receiver.



(a) (b)

Figure 3.15: In-lab measurement setup illustrating the radar system as the transmitter and an X-band horn antenna as the receiver, positioned at different distances: (a) radar without the MLL integrated; (b) radar integrated with the MLL.

As depicted in Fig. 3.15, a standard X-band horn antenna is employed to validate the power transmission enhancement achieved with the designed lens. The horn antenna is placed directly in front of the radar at the same height, ensuring that the received signal originates from the boresight radiation without any tilting issues. The horn antenna is connected to a spectrum analyzer to measure the transmitted power at various distances from the radar, comparing results for configurations with and without the GRIN MLL integration.

To ensure accurate power measurements in the lab setting, the radiation side of the antennas is covered with flexible EMI absorber sheets, as shown in Fig. 3.15. The radar antennas (acting as the transmitter) and the horn antenna (acting as the receiver) are positioned with an aperture-to-aperture spacing of d to simulate real-world in-lab conditions. Fig. 3.15a illustrates the setup configuration for measuring transmitted power when the radar operates without the lens, while Fig. 3.15b shows the same setup with the GRIN MLL attached. Fig. 3.16a to 3.16c compares the power received by the horn antenna on the spectrum analyzer for both cases, radar antennas with and without the lens, at three different distances, $d = 10\lambda, 15\lambda$, and 20λ, to validate the repeatability and effectiveness.

The results show that the transmitted power increases by 10 dB at 10λ, 10.2 dB at 15λ, and 10.1 dB at 20λ distance at 10.2 GHz, when the radar is integrated with the GRIN MLL. The consistent power enhancement across all investigated distances demonstrates the

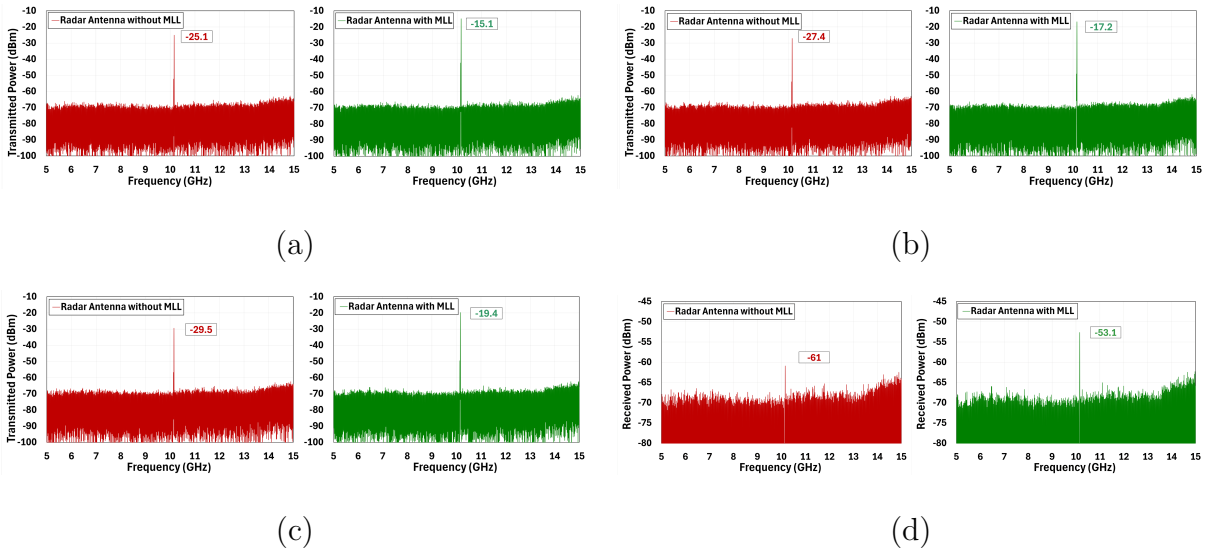


Figure 3.16: Comparative analysis of the power transmitted by the radar with/without the MLL and received by the X-band horn antenna placed at distances of (a) 10λ, (b) 15λ, and (c) 20λ. (d) Comparative analysis of the power received by the radar with/without the MLL in the presence of corner reflector

effectiveness of the designed GRIN MLL and reliability of the in-lab setting measurement approach. While the simulation results in Fig. 3.13b indicate a maximum radar gain at 10.4 GHz, the observed discrepancy suggests minor variations in the operational frequency under certain experimental conditions or configurations. However, as shown in Fig. 3.13b, operating within the 10 to 10.5 GHz range does not introduce significant differences in the results or pose challenges to the design.

In the following measurement analysis, the spectrum analyzer was connected to the IF port of the HB100 radar module, which was positioned in front of a corner reflector to replicate the simulation results illustrated in Fig. 3.13a. Initially, the radar was not able to detect variations in the IF output with and without the lens, due to power saturation at the radar mixer. This mixer combines the TX and RX signals to produce an IF signal, which is then processed to extract data such as range and velocity. When the received signal meets or exceeds the mixer's saturation point, no increase in IF output is observed, despite additional received power. Notably, the HB100 radar module is characterized by its low IF port power output.

To address the issue of high received power levels, increasing the range between the

radar and the target was considered to attenuate the RX signals, facilitating a relative comparison with and without the lens. However, the constraints of our measurement environment, particularly the limited space and practical limitations on the maximum feasible distance between the TX and RX antennas, prevented us from extending the range adequately. Utilizing the corner reflector, as depicted in Fig. 3.14b, we were able to conduct tests at a higher range, receiving a differentiated signal at 35λ where the reflected signal is weaker. At this range, we recorded a received signal strength of -61 dB without the MLL and -53.1 dB with the MLL, thus achieving an enhancement of 7.9 dB in received power, as shown in Fig. 3.16d. Although this result is approximately 2.1 dB lower than the 10 dB enhancement predicted by our simulations, it could be attributed to measurement errors or interference from other materials in the lab setting. Alternatively, this discrepancy may indicate the need to further increase the distance between the radar and the corner reflector in the anechoic chamber, a modification limited by the physical constraints of our measurement setup. Notably, the radar's detection range, as stated in the datasheet, is estimated at 7 meters [175], yet our measurements were conducted at just around 1 meter.

To further validate the radar's radiation enhancement in the boresight direction, the power radiation pattern can be reconstructed using the outlined measurement approach. Fig. 3.15 shows the setup, where the radar module is fixed in position with and without the lens, while the horn antenna is rotated between -90 to 90 degrees in a 1D plane. Transmitted power is recorded at each angle for both elevation and azimuth planes, capturing detailed gain patterns under various scenarios. This configuration enables accurate measurement of the antenna's peak gain at multiple points, ensuring precise identification of the primary propagation direction.

Full-wave simulation is employed to compare the results of the proposed power transmission analysis with those obtained from measurements using this approach. Fig. 3.17 presents the captured data across angles ranging from -45 to 45 degrees in 5-degree increments at 10.2 GHz. The consistency between measurement and simulation results is evident, both with and without the GRIN MLL lens integrated into the setup, demonstrating alignment across various angles.

The findings of this study are summarized in Table 3.2 and compared with various lens designs reported in the literature for integrating with radar antennas for radiation improvement. The GRIN MLL introduced in this work offers a compact, low-profile lens structure designed for integration with bistatic off-the-shelf radar modules featuring TX/RX antennas on the same plane. It reduces the focal point distance, enabling direct mounting to the radar without affecting the reflection coefficient, while significantly enhancing power transmission in the boresight direction, even with the antennas offset relative to the lens. Additionally, the GRIN modified Luneburg lens features a simplified design theory that

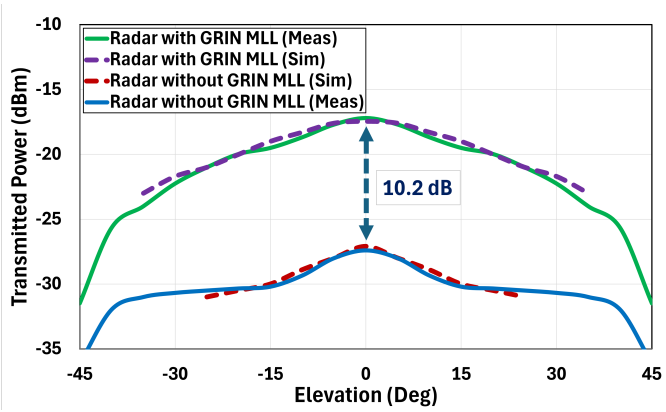


Figure 3.17: Measurement and simulation results of the reconstructed radar radiation pattern for cases with and without the MLL integrated.

Table 3.2: Results comparison between the presented MLL and previously designed lenses for radar integration in the literature.

Ref.	Freq (GHz)	Fabrication Complexity	Lens Dimension	Focal Point Distance	Gain Imp. (dB)	Type of the Lens
[161]	79	Low	$20\lambda \times 10\lambda$	10λ	14	hyperbolic dielectric
[191]	10.5	Low	$5.25\lambda \times 5.25\lambda \times 4.6\lambda$	2.5λ	5.4	Spherical dielectric
[191]	10.5	High	$2.1\lambda \times 2.4\lambda \times 1.82\lambda$	0.21λ	5.5	Planar
[152]	76.5	Low	$19\lambda \times 3.3\lambda$	11.48λ	15.7	Cylindrical
[175]	10.5	Low	$1.75\lambda \times 2.1\lambda \times 2.5\lambda$	0.5λ	6.6	Dielectric Rods Array
[169]	122	High-CNC Machine	$11\lambda \times 11\lambda \times 10.5\lambda$	5.1λ	19	DPHL-T
[169]	122	High-CNC Machine	$7.4\lambda \times 7.4\lambda \times 5.6\lambda$	1.4λ	11.8	DPHL-O
[169]	122	High-CNC Machine	$6.9\lambda \times 6.9\lambda \times 4.1\lambda$	3.2λ	10.6	DFZL
This Work	10.4	Low-3D Printed	$5\lambda \times 5\lambda \times 5\lambda$	0.06λ	10.2	GRIN Luneburg Lens

allows for uniform fabrication using a rapid, cost-effective 3D printing method.

This work paves the way for the development of high-performance, low-profile radar modules with superior detection and communication capabilities. Future research could focus on extending this approach to incorporate radar beam-steering or multi-beam, multi-radar systems. These functionalities, inherent to conventional GRIN Luneburg lenses due to their symmetric permittivity profile, could be adapted for the MLL design to further expand its capabilities when integrated into bistatic radar configurations.

3.4 Summary and Key Takeaways

In the context of radar sensing enhancement, both 3D lens structures and planar metasurfaces offer effective solutions for electromagnetic beam shaping and power focusing. This

thesis first explores 3D lenses such as dielectric rods and GRIN-based structures, due to their proven role in far-field high-gain radar systems. These designs serve as a foundation for validating passive sensing enhancement techniques. However, their limitations in compactness, conformality, and near-field integration, as summarized in Table 3.3, motivate the transition to more flexible alternatives. Planar metasurfaces overcome these challenges by supporting tunable near-field focusing, conformal skin integration, and precise phase control on a compact footprint, making them better suited for biomedical sensing.

Table 3.3: Comparison of 3D Lenses and Planar Metasurfaces for Bio-sensing Radar

Aspect	**3D Lens Structures**	**Planar Metasurfaces**
Geometry	Bulky 3D structure	Flat, compact, and conformal
Focal Point Location	Fixed on the lens surface	Adjustable within the near-field region
Design Flexibility	via GRIN index modification	via phase synthesis analysis
Beam Steering	Mechanical feed rotation	Programmable phase control
Beam Tilting with Radar Integration	High-efficiency tilt achievable with modified lens	Moderate-efficiency tilt via phase synthesis
Power Transfer into Skin	Limited due to reflection and impedance mismatch	High efficiency when impedance matched
Skin Integration	Difficult due to size and curvature	Easily embedded or conformally attached
Miniaturization Potential	requires large aperture for gain	enabled by subwavelength unitcells
SNR and Sensing Depth	High far-field gain but poor near-field resolution	Enhanced SNR and resolution in near-field
Fabrication Process	Straightforward (3D printing)	Requires precise unitcell design and lithography
Operating Regime	Optimized for far-field applications	Specifically designed for near-field sensing
Application Suitability	Best for long-range, directional sensing	Ideal for biomedical and wearable systems

Chapter 4

Radar Near-Field Sensing Using Metasurface for Biomedical Applications

Radar sensing has emerged as a promising technology in biomedical applications due to its ability to perform contactless, non-invasive, and continuous monitoring of physiological parameters. Unlike conventional methods that require direct skin contact or invasive procedures, radar systems utilize electromagnetic waves to detect subtle changes in biological tissues, enabling real-time tracking of vital signs such as respiration, heartbeat, and body movement, even through clothing or bedding. With the miniaturization of hardware and the rise of radar-on-chip solutions, these systems are increasingly suitable for wearable and unobtrusive health monitoring.

However, when it comes to sensing internal physiological parameters such as blood glucose concentration, hydration levels, or dielectric changes in deeper tissues, radar systems face significant limitations. While surface-level monitoring can rely on motion-induced Doppler shifts, subsurface sensing demands the radar signal to penetrate biological layers while maintaining resolution and signal integrity. This is complicated by high dielectric losses, impedance mismatches, and the frequency-dependent absorption of biological media, especially at millimeter-wave frequencies. Additional challenges include multipath reflections, motion artifacts, and the complex electromagnetic behavior of heterogeneous tissues.

When considering the hardware design of a radar system, the radar chipset architecture and an appropriate design of the accompanying antenna are required. When used in bio-

sensing applications, the performance of a radar hardware system is evaluated by utilizing the antenna's near-field sensing capabilities when placed in close proximity to a human body. Near-field-focused (NFF) antenna design has been studied in the literature for a long time for body-centric wireless communications applications [192, 193]. As we established, utilizing the radiated power of the transmitter antenna by focusing the electric field at a specific location close to the radar surface is an effective method for improving near-field sensing [120].

High-profile antennas such as reflectors and aperture antennas are commonly used for near-field sensing due to their strong focusing capabilities [97]. However, their bulky structure makes them unsuitable for compact or low-profile applications. While planar microstrip antennas offer a more compact and easily fabricated alternative [84], a single element typically produces low near-field intensity. To overcome this, near-field focused microstrip arrays have been proposed to enhance power transfer efficiency [99]. Yet, achieving strong focus requires a large number of elements, leading to complex feeding networks, increased fabrication costs, and higher losses. Space-fed planar arrays such as reflectarrays and transmitarrays eliminate complex feed networks and improve efficiency by shaping the phase front [100]. Nonetheless, most existing designs are optimized for far-field operation and lack near-field focusing capability, with high-profile configurations and distant feed antennas that hinder seamless integration with compact mm-wave radar systems.

These constraints highlight the critical importance of advanced electromagnetic wavefront control strategies such as near-field focusing and impedance-matched metasurfaces, for enabling efficient power transfer and spatially localized field enhancement at the tissue interface. In this context, the integration of metasurfaces with radar systems presents a promising avenue for addressing the limitations of conventional antenna configurations, thereby advancing the capabilities of non-invasive biomedical sensing. However, an in-depth review of existing literature indicates a notable gap: current metasurface designs generally lack the structural attributes necessary for low-profile, highly integrated implementation at millimeter-wave frequencies. This deficiency significantly impedes their compatibility with compact radar platforms and undermines their applicability in high-precision, near-field biomedical sensing scenarios.

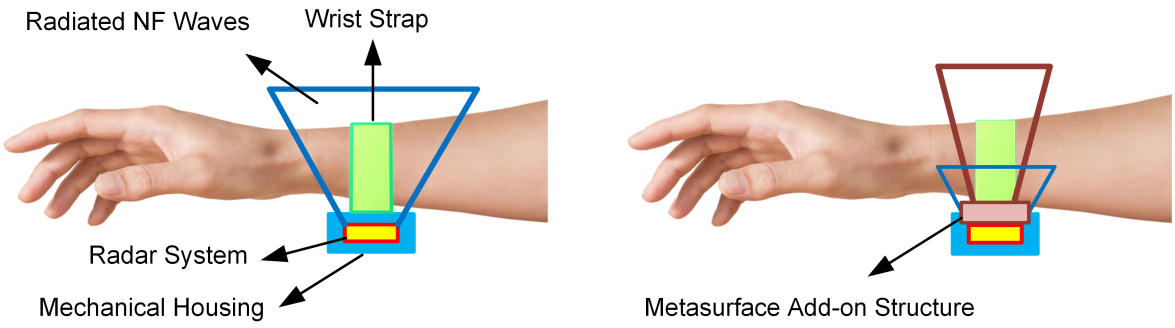
Additionally, the majority of studies on near-field focusing consider the antenna's radiation in free space. The human body creates a different environment in the antenna's radiation region, which leads to detuning and impedance mismatching, which degrades the antenna performance and lowers the penetration power density into the body, making the prior methods unsuitable for biomedical applications when the human body is in contact with the radiating elements [36]. To address this issue, some efforts in literature have been reported. The method involves treating the skin as a layer of the antenna substrate

operating at 2.45 GHz, aiming to decrease the signal scattering from the skin and direct more of the transmitted signal towards the tumor [119]. In a recent study, this issue is addressed by introducing a chest-wearable 60 GHz radar system for continuous monitoring of cardiorespiratory displacement waveforms, evaluating the antenna's performance in close proximity to the skin with an airgap of λ using electromagnetic simulations [43]. Placing an appropriate solid or liquid media between the antenna and the tissue is another approach to effectively reduce antenna mismatching [131]. To mitigate impedance mismatch, however, a number of media layers are required, resulting in a high-profile structure that poses integration difficulties, and applying liquid onto a person's skin can evoke discomfort. Metamaterials and metasurfaces, which are more practical and easier to integrate with radars, can also be used to improve antenna matching in the presence of tissue [132–135]. A bow-tie antenna design utilizing metasurfaces as an impedance-matching layer between the biological tissue and the antenna is proposed to enhance radiating performance when close to the human body at 2.56 GHz [36]. However, creating a metasurface with the intention of enhancing antenna matching close to the human body is insufficient to deliver a highly near-field focused power directed towards the body, and to significantly enhance the near-field sensing capabilities of the radar.

The concept of near-field sensing improvement of a radar system including transmitter/receiver (TX/RX) antennas implies a significant increase in the near-field power density radiated by TX into the body without disturbing antenna impedance matching while improving radar sensing by providing more received power reflected from the body into the RX antenna, representing the signal-to-noise ratio (SNR) enhancement of the radar system. It is therefore extremely challenging to develop a compact, wireless mm-wave radar for biomedical applications meeting the proposed requirements for high near-field sensing, high levels of integration, and low manufacturing costs.

Given a specific mm-wave radar chipset and antenna design, along with a pre-determined human body area of interest, Fig. 4.1a, this study presents an approach for the high near-field sensing of the radar system for biomedical applications by integrating a designed planar transmissive metasurface acting as a buffer between the radar TX/RX on-chip antennas and the human body skin as depicted in Fig. 4.1b. The presented methodology, metasurface-enhanced radar near-field sensing, could be applied to a diverse set of biomedical sensing applications, including glucose monitoring [27, 38, 39], skin cancer detection [41], as well as heart and on-body radar cardiorespiratory monitoring [43].

This thesis underscores its emphasis on real-time diagnostics, with particular focus on the critical need for continuous blood glucose monitoring as a key component in diabetes management. The ultimate goal is to enable seamless integration of glucose sensing capabilities into wearable radar-based devices, highlighting the specialized application of the



(a) (b)

Figure 4.1: (a) A wearable device equipped with radar technology positioned near a human hand; (b) Incorporating a metasurface structure between the radar antennas and the hand to enhance the near-field energy coupling and Signal-to-Noise Ratio (SNR).

proposed metasurface technology. To support this vision, this chapter introduces a structured set of metasurface-enhanced designs aimed at improving near-field electromagnetic field focusing, sensing depth, and signal fidelity. Full-wave electromagnetic simulations, along with fabrication and experimental measurements, are conducted to assess the system's performance, focusing on essential parameters such as antenna impedance matching, signal-to-noise ratio (SNR), and electromagnetic field penetration within realistic human skin models.

The main objectives of the thesis, detailed in the subsequent sections, are as follows:

- **Objective 1:** Design and evaluate a single-frequency near-field-focused metasurface for mm-wave radar integration.
- **Objective 2:** Implement a synchronized multi-radar bio-sensor fusion system for distributed sensing, enabling simultaneous monitoring from multiple skin locations.
- **Objective 3:** Develop a dual-band, independently-tunable dual near-field-focused metasurface capable of simultaneously focusing radar energy at different depths and locations within biological tissue.
- **Objective 4:** Introduce a frequency-scanning multi-radar system with a multi-band non-interleaved metasurface, enabling frequency-dependent multi-focusing for enhanced resolution.

4.1 Objective 1: Radar Near-Field Sensing Using Single-Band Single-Focus Metasurface

Metasurfaces have emerged as a promising technology exemplified by their precise manipulation of incident wave properties and enables exquisite control over electric field propagation. When integrated with radar technology, metasurface-enhanced radar systems offer unparalleled benefits providing higher resolution, increased sensitivity, and enhanced target detection capabilities which fostering advancements in biomedical applications.

In this section, as reported in [194], we present the design of a low-profile planar metasurface tailored for near-field sensing in radar systems intended for biomedical applications. The metasurface structure is designed to be integrated with radar transmitter and receiver antennas, making direct contact with human body skin leading to the significant improvement in the near-field sensing abilities of the radar system. This is achieved by enhancing the absorbed power density transferred from the radar antenna into the skin medium alongside improving the received power level which is reflected from the skin to the radar thus enhancing the overall sensor signal-to-noise ratio. The low-cost passive metasurface design comprises phase-synthesized unicells arranged in a two-layer microstrip array, aiming to achieve suitable impedance matching between radar near-field radiation in free-space and the human skin medium. For measurement verification, a medium with material properties closely resembling the human skin layer within the radar frequency range of 58 to 63 GHz is employed as a representative model. Full-wave electromagnetic simulation is used to validate the metasurface performance, and the results show a high level of agreement with the measured data. Measurement results inside the human skin model demonstrate that using the metasurface enhances the near-field Poynting power density by more than 11 dB. Utilizing radar signal processing, the received power analysis demonstrates more than 11 dB improvement in radar SNR without disturbing input matching, providing better sensing in biomedical applications.

4.1.1 Near-Field-Focused Metasurface Design in Skin Medium

The design process and performance of the metasurface are examined, taking into account the design of the unitcell and the analysis of the phase-synthesized array. The fundamental concept, as per transmitarray theory, involves adjusting the phase of the electric field radiation or the current sources of the array elements on the antenna's aperture. This adjustment is done in such a way that their contributions converge in phase at a specific focal point in the near-field region. In the context of near-field-focused antennas, the radiated

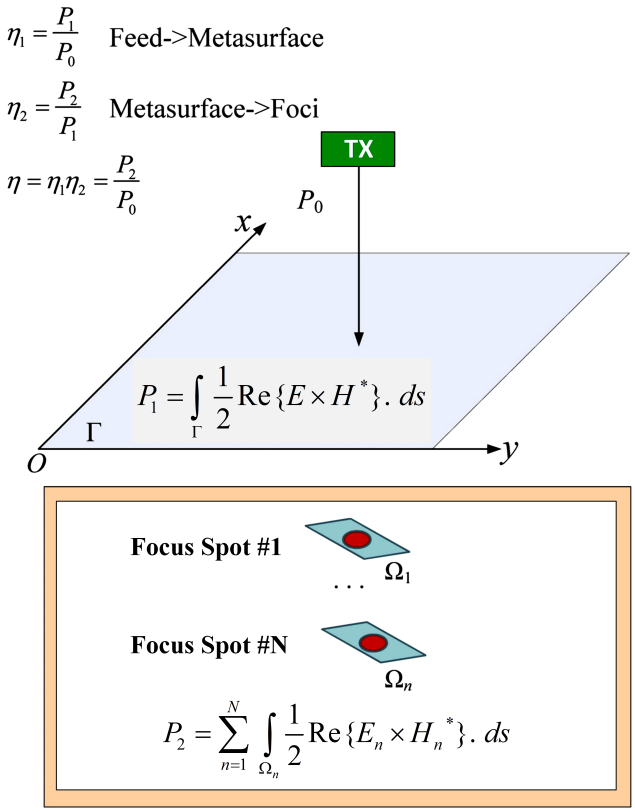


Figure 4.2: Power transferred and efficiency investigation in the near-field focusing using metasurface [103].

field's maximum is achieved near the aforementioned focal point. This implies that the peak of the power density is positioned between the focal point and the antenna's aperture. This is accomplished by using symmetric source-phase tapering, which compensates for the various distances between each source point on the aperture and the focal point. On the other hand, to increase the received power reflected from the human skin model, impedance matching analysis in the metasurface design is highly required [194]. The following discussion covers the theory for the radar antenna radiation in the near field region and unitcell and phase-corrected array designs in the presence of the human skin model.

As investigated in Fig. 4.2, the power P_0 is incident to the metasurface which is considered as a matching network between two mediums with different properties in terms of permittivity and conductivity. A good design of a metasurface will achieve a high efficiency. The efficiency η can be defined as the ratio of the total focused power, P_2 to the

total power radiated by the feeding source, P_0, as $\eta = \eta_1\eta_2 = P_2/P_0$. Where η_1 represents the power transfer efficiency from feeding source to the metasurface, $\eta_1{=}P_1/P_0$, where P_1 is the power captured by the metasurface. η_2 represents the power transfer efficiency from metasurface to foci, $\eta_2{=}P_2/P_1$, where P_2 is the total power captured by the focusing spots. In this section, P_1 and P_2 can be calculated by using numerical integration based on the Poynting theorem. The former is an integration of the Poynting vector on the entire aperture, $\Gamma - plane$ in Fig. 4.2, of the metasurface. The latter is a summation of the power contained at N foci, where the power contained at each focus is obtained by integrating the Poynting vector on the small slice, Ω planes in Fig. 4.2 covering the corresponding focal spot [103]. On the other hand, to increase the received power reflected from the human skin model, impedance matching analysis in the metasurface design is highly required. The following discussion covers the theory for the radar antenna radiation in the near field region and unitcell and phase-corrected array designs in the presence of the human skin model.

To investigate the radar performance based on the theory in the scenarios with and without the metasurface, one can use the Friis radar equation applicable to the near-field region by modifying the parameters for the near-field analysis, including the antenna gain and radar range equation as reported in [195]. For traditional monostatic radar systems with far-field radiation, the radar path gain is given as (4.1).

$$Path\ Gain = \frac{P_{RX}}{P_{TX}} = \underbrace{\frac{G_{TX}}{4\pi R^2}}_{TX}\ \underbrace{\frac{G_{RX}\,\sigma}{4\,(kR)^2}}_{RX} \tag{4.1}$$

where P_{TX} and P_{RX} are the transmitted and received power, G_{TX} and G_{RX} are the transmitter and receiver antenna gain, respectively, k is the wave number, σ is the radar cross section and R is the radar range between the TX and RX antennas.

According to (4.1), Friis's law states that as the range increases, the transmitted and reflected power density in the far field diminishes proportionally to the inverse square of the distance as expressed in (4.2). However, when it comes to the near-field region, [196] reports that electric and magnetic fields behave differently such that this principle needs to be modified as the power decreases at a faster rate than the inverse square. Therefore, the available power in a near-field link is much higher than the usual far-field. Modifying (4.1) using the near-field consideration related to the radar range shows that the received power is proportional to the near electric field as (4.3). Fig. 4.3 provides a comparison of path gain variations relative to radar range, contrasting the far-field and near-field scenarios as represented by (4.2) and (4.3), respectively. It demonstrates that at very short ranges, the

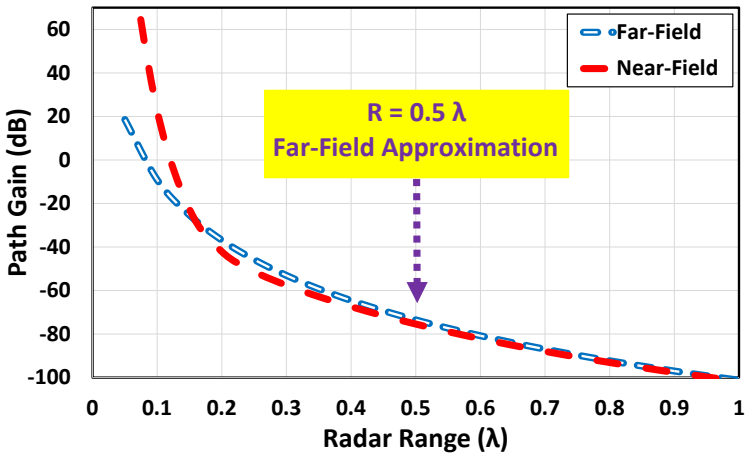


Figure 4.3: Investigation of the path gain versus radar range variations for the near-field in comparison to the far-field.

difference between path gains is in the order of +40 dB approximately. After the range of 0.2 λ, the path gain variations versus the radar range for the near-field, however, is nearly identical to that of the far-field.

$$P_{RX} \sim |E|^2 \sim [\frac{1}{(kR)^2}] \qquad Far - Field \tag{4.2}$$

$$P_{RX} \sim |E|^2 \sim [\frac{1}{(kR)^2} - \frac{1}{(kR)^4} + \frac{1}{(kR)^6}] \qquad Near - Field \tag{4.3}$$

To achieve a concentrated near-field power, the radar range which is the distance between the feeding antenna and the metasurface in contact with skin model is crucial. In such circumstances, the Fabry-Perot Cavity (FPC) Theory emerges as a promising and viable option. As shown in Fig. 4.4, a conventional FPC resonator antenna is formed by placing a structure as a partially reflective surface (PRS) at a proper distance from the ground plane, which creates an air-filled cavity between the PRS and the ground plane and fed by a small antenna or an array [197]. According to the ray theory, the main characteristics of the antenna radiation are determined by the property of the PRS and the distance to the source. Part of the electromagnetic waves radiated by the antenna passes through the coating directly, and the other part is reflected once or several times before passing through the coating. By satisfying the (4.4), electromagnetic waves become superimposed in phase, leading to the enhancement of power on the opposite side [198].

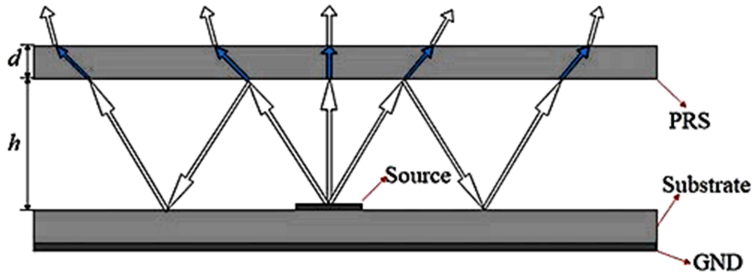


Figure 4.4: A conventional FPC resonator antenna featuring a partially reflective surface (PRS) creating an air-filled cavity between the PRS and the ground plane, fed by a source antenna [197]

$$h = \frac{c}{4\pi f} + (\varphi_{PRS} + \varphi_{GND} - 2N\pi) \quad , \quad N = 0, 1, 2, ... \tag{4.4}$$

where h is the depth of the cavity, f is the resonant frequency of the antenna, c is the velocity of light, N is the order of the resonance mode, φ_{PRS} is the reflection phase of the cladding structure, and φ_{GND} is the reflection phase of the ground plane. Normally, φ_{GND} is π due to its almost full reflection, and φ_{PRS} can be derived from as follows,

$$\varphi_{PRS} = \frac{4\pi h}{c} f + (2N - 1)\,\pi \quad , \quad N = 0, 1, 2, ... \tag{4.5}$$

Utilizing (4.5), one can calculate that by selecting the zero-order mode ($N = 0$) and setting the air gap distance to half-wavelength ($h = \lambda/2$), the resulting phase φ_{PRS} is equal to π. Hence, by applying the discussed Fabry-Perot theory, when a source is emitted, all waves undergo a 180-degree phase shift at the PRS surface. Consequently, one can categorize the waves into two groups: i) waves passing through the PRS without reflection, and ii) waves that are partially reflected from the PRS. In the second category, when the reflected waves reach the source ground, they once again experience a 180-degree phase shift. This implies that the reflected waves from the PRS accumulate a total phase shift of 360 degrees, aligning them in phase with the initial waves radiating from the source. Consequently, this structure manages to maintain the coherence of reflected waves, reinforcing them in phase with the primary radiation, ultimately amplifying the overall power on the opposite side of the PRS.

Therefore, if an airgap distance of $\lambda/2$ (λ in free-space) is considered, in accordance with the Fabry-Perot Cavity (FPC) theory, the proposed metasurface is employed in the

configuration of a FPC which reduces backscattering and increase the peak radiation of the underlying source antenna leading to enhance transferred power density into the skin [197]. As investigated in Fig. 4.3, placing the metasurface and skin model at the range of $\lambda/2$ at 60 GHz, 2.5 mm airgap above the radar antenna, allows using far-field approximation, and utilizing Friis's Law with the transmitted and reflected power variations proportionally to the inverse square of the range, (4.2), is acceptable.

In the near field region, where the electromagnetic wavefronts are not far enough apart to be considered planar waves, the gain of an antenna can be defined in terms of the ratio of the power density in a particular direction to the power density that would be produced by an isotropic radiator at the same distance and with the same input power [199]. Considering the above-mentioned far-field approximation, the relationship between the near axial field strength and the near-field gain can be expressed as (4.6). The axial field strength of the antenna in the near field can also be obtained through the full wave simulation. Thus, increasing the electric field intensity in the near-field region of the antenna using the transmissive metasurface, has a direct impact on the near-field gain improvement at the specific distance and particular direction for both TX and RX radar antennas.

$$G_{TX}, G_{RX} = \frac{\mathrm{Re}\,(\vec{E} \times \vec{H}^{*})\ .\ 2\pi R^{2}}{Input\ Power} \tag{4.6}$$

As a result, according to (4.1), the near-field gain improvement leads to the received power, P_{RX}, enhancement which provides better sensing for the proposed mm-wave radar.

4.1.2 Metasurface As an Impedance Matching Medium

In accordance with the transmitarray theory, using a transmissive metasurface between the radar system and the skin model can provide higher focused transmitted as well as received power to increase SNR. In such instances, the functional role of the metasurface as an impedance matching interface between the radar antenna radiation and the human skin medium is of paramount significance, particularly within the domain of close-range radar applications featuring proximate positioning of metasurfaces alongside radar antennas. In this context, analysis of the metasurface's spatial placement is imperative to determine whether it resides within the far or near-field region of the radar antenna's radiation.

In the far-field region, the electric and magnetic waves move together with synchronized phases and amplitudes fixed by the impedance of free space, $120\pi\ \Omega$. However, in

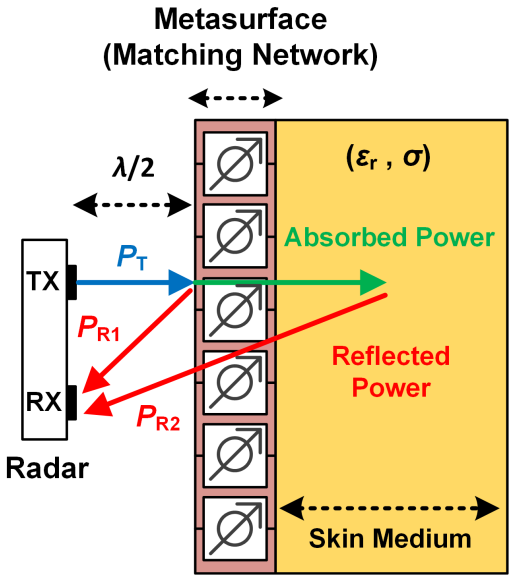


Figure 4.5: The transferred and received power in the radar system in the presence of the metasurface loaded by the skin model

the near-field region, these fields are out of phase and the ratio of electric to magnetic field amplitudes is a strong function of both radial distance to the source and orientation, resulting in non-uniform wave impedance deviation from the standard characteristic impedance of 377 Ω.

When integrating a metasurface into the radar system, the radar transmitter (TX) antenna radiates power P_{T} into the near-field region directed towards the metasurface loaded with a human skin model. Consequently, the power received by the radar RX antenna comprises reflections from the skin medium and the metasurface surface, P_{RX}=P_{R1}+P_{R2}, as shown in Fig. 4.5. In this case, the impedance matching considerations are required in the design of the metasurface such that the reflected power from the metasurface, P_{R1}, is decreased and P_{RX} mostly provides the information coming from the skin medium leading to higher biomedical sensing. To this end, the impedance of the skin medium and the propagated wave in the near-field region of the free space are required.

In such a case, the general wave impedance equations can be used for the near-field region as expressed in (4.7) [200]. Where η_0 is the free-space impedance in the far-field region, β is the propagation constant and R is the distance from the radar antenna surface.

$$Z_E(r) = \eta_0 \times \frac{\left|1 + \frac{1}{j\beta R} + \frac{1}{(j\beta R)^2}\right|}{\left|1 + \frac{1}{j\beta R}\right|} \quad , \quad Z_H(r) = \eta_0 \times \frac{\left|1 + \frac{1}{j\beta R}\right|}{\left|1 + \frac{1}{j\beta R} + \frac{1}{(j\beta R)^2}\right|} \tag{4.7}$$

$$Z_L = \sqrt{\frac{\mu_0}{\varepsilon_0 \varepsilon_r (1 - \frac{j\sigma}{\omega\, \varepsilon_0 \varepsilon_r})}} \tag{4.8}$$

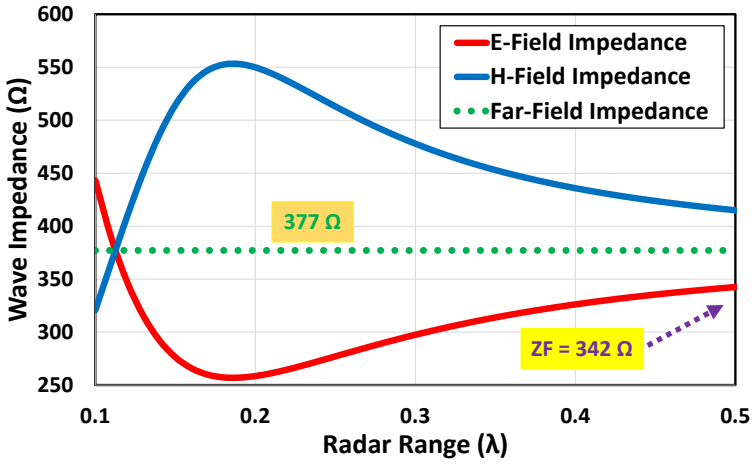
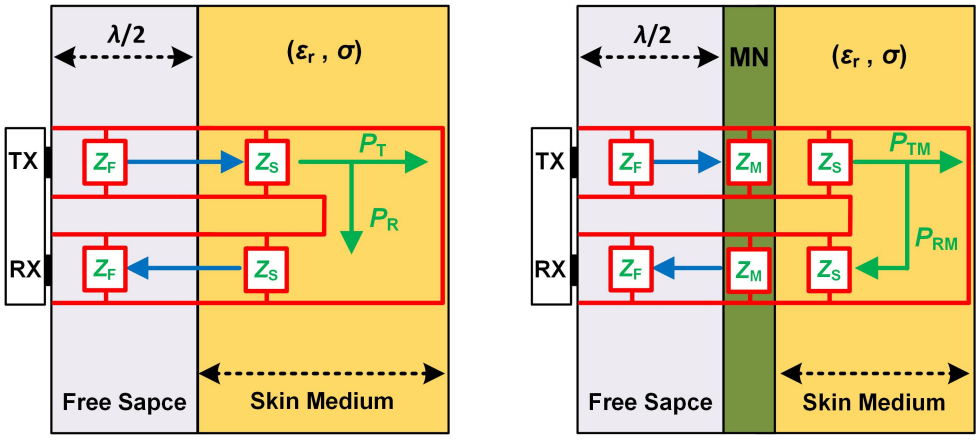


Figure 4.6: The free-space wave impedance variations in the near-field region of the radar.

As investigated, a half-wavelength distance considered in this section, makes the electric and magnetic field phases diverge and as shown in Fig. 4.6, the wave impedance in near-field free-space, $Z_{\mathrm{E}}(r{=}\lambda/2){=}Z_{\mathrm{F}}$, is obtained as 342 Ω at the proposed distance which is close to the free-space wave impedance in the far-field region, 377 Ω. In addition, as expressed in (4.8), $Z_{\mathrm{L}}{=}Z_{\mathrm{S}}$ is defined as the impedance of a general lossy dielectric medium which can be used as the biological load impedance for the skin model [36].

Given Z_{F} and Z_{S}, the transmission line model is a suitable option to consider impedance matching analysis in the metasurface design [36]. To achieve this, the human body skin situated in close proximity to the radar antenna is simplified as a homogenous dielectric slab possessing the characteristic properties of the analyzed anatomical skin region at 60 GHz. The impedance of this slab is determined through the utilization of (4.8). The transmission line using the equivalent circuit model for the radar system integrated with



(a) (b)

Figure 4.7: (a) Analysis of transferred and received power between transmitter (TX) and receiver (RX) antennas in the metasurface-enhanced radar system loaded by skin model. (b) Investigation of the radar system performance using impedance analysis for each medium, comparing the radar system without a metasurface to (c) the radar system with integrated metasurface.

and without metasurface is presented in Fig. 4.7a and 4.7b, respectively. In Fig. 4.7, P_{T} and P_{R} denote the power that is transmitted through and reflected from the skin medium in the absence of the metasurface. Conversely, P_{TM} and P_{RM} symbolize analogous power quantities in the presence of the metasurface matching network. Furthermore, Z_{F} is the free-space wave impedance in the near-field region; however, at the point of metasurface interference, $\lambda/2$ distance from the antenna surface, the exact value of impedance can be used, or it can be approximated with the free-space wave impedance in the far-field as explained above. In that case, the impedance of the metasurface can be adjusted as Z_{M} by simulating an impinging plane wave upon the proposed transmissive unitcell.

4.1.3 Planar Metasurface Unitcell Design in Skin Medium

It is necessary to conduct a design analysis of a periodic unitcell as a transmitting element in order to streamline the design cycle of the proposed transmissive metasurface. The square unitcell used in this study consists of two metallic layers printed on each side of Rogers RO4003, a dielectric substrate, with 1.25 mm thickness. As seen in Fig. 4.8a, the

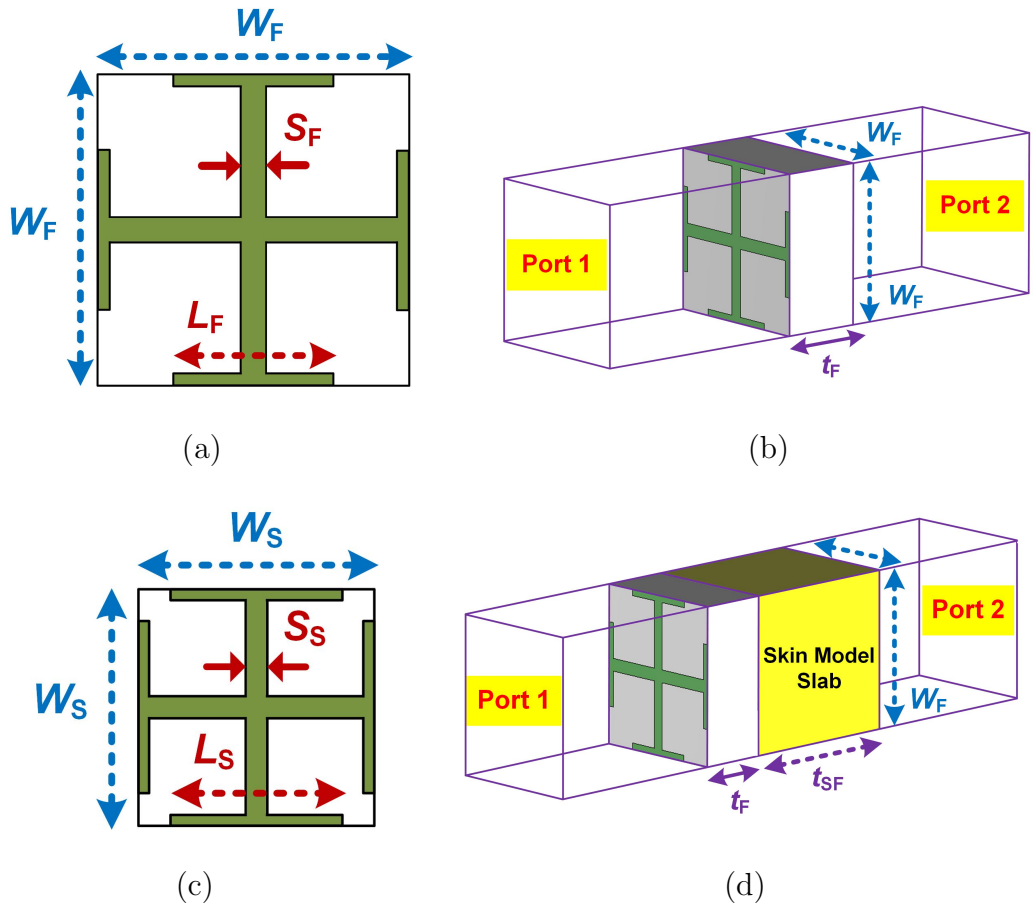


Figure 4.8: Comparative analysis of transmissive metasurface unitcells designed in free-space and human body skin medium. (a) Unitcell dimensions designed for radiation in free space, (b) Simulation representing the Floquet port analysis of the unitcell designed for free-space, (c) Unitcell designed for radiation in human body skin medium, (d) Simulation illustrating the Floquet port analysis of the unitcell in the presence of the human body skin modelled as a dielectric slab. The design parameter values are: W_{F}=2.5, t_{F}=1.25, L_{F}=1.32, S_{F}=0.2, W_{S}=1.1, L_{S}=0.65, S_{S}=0.2, t_{SF}=3 (all in mm).

metallic layer is created by a symmetric crossed planar electrical dipole that offers dual-linear polarization, and each branch size can be altered to control the transmitted fields' phases. A full-wave simulator, HFSS, is used to evaluate the unitcell impedance matching at 60 GHz as shown in Fig. 4.8b using the Floquet port analysis for the infinite array

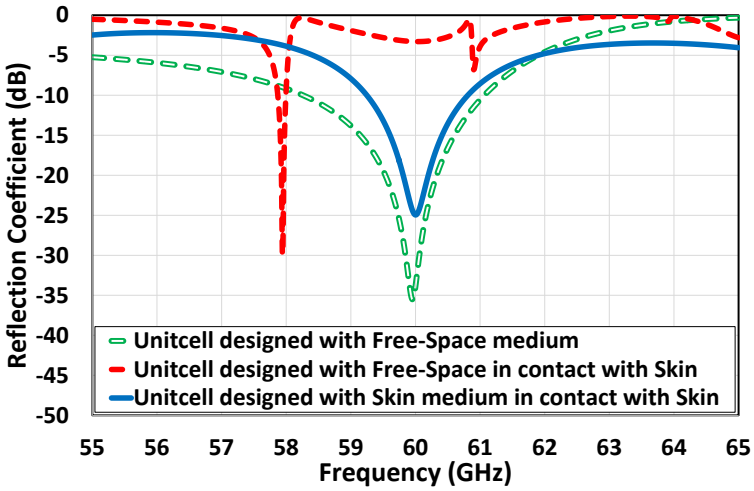


Figure 4.9: Reflection coefficient analysis of the unitcells: designed in free-space medium in contact with and without the human skin model, and designed in the skin medium in contact with the human skin model.

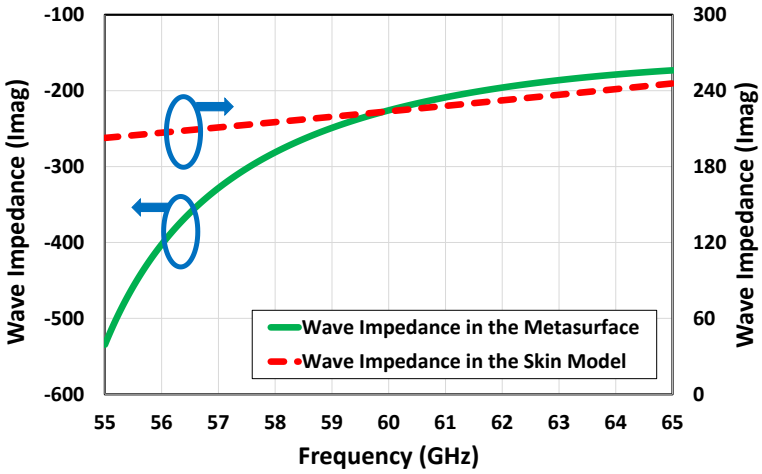


Figure 4.10: The imaginary part variations of the wave impedances versus frequency for the skin model and the designed metasurface.

design. In the realm of biomedical applications, achieving an optimal design to enhance the penetration of electric field intensity into the human body skin necessitates meticulous consideration of the skin's actual model during unitcell design and related simulations, to

ensure proper impedance matching when the unitcell interfaces with skin media, rather than free space. Accordingly, the human body skin is modeled as a dielectric slab with a thickness of 3 mm, incorporating the characteristics of human skin which typically exhibits a permittivity of 7.98 and a conductivity of 36.4 S/m at 60 GHz [201], to be contacted with the metasurface unitcell without any air gaps in between.

To have a proper design for increasing the electric field intensity into the body skin, it is highly necessary to consider the actual model of the skin in the unitcell design and the related simulation such that the unitcell shows a proper impedance matching while working in contact with the skin media, not free space. According to the microstrip design theory, adding a dielectric slab with ϵ_{r} =7.98 instead of ϵ_{r}=1 which is used for free-space medium, increases the effective permittivity of the total environment roughly from 2.2 for the unitcell with free-space, to 5.7 for the unitcell with body skin model providing the advantage of the smaller unitcell dimensions leading to low-profile array while reducing phase error losses. In the design of the unitcell working in free-space, Fig. 4.8a, the typical values of the length and width are considered as 0.5λ (λ is the free-space wavelength at 60 GHz) with a 1.25 mm substrate thickness, while the dimensions of the designed unitcell with human body skin model reduce to 0.22λ with a 0.8 mm substrate thickness, Fig. 4.8c. The other advantage of unicell size reduction is to ensure that $W_F < \lambda$ avoiding more than one spot region appearing in the near-focused region, as a similar concept to the grating lobes occurs in the far-field radiation pattern of any uniformly spaced array [37]. Fig. 4.8d illustrates a simulation model representing the Floquet port analysis of both unitcells in direct contact with the human body skin, modeled as a dielectric slab.

Fig. 4.9 illustrates the reflection coefficient analysis of the designed unitcell working in free space compared to the human skin medium, as depicted in Fig. 4.8b and 4.8d, respectively. The analysis in Fig. 4.9 highlights a significant challenge encountered in the unitcell design, where the reflection from the air-skin interface leads to notable mismatching, distinguishing it from typical metasurface designs reported in the literature. In this study, the modified version of the designed unitcell specifically tailored for in-body skin radiation, as shown in Fig. 4.8c, effectively addresses this issue.

From the reflection coefficient analysis, the unitcell impedance variation in the frequency range of interest is extracted and shown in Fig. 4.10. Comparing wave impedances inside the human skin model, Z_{S}, and wave impedance in the metasurface, Z_{M}, indicates that the design parameters of the metasurface are optimized such that providing a capacitive behavior within the desired frequency band and, in particular, a value close to the skin model impedance but opposite in sign at 60 GHz. Therefore, the designed metasurface unitcell is able to counteract the inductive behavior of the human skin model providing high impedance matching at this frequency range as shown in Fig. 4.9. As a result, us-

ing the designed transmissive metasurface with skin features consideration reveals a high impedance matching at 60 GHz between the radar antenna propagation and the skin model leading to a higher transferred power into the skin medium, $P_{\mathrm{TM}} > P_{\mathrm{T}}$, and higher reflected power received by RX antenna, $P_{\mathrm{RM}} > P_{\mathrm{R}}$.

As a conclusion, concerning the near-field sensing analysis for biomedical applications in this research, the utilization of the suggested crossed dipole structure for the unitcell provides several novelties and advantages as summarized in the following:

i) Practical Innovation: The proposed unitcell introduces a novel approach to metasurface design for biomedical applications, addressing challenges related to reflections at the air-skin interface. This unique characteristic distinguishes it from conventional metasurface designs. Ensuring effective electric field penetration into the body skin requires careful consideration of the actual skin model during unit cell design and simulations. Optimized design parameters provide capacitive behavior within the desired frequency band, particularly aligning closely with the skin model impedance but with an opposite sign at 60 GHz. This design counters the inductive behavior of the human skin, ensuring high impedance matching between the radar antenna and the skin model. The result is increased power transfer into the skin medium and higher reflected power received by the RX antenna;

ii) Size Reduction: The unitcell, incorporating a human body skin model, offers the advantage of smaller dimensions, resulting in a low-profile array and minimizing phase error losses. In contrast to the design for free space [202], [203], [204], where typical dimensions are 0.5 λ in length and width with a 1.25 mm substrate thickness, the unit cell designed with a human body skin model features reduced dimensions of 0.22 λ and a thinner 0.8 mm substrate;

iii) Providing one focused spot with high resolution: Reducing the size of the unit cell has an additional advantage, ensuring that $w_F < \lambda$, preventing the appearance of more than one spot region in the near-focused region. This concept, akin to grating lobes in the far-field radiation pattern of uniformly spaced arrays [203], [204], enables a metasurface with a highly focused focal point, enhancing biomedical sensing capabilities;

iv) Higher efficiency by resilience to Incidence Angle Variations: Crossed dipole unitcells can maintain relatively stable performance over a range of incident angles. This characteristic makes them suitable for applications where the incoming signal angle may vary, such as in near-field biomedical sensing. Taking advantage of the low-profile unitcell with 0.22 λ dimension, when the unitcells are illuminated at various locations, the oblique incidents have a very low impact on the magnitude and phase of the unitcell. Therefore, the phase error loss caused by the oblique incident is negligible, which simplifies the design process while guaranteeing nondestructive effects on the phase difference compensation;

v) Multi-polarization operation: Crossed dipole structure inherently produces dual linearly polarized (horizontal and vertical) as well as circularly polarized radiation due to its symmetrical structure. In the near-field region of an antenna, the emitted electromagnetic fields exhibit complex polarization characteristics, often displaying polarization in different directions. This phenomenon arises due to the intricate interaction of electromagnetic waves in the near-field zone, where the electric and magnetic field components vary significantly with proximity to the antenna. In such a case, it is essential to have a metasurface design that supports and accommodates this diverse range of polarization states, ensuring adaptability to the variable polarization conditions encountered in the near-field zone. Understanding these diverse polarization characteristics in the near field is fundamental for biomedical sensing applications where the specific polarization states play a significant role in determining system performance and functionality. Using a crossed dipole structure allows passing near-field waves with any polarizations leading to higher electric field intensity into the skin medium and as a result, increasing power transferring and higher sensing;

vi) Ease of Fabrication and Integration: Crossed dipole unitcells are often simpler to manufacture and integrate into the metasurface structure, making them a practical choice for large-scale production and deployment;

vii) Reducing undesired reflections from the metal layer: Given that the design is based on the near-field operation and considering a microstrip metasurface design, it is anticipated that undesired reflections may occur when the metallic layer covers a significant portion of the metasurface. In such instances, it is suitable to consider a unit cell design that minimizes the metallic coverage on the surface. Selecting the unit cell design with the crossed dipole structure reduces the metallic coverage, mitigating undesirable reflections, which could otherwise interfere with the intended performance of the metasurface structure.

4.1.4 Planar Metasurface Array Design

In this configuration, the power is provided by a feeding element placed in the focus of the metasurface and the phase shift is introduced by the change in the size of one of the elements of the unitcell. Hence, the requirements for the unitcell should be the same than for FF antenna, which means that by varying a certain parameter of its structure, it would be necessary to obtain a 360-degree phase shift as well as a stability of the results with the incidence angle. The NF of the antenna can be obtained as the sum of the independent FF contributions of each of its elements, which is a modification of the FF model. Indeed, an array NF pattern approximately equal to an assigned FF pattern is obtained once the phase focusing is added to the synthesized FF-focused equivalent array.

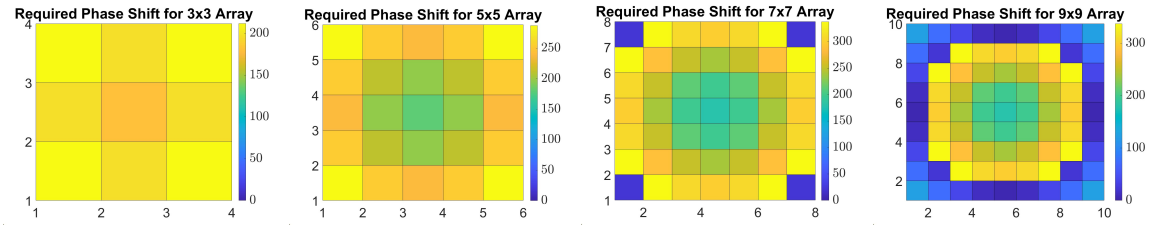
The methods used for the synthesis of NFF antennas can be classified into one of two categories: the conjugate-phase approach and the multiobjective optimization techniques. In the conjugate-phase approach, the phase of the excitation of each antenna radiation source is set to compensate for the phase delay introduced by the path between the source and the assigned focal point, to achieve a constructive interference of all the contributions at the focal point. Additionally, a proper tapering of the amplitude of the source excitation can be chosen to control the level of the secondary lobes around the focal spot region. Otherwise, if a multiobjective optimization technique is applied, it means that both the amplitude and phase of the source excitations are simultaneously determined through adhoc optimization techniques.

The conjugate-phase approach has a clear physical meaning based on a ray-optics model. The optimization based approaches are much more general and flexible in that they allow concurrent optimization of many NFF antenna parameters for almost arbitrary antenna configurations and complex application scenarios. For example, optimization-based approaches can be applied to the synthesis of NFF arrays with unequal elements, NFF antennas radiating in lossy and/or non homogeneous media, antennas radiating in presence of scatterers in their NF region, NF/NF or NF/FF multifocus antennas, and plane-wave generators.

The metasurface layer is a structure where a wave from a feed is incident on a planar array of elements. In order to produce the desired beam shape on the opposite side of the planar array in a particular location in the near- or far-field region, each element is created to add a particular phase shift to the incident electric field while maintaining magnitude in a level close to the maximum. Considering a square planar aperture consists of $N\times N$ radiating elements, with an inter-element distance W_{S} along both axes, the (m,n)th element indicates the center point location of each unitcell in the x-y plane, where m and n are integers, varying between (-N+1)/2 and (N-1)/2, N is considered to be an odd number. The electric field radiated at an observation point P(x,y,z) by the $N\times N$ array expressed as [37],

$$\vec{E}(P) = \sum_{m\,=(-N+1)\,/2}^{(N-1)\,/2} \sum_{n=(-N+1)\,/2}^{(N-1)\,/2} I_{mn}\,\vec{E}_{mn}(P) \tag{4.9}$$

Where I_{mn} and $\vec{E}_{mn}$(P) are the excitation coefficients and the radiated electric field corresponding to the (m,n)th element of the array, respectively. For each element, the feeding-current amplitude is adjusted equal to I_0, while its phase, ϕ_{mn}, is selected so that



(a) (b) (c) (d)

Figure 4.11: Investigation of unitcell required phase shift to design a near-field focused transmitarray metasurface to be placed at $\lambda/2$ distance from the feed based on the number of the elements in x and y directions. (a) 3×3 elements (b) 5×5 elements (c) 7×7 elements (d) 9×9 elements.

all the element contributions add in phase at the focal point F=(0,0, r_0), located along the normal to the array plane,

$$\varphi_{mn} = \frac{2\pi}{\lambda}[\sqrt{(x_m^2 + y_n^2 + r_0^2)} - r_0] + \varphi_0 \tag{4.10}$$

where ϕ_{mn}= ϕ_0 provides the uniform-phase unitcells in planar array making far-field-focused radiation. When the focal distance, r_0, is greater than the aperture size, the above phase tapering is usually approximated with a quadratic law which is valid for the far-field region [205]. When the observation point is close to the array elements, $2\pi R/\lambda<1$, where R is the distance between the radiating element and the observation point, the far-field considerations such as parallel-ray approximation are no longer valid to use in the electric field equation presented in (4.9). Additionally, the exact phase shift calculation as described in (4.10) is necessary to focus the electric field at the focal point r_0, which is situated in the near-field region. Approximation formulas result in phase error losses and non-focusing in the near-field.

The proper dimensions of the array unitcells are obtained by finding the required phase delay compensation of the electric field at the frequency of interest using (4.10) in the planar aperture at the metasurface location. This phase compensation mechanism results in an equal-phase superposition of the propagated fields at the focal point in the near-field region.

Using (4.10), the required E-field phase compensation ranges on the aperture supposed in the metasurface location at r_0=2.5 mm are obtained and the accessible phase ranges in

x and y directions according to the number of the array elements, from 3×3 to 9×9, are investigated and shown in Fig. 4.11. The phase shift required for each array is obtained as $\Delta\phi(3\times3)$=30, $\Delta\phi(5\times5)$=120, $\Delta\phi(7\times7)$=210, $\Delta\phi(9\times9)$=340 degrees which are presented in Fig. 4.11a to 4.11d, respectively. While using more unitcell elements in the metasurface structure increases the electric field intensity, choosing the number of array elements is constrained by the acceptable dimension as determined by the feeding antenna and, above that, the range of the phase range compensation that unitcell can offer.

To design a full planar array metasurface, unit cells that can deliver 360 degrees of phase shift are required to cover the required phase shift range with a minimum at the center element, ϕ_{mn}= ϕ_0, and maximum at the edge elements [206]. As reported in [207], the maximum phase shift that a single-layer transmitarray metasurface unitcell can provide is 90°for −3 dB transmission coefficient regardless of the shape of the conducting element. To increase the amount of phase shift, stacked multiple single-layer unit cells can be used. For the −3 dB transmission bandwidth, the two-layer structure provides a phase shift of up to 180°, whereas the three-layer structure provides a phase shift of up to 300°. Increasing the number of layers also increases the bandwidth for the desired frequency band [204], while increasing design complexity and manufacturing cost.

According to this, the designed unitcell in this section is expected to provide up to 180°phase shift at the magnitude reduction of up to -3dB due to using two metallic layer structures. By changing the length of the metallic crossed dipoles' branches, D_S=L_S+W_S/2, it is demonstrated that the proposed unitcell can provide the desired phase shift range at 60 GHz as shown in Fig. 4.12a. Considering Fig. 4.11, based on the 180°phase shift range that the unitcell provides, a suitable number of the array elements should be selected by including the largest possible aperture to cover the source antenna properly and provide the highest accessible focused power without substantially increasing the phase error loss. Fig. 4.11a and 4.11b show that the 3×3 and 5×5 array elements with required phase compensation of 30°and 120°are not quite effective in a focusing process. Moreover, the 9×9 array with required $\Delta\phi$=340°shown in Fig. 4.11d, makes a large phase error loss due to unitcell phase limitations. Among all options investigated, the array of 7×7 with $\Delta\phi$=210°is the closest one to the available 180°phase shift as shown in Fig. 4.11c. Therefore, the 7×7 array utilizing 49 phase-corrected elements provides the highest power density into the human skin.

The variations of the unitcell transmission coefficients, phase and magnitude, versus incident wave angle, are also investigated and shown in Fig. 4.12b. As shown, taking advantage of the low-profile unitcell with 0.22λ dimension, when the unitcells are illuminated at various locations, the oblique incidents have a very low impact on the magnitude and phase of the unitcell. From Fig. 4.12b, for the proposed metasurface placed at λ/2

distance, the maximum incidence angles up to 70° required at the edge elements causes the phase deviation lower than 4°, while the magnitude makes only 0.04 dB variations. Therefore, the phase error loss caused by the oblique incident is negligible, which simplifies the design process while guaranteeing nondestructive effects on the phase difference compensation.

The preceding investigation pertains to the metasurface unitcell and array, with the analysis conducted at the central frequency of 60 GHz. In light of the designated bandwidth from the source antenna, the proposed radar chipset spanning 58 to 63 GHz, it becomes imperative to assess the fluctuations in transmission coefficients across the entire frequency spectrum within the specified range. This comprehensive evaluation is essential for ascertaining the overall bandwidth of the entire system. Fig. 4.12 illustrates the magnitude and phase responses of the two layers' unitcell for varying lengths of crossed dipole metallic branches. The results are presented across different frequencies within the bandwidth of interest. In Fig. 4.12c, it is observed that the frequency range from 59 GHz to 61 GHz exhibits a favorable transmission magnitude change, with a maximum reduction of 1 dB. Conversely, at 62 GHz, a higher reduction exceeding 3 dB is observed, indicating that the power improvement technique is less effective at this frequency. However, merely examining the transmission coefficient's magnitude is insufficient for determining the bandwidth of the metasurface-enhanced radar design. Consequently, the investigation extends to the transmission coefficient's phase, as depicted in Fig. 4.12d within the desired bandwidth. Notably, the phase response for frequencies ranging from 59.5 to 61.5 GHz appears nearly parallel, providing a constant shift throughout the bandwidth. Given the satisfactory results obtained from both magnitude and phase analyses of the transmission coefficient in the frequency range of 59.5 to 61.5 GHz, it is anticipated that the near-field-focused radar antenna integrated with the designed metasurface, affords a 2 GHz bandwidth to enhance near-field power within the skin.

In this section, the design analysis of the proposed metasurface discusses the unitcell and the transmissive array design using the phase-synthesized technique. The objective is to focus the near-field power inside the human body skin and provide high impedance matching between the antenna near-field radiation and the human skin medium at 60 GHz, reducing power reflection from the air-skin interference. The next explores the simulation results of the millimeter-wave radar integrated with the metasurface. Additionally, the fabrication process and measurement results are provided to demonstrate the feasibility of the presented approach for near-field sensing enhancement required in biomedical applications.

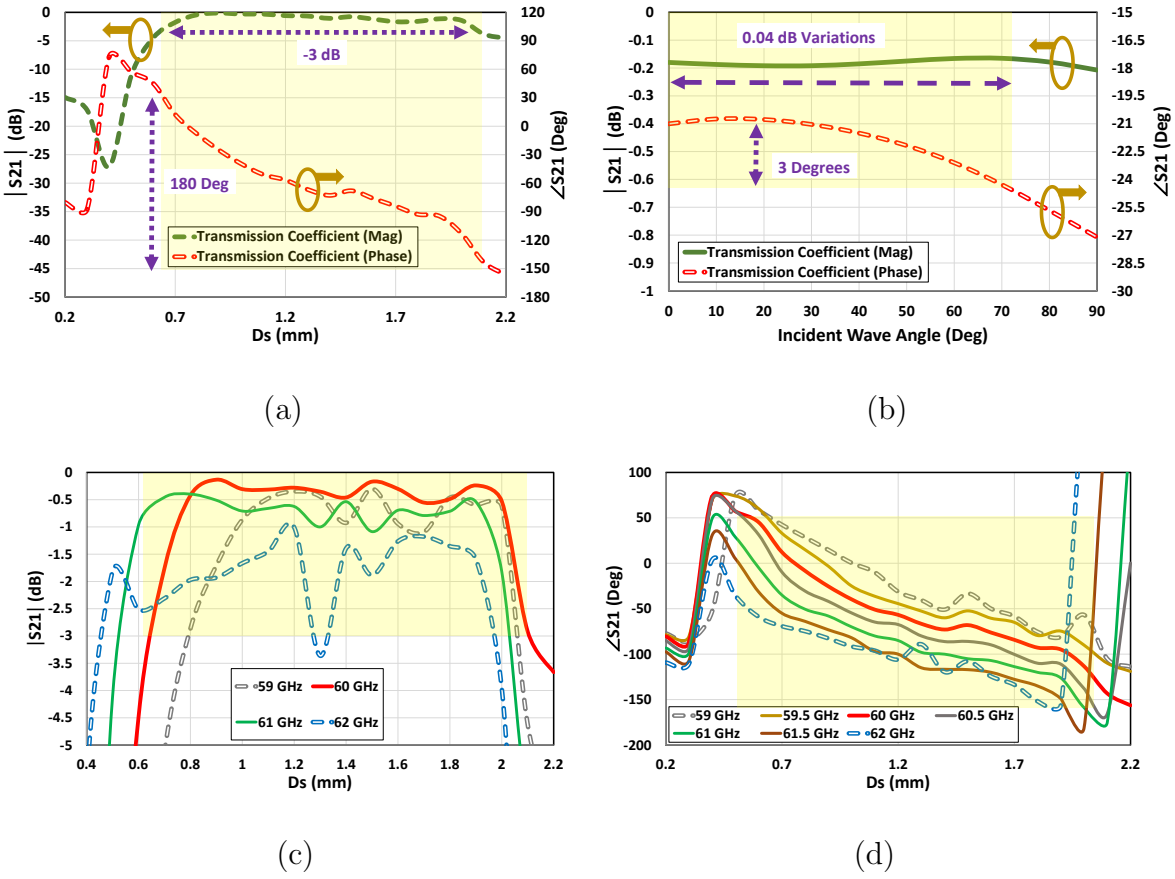


Figure 4.12: Simulated transmission coefficients (S21 magnitude and phase) of the two-layered crossed-dipole unitcell in presence of skin layer. (a) magnitude (Mag) and phase analysis for various metallic branches lengths at center frequency, D_S=L_S+W_S/2; (b) magnitude and phase analysis for various incident angles at center frequency; (c) magnitude investigation across different frequencies within the desired bandwidth; (d) phase investigation across different frequencies within the desired bandwidth.

4.1.5 Simulation Results: Radar System Integrated With and Without Metasurface

This section showcases simulation results detailing the power transmitted into the human skin medium and the power reflected by the skin. A comparative analysis is conducted between scenarios involving the radar integrated with and without the metasurface. The

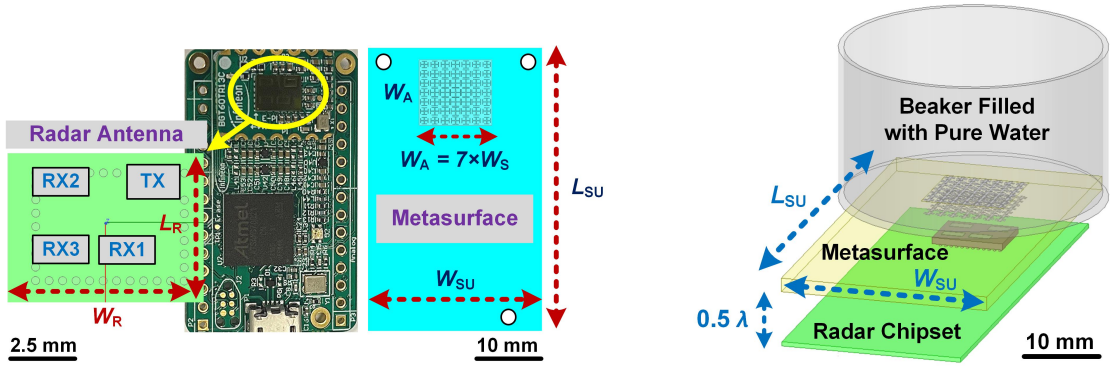
validation of the presented results is further supported by sensitivity analysis. Additionally, a novel phantom model is introduced for the fabrication and measurement process, and the obtained measurement results are compared with the simulation outcomes.

Due to the demand for a compact and low-profile radar structure in biomedical applications, a suitable choice for near-field sensing improvement is using the planar array antennas consisting of a source and a transmissive surface. According to transmitarray theory, considering a microstrip PCB antenna as a source, one can improve its near-field performance in the presence of the human body by adding a surface acting as an impedance-matching network between the source and the human skin [120]. The proposed theory is applicable to any type of radar system utilizing planar TX/RX antennas-on-chip.

As shown in Fig. 4.13a, the Infineon BGT60TR13C radar chipset includes four on-chip antennas, one of which radiates as a transmitter and the others of which serve as receivers [141]. The radar TX antenna can be considered as a feed of the transmitarray, and the planar metasurface located above the radar is used as a transmitting surface. In this section, the designed planar transmissive metasurface is used and it is investigated how the Infineon BGT60TR13C radar chip antenna interacts with and without the proposed metasurface regarding free-space and skin impedance matching, near-field focused power absorbed from the transmitter antenna into the human skin, and radar SNR improvement.

The designed transmissive metasurface consists of 7×7 phase-compensated radiating elements with an inter-element distance, W_S, along both axes as shown in Fig. 4.13b integrated with the radar system. According to the Fabry-Perot theory, the distance between the radar system and the designed transmissive metasurface is adjusted to maximize the radiated field, as equal as $\lambda/2$ at 60 GHz. In order to make the work more feasible and practical in the manufacturing and measurement process, the human body skin is modelled as a phantom considering two interleaved cylindrical dielectric slabs, a beaker made by Pyrex glass (ϵ_r=4.7 and σ=0.5 S/m at 60 GHz [208]) filled by pure water (ϵ_r=11.17 and σ=36.4 S/m at 60 GHz [209]) with 5 mm height contacting the metasurface without air gap. It can be shown that the effective characteristics of the new dielectric medium (combination of the Pyrex beaker and pure water) is sufficiently close to the human body skin at 60 GHz.

Within this frequency range, the external shell (Pyrex Glass) does indeed influence the characteristics of the phantom. As per the literature, human skin exhibits a permittivity of 7.98 at the frequency of 60 GHz; however, the permittivity of pure water at this frequency, under typical room temperature conditions, is 11.17. Consequently, it becomes imperative to consider the impact of the external shell with a relative permittivity of 4.7 in the calculations. In such scenarios, one can perform calculations to determine the effective



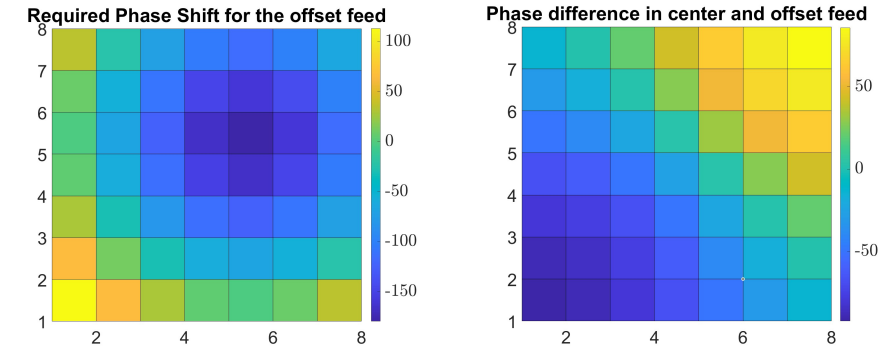
(a) (b)

Figure 4.13: Radar-Metasurface integration for near-field power density measurement using a human skin model phantom. (a) The Infineon BGT60TR13C radar chipset with highlighted transmitter (TX) and receiver (RX) antennas and the designed phase-corrected transmitarray metasurface (b) radar integrated with the metasurface contacting the proposed phantom, a beaker filled with pure water, in replace with human skin model.

permittivity of the entire volume that the metasurface is facing as (4.11), where V_1, V_2, ..., V_n are the volume fractions of the individual components, and ϵ_1, ϵ_2, ..., ϵ_n are their respective permittivities. In this model, the inverse of the effective permittivity is equal to the sum of the volume fractions divided by the permittivities of the individual components.

$$\frac{1}{\varepsilon_r} = (\frac{V_1}{\varepsilon_1}) + (\frac{V_2}{\varepsilon_3}) + ... + (\frac{V_n}{\varepsilon_n}) \tag{4.11}$$

Using (4.11), one can calculate the effective permittivity of pure water in combination with a Pyrex glass beaker. As mentioned above, a Pyrex (ϵ_r=4.7) filled by pure water (ϵ_r=11.17) with 5 mm height contact the metasurface without air gap. Given that the thickness at the bottom of the glass beaker is measured as 1 mm, the volume fractions are calculated as 0.2 for the beaker (1 mm/5 mm = 0.2) and 0.8 for the pure water (4 mm/5 mm = 0.8). Utilizing the (4.11), the effective permittivity of the medium is determined as ϵ_r(effective) = 8.75. Consequently, a comparison between the permittivities of the proposed phantom (8.75) and human skin (7.98) at 60 GHz reveals a difference of approximately 0.77, which is not deemed significant. However, it is important to note that this difference does impact the performance of the metasurface, as explained in the following sensitivity analysis section. Some of the parameters shown in Fig. 4.13 are fixed and selected by the



(a) (b)

Figure 4.14: (a) The required phase shift compensation of the 7×7 array when TX radar source is in the offset, and (b) The phase difference between the case when source is placed in offset with the case source is placed at the center of the 7×7 array.

dimensions of the Infineon radar chipset; W_{SU}=26, L_{SU}=40, W_R=6.5, L_R=5 (all in mm).

According to the phase analysis presented in previous section, the microstrip crossed electric dipoles as transmitting elements are properly designed for the compensation of the differential spatial phase delays from the radar antenna radiation. However, in the design of the proposed metasurface two assumptions have been considered: i) the source antenna should be placed at the center location of the metasurface so that covering the antenna symmetrically; as a consequence, when the metasurface is integrated with the radar system, the TX antenna has an offset from the center of the array causing phase difference between the elements. The required phase shift compensation when the source is offset and how it differs from the case where the source is positioned in the center are investigated as shown in Fig. 4.14. As seen in Fig. 4.14a and 4.14b, when the TX radar antenna is excited, the maximum phase difference of 50°caused by the edge elements affects the array required phase shift leading to phase error loss and E-filed focused deviation. As investigated, this phase error loss causes degradation of 1.2 dB in the maximum accessible focused power density inside the human skin model. Moreover, the offset TX source makes the focused power inside the skin deviates from the orthogonal direction which is not a concern in this application; ii) The radar antenna radiation illuminates the metasurface unitcells in the normal and oblique directions according to its alignment with the array. In such a case, the phase analysis presented in Fig. 4.11 and 4.12 are studied based on the normal incident considerations. Nevertheless, the phase shift delays of the normal incident

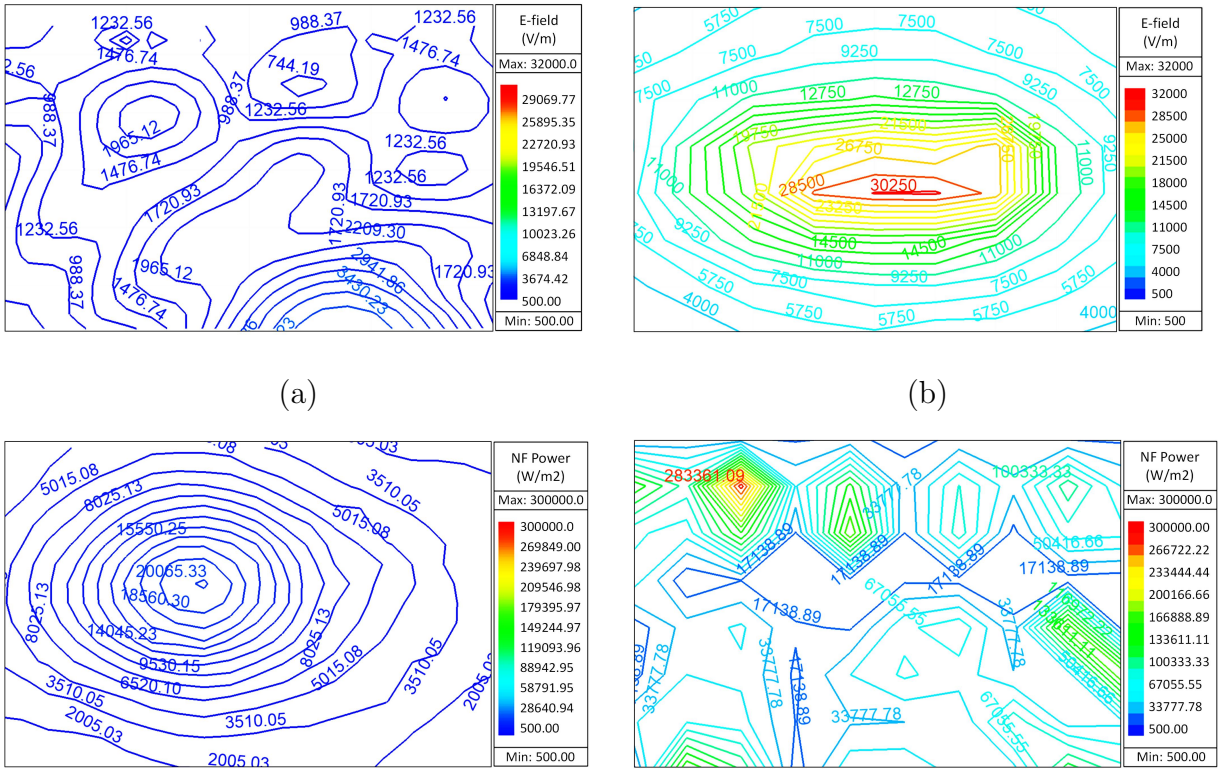


Figure 4.15: Simulated 2D contour plots of radar system transmitter antenna near-field radiation inside the phantom model at 60 GHz, illustrating on a plane positioned 2 mm above the metasurface. (a) radiated electric field (E-Field) intensity of radar system without metasurface (b) radiated electric field intensity of radar system integrated with the metasurface; (c) radiated near field (NF) power density of radar system without metasurface (d) radiated near field power density of radar system integrated with the metasurface.

wave illuminated the unitcell is different from the oblique incident one [204]. Although using the proposed symmetric metasurface increase the NF power radiated from the TX antenna and the received power to the RX antenna; the phase error caused by oblique incident radiation from the feed can prevent reaching the maximum power improvement as can be obtained for a microstrip patch antenna placed at the center of the array [120].

The proposed structure is simulated using a full wave electromagnetic simulator, HFSS, and the results of near electric field magnitude and focused power density of the radar

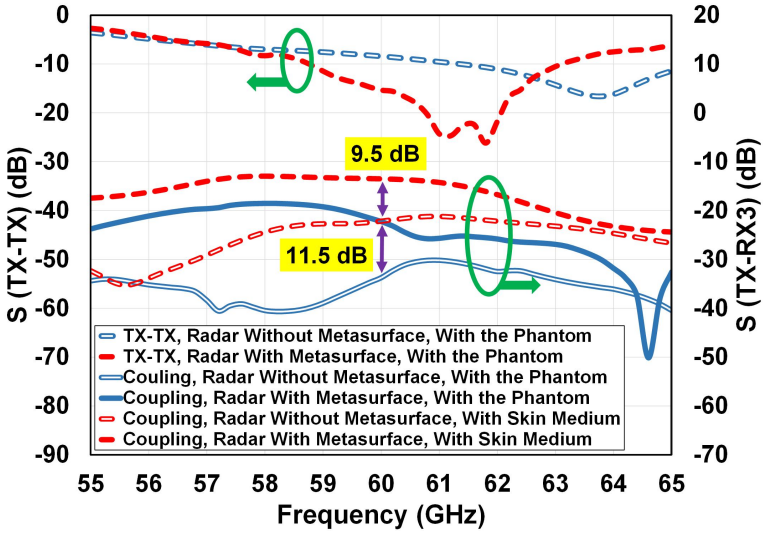


Figure 4.16: The S-parameter analysis, simulated reflection and coupling magnitude of the radar system transmitter (TX) and receiver (RX3) antennas integrated with and without the metasurface in presence of the phantom model.

system in the presence or absence of the proposed transmitarray metasurface are obtained inside the pure water modelled as a cylindrical slab. For this model, the maximum peak of the power density occurs at 2 mm distance above the metasurface, 1 mm above the beaker bottom, inside the pure water model. As shown in Fig. 4.15a and 4.15b, the designed metasurface provides a significant enhancement on the near electric field inside the water which is 8.8 times higher than the radar antenna without metasurface. It is expected that the near-electric-field enhancement provides a very directive near-field power density with high intensity.

Fig. 4.15c and 4.15d show the 2D contour plots of the power density radiated by the TX radar antenna in the presence and absence of the near-field-focused planar metasurface in a rectangular region, lying on the plane in parallel to the array with 2 mm distance. It is apparent that using the near-field-focused metasurface provides 11.5 dB (more than 14 times) improvement in the radiated power density across a z-constant surface above the metasurface inside the beaker-filled with pure water model at 60 GHz.

The S-parameter analysis of the reflection and transmission coefficients, S(TX-TX) and S(TX-RX3), for the radar system with and without metasurface, are also investigated, and compared in Fig. 4.16. The investigation of the reflection coefficient at the radar TX port shows that using a proper design of the unitcell in contact with the skin model makes an

array which is high impedance matched with the beaker-filled with water medium at the frequency bandwidth of 59 to 63 GHz. Fig. 4.16 shows that considering the model of the beaker filled with pure water provides 11.5 dB power reflected enhancement from the Water medium to one of the radar receivers, RX3, leading to significant enhancement of the radar SNR.

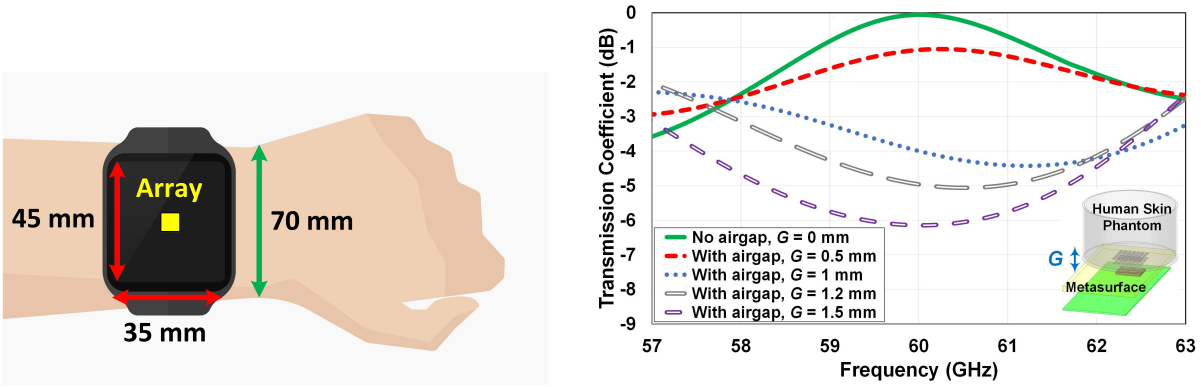
4.1.6 Sensitivity Analysis in Near-Field Bio-Sensing Design

Sensitivity analysis is vital in optimizing the proposed near-field metasurface-enhanced radar for biomedical applications. By discerning pivotal parameters shaping device performance, one can precisely refine the design to attain desired sensitivity and accuracy levels. This process enhances the device's robustness, ensuring consistent functionality across diverse conditions, including varied testing scenarios. Furthermore, sensitivity analysis facilitates precise customization, adapting the radar to meet specific biomedical application requirements.

In this research, sensitivity analysis plays a crucial role in accounting for the non-planarity of the skin surface, the metasurface air gap distance, and inter-individual permittivity changes associated with the proposed phantom, a beaker filled with pure water. Post-performance assessment, the sensitivity analysis extends to additional aspects for a comprehensive examination:

I) The impact of human skin non-uniformity on planar transmissive metasurface performance: The proposed planar metasurface, in conjunction with a rigid structure, may not perfectly conform to the non-planar human body, potentially creating air gaps in certain scenarios. However, this metasurface-enhanced radar near-field sensing method exhibits versatility across biomedical applications, including glucose monitoring, skin cancer detection, and on-body radar cardiorespiratory monitoring. The study emphasizes the development of a highly sensitive millimeter-wave radar for real-time disease diagnostics, with a specific focus on continuous blood glucose monitoring for diabetic care. As a result, the primary objective is to integrate glucose monitoring seamlessly into wearable devices, tailoring the metasurface technology for this targeted application context. Therefore, the probability of a significant gap is minimal when utilizing metasurface-enhanced radar as a wrist-worn wearable device.

This is attributed to the small effective area (7.7×7.7 mm^2) and the secure fit of devices like smartwatches, facilitating practical biomedical sensing. According to existing literature, the average wrist circumference is reported in [210] to be 6.89 inches (17.5 cm) for males and 5.9 inches (15 cm) for females. Considering the smallest wrist circumference,



(a) (b)

Figure 4.17: (a) The metasurface array's scale relative to a wearable device, like a smartwatch worn on a human wrist, showcasing the substantial difference in dimensions; (b) The transmission coefficient analysis of the metasurface unitcell under different air gap conditions between the metasurface and the human skin model

the effective contact area with a wearable device, such as a smartwatch, is approximately 6.5 cm. Illustrated in the Fig. 4.17a, the metasurface array's contact area with the hand is roughly 9 times smaller than the total area. Moreover, tightly fitting devices such as smartwatches ensure a gap-free connection around the wrist. This allows us to treat the effective area as essentially planar, with a high degree of accuracy and minimal space between the body and the metasurface. Therefore, the compact design of the metasurface's effective area makes it particularly well-suited for biomedical sensing across various body parts.

Given that there is generally no substantial gap between the designed metasurface and human body skin, it is also of interest to analyze the performance of the metasurface if there is a gap to the human skin in rare cases. The simulation results involve the radar integrated with a metasurface, considering air gap variations from 0 to 1.5 mm. The simulation analysis encompasses the transmission coefficient of the metasurface unitcell and the transmitted power enhancement of the array structure. The Fig. 4.17b depicts the unitcell analysis considering various air gaps. The investigation demonstrated that a 0.5 mm air gap resulted in a 1 dB reduction in the transmission coupling factor necessary for the effective transfer of high power by the metasurface. Expanding the gap by 1 mm resulted in a more significant impedance mismatch in the near field. This occurred because the 1 mm thick air gap acted as an additional load between the metasurface and the human

skin, leading to a 4 dB reduction in transmitted power. The introduction of additional air gaps resulted in further reductions in transmitted power and an increase in power reflected from the air-skin interface.

Extending the investigation to analyze transmitted power enhancement using the metasurface within the skin medium, while considering air gap distances of 0.5, 1, and 1.5 mm, demonstrates a decrease in near-field power enhancement inside the skin of 1.2, 4.5, and 7.5 dB, respectively. It is crucial to emphasize that the designated near-field focal point, positioned 2 mm above the metasurface, does not penetrate the skin medium in the presence of an air gap measuring 2 mm or more. Consequently, this non-penetration leads to a lack of observed power enhancement. Under these conditions, the outcomes align with those observed when the metasurface is not integrated.

In scenarios where uniformity is pivotal for deploying the presented metasurface-enhanced radar system in various biomedical applications, several strategies can mitigate the impact of non-uniformity. i) Reducing the metasurface array size while preserving resolution enhancement capability addresses non-uniformity concerns by maintaining consistent results in a smaller area. ii) Incorporating a flexible substrate in the metasurface design allows it to conform to body skin contours, effectively minimizing non-uniformity issues. iii) Employing machine learning algorithms, coupled with signal filtering techniques, robustly accounts for skin variability in radar power reception, mitigating interference. iv) Creating a wideband metasurface enables the radar system to operate across frequencies, offering advantages in penetrating the skin at different depths and interacting distinctively with skin features, potentially providing a more comprehensive perspective.

II) Exploration into the critical dynamics of permittivity across inter-individual differences in human skin: The acknowledged typical permittivity value for human skin may vary due to individual differences. The electrical characteristics of human tissues, particularly permittivity and conductivity, demonstrate considerable variability among individuals. The intricate interplay of factors, including hydration levels, age, health status, and tissue composition, adds complexity to the characterization of electrical properties. Permittivity, shaped by tissue composition and structure, tends to exhibit more pronounced variations. In contrast, conductivity, influenced by factors like ion concentration and moisture content, generally shows less noticeable fluctuations.

Since the metasurface is in direct contact with the human body's skin, it is essential to consider the correct values of the permittivity and conductivity of the skin. In general, for bio-sensing applications considering skin medium along with fat, muscle, and bone, the inter-individual differences are high due to the body shape differences. However, for applications such as glucose monitoring or skin cancer detection, it is well documented that

the 60 GHz signal will be rapidly attenuated into the body (within few mm). Therefore, when accounting for individual variations in skin dielectric properties, the changes in permittivity at 60 GHz are not substantial. Thus, our investigation focused on understanding how a maximum of 10% tolerance in permittivity variations impacts the performance of the metasurface.

As investigated in Fig. 4.18, modifying skin permittivity influences the central frequency and decreases the transmission coefficient within the metasurface unitcell. At 60 GHz, a deviation of ±5% causes a transmission coefficient reduction of less than 1 dB, while a deviation of ±10% results in reductions of 2 dB and 1.2 dB, respectively. Extending the evaluation to the array structure, altering permittivity by ±5% leads to transferred power reductions of 1.4 dB and 0.9 dB, respectively. Modifying permittivity by ±10% results in changes leading to power reductions of 2.3 dB and 1.9 dB, respectively.

III) The difference between the power reflected from the proposed dielectric slab as a skin and the beaker-filled with pure water: As investigated in Fig. 4.16, the metasurface in the presence of the skin model provides 9.5 dB enhancement in the reflected power, while 11.5 dB when the beaker filled with pure water is used. As investigated, the difference in material effective permittivity, ϵ, and conductivity, σ, between the human skin model and the beaker filled with pure water accounts for this 2 dB difference in S(TX-RX3) values. As reported in [209], the permittivity and conductivity of pure water at the frequency of 60 GHz, under typical room temperature conditions, are 11.17 and 65.3 S/m, respectively. Consequently, it becomes imperative to consider the impact of the external shell in the calculations. According to the literature, Pyrex glass demonstrates a relative permittivity of 4.7 and a conductivity of 0.5 S/m, at 60 GHz. In such situations, one can compute the effective dielectric properties of composite materials arranged in series across the entire volume facing the metasurface.

The effective permittivity of the overall medium, a beaker filled with pure water, is determined to be 8.75. Consequently, comparing the permittivity of the proposed phantom, 8.75, to that of a typical human skin model, 7.98, at 60 GHz reveals a difference of approximately 0.77. When comparing the permittivity of the phantom with that of human skin, it is noted that the tolerance is within +10%. Consequently, as investigated in Fig. 4.18, the anticipated outcome is a 2 dB reduction in the power transferred into the phantom compared to the power transferred into human skin. In this scenario, it can be inferred that the difference in focused power has been transformed into dissipated and reflected power, contributing to an enhancement in the reflection power when using the phantom as opposed to the human skin slab. On the conductivity front, the calculated conductivity of the phantom (a beaker filled with pure water), at 60 GHz and room temperature stands at 42 S/m. In contrast, the conductivity of human skin at 60 GHz is measured at 36.4 S/m.

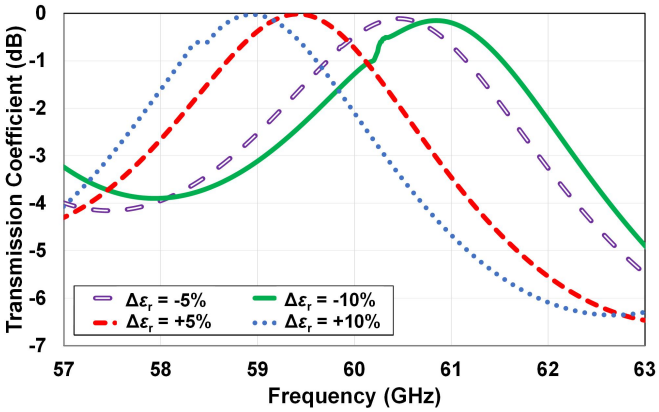


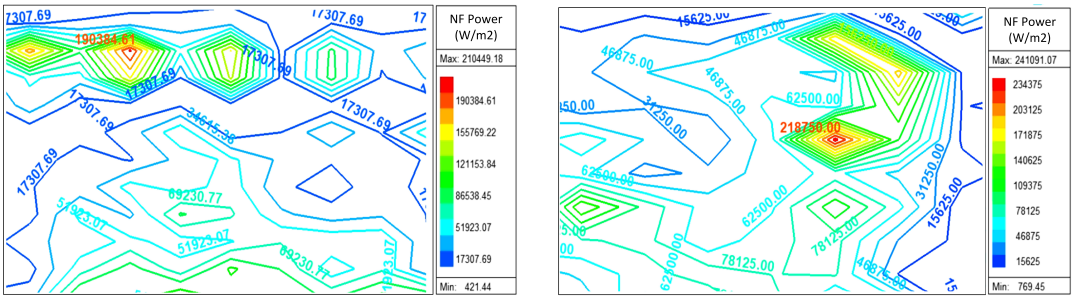
Figure 4.18: Analyzing the transmission coefficient of the metasurface unitcell in response to variations in the permittivity of the human skin model.

This implies that the phantom medium serves as a marginally better conductor, resulting in increased power reflection directed towards the radar.

Therefore, the examination of both permittivity and conductivity indicates that utilizing the proposed phantom, a beaker filled with pure water, results in less transferred power into the medium compared to the human skin medium, leading to an enhancement in power reflection. This is evident in Fig. 9e, where the power reflection from the phantom (11.5 dB) is 2 dB higher than the power reflection from the skin medium (9.5 dB).

IV) Analysis of the Effect of Spacing Between the Metasurface and Radar Antenna Surface: As presented in this research, placing the metasurface and skin model at the range of $\lambda/2$ at 60 GHz, adding a 2.5 mm air gap above the radar antenna provides the highest power concentration into the medium, represented by human skin model. The sensitivity analysis for the variations of the distance between the metasurface with radar antennas' array is supported by the simulations presented in Fig. 4.19. In this figure, the result of the transferred power into the human skin medium, when the metasurface is placed at the optimized distance of 0.5 λ, is compared to the results of the transferred power into the skin medium when the metasurface is placed at the distance of 0.6 λ and 0.4 λ. The results show that increasing the distance by 0.1 λ and decreasing the distance by 0.1 λ resulted in a reduction of the maximum focused power into the skin by 1.1 dB and 1.7 dB, respectively.

In conclusion, integrating the designed metasurface with the proposed radar increases energy into the body skin as well as increases the transferred power between the transmitter and receiver radar antenna while carrying more information from the skin medium. In



(a) (b)

Figure 4.19: Impact of varying air gap distances between the metasurface and radar antennas' surfaces on power distribution above the metasurface, illustrated for distances of (a) 0.4 λ, (b) 0.6 λ.

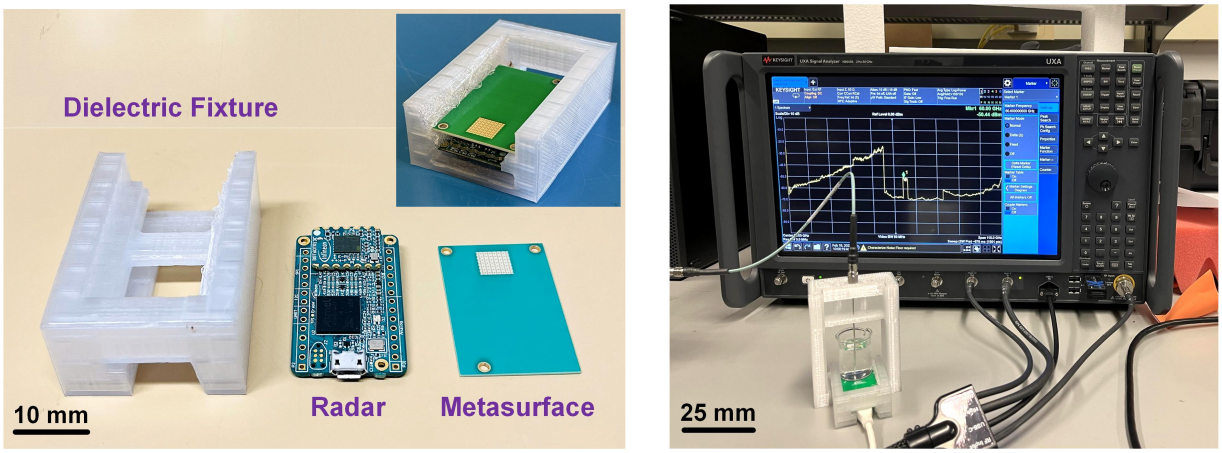
the following, the fabrication process of the designed transmitarray metasurface and the required measurement setup for measuring the near-field power inside the beaker filled with pure water and power reflected to the radar system using radar signal processing are presented and the results are discussed.

4.1.7 Fabrication Setup and Measurement Results

In the fabrication process, the prototype of the transmitarray metasurface, as depicted in Fig. 4.20a, showcases its integration with the radar module. This integration is achieved using a 3D printed dielectric fixture, strategically employed to stabilize the metasurface at a half-wavelength air gap distance above the radar system.

The following measurement procedures are required to evaluate the performance of the metasurface in a near-field radar sensing setup. First, the transmitted power radiated from the radar TX antenna is measured to verify that the metasurface enhances power density and effectively focuses energy within the phantom model. Second, the scattered power received by the radar RX antenna is measured to assess whether the metasurface improves the reflection of signals originating from within the phantom. This two-step process ensures that the metasurface not only facilitates stronger energy delivery into the biological medium but also enhances the reception of reflected signals, thereby improving the overall sensing performance of the radar system.

Regarding the fabrication process, the three steps are required as the following: i)

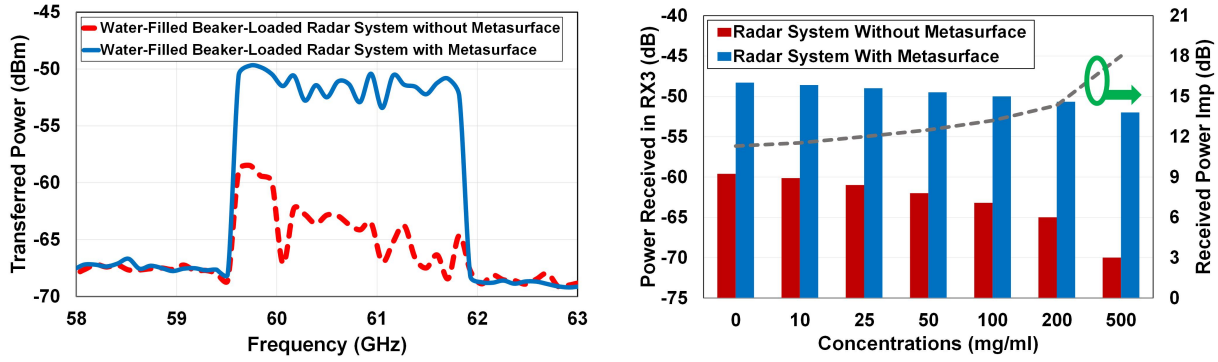


(a) (b)

Figure 4.20: (a) fabricated prototype showcasing the integration process of a radar system with a transmitarray metasurface, utilizing a 3D-printed dielectric housing for enhanced design precision; (b) measurement setup required for measuring near-field power density inside the phantom.

the transmitarray metasurface using printed circuit technology consisting of the phase-compensated two-layer unitcells to realize a low-profile square lattice array with total dimensions of $1.54\lambda \times 1.54\lambda$ printed on both sides of a low-loss dielectric substrate, Rogers-RO4003, with the thickness of 0.8 mm. As shown in Fig. 4.20a, the metasurface is fabricated at the same dimensions as the radar for full integration. The designed array part of the metasurface also covers the radar antenna to provide focused power into the water medium. ii) a dielectric fixture using 3D printing technology to stabilize the metasurface at half-wavelength airgap distance above the radar system as shown in Fig. 4.20a; iii) a dielectric fixture required to be designed and fabricated using 3D printing technology for the measurement setup to make the prob coming out from the Spectrum Analyzer stable inside the beaker-filled with water proving high repeatability in the measurement results of the transferred power as shown in Fig. 4.20b. Furthermore, the dimensions of the measurement dielectric fixture are adjusted to tightly enclose the radar dielectric housing and maintain the position of the beaker at the center of the array.

As shown in Fig. 4.20b, a special probe working at 60 GHz is connected to a spectrum analyzer supporting the frequency range up to 110 GHz and is used for the power measurement. A Pyrex beaker filled with 10 ml pure water is utilized to be placed on top of



(a) (b)

Figure 4.21: Measurement results of metasurface-enhanced radar signal transmission and reflection in presence of the proposed phantom. (a) The measured near-field power density incident by Infineon radar transmitter (TX) antenna inside the beaker-filled with pure water in the presence or absence of the designed transmissive metasurface. (b) The investigation of the measured power reflected from the beaker filled with pure water received by the third receiver radar antenna (RX3) over a period in the presence or absence of the designed transmissive metasurface for different concentration levels of glucose.

the metasurface array with a half-wavelength, 2.5 mm, distance above the radar antenna. The experiment is repeated for the radar system without a metasurface such that very thin cardboard is replaced with the metasurface at the exact location to maintain the beaker at a specified distance above the radar surface. In both cases, the probe is immersed into the beaker with a 1-mm distance above the beaker's bottom surface, which is 2 mm above the metasurface layer location. To obtain accurate results, the signal processing configuration for the FMCW Infineon radar system working at 60 GHz is also presented in the Appendix A and considered in the process.

The measurement results showing the power transferred into the water medium and picked up by the probe are presented and compared in Fig. 4.21a. As can be seen, using the designed transmitarray metasurface enhances the power received by the probe at the operational radar frequency range, from 59.7 to 61.7 GHz. Fluctuations in the enhanced transferred power result from both the distribution of radar power and specific design considerations. Looking specifically at the designed frequency of 60 GHz shows an improvement of 11 dB in the measured near-field power, which is in good agreement with the simulation results representing the power density improvement of 11.5 dB in Fig. 4.15.

The next step is the radar SNR investigation by measuring the reflected power from the water to one of the radar receiver antennas (RX3). The algorithm in Appendix A is used to measuring the received power in a period of time in the cases of the radar system loaded by a beaker-filled with water in the presence or absence of the transmitarray metasurface. To illustrate near-field sensing improvement with higher SNR, different concentration levels of glucose are added to water and the results are analyzed and compared in Fig. 4.21b. As shown, using the near-field-focused metasurface enhances the power reflection from the pure water by 11.3 dB and improves the radar SNR around 13.4-times, which is in good agreement with the simulation results presented in Fig. 4.16. Furthermore, in this experimental study, the effect of varying the dissolved amount of glucose in water in the presence of the metasurface is explored. 200 experiments for each scenario were carried out to provide high repeatability. Although power reflection is reduced by increasing glucose content in both cases, the metasurface clearly improves the received power level by the radar as shown in Fig. 4.21b. The received power in the presence of the metasurface for different sugar concentration levels has a resolution of around 0.5 dB per each 15 mg/ml concentration, validating that the metasurface enhances the overall sensing functionality.

In conclusion, at the end of this section, a detailed comparison and informative descriptions are presented to thoroughly discuss and highlight the novelty and advantages of the proposed method, utilizing the designed metasurface to enhance near-field sensing, which is essential for biomedical applications:

- **Near-Field Theory Considerations:** The metasurface is designed with a methodology tailored for near-field radiation theory, essential for biomedical sensing, in contrast to prior works focusing on usual far-field antenna radiation.
- **Compactness:** In near-field focusing, current antenna designs face integration challenges with low-profile radar due to their bulky structures. This study proposes a low-profile, compact, and planar metasurface for seamless integration with a radar system.
- **Millimeter-wave Operation:** The mm-wave frequency range is selected for its high resolution and precision, bio-compatibility, and reduced interference making it suitable for applications in wearable devices like smartwatches.
- **Direct Human Skin Contact:** Near-field studies typically focus on antenna radiation in free space, but the human body causes detuning and impedance mismatching, degrading performance. Existing methods are unsuitable for direct-contact biomedical applications. The designed metasurface allows skin contact, enabling precise targeting without interference.

- **Impedance Matching Layer:** The metasurface is carefully designed based on impedance matching network theory to achieve highly effective impedance matching between free space and the human skin. This design tackles a significant challenge in the literature by minimizing reflections arising from air-skin interference.
- **Intensify Radiated Near Electric Field:** The metasurface, with phase-synthesized unicells significantly boosts the near-field electric field from the source antenna, achieving an 8.8-fold improvement within the proposed skin phantom medium compared to the radar antenna without the metasurface.
- **Intensify Near-field Transmitted Power:** The metasurface enhances absorbed power in human skin at 60 GHz without affecting source antenna impedance matching. This near-field-focused design yields an 11 dB improvement in radiated power density above the metasurface within the proposed skin phantom medium.
- **Intensify Near-field Reflected Power:** Analyzing the radar's reflection coefficient shows the metasurface amplifying reflected power from human skin by 11.3 dB. This enhancement leads to a notable 13.4-times improvement in radar SNR, enabling effective information transmission and high-performance near-field sensing in biomedical applications.
- **Glucose Sensing Enhancement:** In glucose monitoring, metasurface-enhanced power measurements show a resolution of around 0.5 dB per 15 mg/ml sugar concentration, maintaining a high SNR and confirming enhanced functionality in glucose sensing.

4.2 Objective 2: Multi-Focus Distributed Sensing Using Metasurface-Enhanced Multi-Radar Fusion

With advancements in sensor technology and signal processing algorithms, the adoption of multi-sensor fusion techniques including the radar-based fusion [211], or integration of radar with other sensing modalities such as cameras, LiDAR, and inertial measurement units (IMUs) has gained significant attention across various fields [212], driven by the increasing demand for higher accuracy, reliability, and real-time situational awareness, in the applications such as autonomous systems, intelligent transportation systems, land use mapping and monitoring, surveillance and industrial automation for multi-object tracking [213].

A multi-radar system enhances sensing capabilities by integrating data from multiple spatially distributed radar units, resulting in improved spatial resolution, target localization, and detection probability through triangulation and diverse viewing angles. This configuration enhances system reliability by introducing redundancy and enabling advanced signal processing techniques. Particularly advantageous in dynamic environments, multi-radar setups provide seamless target tracking and superior situational awareness over extensive areas, surpassing the limitations of single-radar systems.

The proliferation of multi-radar sensor networks is particularly evident in healthcare and biomedical monitoring, offering enhanced precision in vital sign detection. The study [214] introduces a fall detection system using range-Doppler radar sensor fusion to improve accuracy and reliability in elderly care. By combining data from multiple UWB radars, the system mitigates occlusions and directional limitations that weaken Doppler signatures when motion misaligns with the radar's line of sight.

Building on the benefits of multi-sensor fusion systems in healthcare, blood glucose monitoring is a critical application that can greatly benefit from this capability. Because glucose is heterogeneously distributed within human skin, which serves as a protective barrier against environmental insults while contributing to vascular capacity, blood pressure regulation, and glucose handling [215]. Glucose levels in the blood can vary significantly depending on the site of measurement, as blood is not uniformly distributed throughout the body. Recent research has extensively investigated various locations on the human body for glucose monitoring, including the hand wrist [216], heel prick [217], hand palm [218], forearm and finger [219], and ear lobe [220]. These studies aim to determine the most reliable and practical sites for accurate glucose measurement; however, the results vary across different measurement locations. [221] demonstrated that glucose levels in the arm were approximately 5% lower than those in the finger, with this difference peaking

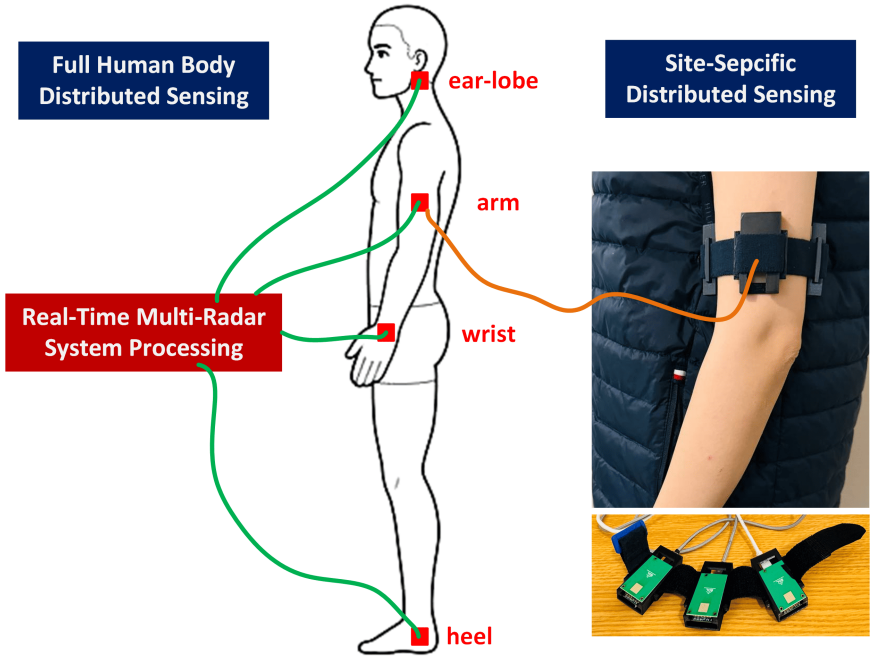


Figure 4.22: Multi-Radar Sensor Fusion System for Distributed Full-Body or Site-Specific Sensing

about 1 hour after a glucose load.

Variations in skin properties, such as blood flow, thickness, and composition across different regions influence radar signal reflections, further complicating measurement accuracy. To address such variability, regulatory standards for glucose meters used by individuals with diabetes at home have been established. According to FDA guidance, 95% of all measured values must fall within 15% of the true value as determined by laboratory measurements, and 99% must be within 20% of the true value [222]. Accepting blood glucose variability through invasive or non-invasive glucose meters reveals that even FDA-approved commercial devices suffer from low accuracy due to the uneven distribution of glucose in human skin. In addition to site-specific differences, physiological dynamics further challenge the accuracy of non-invasive blood glucose meters. One key factor is the physiological lag time of approximately 7–8 minutes, caused by the diffusion of glucose from the intravascular compartment to the subcutaneous interstitial fluid. This delay, coupled with the dynamic nature of glucose transport, can lead to variability even between consecutive measurements on the same meter [223]. These challenges underscore the need for continued advancements in non-invasive glucose monitoring technologies to enhance

measurement consistency and accuracy across diverse conditions.

In the objective 1 [194], a 60 GHz radar module augmented with a near-field-focus metasurface with matching at the skin-device interface is explored for glucose monitoring applications. However, this design constrain the system's ability to address the inherent heterogeneity and variability of glucose distribution across different layers and regions of the skin [224]. As reported in [225], we propose a method at this section to improve the accuracy of this system by utilizing a synchronized multi-radar fusion system. By taking measurements from multiple distinct spots as shown in Fig. 4.22:

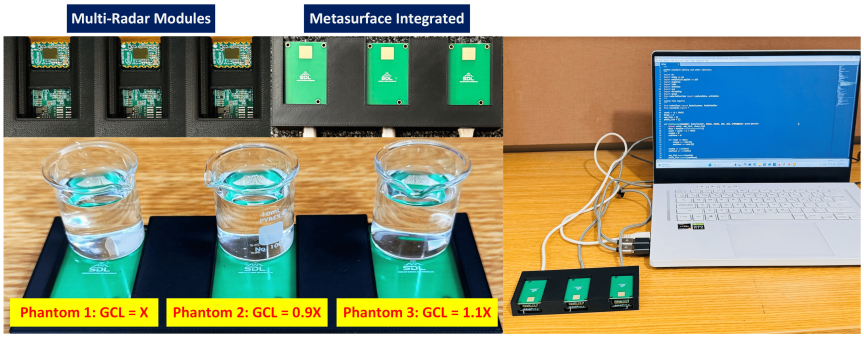
i) The system averages out localized differences, reducing the impact of site-specific variability and achieving more consistent and reliable glucose readings compared to relying on a single measurement point. ii) External factors such as movement, ambient temperature, and electromagnetic interference can affect radar signals. Utilizing multiple measurement points increases the likelihood that at least one signal remains clear and unaffected by such disturbances, ensuring continuous and accurate monitoring. iii) Measurements from different spots enable cross-verification, allowing the detection and correction of discrepancies caused by localized anomalies or sensor errors. iv) Differences in skin properties, such as thickness and hydration levels, as well as environmental factors like humidity and altitude, further contribute to measurement variability, highlighting the importance of multi-point measurement systems in achieving robust and reliable glucose monitoring.

Experimental findings show that the proposed fusion-based system significantly surpasses conventional radar-only approaches, yielding up to a 2.4-fold enhancement in radar signal-to-noise ratio (SNR) when accounting for blood glucose distribution variability caused by a 20% concentration difference across various skin phantoms.

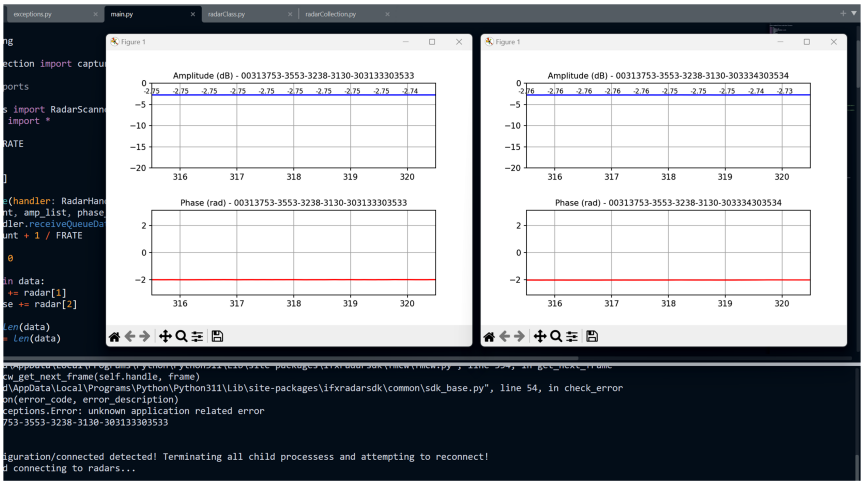
4.2.1 Synchronized Multi-Radar Signal Processing

The objectives of this multi-radar fusion system for non-invasive glucose monitoring are to achieve synchronization of radar operations, ensuring concurrent performance without delays to enhance measurement accuracy, and to enable real-time system visualization for immediate monitoring and analysis. Fig. 4.23a shows the setup of three radars, each enhanced with identical metasurfaces presented in Objective 1 [194], connected to the USB ports of a laptop for real-time signal processing. This configuration enables simultaneous data acquisition and processing to improve measurement accuracy and signal quality.

To facilitate the concurrent capture of multiple radars, a Python multiprocessing program is developed to interface with BTG60TR13C radars, as detailed in Appendix A. The program incorporates three operational flags, live capturing, data collection, and averaging,



(a)



(b)

Figure 4.23: (a) Multi-radar system configuration consisting of three Infineon 60 GHz BGT60TR13C radar modules enhanced with metasurfaces, applied to a human skin phantom model with varying glucose concentration levels (GCL). (b) Real-time visualization of the system's data capture.

which can be combined to provide flexible functionality. Each radar is assigned a dedicated child process, enabling parallel execution and efficient resource management. Depending on the selected mode, each process executes specific tasks, ensuring seamless and scalable multi-radar operation.

The live-capture mode enables the program to visualize data from each connected

radar in a separate window. As illustrated in Fig. 4.23b, an example of two connected radars showcases real-time received power amplitude and phase plots. In each window, both amplitude (in dB) and phase (in radians) are plotted on the vertical axis, while the horizontal axis represents time. Each plot is uniquely identified by a UUID, which is automatically assigned by the operating system upon device connection to the computer. The signal processing details of the synchronized multi-radar sensing system are provided in Appendix A, Section A.2.

4.2.2 Experimental Results with the Multi-Radar Fusion System

To validate the effectiveness of the proposed glucose monitoring system and to compare single-sensor and multi-sensor configurations, four real-world non-invasive glucose monitoring challenges are evaluated:

1) A multi-concentration testing approach is implemented to evaluate the system's performance. Glucose phantoms with adjusted concentrations of 10 mg/dL, 25 mg/dL, 50 mg/dL, 100 mg/dL, and 200 mg/dL are prepared, with additional solutions incorporating a 20% ($\pm$10%) concentration variation, as illustrated in Fig. 4.23a. The signal response is analyzed by measuring the reflected power amplitude variation, initially using a single sensor and then with a multi-sensor array to compare accuracy. The results presented in Fig. 4.24 demonstrate that the multi-sensor configuration enhances detection sensitivity by improving the radar signal-to-noise ratio (SNR) by 2.8 to 3.8 dB across the tested concentration levels.

2) To further assess the system's performance, real-time monitoring of glucose level changes is conducted by gradually varying the glucose concentration over time while capturing data in real time. This evaluation aims to determine the system's capability to continuously track dynamic changes using both single-radar and multi-radar configurations. Changing the glucose concentration level in a beaker, as shown in Fig. 4.23a, simulates localized glucose level variations in a specific part of the human body while remaining constant in other areas. In this scenario, adding a 10% glucose concentration to one beaker while the others contain pure water results in a 0.8 dB reduction in the average received power. Meanwhile, a single radar positioned at the constant pure water locations does not register any significant change, as expected. This demonstrates that the multi-radar setup provides more accurate tracking by utilizing synchronized sensing, which enhances spatial coverage and reduces measurement uncertainties.

3) To assess the impact of environmental factors on glucose measurement accuracy, tests are conducted under varying conditions, including different levels of humidity. In this

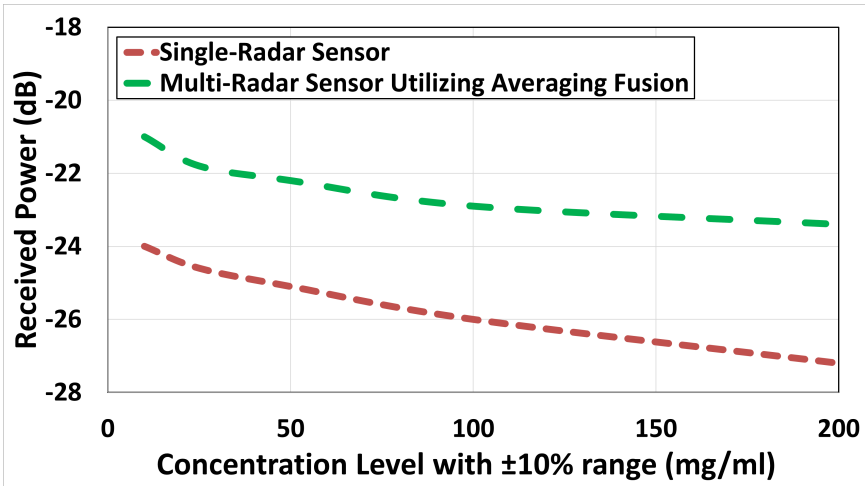


Figure 4.24: Received power measurements representing radar SNR for phantoms with varying glucose concentration levels.

scenario, a piece of humidity paper is placed between the metasurface layer and the beaker containing phantom 1, and the results are compared. As expected, the radar associated with phantom 1 experiences reduced sensing capability due to the barrier obstructing the radiation path, preventing the detection of glucose concentrations. This outcome simulates the limitations of a single-radar sensor when exposed to similar conditions. In contrast, the multi-sensor setup demonstrates improved stability in glucose readings, as the remaining two sensors continue to capture data, ensuring reliable measurements despite the localized obstruction.

4) To investigate the impact of sensor displacement on glucose monitoring accuracy, a scenario similar to the third evaluation is conducted. Sensor displacement can introduce distortions in radar signals due to loss of contact with human skin, leading to impedance mismatching [120]. In this experiment, phantom 1 is removed from the sensor, causing single radar 1 to display a distorted signal. However, in the multi-radar setup, the remaining two radars continue to capture accurate data, demonstrating the system's resilience and improved reliability in maintaining consistent glucose readings despite localized displacement.

This study demonstrates that synchronized multi-radar fusion system provides robust and reliable tracking under dynamic conditions. The multi-radar approach enhances spatial coverage, reduces measurement uncertainties, and ensures consistent data acquisition, making it well-suited for real-life applications requiring accuracy, stability, and resilience.

4.3 Objective 3: Radar Near-Field Sensing Using Dual-Band, Dual-Focus Metasurface

Employing mm-wave radar in bio-sensing provide high sensitivity; however, this comes at the expense of very low penetration depth, limiting its effectiveness for internal body health monitoring as it struggles to transmit adequate power to tissues for precise data acquisition [226]. To overcome the existing limitations of bio-electronic interfaces, metasurfaces can be designed to manipulate electromagnetic fields surrounding the human body.

The development of this thesis follows a stepwise progression, building upon each design iteration to enhance radar-based near-field sensing performance for biomedical applications. The initial focus in Objective 1 [194] is the design and implementation of a low-profile planar near-field-focused metasurface for integration with radar transmitter (TX) and receiver (RX) antennas, allowing it to directly contact the human skin for real-time, non-invasive blood glucose monitoring. This integration increases the absorbed power density from the radar antenna by over 11 dB at a single focal point within the skin medium, while also enhancing the power reflected back from the skin to the radar. This design improvement significantly boosts the sensor's overall signal-to-noise ratio. Expanding on this foundation, Objective 2 [225] introduced a multi-radar sensing architecture, where the same single-band metasurface design from Objective 1 is integrated with three synchronized radar modules. Each radar is positioned at a different location, enabling distributed sensing across multiple areas of the body. This objective focuses on spatial diversity using a consistent frequency band, providing improved accuracy by mitigating spatial variability through multi-location data fusion.

While single focal point bio-sensing radar system can be effective to some extent, it faces significant limitations due to its narrow data capture area and restricted depth of information. The innovative use of near-field multi-focusing in radar bio-sensor enables data collection from multiple focal points at varying depths, enhancing the detection of dielectric changes in biological tissues and improving the signal-to-noise ratio by reducing noise and inconsistencies. This approach marks a transformative step in diagnostic reliability, as it also accounts for physiological variations, such as skin thickness and hydration levels, which would otherwise impact signal quality.

In this Objective, the research advances toward multi-depth sensing by introducing a dual-band, dual-focus metasurface. This single metasurface is capable of producing two distinct focal points at two different frequencies, allowing simultaneous sensing at different tissue depths and locations. This dual-band functionality provides richer physiological information and marks an important transition from purely spatial distribution to

frequency-selective depth control.

In conventional radar and antenna applications, multi-focusing refers to the radar's capability to accurately control the directionality of antenna beams, enabling the detection of multiple targets through beamforming techniques [227]. In [228], a multi-beam and multi-range FMCW radar utilizing a digital beamforming algorithm is presented, designed to cover both long and short detection ranges at 24 GHz. Additionally, [229] introduces a dual circularly-polarized multi-beam antenna aimed at future vehicular radar applications within the 23.5–24.5 GHz frequency band. For off-the-shelf radar modules, integrating a lens or metasurface is an effective and practical solution to achieve multi-focusing capabilities without complex radar hardware modifications. Several multi-beam metasurfaces have been introduced in the literature [230] for integration with a source antenna. Conventional multi-beam metasurfaces, however, typically rely on multiple feeds to generate distinct beams, making them unsuitable for integration with radar modules that incorporate a transmitter antenna. Single-fed multi-beam metasurfaces, on the other hand, divides the available transmitted power across multiple beams, reducing aperture efficiency for each individual beam. This power division results in inadequate energy at each focal point, limiting the radar's ability to effectively penetrate the skin and accurately monitor glucose levels.

Furthermore, for bio-sensing applications where the radar must be in direct contact with the human body, the antenna's propagation area shifts from far-field to near-field, necessitating a shift in design focus from multi-beam to multi NF focusing, as conventional beamforming techniques are no longer suitable in this context. Thus, a gap remains in the development of a multi-focusing metasurface that can seamlessly integrate with radar modules without compromising efficiency, particularly in bio-sensing applications where impedance matching with human skin is essential.

To achieve a multi-focus metasurface with high absorbed power at each specified focal point, two approaches can be explored: generating focal points at different polarizations or at distinct frequencies. [231] demonstrates the design of a reflecting array capable of producing two adjacent beams per feed with orthogonal circular polarization within the Ka band. However, differentiating focal points by polarization is unfeasible for near-field sensing, where all polarizations coexist and cannot be effectively isolated, as in far-field applications. This limitation makes a multi-band, multi-focus metasurface a more suitable solution, enabling each focal point to operate at a distinct frequency. [232] presents a high-gain, dual-band, dual-circularly polarized transmitting array with independent beam control in the Ku-band, utilizing an element with independent phase control capabilities at 12 and 15 GHz. Adopting this multi-band approach in multi-NF-focusing allows precise energy focusing at multiple depths or regions within the skin, improving both penetration

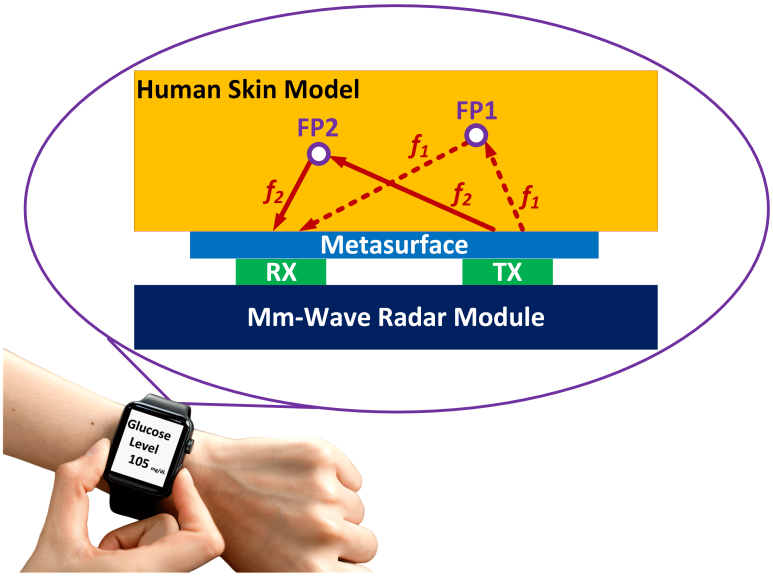


Figure 4.25: The mm-wave radar module integrated with a dual-band metasurface, generating dual near-field focus points within human skin, with the goal of incorporating this functionality into wearable devices.

and measurement accuracy in bio-sensing applications.

This research introduces a dual-band, dual independently-tunable near-field focus metasurface designed to enhance the performance of mm-wave radar-based bio-sensor, 60 GHz mm-wave Infineon radar module, optimized to match the specific characteristics of human wrist skin. This metasurface enables dual focusing of absorbed power within human skin, achieved through a phase-synthesized analysis of the metasurface array, where each focal point is controlled by a distinct frequency band within the radar spectrum, as illustrated in Fig. 4.25. The integration of the proposed metallic slot metasurface with commercially available Infineon radar TX/RX antennas results in a 14.7 dB and 12.4 dB increase in Poynting power density at two distinct points within a human skin phantom model, along with an increase in radar-received power by 11 dB and 12.7 dB at 58.5 GHz and 61.7 GHz, respectively, significantly enhancing the radar's bio-sensing capabilities. Expanding upon the metasurface-enhanced radar system described in [194], this design improves near-field sensing capabilities for bio-sensing applications, with a primary focus on non-invasive glucose monitoring.

4.3.1 Dual-Band, Dual Near-Field Focus Metasurface

This section presents an optimized metasurface design featuring a dual-band unitcell and phase-synthesized array analysis to achieve near-field phase shift compensation. This design is intended for direct contact with human skin and is considered to operate within the mm-wave range, specifically targeting two distinct frequency bands within the radar spectrum from 58 to 63 GHz.

In [204], we introduced a design strategy for a dual-band transmissive array, employing interleaved electric and magnetic dipole slots to minimize mutual coupling, which enables two frequency bands with adjustable separation. The design uses metallic layers without a substrate, enhancing efficiency and achieving a narrower bandwidth that allows closer frequency band placement through precise filtering. This results in S-parameters with a higher quality factor and minimal unwanted resonances within the targeted frequency bands. Additionally, the fabrication cost is reduced by utilizing laser cutting techniques, making this approach both efficient and low-cost.

Inspired by the approach presented in [204], in the present work, the design of a slot-based, dual-band, dual-polarised transmitarray metasurface with low frequency separation to be fit in the mm-wave radar frequency range is reported. This is made possible by using interleaved electric and magnetic dipole slots that result in less mutual coupling leading to two frequency bands with controllable separation that can be very close to or far from each other. Furthermore, by using the layered scatterer approach, a better independence between the two bands is provided. The proposed unitcell has three layers with air gaps in between. Unlike the previous works stated in objective 1, no expensive and lossy dielectrics are used. The elimination of dielectrics results in higher power transmission and lower fabrication cost. Due to its symmetrical structure, the proposed structure can operate either in dual-linear polarization mode with very low coupling in between or in circular polarization mode at each frequency band.

4.3.2 Dual-Band Unitcell and Array Design

The optimized unitcell layout for mm-wave operation is illustrated in Fig. 4.26, forming a dual-band metasurface unitcell with independently tunable frequency bands. As shown, an electric crossed-dipole slot element loaded with stubs is employed to create a band-pass filter at the operational frequency of 59 GHz. By tuning the length of the dipole slots, L_d, and the stub length, L_{ds}, as well as its positions, the center frequency of this band can be controlled. To establish the upper frequency band while minimizing coupling with

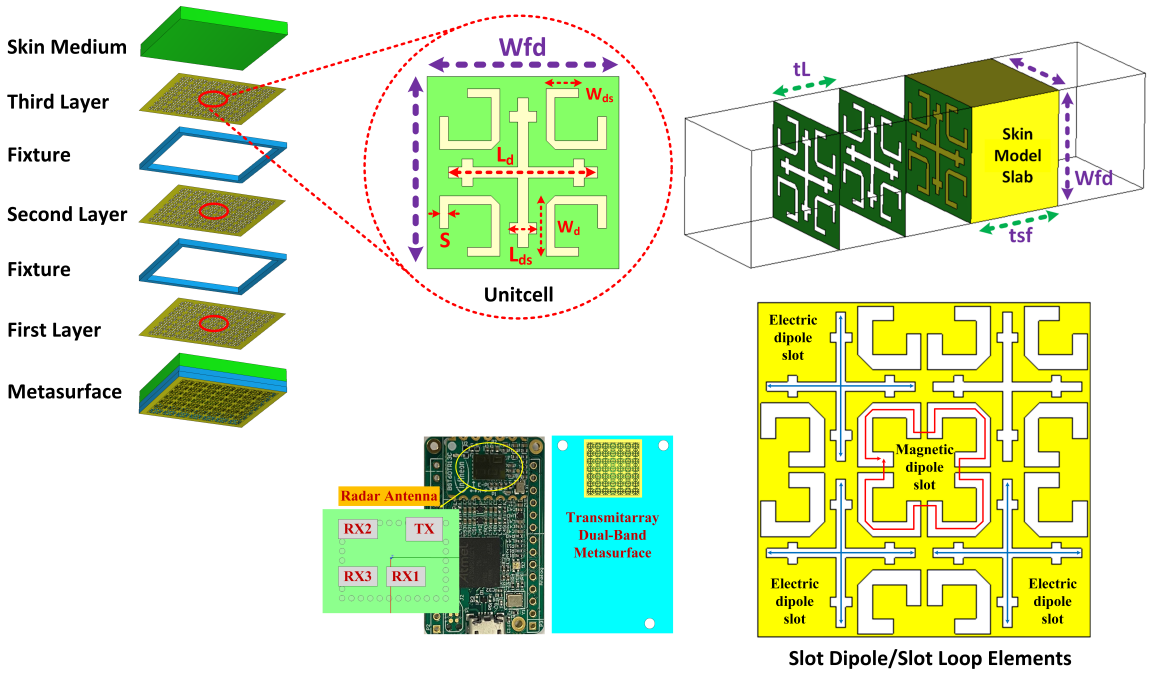


Figure 4.26: Configuration of the mm-wave Infineon radar module antennas alongside the designed dual-band, dual-focus metasurface, incorporating crossed-dipole and square loop slot elements within the unitcell design.

the lower band, a uniplanar compact photonic bandgap (UCPBG) element, acting as a magnetic dipole slot, is employed. A square loop slot element serves as a band-pass filter, precisely tuned to the operational frequency of 61 GHz. Adjusting the dimensions of the etched branches within the loop slot, W_d and W_{ds}, enables control over the upper frequency band. The design parameters are as follows: $L_d = 2.16$, $S = 0.13$, $L_{ds} = 0.48$, $W_d = 0.66$, $W_{ds} = 0.39$, and $W_{fd} = 2.3$ (all in mm). Fig. 4.27 presents the S-parameter (S11) analysis of the slot elements at the designated frequency bands.

Dual-Band Unitcell Analysis

The unitcell dimensions of the metasurface are typically chosen to be approximately half-effective wavelength of the medium to ensure an appropriate resonant response from the array. In the current design, however, the unitcell is engineered to support dual resonance frequencies simultaneously, corresponding to two distinct wavelengths when the unitcell is in direct contact with human skin. To accommodate both resonance frequencies, the

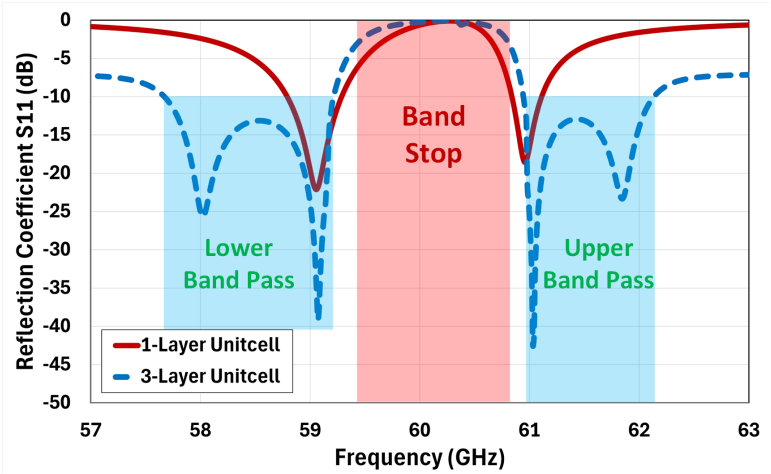
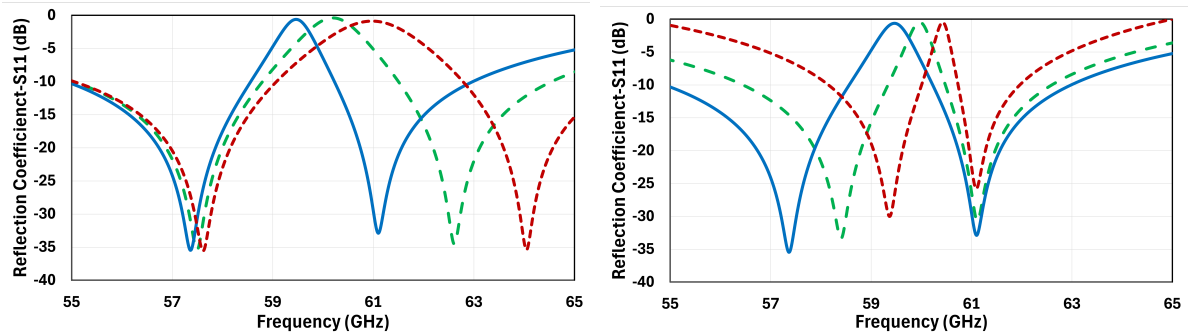


Figure 4.27: S-parameters analysis of the dual-band mm-wave unitcell featuring interleaved slot elements.

unitcell dimensions are determined based on the larger of the two wavelengths, specifically, a free-space wavelength of 5.08 mm and an in-slab wavelength of 2.4 mm at 59 GHz. This ensures that the metasurface can effectively support both frequency bands. In defining the unitcell size, the effective permittivity of the surrounding medium is also taken into account, as it influences the in-slab wavelength. The final unitcell dimensions are chosen to be slightly larger than the half-wavelength criterion. This not only ensures adequate resonance but also allows sufficient spacing between interleaved elements, which helps minimize mutual coupling and facilitates the fabrication process by providing enough metallic width between adjacent features.

The slot parameters for each metasurface are optimized to generate lower and upper-frequency bands within the ranges of 58–59 GHz and 61–62 GHz, respectively, as illustrated in Fig. 4.28. The resonance frequencies can be very close to or far from each other depending on the variation of the slot lengths, L_d and L_{ds} for the lower band, and W_d and W_{ds} for the upper band. As shown in Fig. , by changing each slot length, the relevant resonance frequency is altered independently, with very low effects on another band. Thus, there is excellent independence between the two bands. The widths of the lines in each of the proposed slots, S, is adjusted to determine the bandwidth of each frequency band.



(a) (b)

Figure 4.28: Simulated S11 parameter to investigate independence between two frequency bands: (a) Through changing UC-PBG slot length, (b) Through changing crossed-dipole slot length.

Dual-Focus Array Analysis

As shown in Fig. 4.26, a three-layer metallic unitcell featuring two interleaved elements, a crossed-dipole and a square loop slot, in direct contact with a skin model slab is utilized. The design employs substrate-free metallic layers to enhance efficiency and achieve a narrower bandwidth, enabling precise filtering for closer frequency placement. The skin medium is modeled as a dielectric slab with a t_{sf}=3 mm thickness and dielectric properties of ϵ_r=7.98 and σ=36.4 S/m [194], as shown in Fig. 4.26. For single-band metallic structures, the air gap height is set to a quarter of the free space wavelength to obtain a higher phase response. The present structure has two separate frequency bands, and the air gap height has to satisfy the transmission phase response for both frequency bands. A suitable air gap height between the layers is shown to be the average of the quarter free space wavelengths of both frequency bands, and is set at t_L=λ/4=6 mm, where λ is the highest wavelength, resulting in a compact metasurface with a total thickness of 2.54 mm for direct contact with human skin. Fig. 4.27 shows the S_{11} analysis of the 1-layer and 3-layer unitcell. Compared to the single-layer design, it demonstrates a wider bandwidth and a slight shift in the center frequencies of both assigned bands, resulting from phase error losses due to the averaged air gap distance between the metasurface's metallic layers.

To construct the metasurface array using the designed dual-band unitcell, it is necessary to achieve the desired phase shift across both frequency bands, with each unitcell tuned to provide the appropriate phase compensation based on its position relative to the radar

TX antenna. As investigated in objective 1, the near-field phase shift at each metasurface element in a planar array, for a focal point located at a distance r_0 along the boresight axis, is given by:

$$\phi_{mn} = \frac{2\pi}{\lambda}\left(\sqrt{x_m^2 + y_n^2 + r_0^2} - r_0\right) + \phi_0 \tag{4.12}$$

where:

- (x_m, y_n) are the coordinates of the element in the array,
- λ is the wavelength,
- r_0 is the focal distance from the center of the array,
- ϕ_0 is an optional constant phase offset.

This equation computes the extra path length (converted to phase) between the center element and each element, effectively normalizing the center element's phase to ϕ_0. For the near-field focusing, a more complex configuration where wave propagation occurs through two different media and focuses at two distinct points, the total phase shift becomes:

$$\phi_{mn} = k_1\left(R_1(x_m, y_n) - F_1\right) + \mathrm{Re}(k_2)\left(R_2(x_m, y_n) - F_2\right) + \phi_0 \tag{4.13}$$

where:

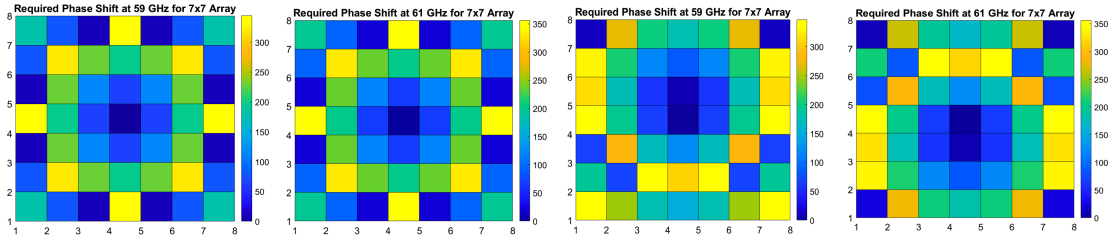
- $k_1 = \dfrac{2\pi}{\lambda_1} = \dfrac{2\pi f}{c}$ is the wavenumber in Medium 1 (free space),
- $k_2 = \dfrac{2\pi f}{c}\sqrt{\varepsilon_r - j\dfrac{\sigma}{\omega\varepsilon_0}}$ is the complex wavenumber in Medium 2 (Human Skin),
- $R_1(x_m, y_n) = \sqrt{x_m^2 + y_n^2 + F_1^2}$ is the distance to the first focal point (Medium 1),
- $R_2(x_m, y_n) = \sqrt{x_m^2 + y_n^2 + F_2^2}$ is the distance to the second focal point (Medium 2),
- F_1, F_2 are the focal distances from the array center,
- ϕ_0 is a constant phase reference (often zero).

This equation models the total spherical wave phase propagation through two regions, each with its own electrical properties, and normalizes to the center element. To achieve dual independent focal points within medium 2, it is essential to tilt the focus positions rather than align them along the same axis. By introducing angular displacement between the focal points, the metasurface can spatially separate the energy concentration zones at distinct lateral locations while maintaining individual frequency control. To scan the NF focus in a specific direction (θ, ϕ), an additional steering phase can be applied:

$$\phi_{mn}^{\text{total}} = \phi_{mn} - \text{Re}(k_2)\left(x_m \sin\theta\cos\phi + y_n \sin\theta\sin\phi\right) \tag{4.14}$$

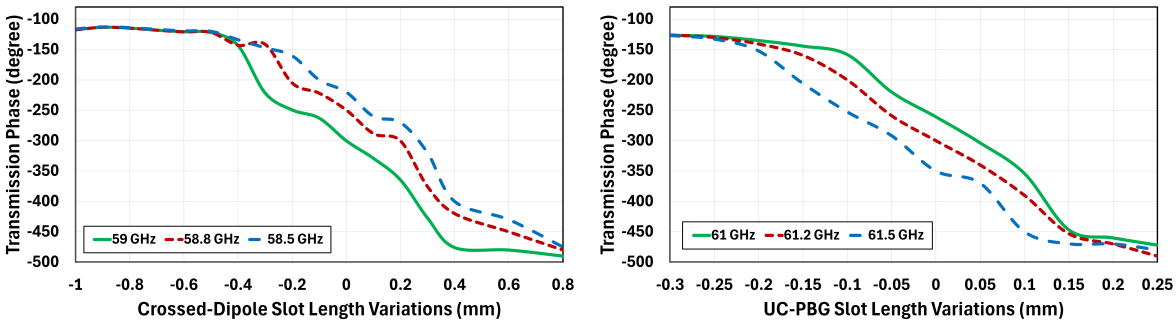
This term aligns the wavefront in the desired angular direction and is typically used in far-field or hybrid near-field scenarios.

In this design, the metasurface utilizes Fabry-Perot resonance theory by positioning the radar antenna and metasurface interface at a distance of half the free-space wavelength. The required phase shift for a 7×7 array of square unitcells, each with dimensions of 2.3 mm^2, at a feed focal point distance of 2.5 mm is illustrated in Fig. 4.29. To achieve the dual-focusing capability, the phase of the array must be adjusted to direct power to distinct focal points within the human skin model, each at a specific frequency. Fig. 4.29a and Fig. 4.29b illustrate the required phase compensation for near-field focusing at boresight, while Fig. 4.29c and Fig. 4.29d present the phase distributions necessary for beam tilting at $\theta = +20°$ and $\theta = -20°$ at the lower and upper frequency bands (59 GHz and 61 GHz), respectively.



(a) (b) (c) (d)

Figure 4.29: Phase synthesis analysis of the metasurface array with 7×7 unitcells, showing phase shift compensation required for (a) focusing at boresight at 59 GHz, and (b) focusing at boresight at 61 GHz, (a) focusing at +20 degrees at 59 GHz, and (b) focusing at -20 degrees at 61 GHz.



(a) (b)

Figure 4.30: Simulated transmission phase shift of three-layer unitcell (a) For lower frequency band, (b) For upper frequency band

As shown in Fig. 4.29, the dual-band unitcell depicted in Fig. 4.26 must provide phase shift compensation of 330 degrees at 59 GHz and 350 degrees at 61 GHz to achieve the required array phase synthesis. This is accomplished by fine-tuning the dimensions of the dipole and loop slot elements. As reported in [207], in designing a transmissive array, a transmission coefficient of 3 dB enables a maximum phase shift of up to 360 degrees for a three-layer metasurface unitcell, irrespective of the structure's shape.

Fig. 4.30 shows the transmission phase response for the triple layers of the proposed unitcell at two frequency bands. As shown in the figure, for the 3-dB transmission bandwidth, the three-layer structure provides a phase shift of up to 300°. Increasing the number of layers provides higher phase shift. As shown in Fig. 4.30a and 4.30b, the phase shift responses of the three considered frequencies in both bands are almost parallel, proving the wide bandwidth shown in Fig. 4.27.

4.3.3 Radar Module Integrated with The Dual-Band Dual-Focus Metasurface

As shown in Fig. 4.26, the Infineon BGT60TR13C radar, operating within a frequency range of 58 to 63 GHz, includes four on-chip antennas, one functioning as the transmitter and the others as receivers [224]. The radar antenna surface is placed at an average distance of 2.5 mm, accounting for variations in phase center location across frequencies [106]. Although the antenna phase center shifts with frequency, this dual-band design

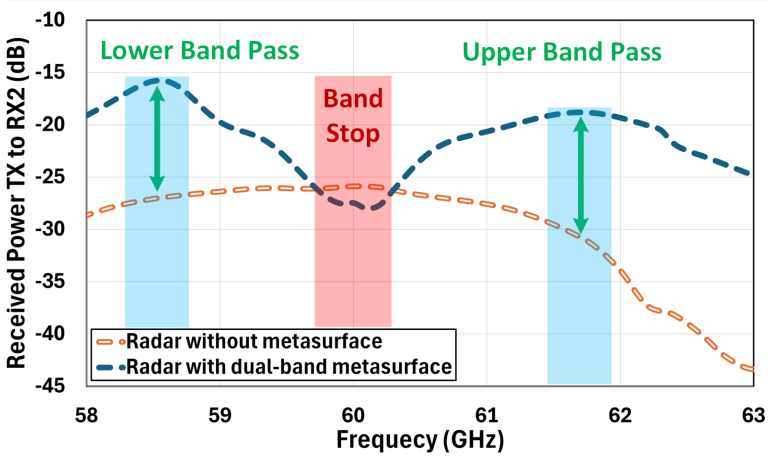
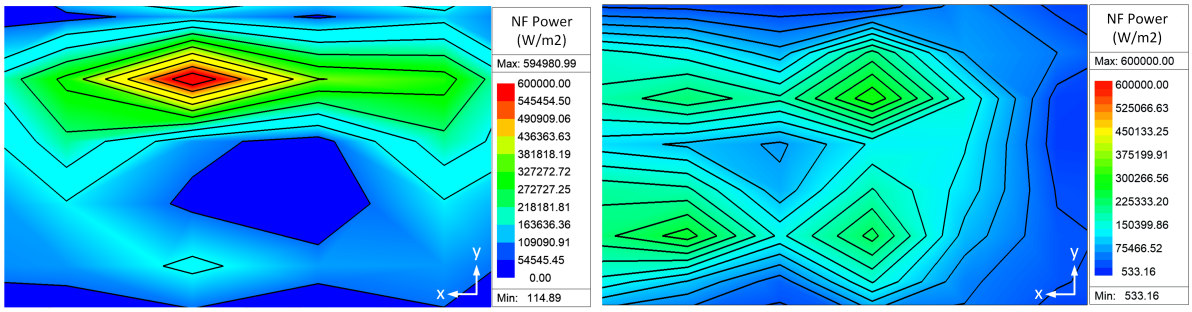


Figure 4.31: S-parameters analysis of the radar received power from TX to RX2, with and without the dual-band metasurface.

approximates the phase center at 60 GHz, introducing a minor phase error loss at both targeted frequency bands.

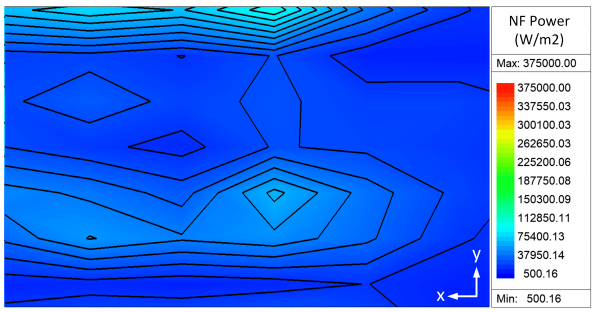
Fig. 4.31 displays the received power at the radar antenna receiver, which captures data from within the skin medium following excitation by the TX antenna, and compares the S-parameters (S_{21}, TX to RX2) for the radar module with and without the integrated dual-band metasurface. The results clearly demonstrate the dual-band metasurface's effectiveness in enabling two distinct frequency bands within the radar spectrum. Specifically, the metasurface increases the received power level by 11 dB at 58.5 GHz and 12.7 dB at 61.7 GHz, while significantly suppressing power at 60 GHz by 11.7 dB relative to the highest peak.

After analyzing the dual-band capability of the designed metasurface, another objective of this research is to control each frequency band to focus transmitted power and capture data from distinct locations within the human skin. Fig. 4.32a to Fig. 4.32f present the 2D contour plots of the power density radiated by the TX radar antenna integrated with the designed metasurface, positioned on a plane parallel to the array at a distance of 2 mm, at the frequency range of 58.5 GHz to 63 GHz. As shown in Fig. 4.32a and 4.32e, the focus points within the human skin are symmetrically distributed along x-axis as designed for ±20 degrees; however, focus tilting is also observed along the y-axis. This effect arises because the radar TX antenna is not centrally positioned relative to the array, disrupting the symmetry assumed in the phase synthesis analysis and leading to deviations in the assigned near-field focal points. Compared to the near-field Poynting power generated

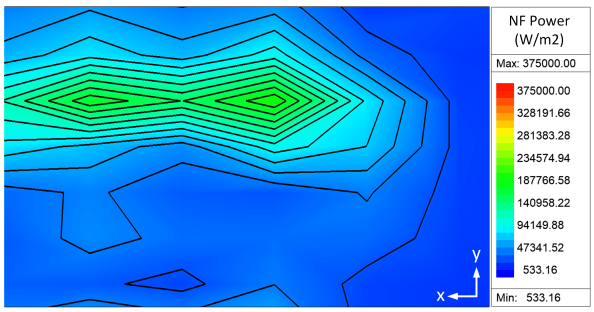


(a)

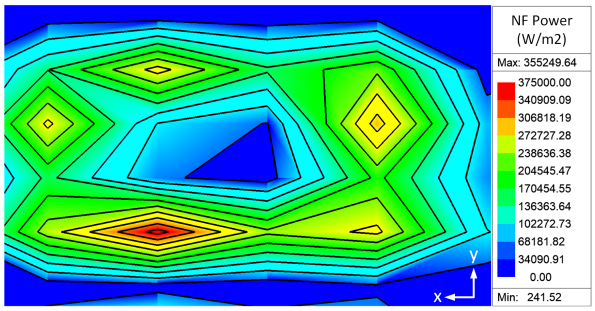
(b)



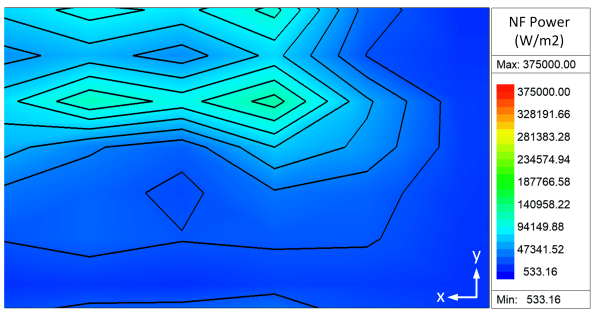
(c)



(d)



(e)



(f)

Figure 4.32: 2D contour plots of near-field power density 2 mm inside the skin model for the dual-band metasurface-enhanced radar system's TX antenna at (a) 58.5 GHz, (b) 59 GHz, (c) 60 GHz, (d) 61 GHz, (e) 62 GHz, and (f) 63 GHz

by the radar TX antenna without the metasurface, which is measured at 20,065 W/m^2 [194], the designed metasurface significantly enhances power absorption within the skin medium, achieving 594,980 W/m^2 at 58.5 GHz, a 14.7 dB improvement (Fig. 4.32a), and 355,249 W/m^2 at 62 GHz, corresponding to a 12.4 dB near-field power enhancement (Fig. 4.32e). By examining deeper penetration into human skin, it is observed that the power enhancement level at 58.5 GHz reaches 12.2 dB at a depth of 2.1 mm, while maintaining the same focal point location. Conversely, at 61.7-62 GHz, deeper penetration results in lower power density and a more dispersed focus over the surface. This aligns with the concept of greater penetration at lower frequencies. It is noteworthy that the proposed analysis in this research study not only enhances the absorbed and received power at two distinct frequencies but also provides two approximately symmetrical focal points within human skin, as depicted in Fig. 4.32, to capture data from different locations.

4.3.4 Sensitivity Analysis in Dual-Band Metasurface

Given the metallic composition of the metasurface in this section, a thorough sensitivity analysis with respect to various parameter changes is essential, as outlined in the following.

Impact of Frequency-Dependent Skin Properties on Dual-Band Response

It is well established that the electromagnetic properties of human skin vary with frequency, with a relative permittivity of $\epsilon_r = 8.09$ and conductivity $\sigma = 36.3$ S/m at 59 GHz, and $\epsilon_r = 7.86$ and $\sigma = 36.5$ S/m at 61 GHz [194]. However, for the purpose of dual-band operation, the unitcell design and optimization were conducted using the skin properties corresponding to the midpoint frequency of 60 GHz, enabling simultaneous analysis across both bands. The sensitivity analysis presented here evaluates the performance of the designed unitcell when subject to the actual skin parameters at each operational frequency, highlighting its robustness and adaptability across the dual-band range.

As shown in Fig. 4.33, variations in skin properties at 59 GHz and 61 GHz result in a nearly equal frequency shift for both bands. This is expected, as the dual-band unitcell was originally designed based on the dielectric properties of skin at 60 GHz. Since the frequency bands shift together, either upward or downward, their relative separation remains unchanged. Importantly, this simultaneous shift does not degrade system performance, as both operating frequencies remain within the radar's functional bandwidth, ensuring continued dual-band operation without destructive interference.

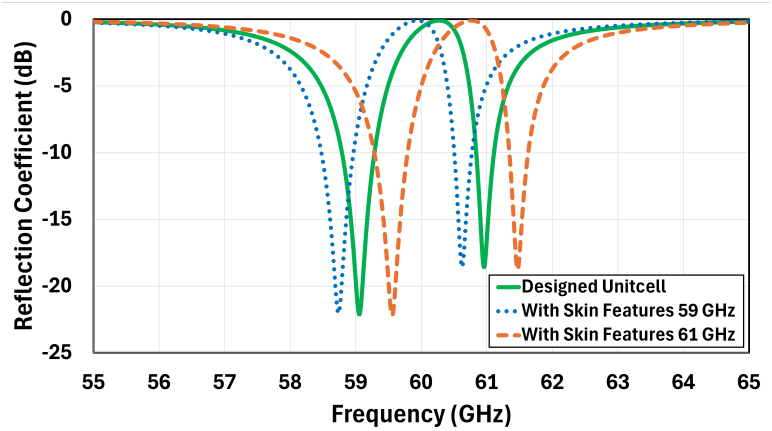


Figure 4.33: S-parameters analysis comparing the responses of the dual-band unitcell to frequency-dependent variations in human skin properties, highlighting the impact of dielectric changes at each operational band.

Metallic Layer Thickness

The fabrication process of this type of metasurface requires precisely cutting slot patterns into metallic copper layers using laser cutting technology. Unlike simulations, where the metal layers are often assumed to have zero thickness, this assumption becomes invalid during physical fabrication due to the finite thickness of the copper sheets. At mm-wave frequencies, where the operational wavelength is on the order of millimeters, even a small metal thickness becomes comparable to the wavelength and can significantly affect the metasurface performance. Therefore, selecting a copper layer with the smallest feasible thickness is ideal to minimize undesired phase or transmission distortions.

However, this introduces a practical trade-off; while thinner copper sheets reduce unwanted effects, they are also more susceptible to bending or deformation, compromising structural integrity. Our investigation revealed that commercially available copper sheets typically start at a thickness of 1 mm. Nonetheless, with proper handling and fabrication care, it is feasible to reduce the thickness to 0.3 mm, or even down to 0.1 mm, which provides a more optimal balance between performance and mechanical stability. In Fig. 4.34, the S-parameter response of the metasurface unitcell is analyzed for various copper thicknesses and compared against the idealized case of zero thickness. The results demonstrate that a copper thickness of 0.1 mm closely replicates the ideal behavior, making it a suitable choice for practical fabrication. This thickness strikes a favorable balance by maintaining accuracy in the response while remaining feasible with available manufacturing techniques.

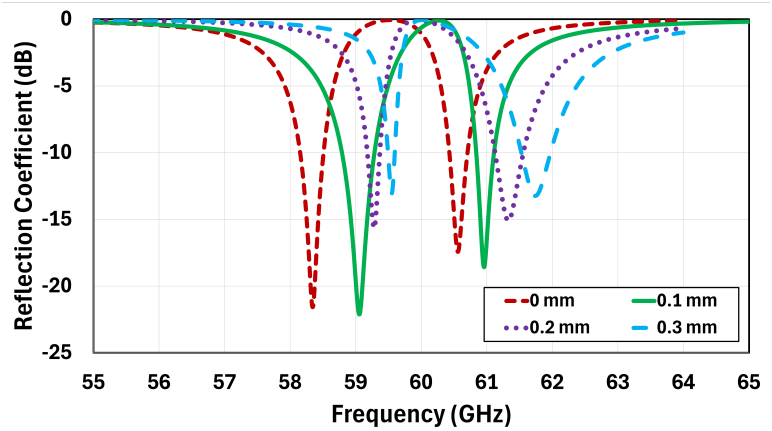


Figure 4.34: S-parameter analysis comparing the responses of the dual-band unitcell under varying metallic layer thicknesses, highlighting deviations from the ideal (zero-thickness) case.

Metallic Layers Surface Distortion

Another topic that holds particular importance in this thesis is the sensitivity of results to surface irregularities. This is especially relevant because the transmitarray antenna under study is entirely designed and fabricated on a thin metallic sheet, 0.1 mm of thickness. As a result of not using a thicker or more rigid metal layer, the structure is more susceptible to bending or warping, particularly under mechanical or thermal stress. Consequently, non-uniformities such as surface undulations may appear across the antenna aperture, as shown in Fig. 4.35.

One of the advantages of the transmitarray antenna is its reduced sensitivity to surface deformations compared to reflective array antennas, which are more affected by physical distortions due to the reliance on precise phase alignment of the reflected wavefront. This distinction has been validated mathematically and confirms the transmit array's suitability for robust applications. The sensitivity of the reflectarray to surface warping is considerably greater, since the signal path includes both the forward and reflected directions, amplifying the impact of any deviation. In contrast, the transmitarray allows the signal to pass through the aperture only once, significantly reducing the cumulative distortion caused by surface imperfections.

Using the existing phase relations between radiated waves in space, we calculate the distance that the waves travel from the feed antenna to the reference plane in both cases: with distortion and without distortion.

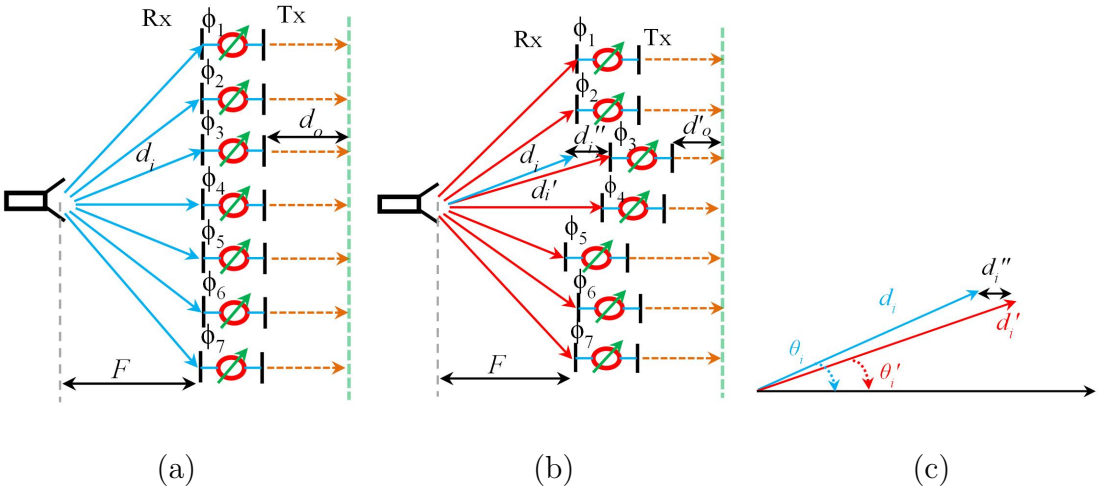


Figure 4.35: Illustration of wave interaction with the surface of a transmit array antenna: (a) without distortion, (b) with distortion, and (c) Vector representation of phase error caused by surface distortion.

According to Fig. 4.35a, the phase value ϕ_i of each element in the transmitting array can be calculated to produce a planar wavefront with constant phase on the reference plane, based on 4.15. In the presence of surface deformation, the amount of phase displacement for each element of the array changes accordingly, and remains constant in the absence of deformation. Based on Fig. 4.35a, the total phase path from the antenna feed to the reference plane is calculated using:

$$\Phi_R = k_0 d_i + \Phi_i + k_0 d_o \tag{4.15}$$

According to Fig. 4.35b, in the case where the surface of the transmitting array is deformed, the total phase path from the antenna feed to the wavefront on the reference plane, Φ'_R, is calculated as:

$$\Phi'_R = k_0 d'_i + \Phi_i + k_0 d'_o \tag{4.16}$$

The phase error between elements that have undergone surface deformation and a structure without surface deformation can be expressed using,

$$\Phi_{\text{Error}} = \Phi_R - \Phi'_R = k_0(d_i) - k_0 d'_i + k_0 d_o - k_0 d'_o \tag{4.17}$$

$$\Phi_{\text{Error}} = k_0(d_i) - k_0(d_i' - d_i'') \tag{4.18}$$

According to the deformation vector of the surface in Fig. 4.35c, the following relation can be used:

$$d_o' = d_o - d_i'' \tag{4.19}$$

d_i can also be substituted based on Fig. 4.35c using,

$$\theta' = \tan^{-1}\left(\frac{\sqrt{x_i^2 + y_i^2}}{F + d_i''}\right) \tag{4.20}$$

$$d_i' = \frac{F + d_i''}{\cos\theta'} \tag{4.21}$$

Therefore, the phase error can be expressed using the physical parameters of the transmitarray and by means of 4.22.

$$\Phi_{\text{Error}} = k_0\left(d_i - \frac{F + d_i''}{\cos\theta'} + d_i''\right) \tag{4.22}$$

In this equation, F is the focal distance of the transmitting array in the case where no surface deformation exists. Based on 4.22, for different values of surface deformation d_i'', the phase error for the transmitting arrays is calculated for an array with an focal length of 2.5 mm and an aperture size of $D = 3.2\lambda$. The results indicate that a surface deviation up to 1 mm in the transmitting metasurface can introduce a phase error of up to 50 degrees across the radiating array, degrading the system's performance.

Distance Between Metallic Layers

In the context of metasurfaces, which are constructed from subwavelength metallic or dielectric layers, the critical concern is not only surface curvature but also the uniformity of the distance between adjacent layers. Any slight variation in interlayer spacing due to fabrication tolerances, can adversely affect the resonant behavior and response of the unit cells. This includes unintended shifts in frequency response, errors in phase compensation, or degraded transmission and reflection efficiency. Therefore, even if a metasurface is

relatively flat macroscopically, maintaining consistent layer spacing on the microscopic scale is essential for ensuring reliable and high-performance operation, particularly in biomedical sensing where precision is paramount.

The variation in the air gap between the metallic layers, from 0.5 mm to 1 mm, demonstrates that both resonance frequencies remain within the radar's operational band, indicating robustness against small structural deviations. However, this variation influences the quality factor (Q-factor) of each band. Specifically, increasing or decreasing the air gap alters the electromagnetic coupling and energy confinement, leading to either broadening or narrowing of the resonance bandwidths. These effects arise due to partial violation of the half-wavelength resonance condition, which is critical in maintaining sharp and efficient frequency responses. Thus, while the design tolerates minor shifts in spacing without detuning the resonances, precise control over the air gap is necessary to preserve optimal performance.

Although the variation of the air gap between the metallic layers from 0.5 mm to 1 mm does not result in noticeable differences in the unit cell's reflection coefficient, it significantly affects the performance of the overall metasurface array in terms of near-field power focusing. This discrepancy arises because S11 alone does not fully capture the behavior of the metasurface; while it indicates the return loss at the unitcell level, it does not account for the phase response or the electromagnetic interactions among the elements within the full array. Near-field focusing is highly sensitive to the phase profile imposed across the aperture, and the air gap between layers directly influences the effective electrical length and inter-layer coupling. Increasing the gap can reduce capacitive coupling and may introduce leakage or diffraction effects, particularly in compact, high-frequency designs. At 60 GHz, where the free-space wavelength is approximately 5 mm, even sub-millimeter variations in structure can lead to significant phase distortions. These changes affect the coherence of the transmitted field, thereby degrading the radiation and reducing the focal intensity. The 0.5 mm gap, in this context, offers superior near-field performance by preserving phase alignment and ensuring constructive interference at the desired focal point.

Additionally, in this design, one of the three metasurface layers is in direct contact with the skin, while the other two reside in air. This introduces a medium mismatch between layers that complicates the behavior. Using identical structural layers across both skin-contact and air regions without proper compensation exacerbates the difficulty in defining a single optimal air gap distance. The electromagnetic properties differ significantly between skin and air, meaning the phase delay, impedance, and effective refractive index experienced by each layer are not uniform. This further underscores the importance of precise air gap tuning, as even a well-designed metasurface can suffer from performance degradation if

these inter-layer medium effects are not properly managed.

4.3.5 Fabrication Process and Measurement Results

The fabrication process of this type of metasurface requires precisely cutting slot patterns into metallic copper layers using laser cutting technology, and making an airgap with the assigned distance as optimized based on simulations. However, in simulations, where the metal layers are often assumed to have zero thickness, this assumption becomes invalid during physical fabrication due to the finite thickness of the copper sheets. At mm-wave frequencies, where the operational wavelength is on the order of millimeters, even a small metal thickness becomes comparable to the wavelength and can significantly affect the metasurface performance. Therefore, selecting a copper layer with the smallest feasible thickness is ideal to minimize undesired phase or transmission distortions.

However, this introduces a practical trade-off; while thinner copper sheets reduce unwanted effects, they are also more susceptible to bending or deformation, compromising structural integrity. Our investigation revealed that commercially available copper sheets typically start at a thickness of 1 mm. Nonetheless, with proper handling and fabrication care, it is feasible to reduce the thickness to 0.3 mm, or even down to 0.1 mm, which provides a more optimal balance between performance and mechanical stability.

As investigated in sensitivity analysis section, Fig. 4.34, the S-parameter response of the metasurface unitcell for various copper thicknesses demonstrate that a copper thickness of 0.1 mm closely replicates the ideal behavior, making it a suitable choice for practical fabrication, while maintaining the robustness of the structure. This thickness strikes a favorable balance by maintaining accuracy in the response while remaining feasible with available manufacturing techniques.

The prototype of the transmissive metasurface was fabricated to validate the simulation results and demonstrate practical feasibility. It features a 7×7 array of the proposed dual-band unit cells, forming an overall aperture size of $3.22\lambda \times 3.22\lambda$ at 60 GHz. Each unitcell was designed through a phase-synthesis process to deliver the phase shifts required to compensate for spatial delays between the radar TX antenna and the metasurface surface. This phase compensation ensures optimal constructive interference at the desired near-field focal points, thereby enhancing the electromagnetic power delivery into the targeted biological tissue. The array was assembled with high alignment accuracy to preserve the designed phase profile, making it suitable for experimental verification in biomedical near-field sensing applications.

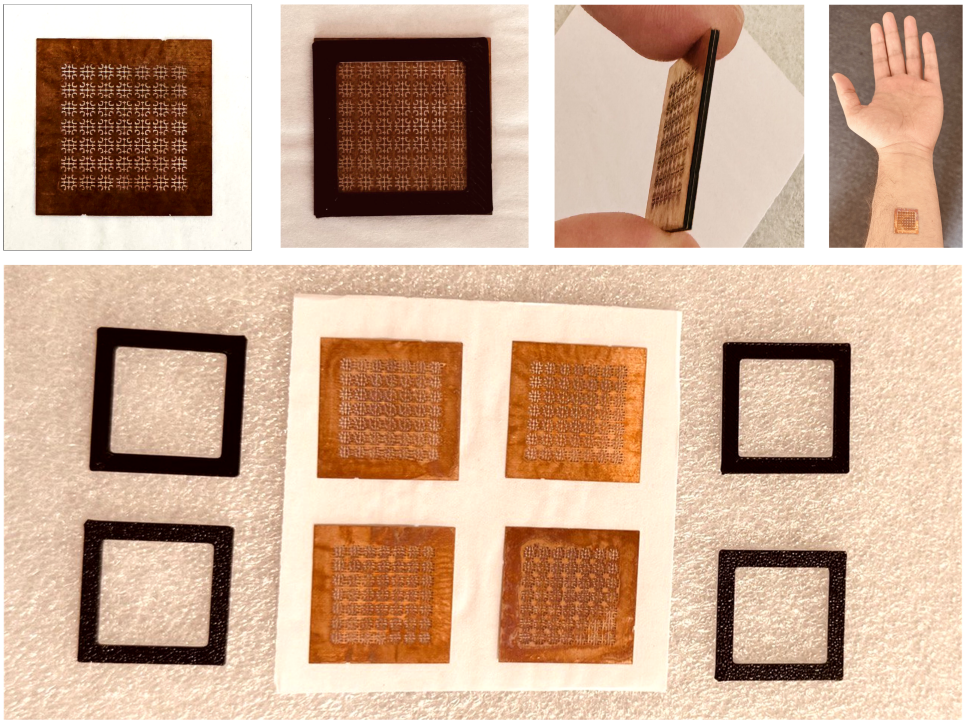


Figure 4.36: Prototype fabrication process of the triple-layer dual-band metasurface, consisting of 0.1 mm thick metallic sheets, assembled using a 3D-printed square frame with a 0.5 mm interlayer spacing. The final assembled structure is shown applied to a human hand for scale comparison, illustrating the compact form factor suitable for wearable biomedical applications.

Fig. 4.36 illustrates the step-by-step fabrication and assembly process of the proposed triple-layer dual-band metasurface designed for near-field biomedical sensing. The structure is composed of three patterned metallic layers, each fabricated from commercially available 0.1 mm thick copper sheets using precision laser cutting technology. These metallic layers are separated and supported by a 3D-printed square frame, engineered with a uniform interlayer spacing of 0.5 mm to maintain consistent air gaps, which are critical to the metasurface's electromagnetic response. The placement of such spacers in the structure does not have significant effects on the simulation results. The choice of materials and thickness balances electrical performance with mechanical stability, preventing deformation during handling and operation. The final assembled metasurface is compact and lightweight, making it well-suited for wearable or on-skin applications. As shown in the final panel, the metasurface is placed on a human hand, providing a clear visualization

of its physical dimensions and confirming its potential for integration in practical, non-invasive medical sensing scenarios. In comparison to PCB fabrication, this method supports low-cost prototyping and customization for future optimization or multi-frequency design iterations.

After completing the fabrication of the prototype metasurface, the structure was subjected to experimental validation using a near-field power measurement setup similar to the one described in Objective 1. A specialized millimeter-wave probe was employed to measure the transmitted power inside a skin-mimicking phantom contained in a Pyrex beaker. The goal of this experiment was to demonstrate the metasurface's ability to enhance power delivery within the phantom at two distinct focal points corresponding to the dual operational frequencies of 59 GHz and 62 GHz.

Two primary challenges were encountered during the measurement process. First, each frequency band requires a different set of dielectric properties, namely permittivity and conductivity, in the phantom to emulate realistic skin responses. This issue was managed by adjusting the water level inside the beaker, thereby tuning the effective dielectric properties of the liquid to suit each frequency. Second, the metasurface was designed to concentrate power into very small, tightly focused spots at different depths. Locating these exact spots manually within the phantom was extremely difficult, limiting the repeatability and spatial resolution of the current measurement approach. To address this challenge, future efforts may involve developing a 3D scanning system using a high-precision stepper motor to automate the scanning of the phantom volume and accurately map the focal points across a defined measurement grid. In the current study, a custom measurement fixture fabricated from low-cost 3D-printed materials was used to support the probe and guide measurements at different grid positions within the phantom. This setup enabled the spatial mapping of power levels to qualitatively validate the dual-focus capability of the metasurface, as shown in Fig. 4.37.

The screenshots from the Spectrum Analyzer provide a clear and detailed validation of the dual-band functionality of the metasurface-integrated radar system. In Fig. 4.38a, the left image displays a prominent transmission peak at 59 GHz with a measured power level of -43.94 dBm, while the right image shows a distinct peak at 62 GHz with a power level of -46.25 dBm. These two peaks clearly demonstrate the dual-band functionality of the metasurface, affirming that it supports independent and simultaneous operation at both frequency bands without mutual interference. The approximately 3 GHz frequency spacing between the bands illustrates strong spectral isolation, which minimizes cross-talk and interference. This behavior aligns well with the simulation results, reinforcing the validity of the design.

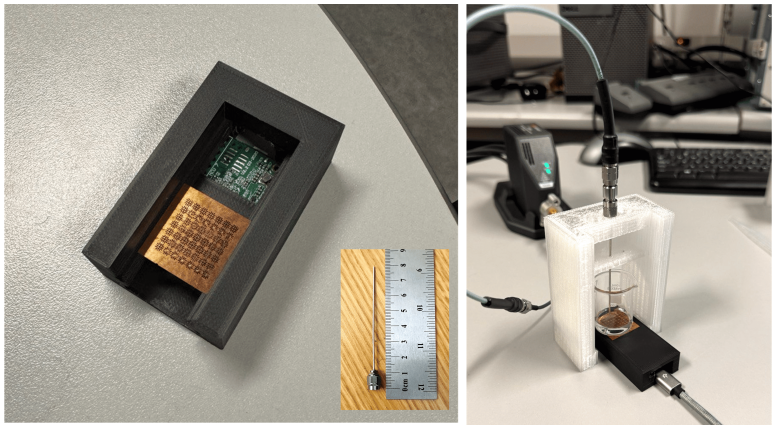
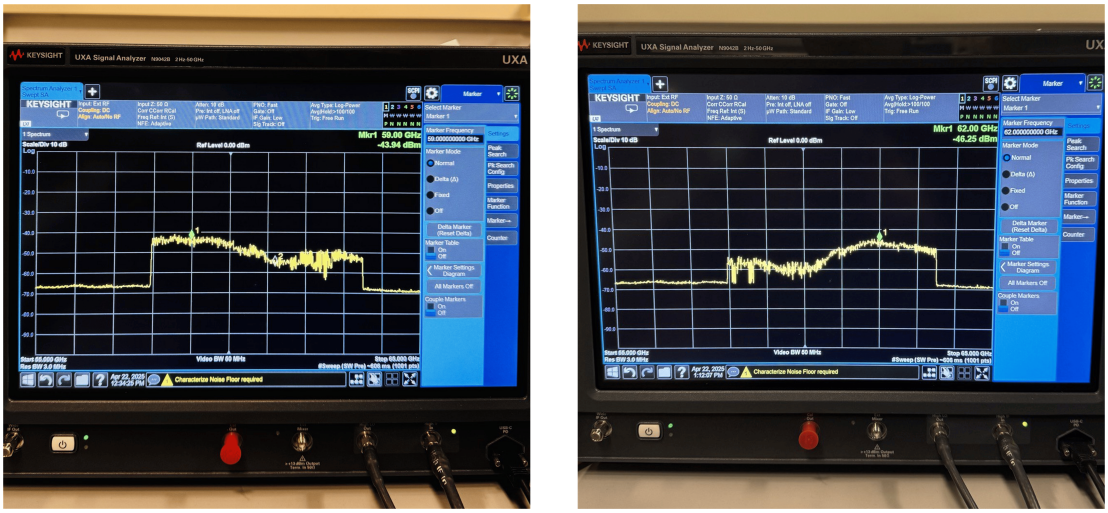


Figure 4.37: Measurement setup for validating transmitted power enhancement at dual frequencies and dual focal depths within the phantom using a dual-band metasurface-enhanced radar system.

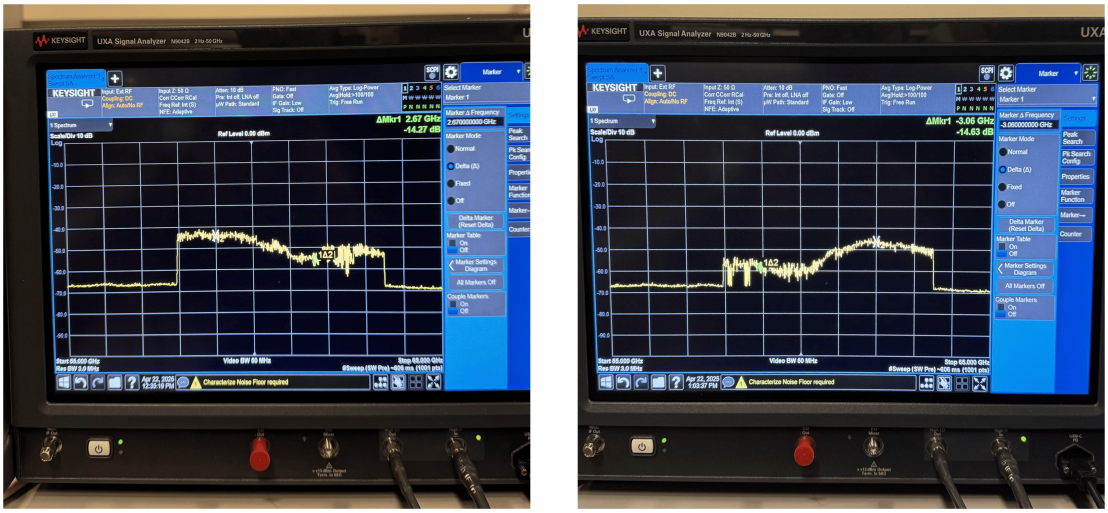
In Fig.4.38b, the left image shows a delta marker measurement between two signal peaks, highlighting a frequency span of 2.67 GHz with a power difference of approximately -14.27 dB, while the right image confirms a 3 GHz separation between the bands and a power difference of -14.63 dB. These measurements demonstrate not only the existence of two distinct operating bands but also their relatively strong isolation, which is crucial for avoiding signal distortion and ensuring independent focusing performance for multi-depth sensing.

Together, the presented measurement results are compiled in Fig. 4.39 to provide a clearer visualization and direct comparison with the radar-only baseline measurement within the phantom. This figure not only highlights the successful realization of the dual-band functionality of the metasurface but also illustrates the substantial enhancement in power focusing achieved at both operational frequencies. Compared to the radar-only configuration, the metasurface-integrated system shows a marked increase in transmitted power density at the target locations, validating the effectiveness of the dual-focus design for enhancing signal delivery into the phantom. These results confirm that the fabricated metasurface is capable of dual-frequency operation, with clean spectral separation. This ensures that each band can independently focus electromagnetic power at different tissue depths, enabling simultaneous monitoring of multi-layer physiological data, a critical feature for improving the accuracy and reliability of non-invasive biomedical sensing technologies such as glucose monitoring.

In conclusion, the developed metallic metasurface, featuring dual-band and indepen-



(a)



(b)

Figure 4.38: Screenshots of the spectrum analyzer display showing the dual-band response of transmitted power at two symmetrical off-axis locations within the phantom; (a) Shows distinct frequency peaks and corresponding power levels at 59 GHz and 62 GHz. (b) Illustrates the spectral isolation and independence between the two bands, confirming effective dual-band, dual-focus performance with minimal cross-band interference.

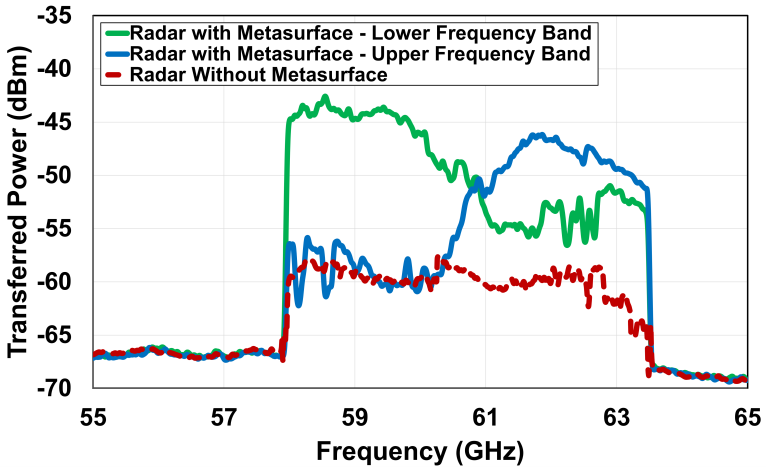


Figure 4.39: Measurement results of the transmitted power density within the phantom for the radar system integrated with and without the dual-band metasurface, demonstrating both dual-band operation and the enhancement in focused power delivery at target locations.

dently tunable dual-focusing capabilities, significantly enhances near-field sensing performance, an essential requirement for accurate biomedical applications. By enabling precise electromagnetic field localization at distinct depths and frequencies, this method addresses the limitations of single-band or single-focus systems. At the end of this section, a detailed comparison and informative analysis are presented to thoroughly emphasize the novelty and advantages of the proposed dual-band approach:

- **Near-Field Theory in Dual-Band Systems:** The dual-band metasurface presented in this work is developed using a design methodology specifically adapted to near-field electromagnetic theory, which is crucial for biomedical sensing applications. Unlike traditional approaches such as dual-beam antennas that primarily target far-field antenna performance, often irrelevant for body-proximate systems, this design accounts for complex near-field interactions. The novelty lies in simultaneously achieving precise phase synthesis and power focusing at two distinct frequencies, enabling the metasurface to interrogate different tissue depths within the human body.

- **Compactness:** This study introduces a planar, low-profile metasurface optimized for seamless integration with mm-wave radar modules. The key innovation lies in achieving dual-band operation within a significantly constrained form factor. While

dual-band metasurfaces typically require spatial separation between resonant elements to minimize mutual coupling, this design overcomes that limitation by employing interleaved metallic slot elements. These elements are designed to support both electric and magnetic dipole responses with minimal interaction, enabling dual-band functionality within a unitcell structure that remains below half the free-space wavelength in dimension.

- **Millimeter-Wave Operation:** The mm-wave frequency band is strategically selected in this study due to its inherent advantages for biomedical sensing, offering high spatial resolution, minimal ambient interference, and improved bio-compatibility. This study presents, for the first time, a dual-band metasurface explicitly designed for mm-wave operation in biomedical contexts. The metasurface is optimized to function within the 58–63 GHz range, enabling multi-depth focusing and signal enhancement for physiological monitoring. This dual-band capability at mm-wave frequencies marks a novel contribution, setting a foundation for next-generation non-invasive diagnostic tools.

- **Direct Human Skin Contact:** Direct contact with biological tissue introduces challenges such as impedance mismatch and frequency detuning, which significantly degrade sensing accuracy. Existing approaches often fail to accommodate these effects, rendering them unsuitable for real-world biomedical applications. In contrast, the dual-band metasurface proposed in this study is specifically engineered for direct skin contact.

- **Impedance Matching Layer:** Building upon the impedance-matching strategy established in Objective 1, the metasurface maintains stable performance in proximity to or in contact with human tissue. As illustrated in Fig. 4.10, the impedance matching graph of the metasurface shows a close alignment between the imaginary part of the surface impedance and that of the human skin at both 59 GHz and 62 GHz, the designated dual-band frequencies for this design. This close impedance correspondence confirms minimal reflection and efficient power transfer into the tissue, which is critical for accurate near-field sensing.

- **Intensify Near-field Transmitted Power:** The proposed dual-band metasurface significantly enhances the absorbed power density at two distinct focal depths within the human skin, enabling improved bio-sensing performance. When integrated with commercially available Infineon radar TX/RX antennas, the metallic slot metasurface achieves an increase in near-field Poynting power density of 14.7 dB at 59 GHz and 12.4 dB at 62 GHz. These results demonstrate the metasurface's effectiveness in

concentrating near-field energy at targeted tissue depths, thereby advancing the radar sensing.

- **Intensify Near-field Reflected Power:** Analysis of the radar's reflected signal reveals that the integration of the dual-band metasurface significantly enhances the received power, improving it by 11 dB at 59 GHz and 12.7 dB at 62 GHz. These enhancements directly translate into substantial improvements in the radar's SNR, achieving more than 12-fold and 18-fold increases at the respective frequencies. This amplified SNR enables more accurate and deeper bio-sensing capabilities.
- **Glucose Sensing Enhancement:** In glucose monitoring, metasurface-enhanced power measurements show a resolution of around 1.5 dB per 15 mg/ml sugar concentration, maintaining a high SNR and confirming enhanced functionality in glucose sensing.

4.4 Objective 4: Frequency-Scanning Multi-Focus Radar Sensing Using Multi-Band Metasurface

Biomedical radar, an emerging technology at the intersection of radar engineering and medical science, has become a pivotal tool with a wide range of clinical applications. Although still in the research and development phase, radar-based methods hold potential as non-invasive tools that could enhance current diagnostic techniques.

In Objective 3, the research advances toward multi-depth sensing by introducing a dual-band, dual-focus metasurface. This single metasurface is capable of producing two distinct focal points at two different frequencies, allowing simultaneous sensing at different tissue depths and locations. This dual-band functionality provides richer physiological information and marks an important transition from purely spatial distribution to frequency-selective depth control.

However, scaling this concept to more than two bands introduces significant design complexity and practical limitations in metasurface synthesis. In that case, multiple radar systems (MRS), as initially presented in objective 2, are recognized as an effective strategy, whereby the fusion and joint processing of measurements provide numerous benefits over a single radar system. As depicted in Fig. 4.40 and discussions in objective 2, biomedical multi-radar systems (BMRS) employ multiple radar units to gather data from different angles and positions, increasing the robustness and accuracy of the detected signals, as averaging measurements from various locations helps mitigate the impact of local physiological variations, including differences in skin thickness, tissue composition, and blood flow. Furthermore, by leveraging spatial diversity and the enhanced resolution that comes from processing multiple simultaneous data streams, BMRS can more effectively isolate the specific signatures that indicate changes in blood properties such as glucose levels, potentially revealing effects of diet, exercise, or medication that might not be evident from a single measurement location.

According to the literature, few efforts have been undertaken to monitor health conditions using biomedical multi-radar systems. In [233], a multi-radar system employing two 2.4 GHz DC coupled radar sensors for non-contact assessment of respiration patterns at both the chest and abdomen. The dual FMCW radar system presented in [234] monitors breathing patterns by detecting the displacements of both the chest and abdomen, which enhances the accuracy of breathing rate (BR) estimation and the detection of breath-hold periods. Furthermore, in [43], a chest-wearable 60 GHz radar system is presented for accurate, continuous monitoring of cardiorespiratory displacement waveforms, respiratory rate, heart rate, and HR variability. The system's multi-radar configuration enhances spatial

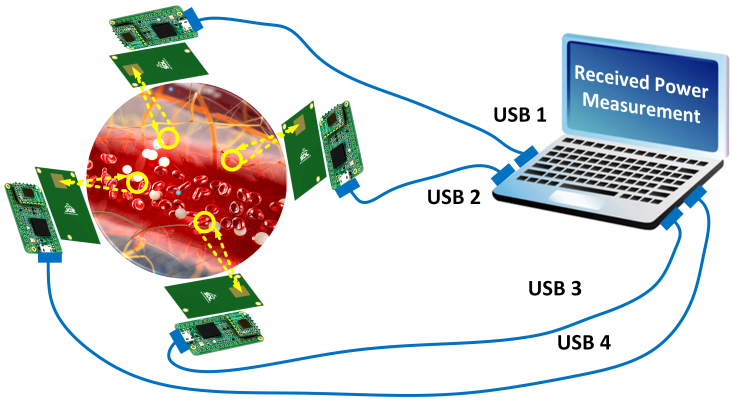


Figure 4.40: Metasurface-enhanced multi-radar near-field system.

resolution, enabling precise detection of subtle chest movements related to cardiac and respiratory functions. The multi-radar systems represent an emerging approach aimed at overcoming the limitations of conventional non-invasive methods, which frequently fall short in accurately capturing the dynamic signal patterns associated with changes in human blood properties [194].

The selection of an optimal microwave frequency range for radar-based bio-sensing applications is governed by several crucial factors, including the required tissue penetration depth and the specific resolution needs of the diagnostic application [226]. Employing a spectrum of frequencies in bio-sensing not only exploits their diverse penetration depths and resolution capabilities but also leverages the distinct ways each frequency interacts with different tissue components. As a result, unlike Objective 2, where identical metasurfaces are used across all radars, the new strategy should leverage frequency diversity by tailoring the metasurface response for each radar's specific operating band. This enables simultaneous multi-location and multi-depth sensing, offering an advanced solution for capturing layered physiological data from different regions of the body.

As we presented in [235], Objective 4 proposes an alternative methodology for enhancing mm-wave radar near-field sensing by introducing a multi-radar near-field frequency-scanning system that utilizes a multi-band non-interleaved metasurface for improved bio-sensing capabilities. Specifically, each radar within the system is integrated with a planar transmissive metasurface, which is uniquely designed for distinct frequencies within the operational frequency range of 58 to 63 GHz. These metasurfaces are integrated with on-chip antennas and are in direct contact with a human skin model. This approach is particularly adept at detecting changes in glucose levels through the extensive surface of

the skin. By capitalizing these targeted frequencies, the system can better penetrate and interact with skin tissues, providing more reliable and precise glucose monitoring, which is crucial for managing conditions such as diabetes.

Multi-radar sensing significantly enhances accuracy and sensitivity in non-invasive, real-time wearable health monitoring. This system gathering data from multiple points to enhance detection capabilities. The methodology utilizes discrete zones of a transmissive metasurface, each composed of phase-synthesized arrays. These zones serve as low-profile impedance matching networks, optimized for specific frequencies within the millimeter-wave radar range, thereby increasing efficiency through higher absorbed power density at different frequencies, which also enables varied penetration depths into human skin. Analysis using a customized phantom, closely resembling human skin, demonstrates significant increases in near-field absorbed power density.

This progression from a single-band, single-location system to a fully distributed, multi-frequency platform highlights the thesis's core contribution: developing flexible, metasurface-enhanced radar sensing strategies that address the spatial and depth-related challenges of biomedical monitoring.

4.4.1 Multi-Radar System for Distributed Human Skin Scanning

The preliminary method presented, which utilizes metasurface-enhanced radar for near-field sensing as reported in [120, 194, 224], is notable for its potential in real-time, non-invasive glucose monitoring. It is crucial to acknowledge that this technique achieves a stable focus within the human body's skin layers. For effective detection and to enhance diagnostic accuracy, it is imperative to perform scans across specific regions of the human skin. This research demonstrates the effectiveness of the mechanical scanning approach for near-field sensing. To advance the feasibility of this work and facilitate real-life implementation, the presented scanning approach could be executed using multiple radar systems on the human body skin, with both the transmitter and receiver antennas positioned closely on the same surface without necessitating movement. This method is akin to the principle employed by Inverse Synthetic Aperture Radars (ISAR), where the object itself is moved during the scanning process [236].

This study, employing transmitarray theory [106], utilizes the commercially available Infineon BGT60TR13C radar chipset, which serves as the feed for the transmitarray, operating within a frequency range of 58 to 63 GHz. To achieve higher accuracy, an efficiently designed near-field-focused metasurface, regarded as a transmissive phase-synthesized array and detailed in objective 1 [194], can be implemented at various operational frequencies

and integrated with each radar module, as demonstrated in Fig. 4.40. This integration leads to the creation of a biomedical multi-radar system, which is capable of significantly increasing the near-field power density into the body, that is achieved without disturbing the antenna impedance matching, while simultaneously improving radar sensing capabilities by enhancing the amount of power reflected from the body back into the RX antenna. As a result, each radar system experiences a boost in the signal-to-noise ratio, significantly improving the performance of the overall system.

Fig. 4.40 shows that each radar module in the metasurface-enhanced multi-radar system is fully synchronized by connecting to a distinct USB COM port on a laptop, enabling simultaneous data capture from different locations within the radar's operational frequency range. The metasurface functions as a frequency selective surface, controlling the specific frequency range for each radar module. This setup is crucial because restricting the radar's frequency range to a single frequency during signal processing would necessitate a significant reduction in bandwidth, potentially degrading radar range resolution and affecting the accuracy of the Doppler frequency shift measurements. This arrangement allows for the collection of health data at various penetration depths, thanks to the involvement of diverse frequencies.

When discussing whether each radar system should utilize multi-band metasurfaces or allocate specific frequency bands to individual radars using non-interleaved metasurfaces, it is crucial to consider the benefits of adhering to FCC-regulated, designated 500 MHz bands within the 60 GHz range for mm-wave FMCW radars [237]. Operating within these specified segments, rather than across the entire 5 GHz bandwidth, greatly enhances spectrum efficiency and reduces interference in this densely populated band. This focused approach not only boosts radar performance through tailored optimization for specific frequencies but also simplifies regulatory compliance and device design.

Fig. 4.41 illustrates the arrangement of the presented biomedical multi-radar sensing system around the human wrist, designed to enhance the accuracy of non-invasive glucose monitoring compared to systems using a single radar enhanced by a near-field metasurface [194]. This configuration allows for space scanning without the need to physically move the entire system. The design strategy involves using as many chipsets as necessary to perform comprehensive sensing tasks. With this system, users no longer need to concern themselves with the limitations of a single radar or a fixed placement for regular glucose monitoring, as the BMRS addresses these challenges by enabling more flexible and reliable measurements.

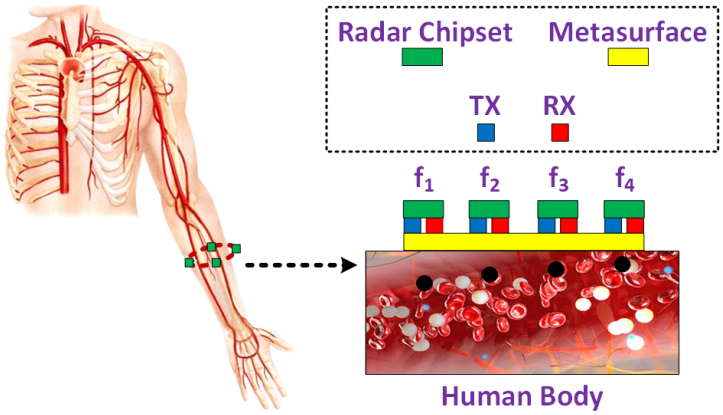


Figure 4.41: Configuration of the metasurface-enhanced multi-radar near-field scanning system, designed as a wearable wristband for easy and continuous real-time glucose monitoring on the human body.

4.4.2 Multi-Band Non-Interleaved Metasurface Design for Multi-Focus Bio-Sensing

In non-invasive glucose monitoring using radar technology, the variation in human body shapes and compositions necessitates the use of radars covering different frequency bands. This approach allows for tailored interactions with diverse tissue types and depths, enhancing the accuracy and effectiveness of monitoring. Different frequencies provide varying penetration depths and resolutions, critical for adapting to individual physiological differences such as varying levels of body fat or muscle.

The optimization process in this study aims to enhance efficiency across the entire frequency range by incorporating the specific dielectric properties of human skin, which vary in response to different frequencies, and conducting a targeted phase-synthesis array analysis for each frequency to reduce phase error losses. As a result, the multi-band non-interleaved metasurface effectively increases the impedance matching between air and human skin at each frequency within the radar range, thereby improving power absorption levels within the skin at each specific frequency.

To advance the functionality of multi-band metasurface-enhanced radar systems for biomedical applications, this section presents two successive design strategies that build upon the foundational work established in Objectives 1 and 2. The first focuses on extending the baseline metasurface unitcell design by adapting its frequency characteristics and scaling the array for enhanced near-field focusing. This provides a practical path-

way for reconfiguring the original design for new operational requirements while preserving its low-profile, skin-matched characteristics. The second section introduces structural enhancements to the unitcell, enabling more advanced functionalities such as improved phase compensation, deeper power focusing, and better control over multi-depth bio-sensing. Together, these designs mark a critical step toward developing flexible and scalable metasurface arrays tailored to the diverse physiological and electromagnetic requirements of real-world biomedical sensing.

Metasurface Unitcell and Array Design: Baseline Structure

In this section, a straightforward initial approach would be to reuse the metasurface design presented in Objective 1, featuring a 7×7 array of elements centered at 60 GHz, and simply modify the center frequency by adjusting the dimensions of the printed crossed-dipole structure. While this method offers certain advantages as a preliminary step, it has inherent limitations. To significantly enhance the sensing performance, the design can be further optimized to improve its phase compensation capability, specifically, by extending the achievable phase range to cover more than 300 degrees. This enhancement would allow for a higher number of array elements, which in turn results in more concentrated focusing and increased reflected power. Consequently, this approach enables improved SNR and higher sensing accuracy, particularly in demanding biomedical applications.

A partial section of the metasurface array, including its square unitcell referenced in [194], is designed to operate at specific frequencies in the radar range from 58 to 63 GHz with 1 GHz increments and is integrated with Infineon BGT60TR13C radar antennas, as depicted in Fig. 4.42. A full-wave simulator is used to evaluate the impedance matching of the unitcell at the proposed frequencies, utilizing Floquet port analysis for the infinite array design. For biomedical applications, the human body skin is modeled as a dielectric slab that contacts the metasurface unitcell directly, without any air gaps. The simulation takes into account the actual characteristics of human body skin, permittivity and conductivity, at their respective frequencies, as detailed in Table 4.1 [201]. The dimensions of the designated unitcell on a substrate with ϵ_r=2.7 and thickness of 1.25 mm, for operating at each frequency band in direct contact with a human skin model are specified as follows: at 58 GHz, $W_s = 1.5$, $L_s = 0.8$, $S_s = 0.2$ mm, at 59 GHz, $W_s = 1.2$, $L_s = 0.8$, $S_s = 0.2$ mm, at 60 GHz, $W_s = 1.1$, $L_s = 0.65$, $S_s = 0.2$ mm, at 61 GHz, $W_s = 0.97$, $L_s = 0.65$, $S_s = 0.2$ mm, at 62 GHz, $W_s = 0.75$, $L_s = 0$, $S_s = 0.1$ mm, at 63 GHz, $W_s = 0.715$, $L_s = 0$, $S_s = 0.1$ mm.

Fig. 4.43 illustrates the reflection coefficient analysis of the designed unitcells at distinct frequencies ranging from 58 to 63 GHz, when in direct contact with the human body

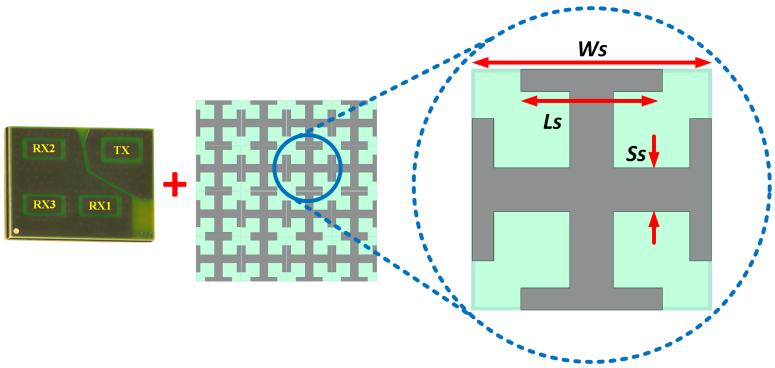


Figure 4.42: General configuration of the mm-wave Infineon radar system with one transmitter and three receiver antennas, incorporating a metasurface in direct contact with a skin model and optimized for specific frequencies within the radar's frequency range from 58 to 63 GHz.

Table 4.1: Variations in the dielectric properties of the human body's skin model in response to different frequencies within the radar range of 58 to 63 GHz.

Frequency (GHz)	Permittivity	Conductivity (S/m)
58	8.21	36.1
59	8.09	36.3
60	7.98	36.4
61	7.86	36.5
62	7.76	36.7
63	7.65	36.8

skin medium, taking into account the characteristics listed in Table 4.1. As depicted in Fig. 4.43, each unitcell achieves an appropriate reflection coefficient at the air-skin interface, demonstrating effective impedance matching when operating in contact with the skin medium, rather than in free space.

To produce the desired beam shape on the opposite side of the metasurface layer in a specific near-field location, each unitcell is designed to introduce a specific phase shift to the incident electric field, while maintaining the magnitude at a level close to the maximum. The expanded phase shift for a multi-radar, multi-band system accounts for the unique operational characteristics of each radar unit across various frequency bands,

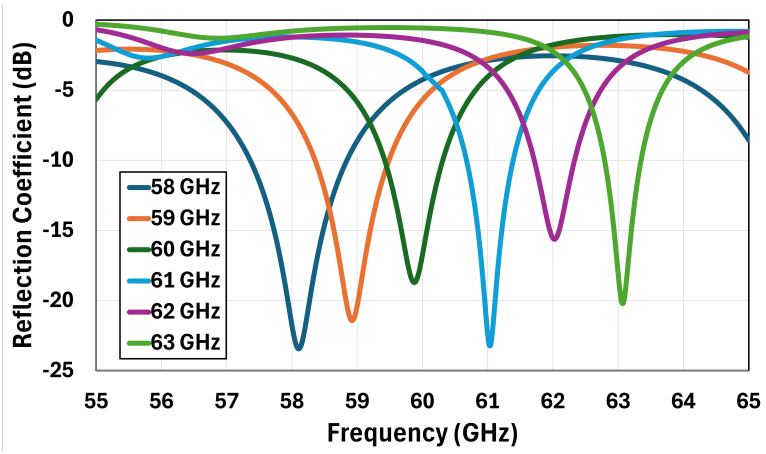


Figure 4.43: Investigation of the reflection coefficient (S11) for the proposed unitcells at their respective frequencies.

$$\phi_{mn}^{ij} = k_1^{ij}\left(\sqrt{x_{mi}^2 + y_{ni}^2 + r_{1ij}^2} - r_{1ij}\right) + \mathrm{Re}(k_2^{ij})\left(\sqrt{x_{mi}^2 + y_{ni}^2 + r_{2ij}^2} - r_{2ij}\right) + \phi_{0ij} \quad (4.23)$$

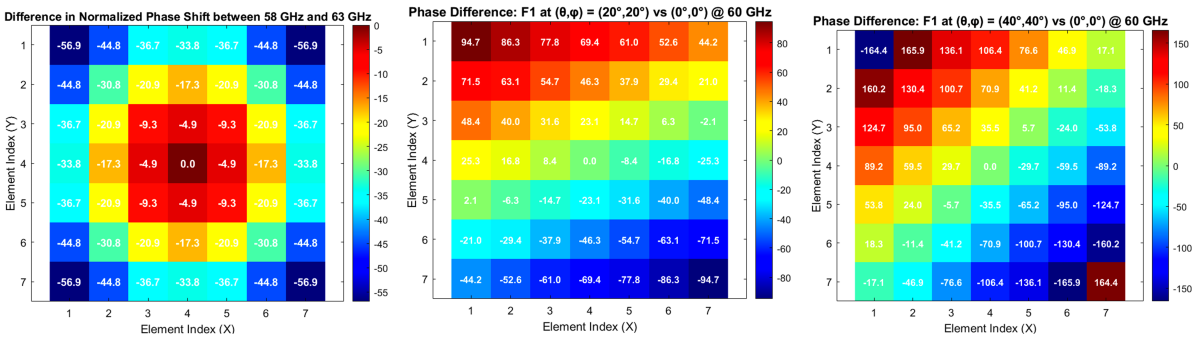
- x_{mi} and y_{ni} denote the coordinates of the (m, n)-th element in the i-th radar's array.
- r_{1ij} is the distance from the array center to the focal point in medium 1.
- r_{2ij} is the distance to a second focal point in medium 2, human skin model.
- $k_1^{ij} = \frac{2\pi}{\lambda_{1ij}} = \frac{2\pi f_{ij}}{c}$ is the wavenumber in medium 1.
- $k_2^{ij} = \frac{2\pi f_{ij}}{c}\sqrt{\varepsilon_{r2ij} - j\frac{\sigma_{2ij}}{\omega_{ij}\varepsilon_0}}$ is the complex wavenumber in medium 2, where:
  - ε_{r2ij} is the relative permittivity of skin medium,
  - σ_{2ij} is the electrical conductivity of skin medium,
  - $\omega_{ij} = 2\pi f_{ij}$ is the angular frequency,
  - ε_0 is the vacuum permittivity.
- $\mathrm{Re}(k_2^{ij})$ extracts the phase propagation component, discarding attenuation.
- ϕ_{0ij} is the initial phase value related to the central cell.

where each radar i and its corresponding frequency band j are considered independently. For every element, the required electric field phase shift, ϕ_{mn}^{ij}, is determined to ensure that all element contributions coherently align in phase at the near-field focal point $F = (0, 0, r_{ij})$, positioned along the normal to the array plane [194]. The variable λ_{ij} denotes the wavelength associated with the j-th frequency band of the i-th radar, reflecting the system's ability to operate across multiple frequencies. The coordinates x_{mi} and y_{ni} define the spatial location of the (m, n)-th element within the i-th radar's array. Additionally, ϕ_{0ij}, the initial phase for each radar-band pair, accounts for calibration offsets or inherent system variations.

The dimensions of the array unitcells are determined by calculating the required phase delay compensation for the electric field at the target frequency, using (4.23) at the planar aperture at the metasurface's location. This enables an equal-phase superposition of the propagated fields at the focal point in the near-field region, allowing the system to operate effectively across various locations and frequencies on skin. Using (4.23), the required E-field phase compensation ranges at the aperture, assumed to be at the metasurface location with ($r_{0ij} = 2.5\,\text{mm}$), are determined. The phase shift necessary for each metasurface, which utilizes a (7×7) array of unitcells, is considered for six distinct frequencies of 58, 59, 60, 61, 62, and 63 GHz.

Considering the other parameters in (4.23) fixed, the required phase shift varies directly with frequency. When a wideband radar antenna is used, the phase difference between the first and last frequency bands becomes significant, resulting in high phase error loss and reducing the radar sensing efficiency at these frequencies. In the structure presented in [194], the radar module antennas operate across a wide frequency range of 58 to 63 GHz; however, the near-field-focused metasurface is optimized for operation at a single frequency. After applying phase synthesis analysis on the metasurface array, the phase-shift difference between the required values at 58 GHz and 63 GHz is approximately 17°, as shown in Fig. 4.44a. In addition, it should be noted that the analysis above assumes the feed location is aligned with the center of the array. However, in most practical cases, such as with the Infineon BGT60TR13C radar antennas, the TX antenna is positioned at the corner and illuminates the metasurface at an offset angle, resulting in oblique incident waves. This offset causes a significant increase in the phase difference. As shown in Fig. 4.44b, a 20 degrees offset results in a 57° phase difference. As shown in Fig. 4.44c, a 40 degrees offset further increases the phase difference to approximately 165° between the required phase shifts across the 58 to 63 GHz frequency range, when using a 7×7 array.

To reduce the phase error, this work introduces a triple bio-sensing radar system integrated with a multi-band, non-interleaved metasurface, as illustrated in Fig. 4.45a. The optional frequencies of 58, 60, and 61 GHz are chosen to assess the metasurface's capability

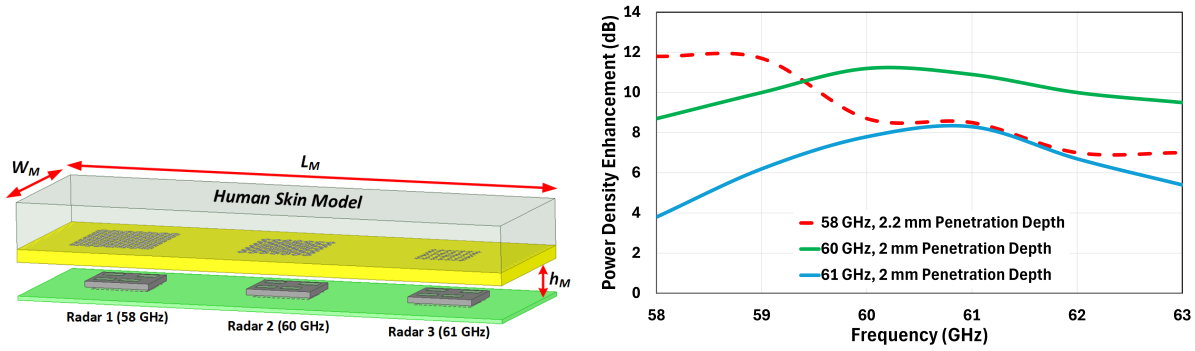


(a) (b) (c)

Figure 4.44: Phase shift differences required for mapping the 7×7 metasurface array using the designed metasurface between 58 and 63 GHz: (a) when the feed is aligned with the center of the array, and (b) when the feed is located at a 20 degrees offset, (c) (b) when the feed is located at a 40 degrees offset.

to enhance the power density level within human skin at different frequencies. As shown in Fig. 4.45b, the 60 GHz metasurface can increase the power density at a 2 mm penetration depth by 11.5 dB, with performance decreasing at both lower and higher frequencies. Decreasing the frequency to 58 GHz and using a metasurface specifically designed for this frequency increases the penetration depth as expected. At the same measurement point as the 60 GHz metasurface, the 58 GHz metasurface provides a maximum power enhancement of 11.8 dB, at a penetration depth of 2.2 mm. This analysis shows that using the 58 GHz metasurface not only increases the power density inside human skin but also increases the penetration depth. Furthermore, utilizing the 61 GHz metasurface results in a maximum power enhancement of 8.3 dB at a penetration depth of 2 mm. As expected, at 61 GHz, the power density is higher at shallower depths, so at the same depth level as the 60 GHz metasurface, it provides lower power enhancement. This analysis highlights the potential of using variable frequencies to target multiple skin sites, significantly enhancing the detection of blood glucose variations and the identification of physiological parameters by providing more comprehensive data.

It is important to note that the metasurfaces operating at the three selected frequencies do not have the same aperture size, which impacts the results. As the number of elements increases, it is crucial to enhance the phase-shift capability of the metasurface unitcells, ideally achieving a full 360° phase compensation. Failure to provide sufficient phase-shift compensation leads to phase errors, which can diminish the power enhancement.



(a) (b)

Figure 4.45: (a) The multi-bio-sensing radar system integrated with a multi-band non-interleaved metasurface, (b) Enhancement of power density within the human skin model, investigated across various penetration depths and operational frequencies.

To address traditional variabilities among humans and how they use wearables, this research introduces a multi-radar near-field sensing system enhanced with a multi-band non-interleaved metasurface, significantly improving non-invasive health monitoring. The system utilizes commercial off-the-shelf radar units with on-chip antennas, with the metasurface being used to optimize power absorption and tissue penetration across different frequencies, enabling low-cost and high-sensitivity detection of physiological parameters. This approach lays the groundwork for future advancements in wearable healthcare devices and continuous health monitoring, offering a scalable and adaptable solution for personalized diagnostics.

Metasurface Unitcell and Array Design: Structural Enhancements

This section advances the baseline metasurface design introduced earlier by addressing key limitations in phase compensation, focal depth control, and array scalability for enhanced bio-sensing performance. While the previous section focuses on adapting the original 7×7 unitcell array for frequency-scanning application, this section introduces two significant innovations that elevate the metasurface's capabilities:

First, the array is expanded from a 7×7 to a 9×9 configuration, which increases the aperture size and, consequently, improves spatial resolution and power focusing at greater depths within biological tissue. However, this increase also introduces a critical design

challenge, achieving broader phase compensation across a larger array. To address this, the metasurface architecture is enhanced by increasing the number of stacked layers from two to three, allowing a higher cumulative phase shift necessary to achieve a phase range exceeding 300°, which is essential for precise near-field focusing in large-aperture arrays.

Second, rather than merely stacking identical layers to generate the required phase gradient, this design incorporates a uniplanar compact photonic bandgap (UC-PBG) microstrip layer as the intermediate layer. The two metasurface designs may behave differently when integrated into a broader system, such as a radar, antenna array, or sensor. The UC-PBG-enhanced design is likely to yield improved system performance due to reduced mutual coupling between layers, better isolation, and sharper filtering characteristics. In [238], the UC-PBG structure is strategically positioned between two annular slot resonators, serving both as a coupling interface and as an additional resonant element. This configuration transforms the metasurface from a two-resonator system into a three-resonator network (slot–UC-PBG–slot), significantly broadening the phase tuning range. As demonstrated through their equivalent circuit analysis, the UC-PBG layer introduces a series-parallel resonance that enables full 360° phase compensation using only two dielectric layers, thus avoiding the need for additional structural thickness. By introducing a resonance in close proximity to that of the slot, the UC-PBG enables fine phase control, achieving both a wide phase range and a relatively flat transmission response.

In addition, replacing the middle layer with a UC-PBG structure can also influence the angular stability of the metasurface. This results in more consistent performance regardless of the wave's angle or polarization state. In addition, during phase synthesis analysis, each element of the metasurface array must be designed to exhibit a distinct phase shift to form the desired focusing pattern. Typically, this requires altering the physical dimensions, such as the lengths of the printed dipoles, which unintentionally shifts the resonance frequency and degrades performance at the target frequency. By introducing a UC-PBG layer, a secondary resonance is created in close proximity to the primary resonance, effectively stabilizing the frequency response even when the dipole dimensions are varied.

In metasurface design, utilizing a thinner substrate often results in higher near-field focus power, and this improvement can be attributed to several interrelated factors. First, thinner substrates help reduce dielectric losses. At high frequencies, such as those in the millimeter-wave range, thicker dielectric materials tend to absorb more energy due to increased interaction with the lossy medium. A thinner substrate, by contrast, minimizes the volume of material that the electromagnetic wave passes through, thereby preserving more of the transmitted energy and enhancing the intensity of the focused power within the desired region. Second, a thinner substrate imposes less dielectric loading. Loading in thicker substrates slows down the propagation of waves, resulting in increased scatter-

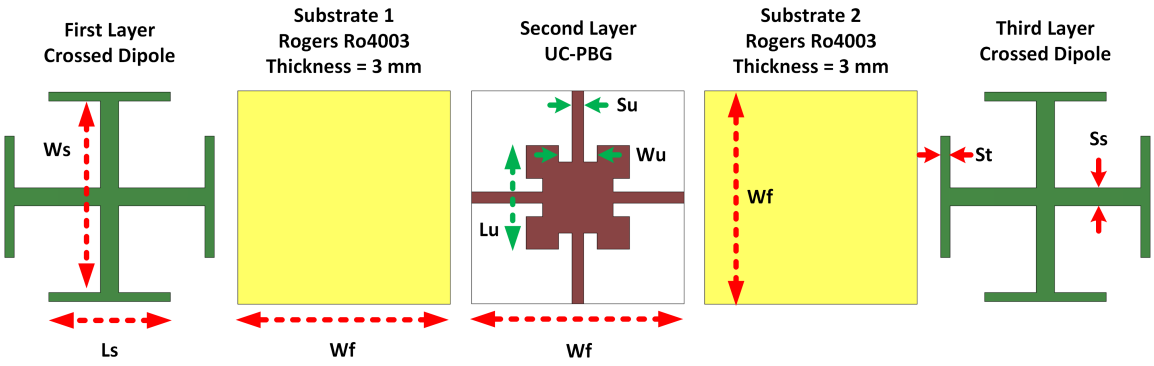


Figure 4.46: New metasurface unitcell design composed of three layers: two crossed-dipole microstrip structures on the top and bottom layers, with a UC-PBG layer integrated in the middle to enhance phase compensation and resonance control.

ing and phase aberrations. However, at mm-wave frequencies, thinner metasurfaces can struggle with efficient wave propagation, especially at lower frequency bands where the wavelength is longer relative to the structure's thickness. The presence of the UC-PBG layer alleviates this limitation by providing high-Q S-parameter responses, particularly within thin metasurface implementations, improving resonance control and energy transmission through its engineered electromagnetic bandgap characteristics.

In this context, the newly proposed unitcell structure for the multi-band non-interleaved metasurface is introduced and illustrated in Fig. 4.46. This enhanced configuration integrates two microstrip crossed-dipole layers with a UC-PBG structure in the middle, enabling improved phase compensation, printed on two substrate Rogers Ro4003 with 0.6 mm thickness and unitcell dimensions of w_f=1.5. The design parameters are selected to support multi-frequency operation while maintaining compactness and efficient transmission: L_s=0.84, W_s=1.37, S_s=0.13, S_t=0.065, L_u=0.73, W_u=0.27, S_u=0.08 mm at 62 GHz, L_s=0.89, W_s=1.37, S_s=0.13, S_t=0.065, L_u=0.79, W_u=0.21, S_u=0.08 mm at 61 GHz, L_s=0.94, W_s=1.32, S_s=0.18, S_t=0.09, L_u=0.99, W_u=0.41, S_u=0.08 mm at 60 GHz, L_s=0.99, W_s=1.32, S_s=0.18, S_t=0.09, L_u=1.09, W_u=0.51, S_u=0.08 mm at 59 GHz, and L_s=1.04, W_s=1.32, S_s=0.18, S_t=0.09, L_u=1.15, W_u=0.57, S_u=0.08 mm at 58 GHz. These parameters work collectively to define the resonance behavior at distinct frequency bands within the 58–63 GHz range, enabling control of the phase profile necessary for multi-focus near-field bio-sensing.

The results presented in Fig. 4.47 illustrate the reflection coefficient (S11) response of the newly proposed metasurface unitcell composed of three layers. This design incorporates

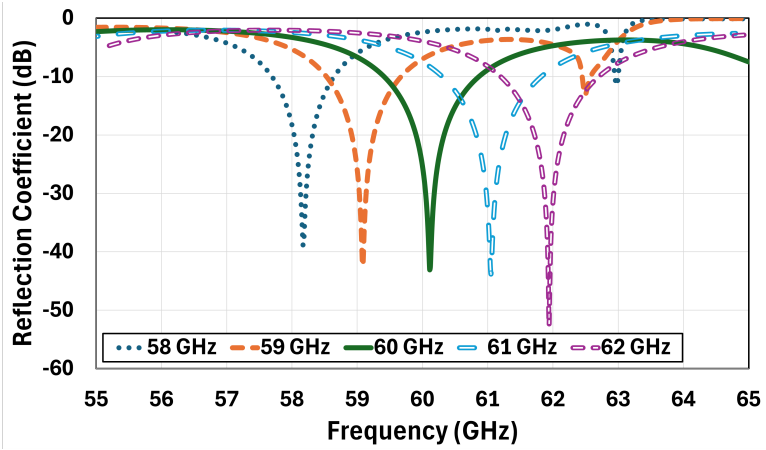


Figure 4.47: Reflection coefficient (S11) analysis of the newly designed metasurface unitcell composed of three layers, demonstrating that the inclusion of the UC-PBG layer enhances the quality factor and sharpens the resonance response.

a UC-PBG layer sandwiched between two crossed-dipole microstrip structures. As shown, the inclusion of the UC-PBG layer significantly enhances the quality factor of the structure. This leads to a sharper and more defined resonance, improving the phase selectivity and tuning precision of the metasurface.

After designing the three-layer unitcell to operate across the desired frequency range, the next step involves constructing the full metasurface array using phase-synthesis analysis. Initially, it is essential to determine the phase compensation distribution required for the 9×9 array elements to achieve the desired focusing behavior. Specifically, the design aims to optimally receive the radar signal at a focal point located 2.5 mm away from the metasurface (receiving side) and focus the transmitted energy at another near-field focal point positioned 2 mm above the metasurface (transmitting side). Fig. 4.48 illustrates the resulting phase distribution mapping, derived using the near-field phase synthesis equation tailored for this configuration.

Fig. 4.49 presents the simulated transmission coefficient (S21) magnitude and phase responses of the proposed three-layer unitcell, evaluated at the start and end frequencies, 58 GHz and 62 GHz, within the targeted operating bandwidth. The results demonstrate that the structure maintains a high transmission magnitude with low insertion loss across the required phase tuning range. Additionally, the phase response exhibits a smooth and wide variation, achieving approximately 310 degrees at 58 GHz and 350 degrees at 62 GHz, which is critical for effective near-field phase compensation in the design of the

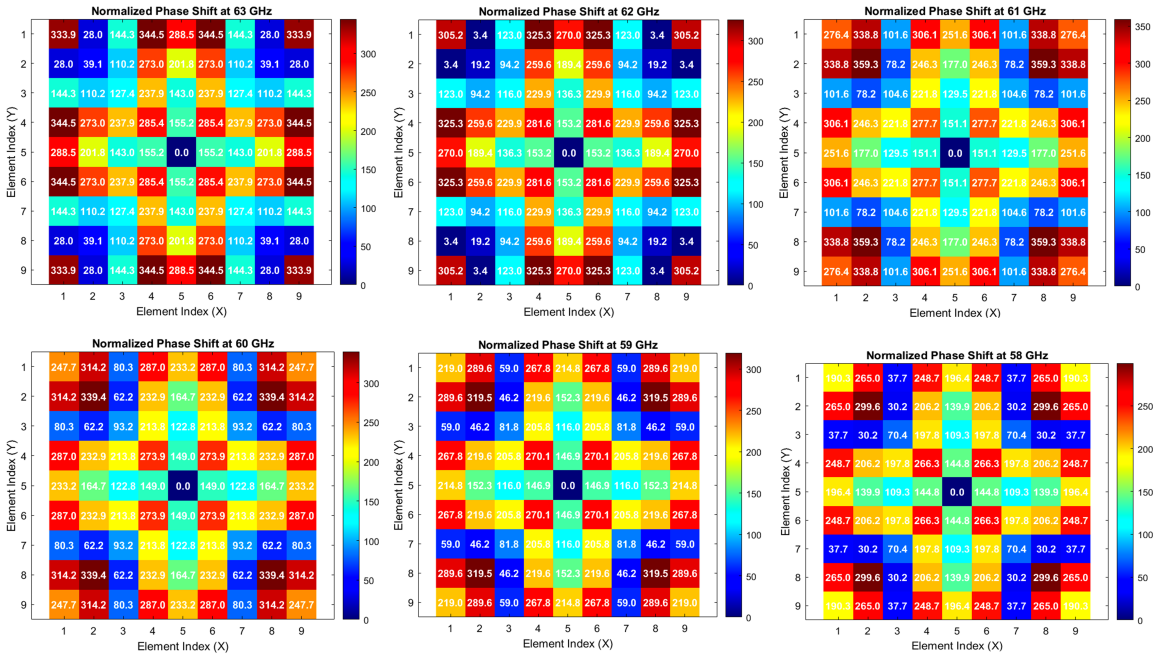


Figure 4.48: Required phase distribution for the 9×9 metasurface array, synthesized using near-field focusing equations to achieve dual focal points at 2.5 mm above and 2 mm below the metasurface.

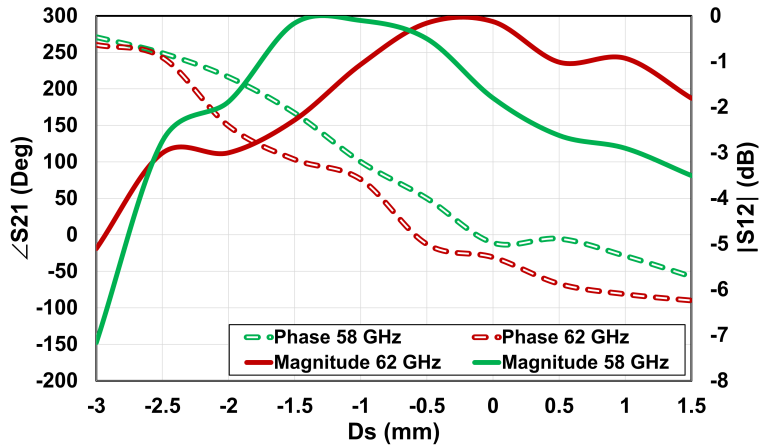


Figure 4.49: Simulated transmission coefficients (S21 magnitude and phase) of the three-layer unitcell across the starting and ending frequency points within the desired bandwidth.

9×9 metasurface array. In Fig. 4.49, the D_s is defined based on the design parameters as $D_s = 2.66L_s + 2.66W_u + 6.66L_u - 4.2133$. The introduction of the UC-PBG layer between the crossed-dipole structures enables broader and more controllable phase coverage while maintaining efficient transmission performance, thereby ensuring enhanced focusing capability and robustness for multi-frequency near-field bio-sensing applications.

Utilizing the phase synthesis approach and maintaining constant unitcell dimensions across different frequencies, unlike the previous section, this design implements a 9×9 metasurface array over the desired frequency range while preserving a consistent overall aperture size. This method ensures uniform spatial coverage and facilitates direct comparison of focusing performance across multiple frequencies. As a result, the 9×9 configuration achieves improved near-field focusing and power enhancement for all selected frequencies, offering a more robust and scalable solution for multi-frequency biomedical sensing applications.

Integrating the proposed metasurfaces with the mm-wave Infineon radar, and following the same measurement process used to evaluate transmitted power density enhancement and focusing within the phantom, as well as the power reflected and received by the radar receiver antenna, the experimental results are presented. Four operating frequencies—58, 59, 61, and 62 GHz—are selected for evaluation, corresponding to the design frequencies of the respective metasurfaces. The transmitted power focused inside the phantom for each of these frequencies is depicted in Fig. 4.50 to Fig. 4.53, respectively. In each 2D contour plot illustrating the power distribution above the metasurfaces, measurements at adjacent frequencies are also included to confirm that the power focusing is most dominant at the intended design frequency for each metasurface.

The structures of the three-layer metasurface arrays corresponding to each operational frequency are also included in Fig. 4.50 to Fig. 4.53. The presented results demonstrate that, at a plane positioned 2 mm above each designed metasurface, the transmitted power density within the phantom is significantly enhanced. Specifically, the metasurfaces designed for 58, 59, 61, and 62 GHz provide transmitted power enhancements of 16.5 dB, 16.1 dB, 14.5 dB, and 12.5 dB, respectively. These improvements lead to a strong power focusing effect at a localized point inside the phantom, confirming the metasurfaces' effectiveness in near-field energy concentration across the targeted multi-band frequency range.

Fig. 4.54 presents the impedance matching analysis through the reflection coefficient of the radar TX antenna, along with the enhancement of the reflected power at each designed metasurface across the different operating frequencies. Specifically, Fig. 4.54a to Fig. 4.54d demonstrate that the integration of each metasurface effectively tunes the resonance frequency of the TX antenna to align with the corresponding designed frequency.

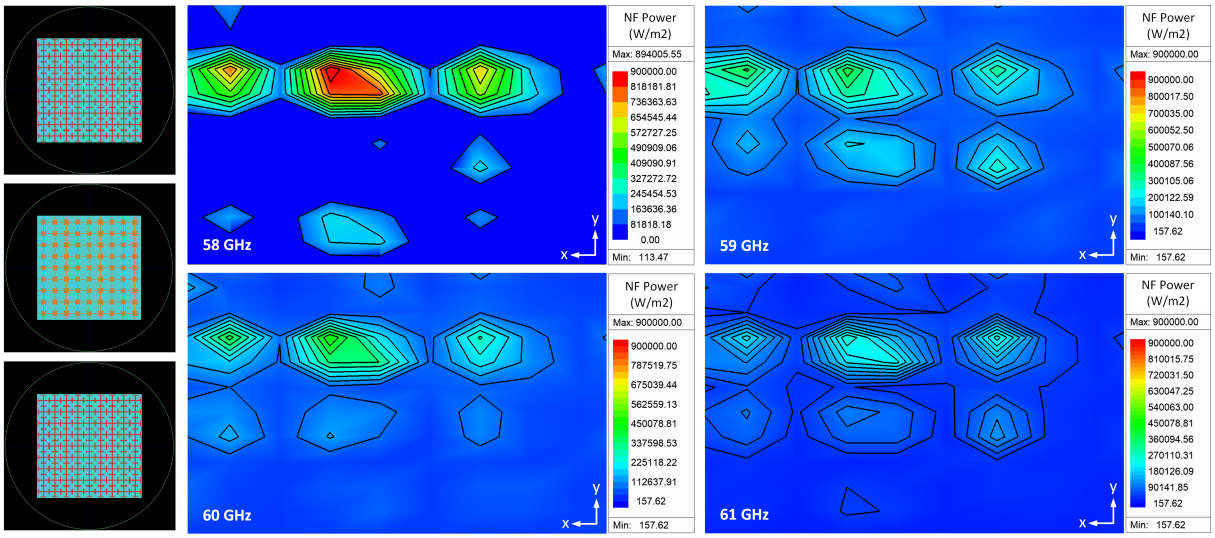


Figure 4.50: Simulated 2D contour plots of the radar system TX antenna's radiated near-field power density within the phantom model, evaluated on a plane positioned 2 mm above the multi-band non-interleaved metasurface, at 58 GHz

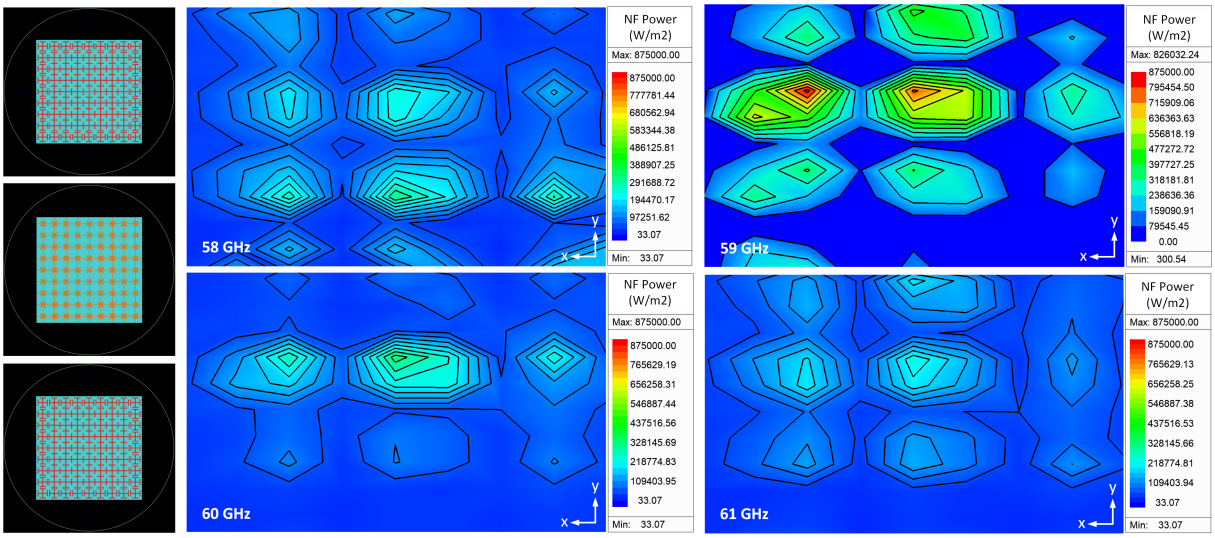


Figure 4.51: Simulated 2D contour plots of the radar system TX antenna's radiated near-field power density within the phantom model, evaluated on a plane positioned 2 mm above the multi-band non-interleaved metasurface, at 59 GHz

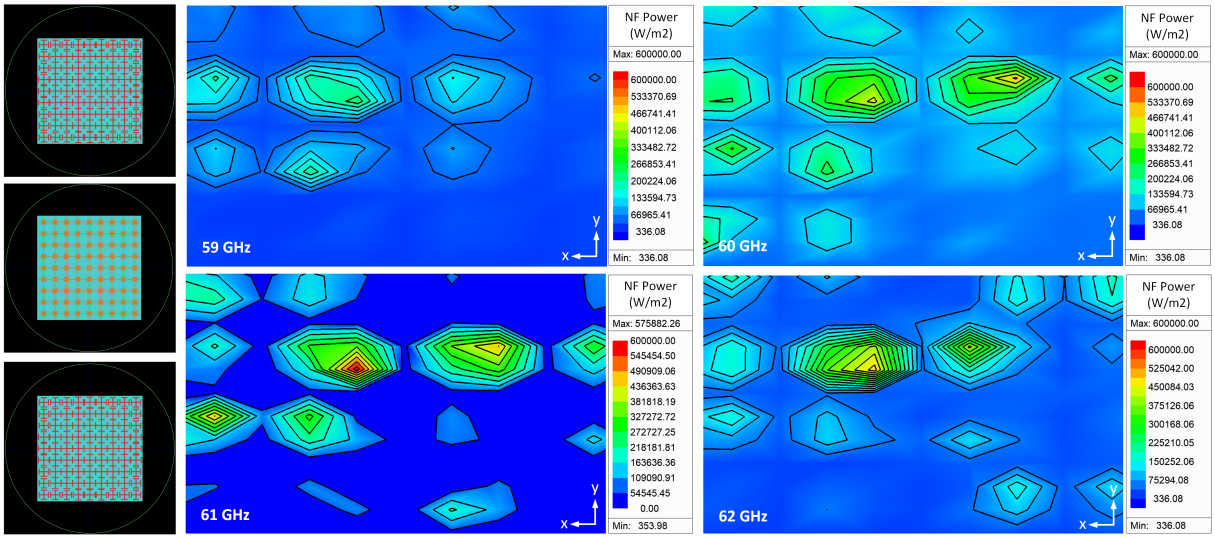


Figure 4.52: Simulated 2D contour plots of the radar system TX antenna's radiated near-field power density within the phantom model, evaluated on a plane positioned 2 mm above the multi-band non-interleaved metasurface, at 61 GHz

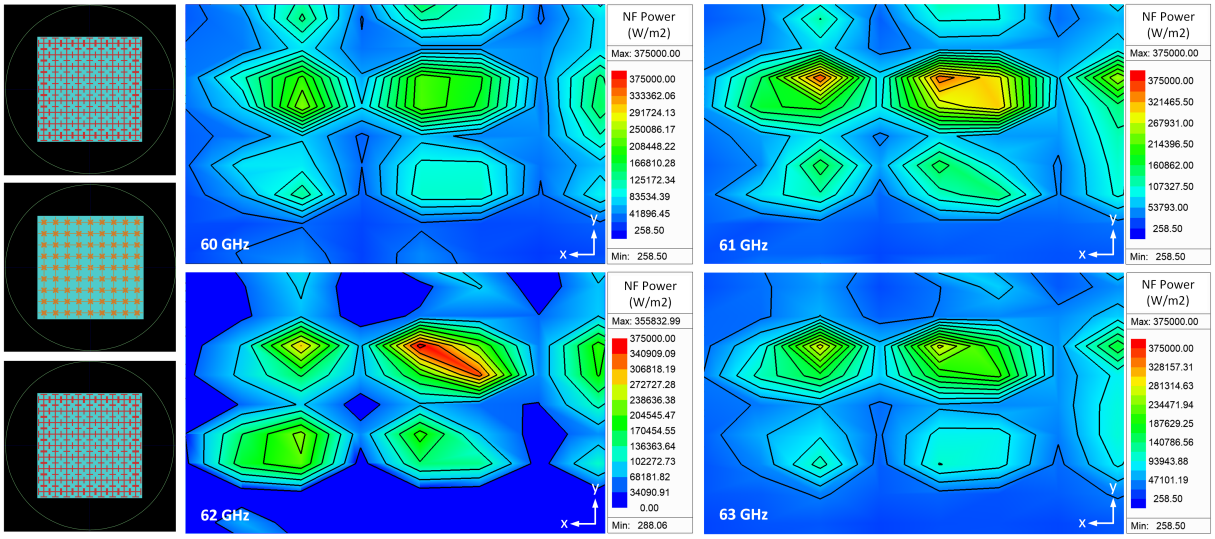


Figure 4.53: Simulated 2D contour plots of the radar system TX antenna's radiated near-field power density within the phantom model, evaluated on a plane positioned 2 mm above the multi-band non-interleaved metasurface, at 62 GHz

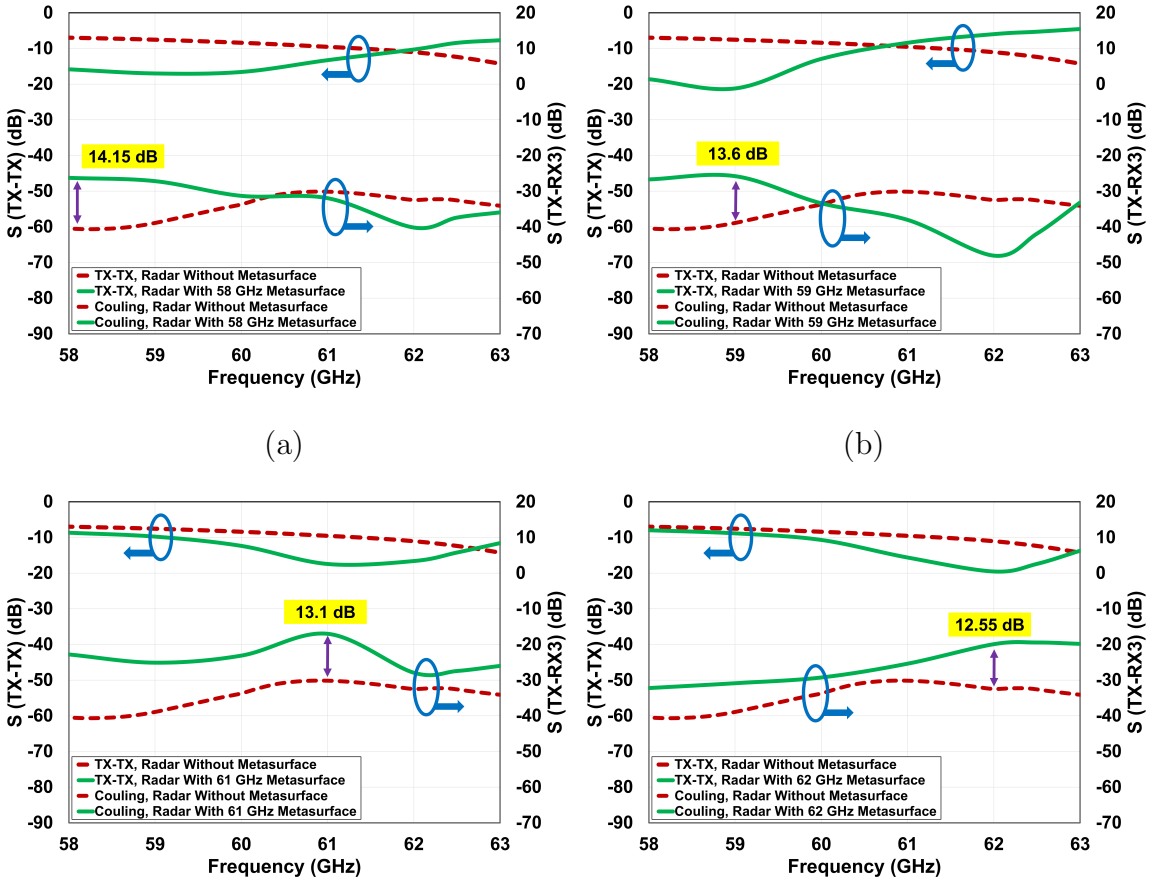


Figure 4.54: S-parameter analysis showing the simulated reflection and coupling magnitudes of the radar system transmitter (TX) and receiver (RX3) antennas, integrated with and without the metasurface in the presence of the phantom model: (a) at 58 GHz, (b) at 59 GHz, (c) at 61 GHz, and (d) at 62 GHz.

Moreover, the received power captured by the RX3 antenna confirms that the metasurfaces designed at 58, 59, 61, and 62 GHz achieve reflected power enhancements of 14.15 dB, 13.1 dB, 13.6 dB, and 12.55 dB, respectively. These results validate the metasurfaces' ability to significantly improve near-field reflection and sensing performance at their targeted frequency bands.

4.4.3 Fabrication Process and Measurement Results

Following the successful design and simulation, the fabrication process involved creating four metasurfaces, each specifically designed to operate at the specified center frequencies (58 GHz, 59 GHz, 61 GHz, and 62 GHz). As discussed in the previous section, each metasurface consists of a 9×9 unitcell array, with each unitcell measuring 1.5 mm^2, resulting in a total array dimension of 13.5 mm $\times$ 13.5 mm.

Each metasurface was fabricated individually on a circular aperture with diameter of 20 mm to ensure compact integration with the mm-wave radar antenna system, as shown in Fig 4.55. The fabrication was carried out on a Rogers RO4003 substrate with a total thickness of 0.6 mm, incorporating three layers for each metasurface: the top and bottom layers composed of crossed-dipole microstrip elements, and a UC-PBG structure placed in the middle layer.

To lower fabrication costs, provide a more compact structure, and make the metasurfaces suitable for multi-radar distributed sensing applications, all four circular-aperture metasurfaces were fabricated together on a single shared panel, as illustrated in Fig 4.55. The design of the panel allows each metasurface to be easily distinguished and separated along pre-defined mechanical cuts without damaging the active metasurface regions. This manufacturing approach offers both economic efficiency and practical flexibility for single or multi-unit experimental setups.

After the fabrication process, the metasurfaces were prepared for measurement evaluation, following the previously established method for assessing transmitted power enhancement within the phantom as well as reflected power. To fully validate the performance of all fabricated metasurfaces, the measurement process was repeated four times, once for each designed frequency. Due to the modification in the aperture shape, a newly designed 3D-printed fixture was developed to securely hold the circular metasurfaces at a distance of 2.5 mm above the radar antenna surface, while the phantom model was placed directly on top of the metasurface, as shown in Fig. 4.56. A specialized mm-wave probe was employed to measure the transmitted power inside the phantom model, with the captured power displayed on the Spectrum Analyzer. The measurement results corresponding to each of the four metasurfaces are presented in Fig. 4.56.

Fig. 4.57 illustrates the measurement results of the transmitted power density enhancement using the fabricated multi-band non-interleaved metasurfaces, evaluated with the radar system in the presence of the phantom model. The results are presented for four different metasurfaces designed at distinct target frequencies of 58 GHz, 59 GHz, 61 GHz, and 62 GHz, shown in subfigures (a) to (d), respectively. In each plot, the green

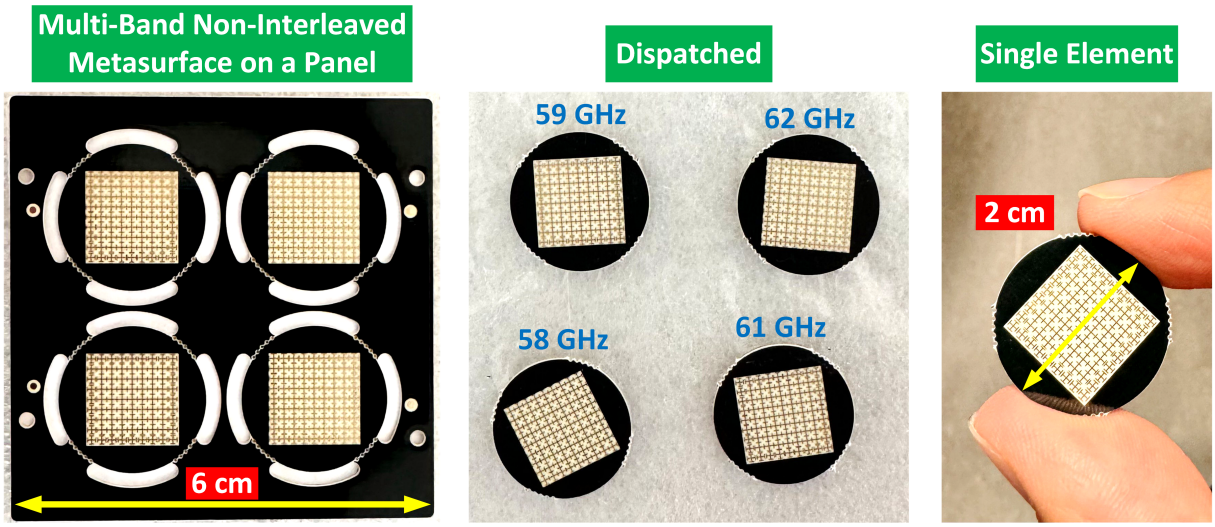


Figure 4.55: Fabricated multi-band non-interleaved metasurface on a single panel, separated circular metasurfaces after dispatching, and individual circular metasurface element ready for integration.

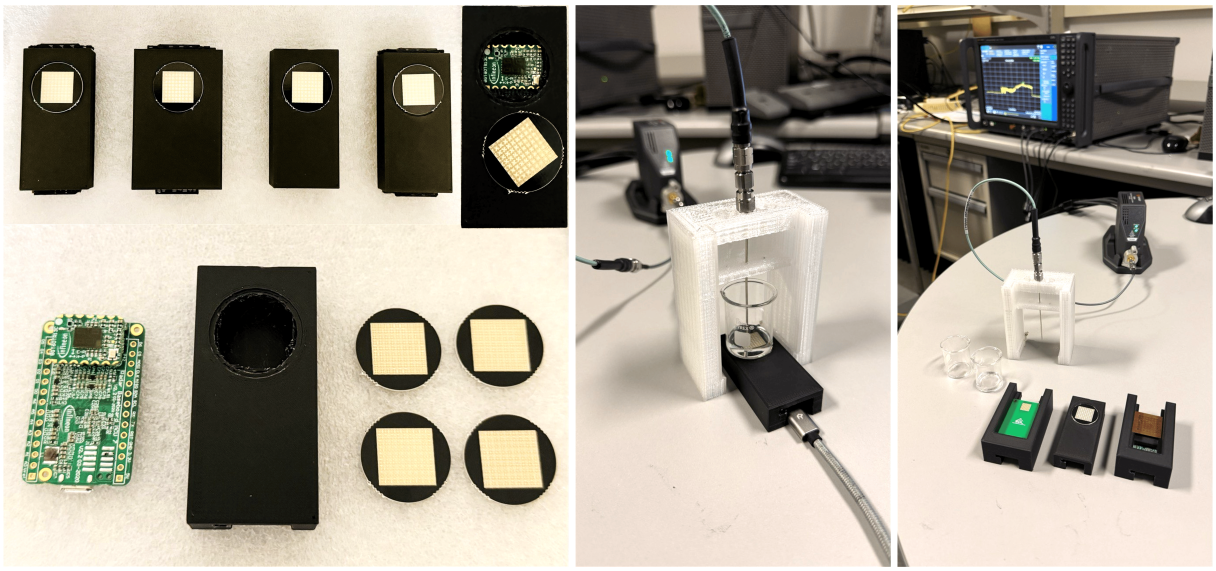


Figure 4.56: Measurement setup for evaluating near-field transmitted power density inside the phantom at different frequencies, using the fabricated multi-band non-interleaved metasurfaces integrated with the radar system.

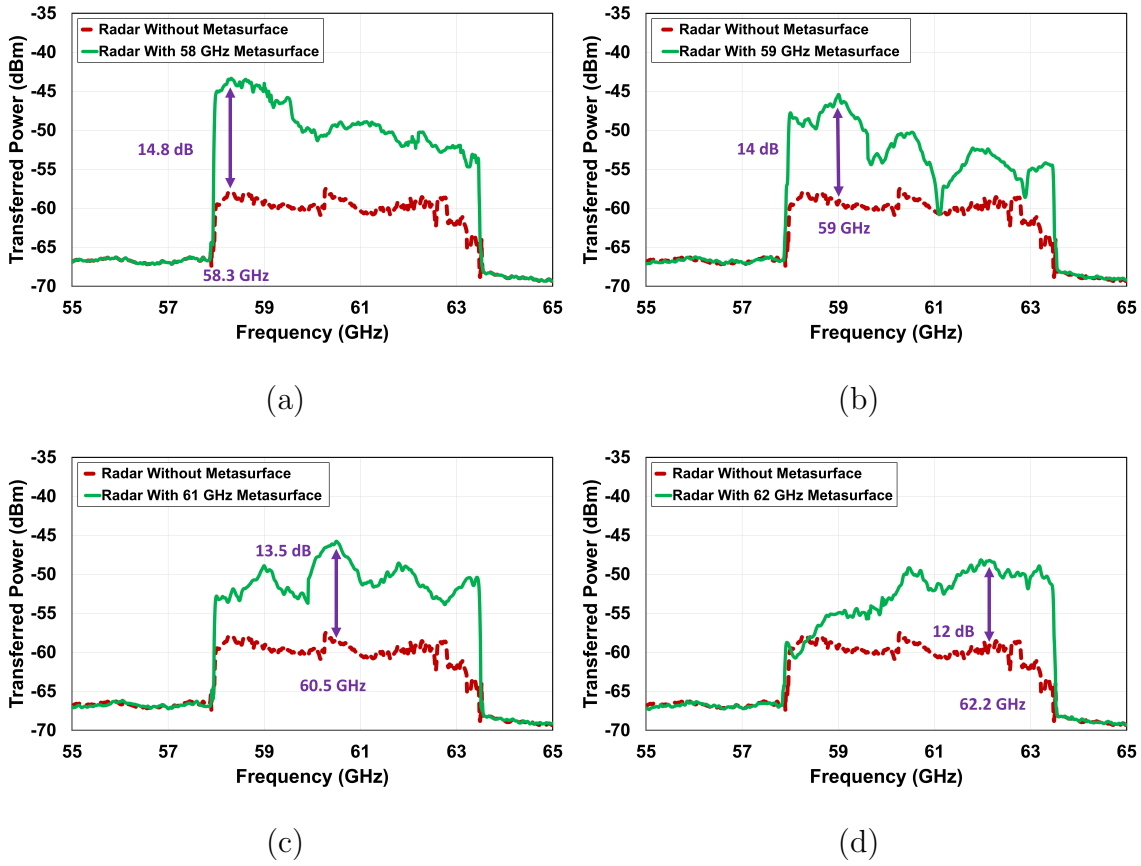


Figure 4.57: S-parameter analysis showing the simulated reflection and coupling magnitudes of the radar system transmitter (TX) and receiver (RX3) antennas, integrated with and without the metasurface in the presence of the phantom model: (a) at 58 GHz, (b) at 59 GHz, (c) at 61 GHz, and (d) at 62 GHz.

curve corresponds to the radar system integrated with the metasurface, while the red curve represents the radar-only system without any metasurface enhancement.

In Fig. 4.57a, the metasurface designed for 58 GHz demonstrates a strong focusing effect, with the maximum transmitted power enhancement observed at approximately 58.3 GHz. A notable power increase of 14.8 dB is achieved compared to the radar-only case, confirming the effectiveness of the metasurface in concentrating power at the desired frequency. Similarly, Fig. 4.57b presents the result for the 59 GHz metasurface, where a peak transmitted power enhancement of 14 dB is recorded at 59 GHz, aligned with the design.

Fig. 4.57c displays the results for the metasurface targeting 61 GHz. Although a slight shift in the peak response is observed at around 60.5 GHz, the transmitted power enhancement remains significant, reaching 13.5 dB. This minor frequency shift can be attributed to fabrication tolerances, substrate variations, or environmental factors affecting the dielectric properties during measurement. Nevertheless, the overall improvement remains substantial, demonstrating the robustness of the metasurface design against practical imperfections. In Fig. 4.57d, the metasurface designed for 62 GHz exhibits a transmitted power enhancement of 12 dB centered at 62.2 GHz. While slightly lower than the enhancements observed at lower frequencies, this still represents a strong power improvement, enabling effective near-field sensing at this high frequency.

Across all four metasurface designs, consistent performance improvements between 12 dB and 15 dB are demonstrated, validating the multi-band metasurface approach for enhancing near-field transmitted power. The clear separation between the radar-only and radar-with-metasurface curves highlights the significant contribution of the metasurface in boosting the transmitted signal strength inside the phantom model. Additionally, minor frequency shifts observed are within acceptable limits and do not affect the performance, ensuring the practical feasibility of the metasurface integration with commercial radar systems for biomedical sensing applications.

Table 4.2 presents a direct comparison between the simulated and measured focused transmitted power levels. The slightly larger discrepancies observed between simulation and measurement results at lower frequencies (58 GHz and 59 GHz) can primarily be attributed to two practical factors. First, in the experimental setup, all metasurfaces were positioned at a fixed distance of 2.5 mm (λ at 60 GHz) above the radar antenna surface. While this distance was optimized for near-field focusing at the designed frequencies, the effect of such a gap becomes more significant at lower frequencies where the wavelength

Table 4.2: Comparison of Simulated and Measured Focused Transmitted Power Inside the Skin for Multi-Radar Sensing with Multi-Band Multi-Focus Non-Interleaved Metasurface

Frequency (GHz)	**Simulated Power (dB)**	**Measured Power (dB)**
58	16.5	14.15
59	16.1	13.6
61	14.5	13.1
62	12.5	12.55

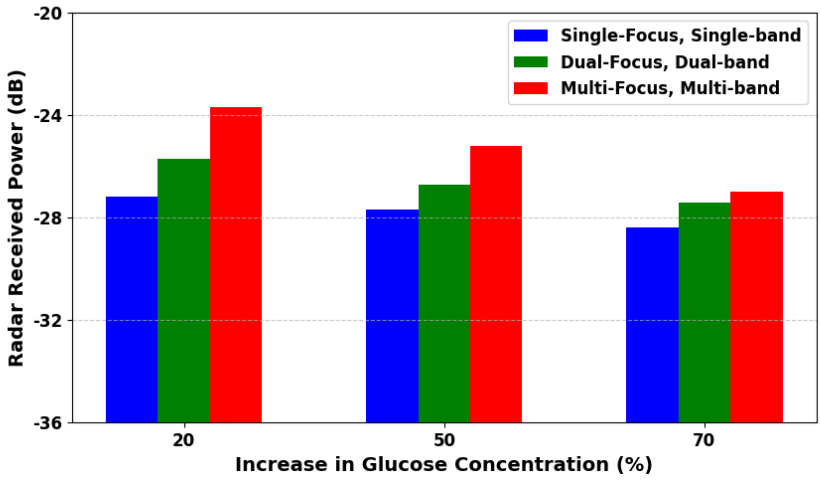


Figure 4.58: Signal-to-noise ratio analysis for varying glucose concentration levels, comparing the performance of single-band single-focus, dual-band dual-focus, and multi-band multi-focus non-interleaved metasurface designs.

is larger, leading to phase deviations and reduced focusing efficiency compared to the higher-frequency designs. Second, accurately replicating the exact dielectric properties, specifically permittivity and conductivity, of the skin phantom model used in simulations is challenging in practice. Small variations in material composition, mixing ratios, or temperature conditions can cause deviations from the intended electromagnetic properties, particularly at lower frequencies where material dispersion is more pronounced.

The final stage of the evaluation focuses on investigating the radar system's signal-to-noise ratio (SNR) by analyzing the reflected power from a skin phantom, modeled by a beaker filled with pure water. To assess the improvements in near-field sensing with enhanced SNR, varying glucose concentration levels were introduced into the phantom, altering its permittivity. The results for the two proposed methods; the dual-band dual-focus metasurface (Objective 3) and the multi-band non-interleaved metasurface (Objective 4), are analyzed and compared, as presented in Fig. 4.58. As illustrated, increasing the glucose concentration from 20% to 70% reveals that the dual-focus metasurface consistently achieves higher SNR compared to the single-focus metasurface. Furthermore, the multi-band non-interleaved metasurface outperforms both approaches, offering the highest SNR and improved differentiation between varying glucose concentration levels. This capability to detect subtle dielectric changes corresponding to glucose variations across different skin

locations highlights the enhanced sensitivity and precision of the system. Specifically, in the power reflection and sensing analysis using the multi-band non-interleaved metasurface, it is observed that a 10% increase in glucose concentration results in approximately a 3.5 dB difference between the averaged results of the multi-radar and single-radar measurement approaches. This confirms the advantage of multi-sensor distributed sensing for achieving more accurate and reliable non-invasive glucose monitoring.

Chapter 5

Conclusion and Future Works

In this chapter, the preliminary findings of this research are summarized, and possible future works are pointed out with a suggested timeline.

5.1 Conclusions

On-body radar sensors represent a significant advancement in biomedical sensing technology, enabling continuous, real-time tracking of vital signs, glucose levels, and other physiological metrics. These capabilities support early diagnosis, more effective treatment, and improved patient outcomes. However, enhancing radar sensing is crucial to meet the demands for accuracy, sensitivity, and reliability.

In the hardware configuration of these radar systems, it is commonly assumed that the radar chipset architecture is predetermined, leaving the design of the antenna as the primary variable, especially for glucose monitoring, where antenna near-field performance is crucial to ensure accurate measurements without any gap between the antenna and the human body skin. Most commonly used radars, which are off-the-shelf and commercially available at an affordable price, can enhance their performance through the integration of lenses, eliminating the need for retooling or re-manufacturing. However, despite these enhancements, current designs are still insufficient for biomedical applications such as blood glucose monitoring. As a result, no commercial radar-based glucose monitoring or biomedical devices are currently available on the market.

The challenges associated with radar antenna design for biomedical applications are multifaceted, including frequency selection, physical design complexity, and near-field op-

Table 5.1: Comparative Analysis of Low-Frequency and Mm-Wave Radar Sensing for Biomedical Applications

Criteria	**Low-Frequency Radar**	**mm-Wave Radar**
Penetration Depth	High; suitable for deeper tissues	Limited to superficial tissue layers
Spatial Resolution	Low; less precise targeting	High; enables higher sensing
Sensitivity to Dielectric Changes	Lower due to weaker interaction	Higher due to strong dielectric contrast
Power Consumption	Generally lower	higher
Susceptibility to Interference	High multipath and environmental interference	Lower interference in controlled near-field region
Fabrication and Integration	Challenging for miniaturization	Easier with on-chip integration
Quality Factor	Higher due to lower tissue loss tangent	Lower due to higher tissue absorption and increased dielectric losses
Best Use Case	Bulk tissue analysis or deeper targets	Surface-layer analysis and wearable monitoring, such as glucose

eration requirements. Lower frequencies offer deeper penetration but poor resolution, while higher frequencies suit skin-layer targeting but have limited tissue penetration. Table 5.1 outlines the advantages and disadvantages of using low versus mm-wave frequency bands for the proposed topologies in this thesis, particularly in the context of glucose monitoring, where selecting the appropriate frequency presents a significant challenge.

In addition, high-profile antenna structures, such as horns and planar array antennas operating in the near-field, are often suffer from several issues, including complex designs, high profiles, and lossy feeding networks, leading to inefficiencies and impracticalities in real-world applications. Moreover, the conventional approach of defining the far-field by placing the focal point far from the antenna restricts the ability to focus very close to

the aperture, presenting a significant limitation in targeting specific areas in biomedical scenarios. In the realm of near-field antenna design, it is crucial to emphasize that the far-field design parameters should not be indiscriminately applied. While radiation pattern, antenna gain, directivity, and sidelobe level are indeed important considerations in most applications, they should be interpreted differently in the context of near-field antennas. The primary objective of near-field antenna design is to optimize the performance and characteristics of the antenna in close proximity to the radiating source, typically within a wavelength or less. Therefore, the emphasis shifts towards achieving efficient power transfer, minimizing near-field distortions, and tailoring the antenna's characteristics to meet the specific needs of short-range communication systems. Applying far-field design parameters without modification in the near-field context can lead to less-than-ideal performance and potentially negate the benefits of using near-field antennas.

Furthermore, the absence of attention to impedance matching in the near-field significantly limits the practical use of these antennas for direct contact with the human body, a critical aspect in integrating them into medical devices. In medical microwave imaging, antennas are positioned in close proximity to the body to capture faint echoes from the internal organs, which are often obscured by strong reflections from the skin. Given the antennas' extremely close proximity to the body, it is vital to carefully consider the characteristics of near-field antennas. The challenge arises when attempting to integrate these antenna structures with compact devices like radars or sensors, impeding their practicality in real-time health monitoring applications. Most existing reviews primarily concentrate on near-field antennas with larger sizes and focal points located beyond the free-space wavelength. As a result, these studies are unsuitable for compact and lightweight integration into devices meant for real-time health monitoring, a crucial necessity in practical biomedical applications.

With the identified bio-radar antenna challenges and outlined solutions, the development of an advanced radar system is critical. In Chapter 3, we introduced the development of lens-based structures, specifically dielectric rod arrays and gradient-index (GRIN) Luneburg lenses, to significantly enhance radar power transmission and address the beam offset issue inherent to bistatic radar configurations, where the TX and RX antennas are placed on the same plane but spatially offset from the central axis. These lenses demonstrated a strong ability to correct beam alignment and improve electromagnetic field concentration in the desired direction, ensuring more effective sensing and signal reception. These designs address key challenges in low-frequency radar sensing for external monitoring, such as limited spatial resolution and inadequate focusing, while maintaining the compactness required for portable medical devices. The contributions outlining this technique are detailed in our prior works [175, 185, 191, 194, 239, 240].

However, while the proposed 3D lens structures offer high gain and directional accuracy in far-field applications, their practicality for near-field biomedical sensing, particularly for internal health biomarkers, is limited. Optimal performance often requires high-profile geometries, resulting in bulky, non-conformal designs that are difficult to integrate with the human body and suboptimal for focusing within lossy biological tissues. Additionally, their design for free-space radiation and inherent structural complexity present challenges for impedance matching with human tissue and integration with compact radar modules in wearable or on-body systems. It is also important to note that dielectric lenses, such as GRIN Luneburg lenses, offer cost-effective fabrication when designed for low-frequency operation. However, transitioning to millimeter-wave frequencies substantially increases manufacturing complexity and associated costs. This is primarily due to the stringent precision requirements and challenges in fabricating miniature 3D unit cells at sub-wavelength scales, which demand advanced techniques and tighter tolerances.

The second phase of this research introduces novel radar-based approaches for near-field biomedical sensing, specifically designed to address existing challenges in accuracy, sensitivity, and system integration.

Metasurfaces, with their precise control over electromagnetic waves, significantly enhance resolution and sensitivity when integrated into millimeter (mm)-wave radar systems. This thesis presents the latest developments in metasurface technology for biomedical sensing, featuring an adaptable, compact, near-field-focused transmissive array designed for air-skin interface matching. Constructed using frequency-selective surface theory, the metasurface comprises layers of phase-synthesized unitcells and seamlessly integrates with commercially available radar operating within the 58–63 GHz frequency band. The evolution of this system is depicted, starting with a single-focus metasurface, Fig. 5.1a, and advancing to dual-focus configurations, Fig. 5.1b, that overcome the inherent limitations of the previous design. Furthermore, this approach is extended to multi-focus sensor architectures, where data fusion from multiple radars enhances power delivery to the skin at various depths and locations, Fig. 5.1c and 5.1d. The design effectively concentrates absorbed power density within the skin, while radar signal processing analysis demonstrates a corresponding improvement in the signal-to-noise ratio.

To overcome these limitations, we transitioned to the development of low-profile, planar metasurfaces, as presented in Chapter 4. These structures offer precise phase control and electromagnetic wave manipulation capabilities within a much more compact and conformal form factor. Unlike traditional bulky lenses, metasurfaces are more adaptable for near-field operation in biomedical environments, enabling better integration with skin-contact radar systems while still achieving enhanced power delivery and spatial focusing within the human body.

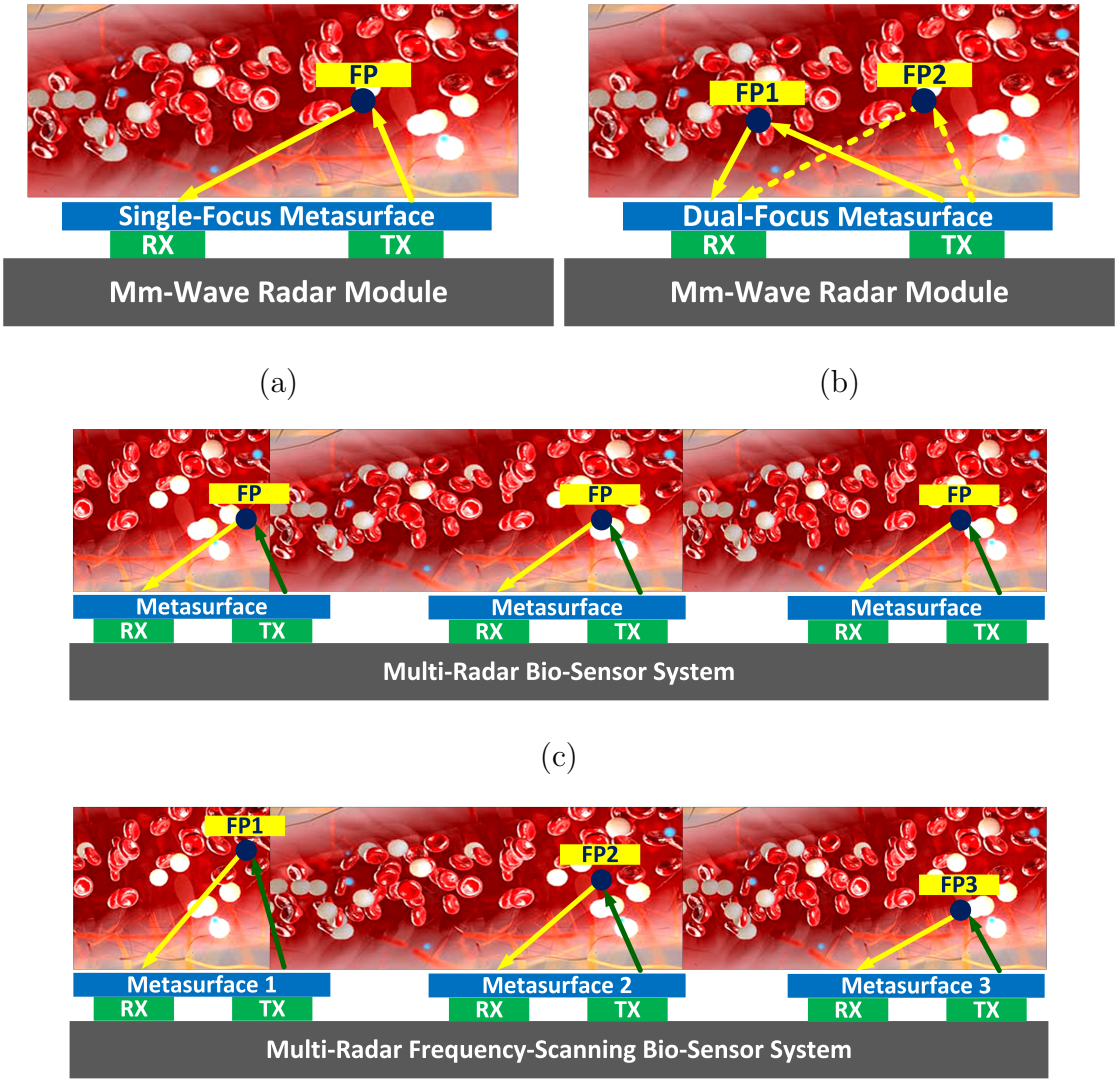


Figure 5.1: Advancements in blood glucose sensing with metasurfaces: (a) Single-focu;, (b) Dual-focus with dual-band capability for dual-depth sensing (Depth Sensing); (c) Multi-focus radar sensing enhanced with identical near-field focus metasurfaces (Spatial Sensing); (d) Multi-focus non-interleaved metasurfaces for distributed sensing via multi-radar fusion (Spatial+Depth Sensing).

The objective 1 introduced a low-profile planar metasurface which is specifically designed with impedance matching capabilities, seamlessly integrated with radar transmitter and receiver antennas, facilitating direct contact with a human body simplified model to enable substantial advancements in near-field sensing performance for biomedical applications. The key aspects contributing to the metasurface's remarkable radar near-field sensing were the enhanced power density absorption from the radar antenna transmitter into a controlled medium alongside the elevated received power level by the radar antenna receiver, leading to a higher system signal-to-noise ratio. Specifically, inside the simplified liquid container as a human skin phantom, the use of the metasurface led to an improvement of more than 11 dB in the near-field Poynting power density. Moreover, through radar signal processing, the analysis revealed an additional improvement of over 11 dB in radar signal-to-noise ratio, thereby enhancing the sensor sensing abilities. This metasurface focuses near-field Poynting power on a single spot 2 mm beneath the skin, targeting glucose measurements from the skin dermis layer, as shown in Fig. 5.1a. The contributions outlining this technique are detailed in our prior works [120, 141, 194, 224, 241–243], where we present the design, implementation, and evaluation of metasurface-enhanced radar systems for near-field sensing across single-frequency single-focus configurations for wearable biomedical applications.

While single-metasurface radar systems provide localized high-resolution sensing, they fall short in addressing the spatial variability of glucose distribution across different regions of the skin. Glucose levels vary significantly depending on the anatomical site — for example, concentrations in the arm can be up to 5% lower than those in the finger. A system with only one focal point captures data from a narrow area, making it incapable of accounting for the broader physiological heterogeneity. In addition, variations in skin thickness, hydration, and tissue composition further degrade signal reliability when limited to a single sensing location.

Designing a near-field focus metasurface with multi-focusing capability offers a promising pathway to overcome the limitations of single-focus systems in biomedical sensing. However, when this is implemented using a single-fed metasurface, the transmitted power must be divided among multiple focal points. This division inherently reduces the aperture efficiency, resulting in diminished electromagnetic energy delivered to each focus. Consequently, the reduced energy at individual focal locations compromises both the signal-to-noise ratio and the spatial resolution of the radar system, ultimately limiting the accuracy and effectiveness of physiological parameter detection. These constraints underscore the necessity of a multi-radar system, where identical single-focus metasurfaces are deployed across different body regions. Such a distributed sensing configuration allows concurrent data collection from multiple anatomical sites, effectively compensating for site-specific

physiological discrepancies and significantly improving the robustness of glucose monitoring.

This thesis extends this methodology to multi-focus bio-sensor system, as demonstrated in Fig. 5.1c, where data fusion from multiple sensors enhances spatial resolution by capturing data from various skin locations at the same penetration depths. In this work, a radar near-field scanning system is proposed, drawing inspiration from inverse synthetic aperture radar (ISAR) techniques. The proposed method eliminates the need for mechanical movement by leveraging a Synchronized Multi-Radar Bio-Sensor System for real-time distributed sensing, utilizing millimeter-wave radar modules enhanced by skin-matched metasurfaces to monitor physiological parameters across multiple skin sites, in which the human body remains stationary or in natural motion while multiple radar sensors operate simultaneously. This approach establishes a flexible, scalable radar sensing framework for high-resolution, real-time biomedical monitoring. By simultaneously capturing data from three distinct locations and employing advanced signal processing algorithms for multi-radar synchronization, the system mitigates intrasubject and intersubject variability caused by differences in skin composition, blood flow, and environmental factors, enhancing spatial coverage, compensating for inconsistencies, and providing a more reliable assessment of biomedical conditions. Experimental results demonstrate that the proposed fusion-based system outperforms radar-only solutions, achieving up to a 2.4-times improvement in radar SNR when addressing blood glucose distribution inconsistencies with a 20% glucose concentration variation across different skin phantoms. This configuration allows simultaneous data capture from multiple skin sites, increasing physiological coverage and robustness. A detailed presentation of this methodology and its performance evaluation is provided in our publication [225, 244].

While single-frequency radar systems can provide localized sensing, such systems offer restricted depth of information, as they cannot effectively detect dielectric changes occurring at different tissue layers, limiting the radar's utility in analyzing subsurface biological properties. This limitation is particularly critical in glucose monitoring, where dielectric properties vary with tissue depth, and physiologically meaningful glucose concentrations may reside at different layers depending on the individual or site. The situation is further complicated by the 7–8 minute physiological lag between blood and interstitial glucose, as well as dynamic glucose transport, which can cause up to 10% variation in consecutive readings. A single-focus metasurface, regardless of whether it is deployed with one or multiple radars, cannot capture this depth variability. To address this, multi-frequency operation becomes essential. One effective solution is the use of a dual-band, dual-focus metasurface that enables a single radar to sense at two distinct tissue depths simultaneously.

This thesis proposes advancements in near-field-focused metasurface technologies to en-

hance the accuracy of the radar system by progressing towards dual-focus configurations, as illustrated in Fig. 5.1b, addressing the limitations inherent to single-focus designs. This work introduces a dual-band, dual independently-tunable near-field focus metasurface designed to enhance the performance of mm-wave radar-based bio-sensor. This metasurface enables dual focusing of absorbed power within human skin, achieved through a phase-synthesized analysis of the metasurface array, where each focal point is controlled by a distinct frequency band within the radar spectrum. The integration of the proposed metallic slot metasurface with commercially available Infineon radar TX/RX antennas results in a 14.7 dB and 12.4 dB increase in Poynting power density at two distinct points within a human skin phantom model, along with an increase in radar-received power by 11 dB and 12.7 dB at 58.5 GHz and 61.7 GHz, respectively, significantly enhancing the radar's bio-sensing capabilities. A detailed presentation of this methodology and its performance evaluation is provided in our publication [245].

Although this dual-band functionality provides richer physiological information and marks an important transition from purely spatial distribution to frequency-selective depth control, scaling this concept to more than two bands introduces significant design complexity and practical limitations in metasurface synthesis.

To address this challenge, a Frequency-Scanning Multi-Radar System with Multi-Band Non-Interleaved Metasurface is presented. This work presents a near-field radar sensing system that targets multiple skin locations and depths by integrating a multi-radar architecture with frequency-selective metasurfaces. Specifically, a Multi-Radar System with Multi-Band Non-Interleaved Metasurface is developed, where each radar module is coupled with a custom-designed metasurface operating at a distinct frequency band. This configuration enhances the detection of physiological parameters, including the identification of blood-related abnormalities, by enabling frequency-dependent penetration and localized energy delivery. The proposed metasurface employs discrete, non-overlapping zones composed of phase-synthesized unitcell arrays. Each zone functions as a low-profile impedance-matching network, optimized for a designated frequency within the 58–63 GHz millimeter-wave range. This design increases the near-field efficiency by concentrating absorbed power at targeted skin depths, with frequency-dependent tuning allowing multi-depth interrogation.

Experimental validation using a customized skin-mimicking phantom demonstrates significant improvements in near-field absorbed power density. Specifically, transmitted power enhancements of 16.5 dB, 16.1 dB, 14.5 dB, and 12.5 dB were achieved at 58 GHz, 59 GHz, 61 GHz, and 62 GHz, respectively, confirming the effectiveness of the metasurface designs across the targeted multi-band operational range. Moreover, the received power captured by the RX3 antenna confirms that the metasurfaces designed at 58, 59, 61, and

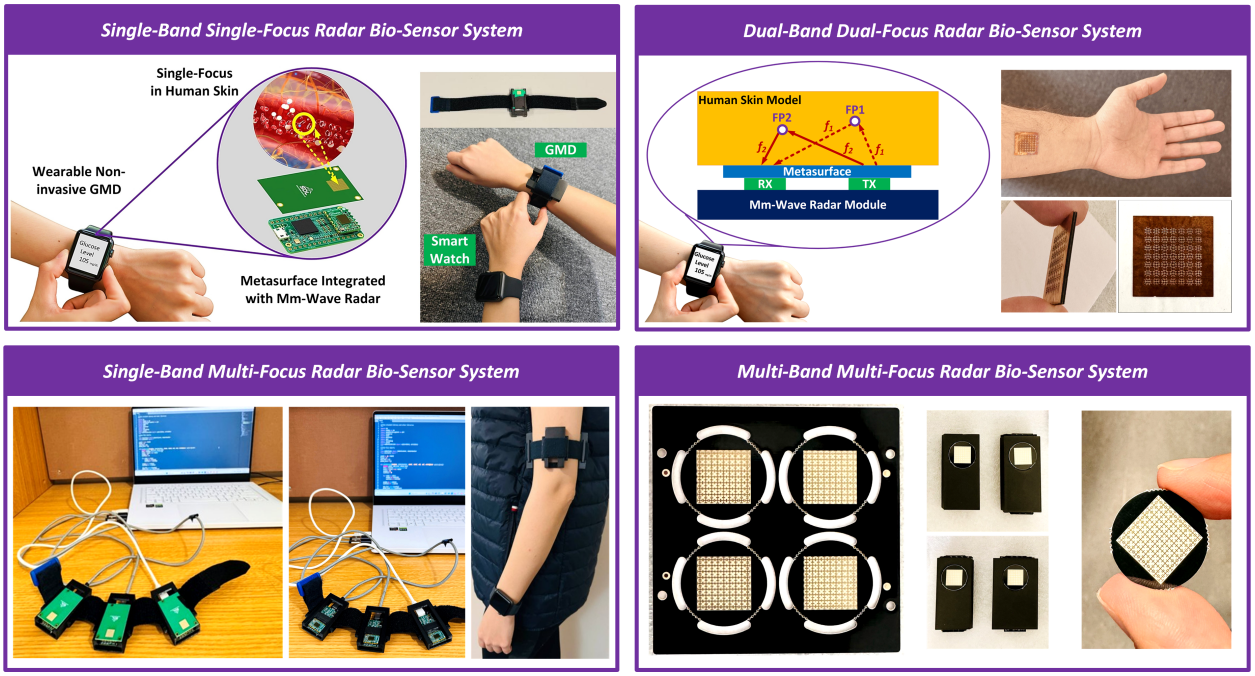


Figure 5.2: Developed radar-based bio-sensor systems for non-invasive glucose monitoring, showcasing the evolution from single-band single-focus design to advanced multi-band multi-focus sensing.

62 GHz achieve reflected power and SNR enhancements of 14.15 dB, 13.6 dB, 13.1 dB, and 12.55 dB, respectively. These results validate the metasurfaces' ability to significantly improve near-field reflection and sensing performance at their targeted frequency bands. This frequency-scanning strategy facilitates multi-depth, multi-location sensing, enabling a more comprehensive volumetric assessment of dielectric changes within biological tissue. A detailed presentation of this methodology and its performance evaluation is provided in our publication [235].

This progression from a single-band, single-focus system to a fully distributed, multi-frequency platform, highlights the central contribution of this thesis: the development of adaptable, metasurface-integrated radar sensing strategies that overcome the spatial and depth limitations of conventional non-invasive wearable biomedical sensing, as illustrated in Fig. 5.2. Table 5.2 highlights the key contributions of this thesis in addressing the research gaps outlined in Chapter 2.

To assess the improvements in near-field sensing with enhanced signal-to-noise ratio, varying glucose concentration levels were introduced into the phantom, altering its per-

Table 5.2: Radar-Based Biomedical Sensing Challenges and the Corresponding Solutions Presented in This Thesis

Challenges	**Solutions**
Inappropriate operational frequency band	Mm-wave frequency selection for dermis-layer penetration, utilizing its homogeneous blood distribution and minimizing interference from surrounding tissues.
Complex designs, high profiles, lossy feeding networks, high fabrication cost	Simple, low-profile, and compact design with low cost, ideal for integration into wearable devices.
Employing the traditional method of Far-Field	Employing the Near-Field theory analysis.
Disregarding impedance matching between the NF antenna radiation and the human body	Using matching layers to improve coupling efficiency between air and skin media.
Failure to concentrate power in the intended body region	Directing NF transmitted power to the specific targeted body region.
Limited sensing due to co-located TX and RX antennas in the radar system	Enhancing radar sensing by increasing the reflected power from the body to the RX antenna using spatially optimized antenna configurations.
Low accuracy caused by the inhomogeneous distribution of blood across different skin regions	Implementing distributed near-field sensing using synchronized multi-radar systems to increase spatial coverage and improve measurement robustness.
Inability to detect signals at varying penetration depths	Using multi-band radar sensing to perform depth-resolved measurements, allowing better characterization of layered physiological structures.

mittivity properties to simulate physiological changes. The results for the three proposed methods, the single-band single-focus metasurface (Objectives 1 and 2), dual-band dual-

focus metasurface (Objective 3) and the multi-band non-interleaved metasurface (Objective 4), are analyzed and compared. It shows that increasing the glucose concentration from 20% to 70% reveals that the multi-focus multi-band setup consistently provides the highest received power, offering the highest SNR and improved differentiation between varying glucose concentration levels, followed by the dual-focus dual-band, and finally the single-focus single-band configuration. This capability to detect subtle dielectric changes corresponding to glucose variations across different skin locations highlights the enhanced sensitivity and precision of the system. Specifically, in the power reflection and sensing analysis using the multi-band non-interleaved metasurface, it is observed that a 10% increase in glucose concentration results in approximately a 2.5-3.5 dB difference between the averaged results of the multi-radar and single-radar measurement approaches. This confirms the advantage of multi-sensor distributed sensing for achieving more accurate and reliable non-invasive glucose monitoring.

In anticipation of future developments, the research thesis outlines upcoming directions, emphasizing the continual exploration of radar near-field sensing in various biomedical applications. This involves clinical human trials, advancing the metasurface-enhanced approach and introducing innovative scanning methods for near-field biomedical sensing.

5.2 Initial Evaluation and Pre-Clinical Validation in Human Subjects

This section presents the initial evaluation and pre-clinical validation of the proposed radar-based sensing system on human subjects, serving as a crucial step toward assessing its real-world applicability. To simulate controlled physiological changes in glucose levels, a small-scale pre-clinical trial was conducted on healthy lab volunteers. The participants were in a fasting state during the early morning to ensure a consistent baseline. Each subject consumed a large glass of apple juice containing approximately 25% sugar by volume, intended to induce a noticeable rise in blood glucose levels. Radar measurements were then taken at multiple time intervals post-consumption, allowing us to observe and record the dynamic electromagnetic responses corresponding to glucose concentration changes in the body over time.

These preliminary tests helped evaluate the feasibility of using near-field radar sensors integrated with the metasurface platform for tracking glucose-related dielectric changes in a non-invasive manner. While not a full clinical study, this early human subject testing provides valuable insights into system performance in realistic conditions, and lays the

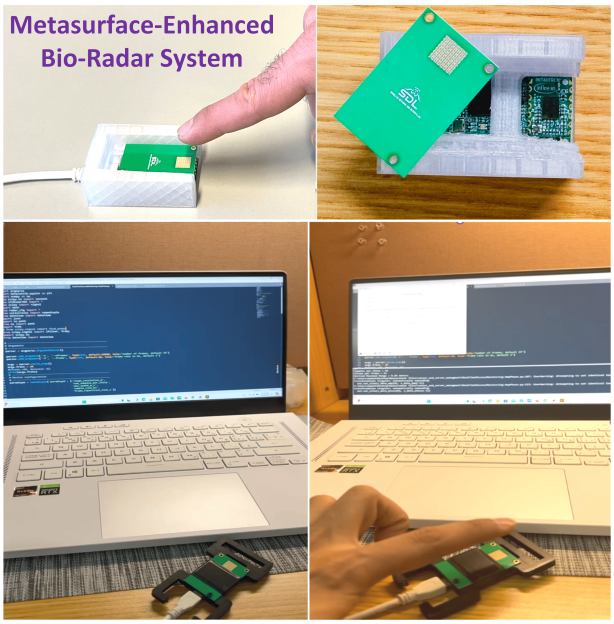
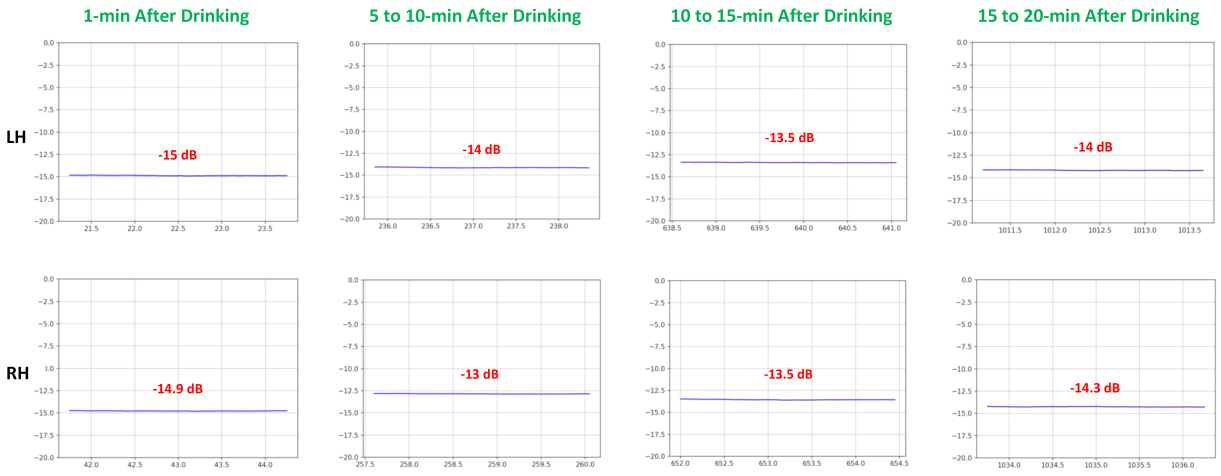


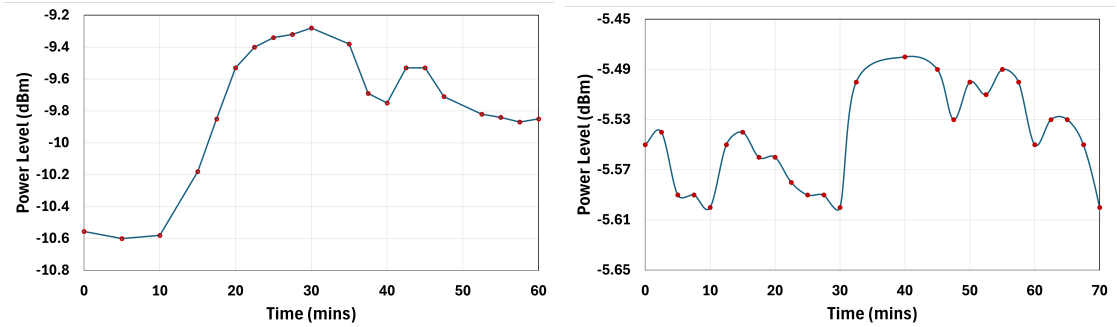
Figure 5.3: Measurement setup showing the mm-wave radar module integrated with a single-focus metasurface. The system is connected to a data acquisition interface, with real-time data captured using a Python script.

groundwork for future clinical investigations.

Fig. 5.3 illustrates the experimental setup used for initial human testing, where the Infineon millimeter-wave radar module is integrated with a single-focus metasurface introduced in Objective 1. The radar system is connected to a computer running a Python-based data acquisition program, enabling real-time signal capture during the glucose intake experiment. Fig. 5.4 presents the initial results obtained from radar measurements. In this preliminary evaluation, three participants were seated in a stationary position for approximately one hour. Each subject consumed a glass of apple juice (containing approximately 25% sugar) at the 10-minute mark. The radar response exhibited distinguishable signal spikes following juice consumption, indicating sensitivity to elevated glucose levels. However, the magnitude and timing of these responses varied across individuals, reflecting physiological variability. During the measurements, subjects placed their fingertip directly in contact with the metasurface. Although care was taken to minimize external interference, minor motion artifacts, such as finger movement, variable pressure on the surface, or the formation of air gaps, may have contributed to inconsistencies in the signal. Additionally, factors such as skin type, thickness, moisture, or perspiration could influence the



(a)



(b) (b)

Figure 5.4: Initial radar measurement results from human subjects using the single-focus metasurface-integrated mm-wave radar module. The plots illustrate the variations in radar signal response over time, reflecting individual physiological differences in glucose absorption and skin interaction; (a) subject 1, evaluation on right and left hand finger; (b) subject 2; and (c) subject 3.

radar's sensitivity and accuracy.

These observations raise important questions about inter-subject variability and environmental influences, which must be addressed in future clinical trials. While this thesis focuses on the technological development of bio-radar sensing, spanning from single-focus

to multi-frequency, multi-radar platforms (Objectives 1–4), the next phase will involve large-scale clinical testing. These trials will incorporate clustering of data across diverse user groups and may eventually employ machine learning algorithms to refine signal interpretation and improve diagnostic accuracy. Such validation lies beyond the scope of this thesis but is actively pursued by our research team as part of the commercialization pathway, with results expected in the near future.

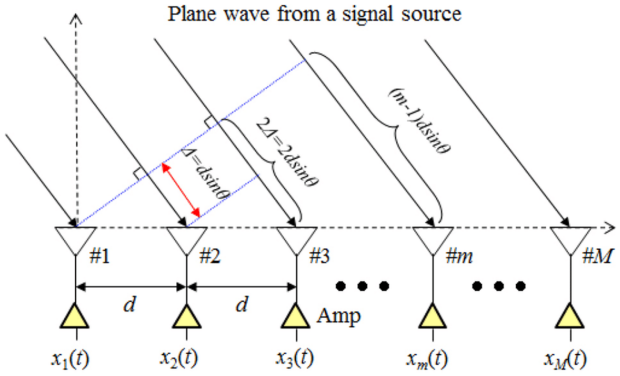
5.3 Future Works

The increasing interest within engineering and life science communities in utilizing radar system for healthcare sensing has driven continued advancements in this technology. Nevertheless, substantial technical challenges persist, requiring resolution for the practical implementation of this sensor technology to benefit humanity. This section addresses the remaining tasks essential to completing this research, outlining four main objectives for future work, as discussed in the following sub-sections.

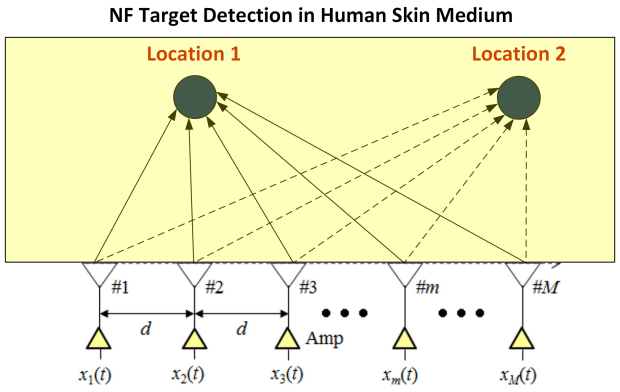
5.3.1 Reconfigurable Metasurface for Multi-Focus Sensing

In Objective 3, a dual-band, dual-focus metasurface was introduced, enabling simultaneous near-field focusing at two distinct spatial locations and frequencies. While this marked a significant advancement in enhancing both spatial and depth resolution in radar-based biomedical sensing, the next evolution lies in introducing reconfigurable metasurfaces that can electronically steer the focal point across the near-field domain, analogous to beam steering in phased array antennas. This approach offers dynamic control over energy concentration within the human body skin, enabling precision sensing without physical repositioning or reconfiguration of the hardware.

In traditional radar and antenna systems, beam steering or multi-focusing is commonly applied in far-field scenarios for multi-target detection, typically achieved through phased arrays or MIMO configurations. These techniques have proven effective in applications such as surveillance, automotive radar, and defense, where precise control of beam direction and shape enhances target localization and tracking. In this configuration, the phased-array antenna operates under the far-field approximation, assuming parallel wavefronts and equal path distances from each array element to the target, as illustrated in Fig. 5.5a, where θ is the angle of incoming wave, d is the antenna spacing, Δ shows the propagation path difference between adjacent antenna elements, $\Delta = d\sin\theta$), m is the number of antenna elements, and $x_m(t)$ is the received signal at the m-th antenna element.



(a)



(b)

Figure 5.5: (a) Beam steering in a phased-array antenna system for far-field target detection; (b) Electronic focus steering using a reconfigurable metasurface for near-field energy localization within human body skin.

However, when transitioning to near-field biomedical sensing, such far-field paradigms must be reimagined, as the wavefront behavior and energy distribution in the near-field differ fundamentally from those in the far-field. Specifically, directing power to discrete subcutaneous focal points requires careful spatial phase synthesis at sub-wavelength distances, as shown in 5.5b, beyond the capability of conventional far-field beamforming methods.

To address this gap, we propose the design of a reconfigurable near-field metasurface, in which electronic elements such as PIN diodes or MEMS switches are integrated within the

metasurface unit cells. This configuration enables dynamic phase tuning, allowing the focal point to be electronically shifted across various positions on or beneath the skin—effectively steering the near-field focus in real time. Such a design can be conceptualized as a near-field beam steering platform, tailored for biomedical applications, such as non-invasive glucose monitoring or early-stage cancer detection.

This capability is particularly critical for glucose monitoring, where glucose concentrations can vary spatially due to localized physiological factors such as tissue hydration, skin thickness, or blood vessel distribution. However, implementing multi-focusing using passive, single-fed metasurfaces introduces the challenge of power division across multiple foci, leading to reduced aperture efficiency and decreased energy at each focal point. This limitation can be overcome by transitioning to frequency-controlled or electronically reconfigurable designs, where each focal point is excited selectively, either by operating at a distinct frequency band or by toggling the phase configuration through active components.

5.3.2 Near-Field Scanning System for Enhanced Bio-Sensing at Low Frequencies

In [226], we introduces a near-field scanning system designed for bio-sensing applications, with a primary focus on operating at low frequencies. The utilization of low frequencies in communication systems allows signals to navigate through tissues with reduced absorption and scattering, enabling more reliable and efficient communication within the intricate environments of the human body. However, low-frequency communications face a challenge in resolution when compared to mm-wave frequencies. This challenge stems from the inherent characteristics of low-frequency signals, characterized by longer wavelengths. Consequently, the capacity to discern fine details or achieve precision in data resolution becomes constrained. This limitation becomes particularly relevant in applications that demand high-resolution imaging and precise sensing.

The proposed system, operating in close proximity, utilizes the near-field scanning method and leverages evanescent waves to enhance resolution and accuracy. By capitalizing on the advantages of low frequencies, the proposed system achieves greater penetration into the human body, revealing finer details crucial for precise bio-sensing, though with a compromise in resolution. Employing a near-field scanning technique, the system detects subtle variations in the biological properties of the human body. This underscores its efficacy in capturing intricate details while compensating for the reduced resolution. Simulations and measurement results highlight the system's proficiency in detecting 10% deviations in physiological parameters, achieved through scanning steps of 1 cm.

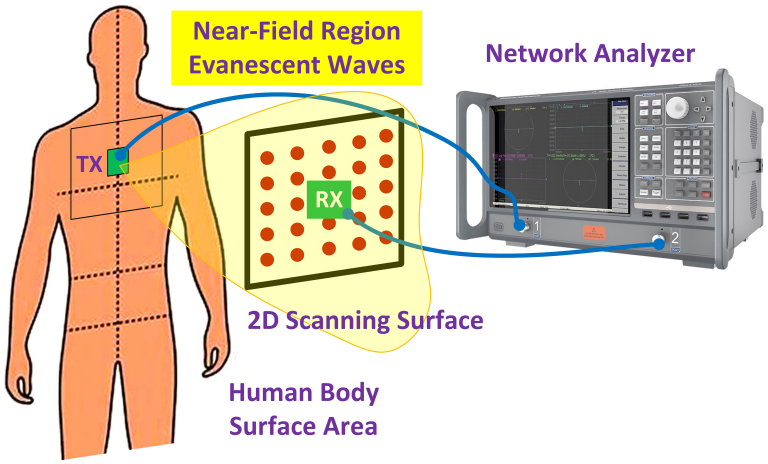


Figure 5.6: The near-field scanning system setup for bio-sensing

In the near-field mechanical scanning approach presented in [226], the methodology is inspired by the principles derived from Synthetic Aperture Radars (SAR), featuring a movable system with an extensive scanning area. This system incorporates a low-frequency setup with TX and RX antennas operating at 2.4 GHz, as depicted in Fig. 5.6, enabling near-field pattern sensing from the human body.

The operational procedure involves positioning the TX antenna in close proximity to the human body's surface to detect variations in its near-field evanescent wave, subsequently transmitted to the RX side. In this configuration, the RX antenna is strategically placed in front of the body area within the other side of the TX antenna's near-field region. The RX antenna's mobility allows for two-dimensional scanning of the area parallel to the human surface, with the TX antenna situated at the center of the scanning surface.

As illustrated in 5.6, both TX and RX antennas are connected to the two ports of a Network Analyzer, and the mutual coupling (S21) is measured and recorded at each point, contributing to the formation of the near-field pattern. Any deviations in the evanescent waves' radiation within the near-field region, attributed to the presence of abnormalities in the body, result in the generation of a new near-field pattern. Collecting near-field data from various scanned points yields a comprehensive sensing pattern, and the comparative analysis of these patterns in diverse scenarios provides highly accurate near-field bio-sensing for biomedical applications.

Initial experiments for proving the concept have demonstrated the feasibility of this method. In the experimental setup depicted in Fig. 5.7, a radar system is employed at the

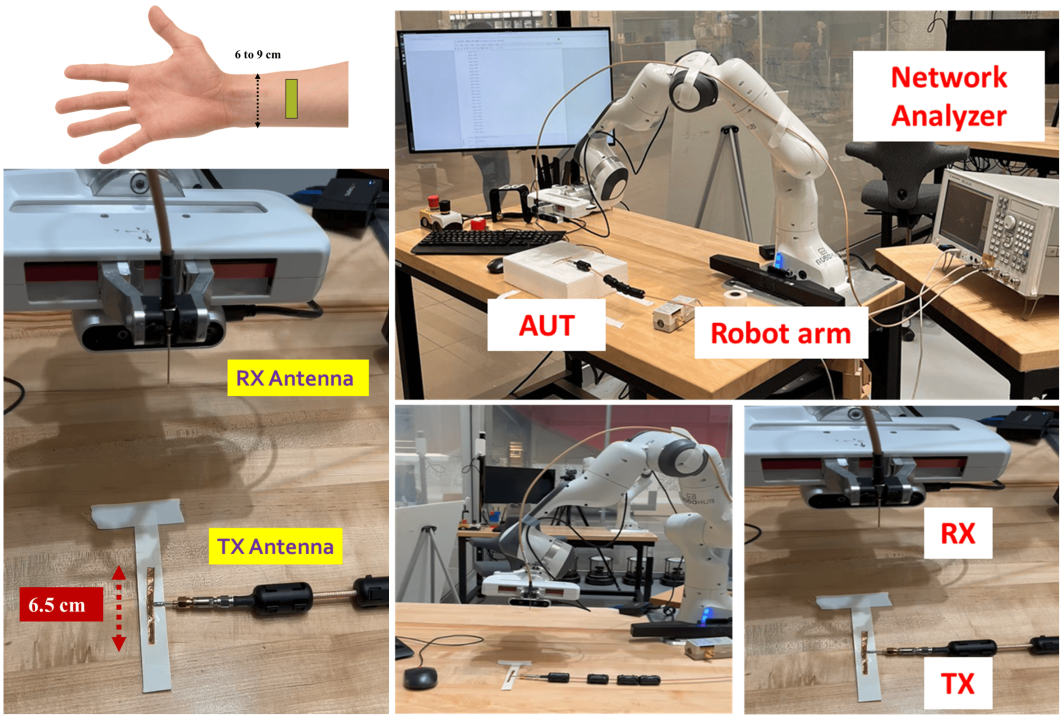


Figure 5.7: The measurement setup for the near-field scanning approach

early stages of development, featuring a readily available printed dipole antenna operating at 2.4 GHz as a transmitter (TX) and a simple probe as a receiver (RX). The objective of this experiment is to investigate the antenna's near-field behavior at different measured spots using the scanning approach. By systematically scanning a section of a desired medium with equal steps on a plane placed parallel to the dipole antenna, a near-field pattern of the received waves can be obtained. As illustrated in Fig. 5.8, the probe tip is positioned at a distance of 5 cm above the dipole antenna, held by a gripper attached to a robot arm. The robot is programmed to perform scanning on a planar grid parallel to the dipole antenna surface, covering dimensions of 10x10 cm with a step size of 1 cm.

To validate the measurement results, full-wave simulation analysis is also employed. As depicted in Fig. 5.8, the simulation incorporates the dipole antenna with precise dimensions, accounting for the effects of the SMA port, coaxial cable, and a probe positioned at the exact distance. It can be shown that Despite accounting for the asymmetrical and non-ideal aspects of the fabricated dipole antenna, both the simulation and measurement near-field patterns exhibit a notable agreement.

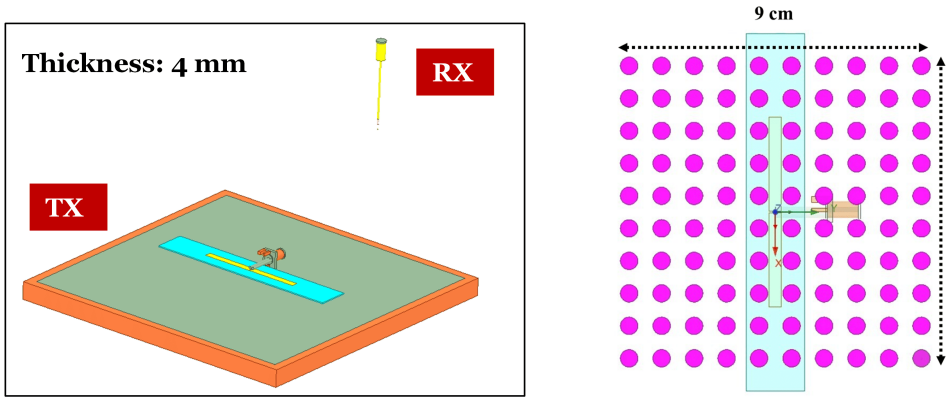


Figure 5.8: Simulation setup for the scanning approach, TX and RX antennas; with Scanning surface at 5 cm above the TX.

The next step is to proceed to analyze effectiveness and accuracy of the scanning approach for biomedical detection. In the first scenario, the focus is on determining whether the near-field sensing of the dipole antenna can detect changes in the dielectric permittivity of the underlying medium. To explore this, a uniform dielectric slab with 1 cm thickness is replaced instead of the foam layer and positioned at a 7 mm distance beneath the dipole antenna, as illustrated in Fig. 5.8.

In the simulation and measurement process, it is essential to develop a skin-mimicking phantom that accurately replicates the dielectric properties of human skin at 2.4 GHz, with a relative permittivity of $\epsilon_r = 38$ and conductivity $\sigma = 1.46$ S/m, as reported in [246]. To this end, a Pyrex container with a 1 cm wall thickness is used, filled with a mixture of pure water and 55% glycerin by volume. As noted in [247], this composition closely reproduces the frequency-dependent electrical characteristics of human skin. The phantom model, along with the permittivity and conductivity variations across the 0–3 GHz range, is illustrated in Fig. 5.9, providing a reliable medium for validating radar performance under near-field scanning conditions.

As illustrated in Fig. 5.6, the portable TX antenna is strategically placed on the human body for detection. Subsequently, an individual standing at a specific distance undergoes surface scanning, including the RX antenna, facilitated by a programmable robot arm. The robot arm is capable of moving in various directions, scanning the space with a resolution of 1 mm or less. The low-frequency radar captures the near-field power from the human body, which is received by the RX antenna at different scanning positions.

Fig. 5.10 demonstrates the effectiveness of SAR-based near-field scanning for detecting

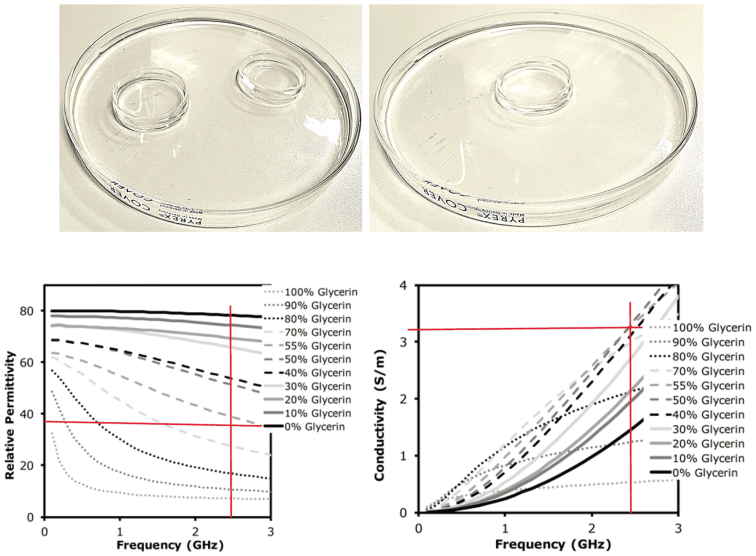


Figure 5.9: Dielectric skin phantom model used for near-field radar measurements. The Pyrex container is filled with a water-glycerin mixture (55% glycerin by volume), emulating human skin electrical properties.

variations in dielectric properties, which are critical for biomedical sensing applications such as glucose monitoring. The figure presents the collection of a series of 2D contour plots, illustrating near-field power distribution from various scanned points produces a near-field sensing pattern for varying relative permittivity (ε_r) values, ranging from 38 to 50. Each plot represents the spatial distribution of radar power over a scanned area, where the x- and y-axes represent the spatial coordinates across the scanning plane, the color scale denotes the received power levels in dB, with darker blue areas indicating regions of stronger reflection or absorption, corresponding to more focused or absorbed energy. As ε_r increases, the power distribution changes, indicating that the radar system is sensitive to the dielectric variations in the medium, such as those caused by physiological changes in tissue properties.

Comparing these patterns in different scenarios enables the identification of the presence of any abnormalities or glucose variations with distinct permittivity inside the body, as presented in Fig. 5.11. The bar graph quantifies the variation in power across the scanning area for each dielectric permittivity step. It plots x-axis: Percentage variation in dielectric permittivity (from 2% to 32%), and y-axis: Corresponding power variation range (in dB) observed in the scanning area. The results show a clear, monotonic increase in power variation as the permittivity deviates further from the baseline, with a maximum variation

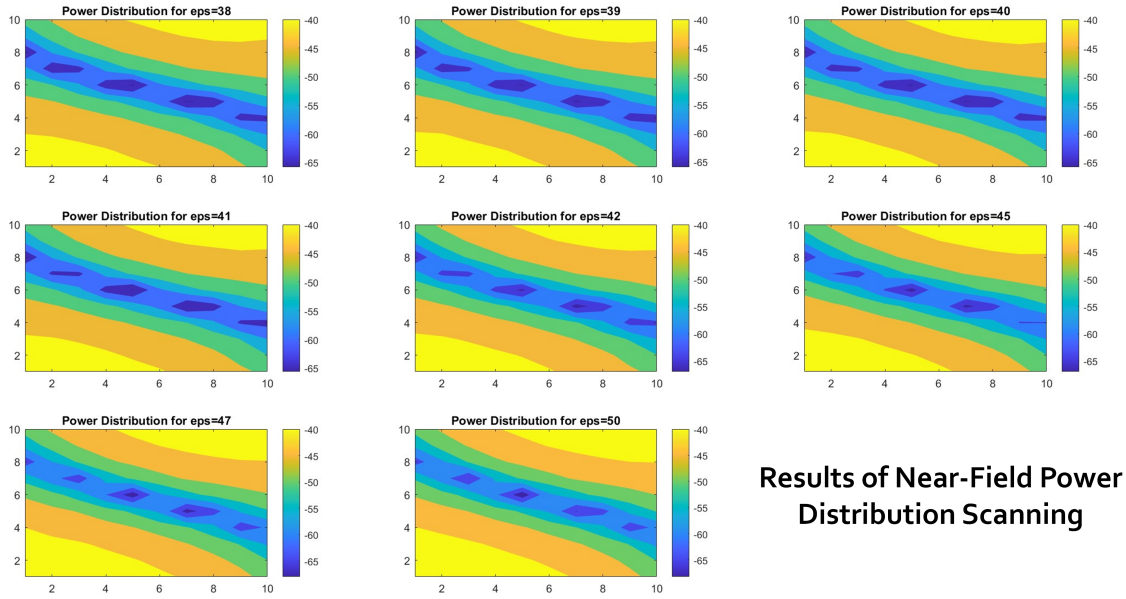


Figure 5.10: Near electric field pattern captured by scanning the RX antenna at different permittivity values deviating from the baseline human skin permittivity at 2.4 GHz, illustrating the radar's ability to detect dielectric abnormalities in biological tissue.

of over 9 dB for a 32% change. This behavior confirms the strong sensitivity of the radar system to dielectric changes, validating the system's potential for accurate detection of tissue dielectric properties. It is evident that the results are promising and even minor variations of 10% in the dielectric constant are detectable through the antenna's near-field.

In the second scenario, to further validate the potential of near-field radar sensing for biomedical applications, a 1×1 cm dielectric cube, modeling a localized abnormality such as glucose inconsistency within the skin, is embedded at a random position within the dielectric slab, as illustrated in Fig. 5.12. During the measurement process, this cube is physically realized using a small Pyrex container with a diameter of 1 cm. The experimental setup is used to compare the near-field electric field distributions resulting from variations in the cube's dielectric constant. As shown in Fig. 5.12, even a modest 10% change in the dielectric constant yields detectable variations in the near-field pattern, demonstrating the system's sensitivity to subtle permittivity differences—critical for applications such as glucose monitoring or early-stage anomaly detection.

In this section, the effectiveness of the scanning approach for near-field sensing has been successfully demonstrated. As a future endeavor to advance the practical feasibility of this

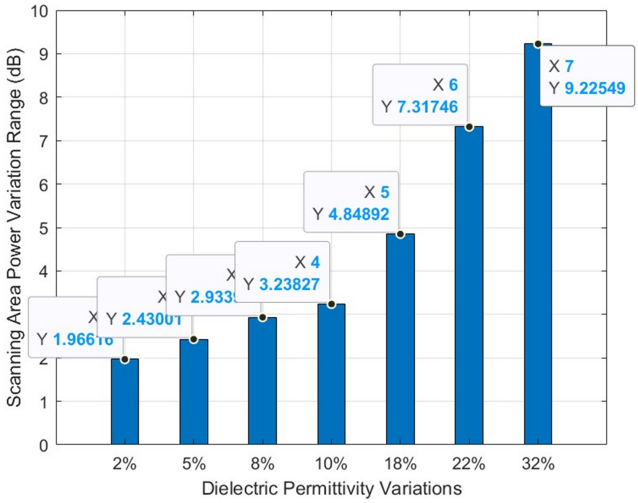


Figure 5.11: Comparing the scanned near-field electric field patterns by subtracting them from the baseline scenario facilitates the identification of abnormalities or glucose-induced permittivity variations within the body.

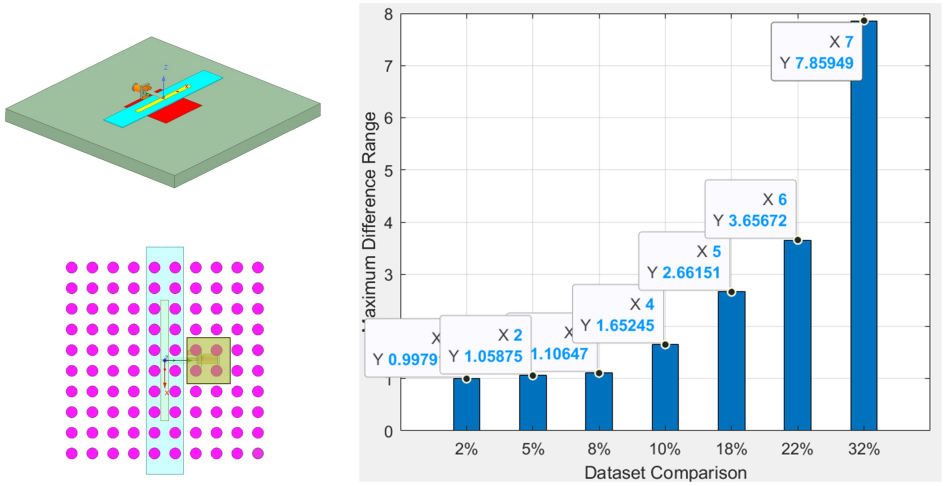


Figure 5.12: Near-field scanning scenario involving a 1×1 cm cube embedded within a dielectric slab beneath the dipole antenna. The bar chart results illustrate the system's capability to detect permittivity variations within the cube, demonstrating the sensitivity of near-field sensing to localized dielectric anomalies.

work, the proposed near-field scanning approach can be implemented using a low-frequency radar system in place of the vector network analyzer (VNA) for data acquisition and signal processing, paving the way for real-world deployment.

5.3.3 GRIN Planar Luneburg Lens for Near-Field Focusing in Biomedical Sensing

Expanding upon the foundational work presented in Chapter 3, this section addresses a critical limitation observed in the metasurface-enhanced radar system developed in Chapter 4, namely, the off-center near-field focusing resulting from the lateral offset of the radar antenna relative to the metasurface aperture. This misalignment causes the electromagnetic energy to concentrate at a focal point away from the system's boresight, leading to unpredictable reflection paths. As a result, the reflected power from the tissue or phantom is no longer directed toward the radar receiver antenna, thereby compromising the sensing accuracy and reliability. This issue is particularly problematic in radar systems with only a single transmitter and receiver pair, where the focal point misalignment can lead to near-zero reception despite localized energy absorption within the target.

In the prototype system using the Infineon radar, which includes three spatially separated receiver antennas, this limitation is partially mitigated, as at least one receiver is more likely to capture the redirected reflected signal. However, for broader applicability, especially in compact radar configurations, this misalignment must be resolved at the design stage. Correcting the off-center focusing through phase-synthesis analysis in the metasurface design presents a considerable challenge. Specifically, achieving precise near-field phase compensation requires an accurate mapping between the radar aperture offset and the desired focal location. In the absence of a rigorous analytical model or prior phase response characterization, designing the phase profile to steer the focus onto the boresight becomes computationally intensive and prone to inaccuracies, especially under complex boundary conditions such as air–skin interfaces.

To address these limitations, a promising future direction is the development of a planar gradient-index (GRIN) Luneburg lens structure tailored for near-field bio-sensing applications. Unlike the high-profile, spherical GRIN lens introduced in Chapter 2, optimized for far-field applications, this planar implementation would be designed to focus electromagnetic energy precisely within the human skin while maintaining compatibility with low-profile, wearable radar systems. Such a lens would not only offer improved control over near-field wavefront shaping but also ensure accurate boresight power coupling to both the TX and RX antennas, enabling more efficient biomedical sensing performance.

5.3.4 Non-Invasive Bio-Sensing Using Metasurface-Enhanced Radar and Optical Spectroscopy Fusion

Achieving high-accuracy non-invasive glucose monitoring remains a central challenge in biomedical sensing due to the physiological complexities of glucose transport, variability across body sites, and the inherently weak dielectric contrast of glucose within biological tissues. Traditional sensing methods frequently encounter limitations such as inconsistent readings, shallow penetration depths, and low signal-to-noise ratios, challenges that are particularly evident when systems are restricted to single-frequency operation or localized point measurements. As established in this thesis, multi-frequency radar sensing offers a powerful improvement by enabling spatially and depth, resolved data acquisition. This approach captures glucose-induced dielectric variations from multiple skin layers and anatomical sites, thereby enhancing robustness and sensing resolution.

However, despite these advances, multi-frequency radar alone may still fall short of achieving the level of precision required for clinical-grade glucose monitoring, especially given individual physiological variability and environmental influences. To address this gap, the integration of radar with complementary modalities, particularly optical sensors, presents a compelling path forward. This synergistic fusion can enhance signal accuracy, compensate for weaknesses in individual modalities, and offer real-time, non-invasive glucose monitoring with higher confidence. Such hybrid systems represent a promising direction for next-generation biomedical diagnostics.

We introduce a proof-of-concept wearable platform in the form of a smart earring designed for non-invasive glucose monitoring by fusing two sensing modalities: 60 GHz millimeter-wave metasurface-enhanced radar and 940 nm near-infrared (NIR) optical spectroscopy, as presented in [242]. The earring is 3D-printed and ergonomically optimized to collect simultaneous measurements from the earlobe, an anatomically favorable site due to its minimal muscle tissue and high user comfort. As shown in Fig. The mm-wave radar operates in reflection mode, capturing variations in the dielectric properties of tissue as glucose levels change, while the optical sensor functions in transmission mode, measuring the amount of absorbed and scattered light, which also correlates with glucose concentration.

The key contribution of this work is the demonstration that combining both sensing techniques significantly improves glucose monitoring accuracy, as shown in Fig. 5.13. Individually, the radar and optical sensors achieved average measurement errors of 13.42% and 7.99%, respectively. However, when their data was fused using a Kalman filtering algorithm, the error was reduced to 5.99%. This improvement reflects the complementary nature of the two modalities: radar performs better at higher glucose concentrations due to more pronounced dielectric changes, whereas optical sensing offers higher sensitivity at

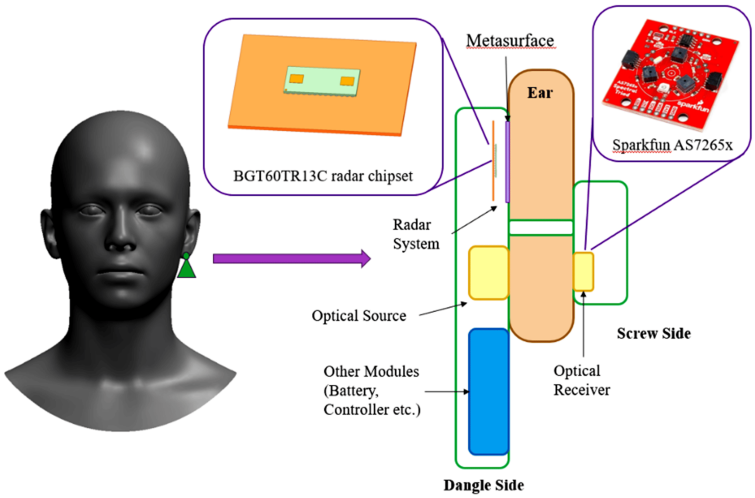


Figure 5.13: Multi-technology fusion setup integrating a metasurface-enhanced mm-wave radar and an optical sensor for high-accuracy, non-invasive glucose monitoring at the earlobe.

lower glucose levels where scattering dominates. The use of sensor fusion also addresses many challenges associated with each individual modality. For instance, radar sensors are susceptible to motion artifacts and environmental noise such as humidity, while optical sensors can experience saturation or signal degradation at higher concentrations. By integrating both, the system becomes more robust to external influences and physiological variability.

The device's wearable format also supports the practical need for continuous, unobtrusive monitoring in real-world settings, potentially enabling real-time alerts for individuals with diabetes or glucose regulation concerns. Therefore, this work validates the use of multimodal sensing by showing that combining radar and optical spectroscopy leads to improved glucose monitoring performance. The dual-mode approach leverages the strengths of both technologies, electromagnetic wave reflection and optical transmission, to provide a broader dynamic range and increased measurement reliability.

Together, multi-frequency, multi-technology strategies establish a flexible, scalable platform for non-invasive glucose monitoring with enhanced resolution, deeper tissue penetration, and improved tolerance to biological variability. The resulting system architecture supports real-time bio-signal acquisition and paves the way for more reliable wearable health monitoring solutions in the future work.

References

[1] Shuqin Dong, Li Wen, Yangtao Ye, Zhi Zhang, Yi Wang, Zhiwei Liu, Qing Cao, Yuchen Xu, Changzhi Li, and Changzhan Gu. A review on recent advancements of biomedical radar for clinical applications. *IEEE Open Journal of Engineering in Medicine and Biology*, 2024.

[2] Denghao Li, Yukun Huang, Huaqing Li, Jingran Cheng, Wenwen Zhu, and Haoming Feng. A novel approach to accurate respiratory rate and heart rate estimation via fmcw radar. *IEEE Sensors Journal*, 2025.

[3] Kun Liu, Min Li, Chu He, Xu Tian, Junbin Mao, Min Zeng, and Jin Liu. Unisleeppos: Sleep posture identification system utilizing millimeter-wave radar. In *2024 IEEE International Conference on Bioinformatics and Biomedicine (BIBM)*, pages 2232–2237. IEEE, 2024.

[4] Shadi Abudalfa and Kevin Bouchard. A hybrid vision transformer and residual neural network model for fall detection using uwb radars. *Applied Intelligence*, 55(3):1–17, 2025.

[5] Ala Eldin Omer, Lu Shi, Juewen Liu, and George Shaker. Unveiling challenges in non-invasive blood glucose monitoring: Impact of medications on the electromagnetic properties of blood. *IEEE Open Journal of Antennas and Propagation*, 2025.

[6] KD Stephan, JB Mead, DM Pozar, L Wang, and JA Pearce. A near field focused microstrip array for a radiometric temperature sensor. *IEEE transactions on antennas and propagation*, 55(4):1199–1203, 2007.

[7] Domenica AM Iero, Lorenzo Crocco, and Tommaso Isernia. Thermal and microwave constrained focusing for patient-specific breast cancer hyperthermia: A robustness assessment. *IEEE Transactions on Antennas and Propagation*, 62(2):814–821, 2013.

[8] Sanghoek Kim, John S Ho, and Ada SY Poon. Wireless power transfer to miniature implants: Transmitter optimization. *IEEE Transactions on Antennas and Propagation*, 60(10):4838–4845, 2012.

[9] Yuanwei Liu, Jiaqi Xu, Zhaolin Wang, Xidong Mu, and Lajos Hanzo. Near-field communications: What will be different? *IEEE Wireless Communications*, 32(2): 262–270, 2025.

[10] Md Atiqur Rahman Ahad and Atsushi Inoue. *Vision, Sensing and Analytics: Integrative Approaches*. Springer, 2021.

[11] Woobin Kim, Hyeong-Rae Im, Yeong-Hoon Noh, Ic-Pyo Hong, Hyun-Sung Tae, Jeong-Kyu Kim, and Jong-Gwan Yook. Near-field to far-field rcs prediction on arbitrary scanning surfaces based on spherical wave expansion. *Sensors*, 20(24):7199, 2020.

[12] Gianluca Ciattaglia, Adelmo De Santis, Linda Senigagliesi, Michela Raimondi, Antonio Nocera, Ennio Gambi, and Susanna Spinsante. The impact of automotive radar configuration on power consumption: The case of ti awr1843. In *2024 IEEE International Workshop on Metrology for Automotive (MetroAutomotive)*, pages 29–34. IEEE, 2024.

[13] Lakshi Prosad Roy et al. Through-the-wall hb100 radar signal processing for estimating frequency of vibrating diaphragm. In *2020 IEEE Region 10 Symposium (TENSYMP)*, pages 851–854. IEEE, 2020.

[14] Ariele Sapienza. Joint communication and sensing for eye tracking and gesture recognition with fmcw radar in smart glasses. 2023.

[15] Serene Abu-Sardanah. Cardio-respiratory health monitoring using a wearable radar system. 2023.

[16] Florian Engels, Philipp Heidenreich, Markus Wintermantel, Lukas Stäcker, Muhammed Al Kadi, and Abdelhak M Zoubir. Automotive radar signal processing: Research directions and practical challenges. *IEEE Journal of Selected Topics in Signal Processing*, 15(4):865–878, 2021.

[17] Boxun Yan and Ian P Roberts. Advancements in millimeter-wave radar technologies for automotive systems: A signal processing perspective. *Electronics*, 14(7):1436, 2025.

[18] Wael Abdullah Ahmad and Xiang Yi. How will radar be integrated into daily life?: mm-wave radar architectures for modern daily life applications. *IEEE Microwave Magazine*, 23(5):30–43, 2022.

[19] Muhammad Ali Jamshed, Kamran Ali, Qammer H Abbasi, Muhammad Ali Imran, and Masood Ur-Rehman. Challenges, applications, and future of wireless sensors in internet of things: A review. *IEEE Sensors Journal*, 22(6):5482–5494, 2022.

[20] Liangyu Gan, Yuan Liu, Yanzhong Li, Runxi Zhang, Leilei Huang, and Chunqi Shi. Gesture recognition system using 24 ghz fmcw radar sensor realized on real-time edge computing platform. *IEEE Sensors Journal*, 22(9):8904–8914, 2022.

[21] Changzhan Gu and Jaime Lien. A two-tone radar sensor for concurrent detection of absolute distance and relative movement for gesture sensing. *IEEE sensors letters*, 1(3):1–4, 2017.

[22] Marco Mercuri, Ilde Rosa Lorato, Yao-Hong Liu, Fokko Wieringa, Chris Van Hoof, and Tom Torfs. Vital-sign monitoring and spatial tracking of multiple people using a contactless radar-based sensor. *Nature Electronics*, 2(6):252–262, 2019.

[23] Steffen Scherr, Benjamin Göttel, Serdal Ayhan, Akanksha Bhutani, Mario Pauli, Wolfgang Winkler, J Christoph Scheytt, and Thomas Zwick. Miniaturized 122 ghz ism band fmcw radar with micrometer accuracy. In *2015 European Radar Conference (EuRAD)*, pages 277–280. IEEE, 2015.

[24] Nils Pohl, Timo Jaeschke, and Klaus Aufinger. An ultra-wideband 80 ghz fmcw radar system using a sige bipolar transceiver chip stabilized by a fractional-n pll synthesizer. *IEEE Transactions on Microwave Theory and Techniques*, 60(3):757–765, 2012.

[25] Alexandros Ninos, Jürgen Hasch, Mario Emilio Pizano Alvarez, and Thomas Zwick. Synthetic radar dataset generator for macro-gesture recognition. *IEEE Access*, 9: 76576–76584, 2021.

[26] Fan Liu, Yuanhao Cui, Christos Masouros, Jie Xu, Tony Xiao Han, Yonina C Eldar, and Stefano Buzzi. Integrated sensing and communications: Toward dual-functional wireless networks for 6g and beyond. *IEEE journal on selected areas in communications*, 40(6):1728–1767, 2022.

[27] Ala Eldin Omer, George Shaker, Safieddin Safavi-Naeini, Hamid Kokabi, Georges Alquié, Frédérique Deshours, and Raed M Shubair. Low-cost portable microwave

sensor for non-invasive monitoring of blood glucose level: Novel design utilizing a four-cell csrr hexagonal configuration. *Scientific Reports*, 10(1):15200, 2020.

[28] Kyeongha Kwon, Jong Uk Kim, Yujun Deng, Siddharth R Krishnan, Jungil Choi, Hokyung Jang, KunHyuck Lee, Chun-Ju Su, Injae Yoo, Yixin Wu, et al. An on-skin platform for wireless monitoring of flow rate, cumulative loss and temperature of sweat in real time. *Nature Electronics*, 4(4):302–312, 2021.

[29] Mallika Bariya, Hnin Yin Yin Nyein, and Ali Javey. Wearable sweat sensors. *Nature Electronics*, 1(3):160–171, 2018.

[30] Mostafa Alizadeh, George Shaker, João Carlos Martins De Almeida, Plinio Pelegrini Morita, and Safeddin Safavi-Naeini. Remote monitoring of human vital signs using mm-wave fmcw radar. *IEEE Access*, 7:54958–54968, 2019.

[31] Xiaonan Hui and Edwin C Kan. Monitoring vital signs over multiplexed radio by near-field coherent sensing. *Nature Electronics*, 1(1):74–78, 2018.

[32] Plinio Pelegrini Morita, AS Rocha, George Shaker, D Lee, J Wei, B Fong, A Thatte, A Karimi, L Xu, A Ma, et al. Comparative analysis of gait speed estimation using wideband and narrowband radars, thermal camera, and motion tracking suit technologies. *Journal of Healthcare Informatics Research*, 4:215–237, 2020.

[33] Zhijun Xiao, Chenxi Yang, Yumin Li, Yantao Xing, Caiyun Ma, Yuwei Zhang, Xi Long, Jianqing Li, and Chengyu Liu. Human eye activity monitoring using continuous wave doppler radar: A feasibility study. *IEEE Transactions on Biomedical Circuits and Systems*, 2023.

[34] Rahmat Ullah, Imran Saied, and Tughrul Arslan. Multistatic radar-based imaging in layered and dispersive media for biomedical applications. *Biomedical Signal Processing and Control*, 82:104568, 2023.

[35] Rohit Chandra, Huiyuan Zhou, Ilangko Balasingham, and Ram M Narayanan. On the opportunities and challenges in microwave medical sensing and imaging. *IEEE transactions on biomedical engineering*, 62(7):1667–1682, 2015.

[36] Danilo Brizi, Maria Conte, and Agostino Monorchio. A performance-enhanced antenna for microwave biomedical applications by using metasurfaces. *IEEE Transactions on Antennas and Propagation*, 71(4):3314–3323, 2023.

[37] A Buffi, Paolo Nepa, and Giuliano Manara. Design criteria for near-field-focused planar arrays. *IEEE Antennas and Propagation Magazine*, 54(1):40–50, 2012.

[38] Ala Eldin Omer, George Shaker, Safieddin Safavi-Naeini, Kevin Murray, and Richard Hughson. Glucose levels detection using mm-wave radar. *IEEE Sensors Letters*, 2 (3):1–4, 2018.

[39] Ala Eldin Omer, Safieddin Safavi-Naeini, Richard Hughson, and George Shaker. Blood glucose level monitoring using an fmcw millimeter-wave radar sensor. *Remote Sensing*, 12(3):385, 2020.

[40] Stefano Moscato, Giulia Matrone, Marco Pasian, Andrea Mazzanti, Maurizio Bozzi, Luca Perregrini, Francesco Svelto, Giovanni Magenes, Paolo Arcioni, Paul Summers, et al. A mm-wave 2d ultra-wideband imaging radar for breast cancer detection. *International Journal of Antennas and Propagation*, 2013, 2013.

[41] Amir Mirbeik-Sabzevari, Sensen Li, Edgar Garay, Huy-Thong Nguyen, Hua Wang, and Negar Tavassolian. Synthetic ultra-high-resolution millimeter-wave imaging for skin cancer detection. *IEEE Transactions on Biomedical Engineering*, 66(1):61–71, 2018.

[42] Jessi E Johnson, Oliver Shay, Chris Kim, and Catherine Liao. Wearable millimeter-wave device for contactless measurement of arterial pulses. *IEEE transactions on biomedical circuits and systems*, 13(6):1525–1534, 2019.

[43] Serene Abu-Sardanah, Ali Gharamohammadi, Omar M Ramahi, and George Shaker. A wearable mm-wave radar platform for cardiorespiratory monitoring. *IEEE Sensors Letters*, 2023.

[44] Changzhi Li, Victor M Lubecke, Olga Boric-Lubecke, and Jenshan Lin. A review on recent advances in doppler radar sensors for noncontact healthcare monitoring. *IEEE Transactions on microwave theory and techniques*, 61(5):2046–2060, 2013.

[45] Carlo Massaroni, Andrea Nicolò, Emiliano Schena, and Massimo Sacchetti. Remote respiratory monitoring in the time of covid-19. *Frontiers in physiology*, 11:635, 2020.

[46] Mehran Baboli, Aditya Singh, Bruce Soll, Olga Boric-Lubecke, and Victor M Lubecke. Wireless sleep apnea detection using continuous wave quadrature doppler radar. *IEEE Sensors Journal*, 20(1):538–545, 2019.

[47] Mehran Baboli, Aditya Singh, Bruce Soll, Olga Boric-Lubecke, and Victor M Lubecke. Good night: Sleep monitoring using a physiological radar monitoring system integrated with a polysomnography system. *IEEE Microwave Magazine*, 16(6): 34–41, 2015.

[48] Liang Liu, Mihail Popescu, Marjorie Skubic, Marilyn Rantz, Tarik Yardibi, and Paul Cuddihy. Automatic fall detection based on doppler radar motion signature. In *2011 5th International Conference on Pervasive Computing Technologies for Healthcare (PervasiveHealth) and Workshops*, pages 222–225. IEEE, 2011.

[49] Marco Mercuri, Ping Jack Soh, Gokarna Pandey, Peter Karsmakers, Guy AE Vandenbosch, Paul Leroux, and Dominique Schreurs. Analysis of an indoor biomedical radar-based system for health monitoring. *IEEE Transactions on Microwave Theory and Techniques*, 61(5):2061–2068, 2013.

[50] Sherif Abdulatif, Fady Aziz, Pelin Altiner, Bernhard Kleiner, and Urs Schneider. Power-based real-time respiration monitoring using fmcw radar. *arXiv preprint arXiv:1711.09198*, 2017.

[51] Domenico Zito, Domenico Pepe, Martina Mincica, Fabio Zito, Alessandro Tognetti, Antonio Lanatà, and Danilo De Rossi. Soc cmos uwb pulse radar sensor for contactless respiratory rate monitoring. *IEEE transactions on biomedical circuits and systems*, 5(6):503–510, 2011.

[52] Jussi Kuutti, Mikko Paukkunen, Miro Aalto, Pekka Eskelinen, and Raimo E Sepponen. Evaluation of a doppler radar sensor system for vital signs detection and activity monitoring in a radio-frequency shielded room. *Measurement*, 68:135–142, 2015.

[53] Abhishek Kandwal, Louis WY Liu, Jamal Deen, Rohit Jasrotia, Binod Kumar Kanaujia, and Zedong Nie. Electromagnetic wave sensors for non-invasive blood glucose monitoring: Review and recent developments. *IEEE Transactions on Instrumentation and Measurement*, 2023.

[54] SJ Jebasingh Kirubakaran, M Anto Bennet, and NR Shanker. Non-invasive antenna sensor based continuous glucose monitoring using pancreas dielectric radiation signal energy levels and machine learning algorithms. *Biomedical Signal Processing and Control*, 85:105072, 2023.

[55] Xia Xiao and Qinwei Li. A noninvasive measurement of blood glucose concentration by uwb microwave spectrum. *ieee antennas and wireless propagation letters*, 16: 1040–1043, 2016.

[56] Sina Kiani, Pejman Rezaei, and Mina Fakhr. Dual-frequency microwave resonant sensor to detect noninvasive glucose-level changes through the fingertip. *IEEE Transactions on Instrumentation and Measurement*, 70:1–8, 2021.

[57] Ala Eldin Omer, George Shaker, Safieddin Safavi-Naeini, Georges Alquié, Frédérique Deshours, Hamid Kokabi, and Raed M Shubair. Non-invasive real-time monitoring of glucose level using novel microwave biosensor based on triple-pole csrr. *IEEE Transactions on Biomedical Circuits and Systems*, 14(6):1407–1420, 2020.

[58] Zengxiang Wang, Xia Xiao, Yanwei Pang, and Wenling Su. Accurate blood glucose level monitoring using microwave imaging. *Measurement Science and Technology*, 35 (7):076120, 2024.

[59] Anmole S Bolla and Ronny Priefer. Blood glucose monitoring-an overview of current and future non-invasive devices. *Diabetes & Metabolic Syndrome: Clinical Research & Reviews*, 14(5):739–751, 2020.

[60] George Shaker, Karly Smith, Ala Eldin Omer, Shuo Liu, Clement Csech, Udeshaya Wadhwa, Safieddin Safavi-Naeini, and Richard Hughson. Non-invasive monitoring of glucose level changes utilizing a mm-wave radar system. *International Journal of Mobile Human Computer Interaction (IJMHCI)*, 10(3):10–29, 2018.

[61] Reza Nikandish, Caroline Sheedy, Jiayu He, Ruth Crowe, and Deeksha Rao. Contactless glucose sensing using miniature mm-wave radar and tiny machine learning. *IEEE Journal of Microwaves*, 2024.

[62] Yuyang Sun, Helena Cano-Garcia, Efthymios Kallos, Fergus O'Brien, Adeyemi Akintonde, Diana-Elena Motei, Oana Ancu, Richard William Alexander Mackenzie, and Panagiotis Kosmas. Random forest analysis of combined millimeter-wave and near-infrared sensing for noninvasive glucose detection. *IEEE Sensors Journal*, 23(17): 20294–20309, 2023.

[63] Sami Gabriel, RW Lau, and Camelia Gabriel. The dielectric properties of biological tissues: Iii. parametric models for the dielectric spectrum of tissues. *Physics in medicine & biology*, 41(11):2271, 1996.

[64] Lulu Wang. Microwave imaging and sensing techniques for breast cancer detection. *Micromachines*, 14(7):1462, 2023.

[65] Anuradha Singh. *A NON-CONTACT VITAL SIGNS MONITORING APPROACH USING FMCW mmWAVE RADAR*. PhD thesis, Auckland University of Technology, 2023.

[66] Yuanwei Liu, Zhaolin Wang, Jiaqi Xu, Chongjun Ouyang, Xidong Mu, and Robert Schober. Near-field communications: A tutorial review. *IEEE Open Journal of the Communications Society*, 4:1999–2049, 2023.

[67] Cansu Eren, Saeid Karamzadeh, and Mesut Kartal. The artifacts of human physical motions on vital signs monitoring. In *2019 Scientific Meeting on Electrical-Electronics & Biomedical Engineering and Computer Science (EBBT)*, pages 1–5. IEEE, 2019.

[68] Beatriz Soares, Carolina Gouveia, Daniel Albuquerque, and Pedro Pinho. Impact and classification of body stature and physiological variability in the acquisition of vital signs using continuous wave radar. *Applied Sciences*, 14(2):921, 2024.

[69] International Commission on Non-Ionizing Radiation Protection et al. Guidelines for limiting exposure to electromagnetic fields (100 khz to 300 ghz). *Health physics*, 118 (5):483–524, 2020.

[70] Shekh Md Mahmudul Islam. Radar-based remote physiological sensing: Progress, challenges, and opportunities. *Frontiers in Physiology*, 13:955208, 2022.

[71] Kyoung-Sub Oh, Pei-Yuan Qin, and Dong-Wook Seo. Near-field radar equation based on fresnel diffraction formula to detect short-ranged targets for automotive radar. *Journal of Electromagnetic Engineering and Science*, 24(2):161–169, 2024.

[72] Paolo Nepa and Alice Buffi. Near-field-focused microwave antennas: Near-field shaping and implementation. *IEEE Antennas and Propagation Magazine*, 59(3):42–53, 2017.

[73] Marcelo B Perotoni and Cynthia Junqueira. X-band printed fresnel zone plate antenna: Design, simulation, and field measurements. *Microwave and Optical Technology Letters*, 57(11):2604–2609, 2015.

[74] Paolo Nepa, Alice Buffi, Andrea Michel, Giuliano Manara, et al. Technologies for near-field focused microwave antennas. *International Journal of Antennas and Propagation*, 2017, 2017.

[75] Darwin Blanco, Jose Luis Gómez-Tornero, Eva Rajo-Iglesias, and Nuria Llombart. Radially polarized annular-slot leaky-wave antenna for three-dimensional near-field microwave focusing. *IEEE Antennas and Wireless Propagation Letters*, 13:583–586, 2014.

[76] Sébastien Clauzier, Stéphane Avrillon, Laurent Le Coq, Mohamed Himdi, Franck Colombel, and Erwan Rochefort. Slotted waveguide antenna with a near-field focused beam in one plane. *IET Microwaves, Antennas & Propagation*, 9(7):634–639, 2015.

[77] Hsi-Tseng Chou, Chien-Te Yu, Kai-Te Wang, and Paolo Nepa. A simple design of patch antenna array with an optimized field distribution in the near-zone for rfid applications. *IEEE Antennas and Wireless Propagation Letters*, 13:257–260, 2014.

[78] Saber H Zainud-Deen, Hend A Malhat, and Kamal H Awadalla. Near-field focusing dielectric resonator antenna array for fixed rfid readers. *International Journal of Engineering Business Management*, 4(Godište 2012):4–23, 2012.

[79] Yu Jian Cheng and Fei Xue. Ka-band near-field-focused array antenna with variable focal point. *IEEE transactions on antennas and propagation*, 64(5):1725–1732, 2016.

[80] Alejandro Javier Martinez-Ros, José Luis Gómez-Tornero, and George Goussetis. Holographic pattern synthesis with modulated substrate integrated waveguide line-source leaky-wave antennas. *IEEE Transactions on Antennas and Propagation*, 61 (7):3466–3474, 2013.

[81] JJ Bai, LD Ma, Q Chen, GF Zhang, and YQ Fu. Design of millimeter wave near-field focused array antenna. In *2016 IEEE International Conference on Microwave and Millimeter Wave Technology (ICMMT)*, volume 2, pages 668–670. IEEE, 2016.

[82] Hsi-Tseng Chou, Pai-Han Hsueh, Tso-Ming Hung, Li-Ruei Kuo, and Hsi-Hsir Chou. A dual-band near-field focused reflectarray antenna for rfid applications at 0.9 and 2.4 ghz. *Radio Science*, 46(06):1–8, 2011.

[83] Bai-Qiang You, Yu-Xi Liu, Jian-Hua Zhou, and Hsi-Tseng Chou. Numerical synthesis of dual-band reflectarray antenna for optimum near-field radiation. *IEEE Antennas and Wireless Propagation Letters*, 11:760–762, 2012.

[84] Hsi-Tseng Chou, Tso-Ming Hung, Nan-Nan Wang, Hsi-Hsir Chou, Chia Tung, and Paolo Nepa. Design of a near-field focused reflectarray antenna for 2.4 ghz rfid reader applications. *IEEE Transactions on Antennas and Propagation*, 59(3):1013–1018, 2010.

[85] Saber H Zainud-Deen, Shaymaa M Gaber, Hend A Malhat, and Kamal H Awadalla. B10. multilayer dielectric resonator antenna transmitarray for near-field and far-field fixed rfid reader. In *2012 29th National Radio Science Conference (NRSC)*, pages 81–88. IEEE, 2012.

[86] Wan-Ting Hung, Jen-Jung Tung, and Shih-Yuan Chen. A focusing reflectarray and its application in microwave virus sanitizer. *Radio Science*, 49(10):890–898, 2014.

[87] Enrique G Plaza, Germán León, Susana Loredo, and Fernando Las-Heras. Near-field focusing transmitarray lens. In *2015 9th European Conference on Antennas and Propagation (EuCAP)*, pages 1–5. IEEE, 2015.

[88] Ahmed Toaha Mobashsher and AM Abbosh. Performance of directional and omnidirectional antennas in wideband head imaging. *IEEE Antennas and Wireless Propagation Letters*, 15:1618–1621, 2016.

[89] Yifan Wang, Amin M Abbosh, Bassem Henin, and Phong Thanh Nguyen. Synthetic bandwidth radar for ultra-wideband microwave imaging systems. *IEEE Transactions on Antennas and Propagation*, 62(2):698–705, 2013.

[90] João M Felício, José M Bioucas-Dias, Jorge R Costa, and Carlos A Fernandes. Antenna design and near-field characterization for medical microwave imaging applications. *IEEE Transactions on Antennas and Propagation*, 67(7):4811–4824, 2019.

[91] Chan Hwang See, Raed A Abd-Alhameed, Siau Wei Jonis Chung, Dawei Zhou, Hussain Al-Ahmad, and Peter S Excell. The design of a resistively loaded bowtie antenna for applications in breast cancer detection systems. *IEEE Transactions on Antennas and Propagation*, 60(5):2526–2530, 2012.

[92] AT Mobashsher and AM Abbosh. Compact 3-d slot-loaded folded dipole antenna with unidirectional radiation and low impulse distortion for head imaging applications. *IEEE Transactions on Antennas and Propagation*, 64(7):3245–3250, 2016.

[93] Emily Porter, Hadi Bahrami, Adam Santorelli, Benoit Gosselin, Leslie A Rusch, and Milica Popović. A wearable microwave antenna array for time-domain breast tumor screening. *IEEE transactions on medical imaging*, 35(6):1501–1509, 2016.

[94] David Gibbins, Maciej Klemm, Ian J Craddock, Jack A Leendertz, Alan Preece, and Ralph Benjamin. A comparison of a wide-slot and a stacked patch antenna for the purpose of breast cancer detection. *IEEE transactions on antennas and propagation*, 58(3):665–674, 2009.

[95] Jeremie Bourqui, Michal Okoniewski, and Elise C Fear. Balanced antipodal vivaldi antenna with dielectric director for near-field microwave imaging. *IEEE Transactions on Antennas and Propagation*, 58(7):2318–2326, 2010.

[96] Reza K Amineh, Maryam Ravan, Aastha Trehan, and Natalia K Nikolova. Near-field microwave imaging based on aperture raster scanning with tem horn antennas. *IEEE Transactions on Antennas and Propagation*, 59(3):928–940, 2010.

[97] L Shafai, AA Kishk, and A Sebak. Near field focusing of apertures and reflector antennas. In *IEEE WESCANEX 97 Communications, Power and Computing. Conference Proceedings*, pages 246–251. IEEE, 1997.

[98] Shimul Saha, Helena Cano-Garcia, Ioannis Sotiriou, Oliver Lipscombe, Ioannis Gouzouasis, Maria Koutsoupidou, George Palikaras, Richard Mackenzie, Thomas Reeve, Panagiotis Kosmas, et al. A glucose sensing system based on transmission measurements at millimetre waves using micro strip patch antennas. *Scientific reports*, 7(1):6855, 2017.

[99] Long Shan and Wen Geyi. Optimal design of focused antenna arrays. *IEEE Transactions on Antennas and Propagation*, 62(11):5565–5571, 2014.

[100] Shixing Yu, Na Kou, Zhao Ding, and Zhengping Zhang. Design of dual-polarized reflectarray for near-field shaped focusing. *IEEE Antennas and Wireless Propagation Letters*, 20(5):803–807, 2021.

[101] Long Li, Pei Zhang, Fangjie Cheng, Mingyang Chang, and Tie Jun Cui. An optically transparent near-field focusing metasurface. *IEEE transactions on microwave theory and techniques*, 69(4):2015–2027, 2021.

[102] Aleksandr Markvart, Mingzhao Song, Stanislav Glybovski, Pavel Belov, Constantin Simovski, and Polina Kapitanova. Metasurface for near-field wireless power transfer with reduced electric field leakage. *IEEE Access*, 8:40224–40231, 2020.

[103] Shixing Yu, Haixia Liu, and Long Li. Design of near-field focused metasurface for high-efficient wireless power transfer with multifocus characteristics. *IEEE Transactions on Industrial Electronics*, 66(5):3993–4002, 2018.

[104] Álvaro F Vaquero, Marcos Rodríguez Pino, Manuel Arrebola, Sérgio A Matos, Jorge R Costa, and Carlos A Fernandes. Evaluation of a dielectric-only transmitarray for generating multi-focusing near-field spots using a cluster of feeds in the ka-band. *Sensors*, 21(2):422, 2021.

[105] Saber H Zainud-Deen, WM Hassan, and HA Malhat. Near-field focused folded transmitarray antenna for medical applications. *Wireless Personal Communications*, 96: 4885–4894, 2017.

[106] Mohammad Omid Bagheri, Hamid Reza Hassani, and Abdel Razik Sebak. Stable phase-centre horn antenna using 3d printed dielectric rod for aperture efficiency improvement of space-fed antennas. *IET Microwaves, Antennas & Propagation*, 16 (14):888–897, 2022.

[107] JT Loane and S-W Lee. Gain optimization of a near-field focusing array for hyperthermia applications. *IEEE Transactions on Microwave Theory and Techniques*, 37 (10):1629–1635, 1989.

[108] Xiaoping He, Wen Geyi, and Shenyun Wang. Optimal design of focused arrays for microwave-induced hyperthermia. *IET Microwaves, Antennas & Propagation*, 9(14): 1605–1611, 2015.

[109] Farzad Tofigh, Javad Nourinia, MohammadNaghi Azarmanesh, and Kayvan M Khazaei. Near-field focused array microstrip planar antenna for medical applications. *IEEE antennas and wireless propagation letters*, 13:951–954, 2014.

[110] NS Karnik, R Tulpule, M Shah, PS Verma, CY Huang, JY Cha, A Pandya, S Usman, V Pulipati, P Pagadala, et al. Design, simulation and experimental study of near-field beam forming techniques using conformal waveguide arrays. *IET microwaves, antennas & propagation*, 4(2):162–174, 2010.

[111] Hsi-Tseng Chou, Kuo-Lung Hung, and Hsi-Hsir Chou. Design of periodic antenna arrays with the excitation phases synthesized for optimum near-field patterns via steepest descent method. *IEEE transactions on antennas and propagation*, 59(11): 4342–4345, 2011.

[112] Jiangli Shang and Ying Yu. An ultrawideband capsule antenna for biomedical applications. *IEEE Antennas and Wireless Propagation Letters*, 18(12):2548–2551, 2019.

[113] GS Deepthy and M Nesasudha. Analysis of substrate materials in microstrip antenna for biomedical applications. *Materials Today: Proceedings*, 2023.

[114] Chi-Fuk So, Kup-Sze Choi, Thomas KS Wong, and Joanne WY Chung. Recent advances in noninvasive glucose monitoring. *Medical Devices: Evidence and Research*, pages 45–52, 2012.

[115] Jayoung Kim, Alan S Campbell, and Joseph Wang. Wearable non-invasive epidermal glucose sensors: A review. *Talanta*, 177:163–170, 2018.

[116] IA Novikov. Noninvasive determination of blood glucose concentration by comparing the eardrum and head skin temperatures. *Biomedical Engineering*, 51(5):341–346, 2018.

[117] Elise C Fear. Microwave imaging of the breast. *Technology in Cancer Research & Treatment*, 4(1):69–82, 2005.

[118] Paul M Meaney, Margaret W Fanning, Dun Li, Steven P Poplack, and Keith D Paulsen. A clinical prototype for active microwave imaging of the breast. *IEEE Transactions on Microwave Theory and Techniques*, 48(11):1841–1853, 2000.

[119] Sudhir Shrestha, Mangilal Agarwal, Joshua Reid, and Kody Varahramyan. Microstrip antennas for direct human skin placement for biomedical applications. *PIERS Proceedings, Cambridge, USA*, 2010.

[120] Mohammad Omid Bagheri and George Shaker. Near-field enhancement of microstrip antenna using engineered superstrate for biomedical applications. In *2022 IEEE International Symposium on Antennas and Propagation and USNC-URSI Radio Science Meeting (AP-S/URSI)*, pages 1038–1039. IEEE, 2022.

[121] Long Li, Haixia Liu, Huiying Zhang, and Weiming Xue. Efficient wireless power transfer system integrating with metasurface for biological applications. *IEEE Transactions on Industrial Electronics*, 65(4):3230–3239, 2017.

[122] Shuyan Zhang, Myoung-Hwan Kim, Francesco Aieta, Alan She, Tobias Mansuripur, Ilan Gabay, Mohammadreza Khorasaninejad, David Rousso, Xiaojun Wang, Mariano Troccoli, et al. High efficiency near diffraction-limited mid-infrared flat lenses based on metasurface reflectarrays. *Optics express*, 24(16):18024–18034, 2016.

[123] Rana Sadaf Anwar, Lingfeng Mao, and Huansheng Ning. Frequency selective surfaces: A review. *Applied Sciences*, 8(9):1689, 2018.

[124] Ben A Munk. *Frequency selective surfaces: theory and design*. John Wiley & Sons, 2005.

[125] Filippo Costa, Agostino Monorchio, and Giuliano Manara. An overview of equivalent circuit modeling techniques of frequency selective surfaces and metasurfaces. *The Applied Computational Electromagnetics Society Journal (ACES)*, pages 960–976, 2014.

[126] Maria Garcia-Vigueras, Francisco Mesa, Francisco Medina, Raul Rodriguez-Berral, and Jose L Gomez-Tornero. Simplified circuit model for arrays of metallic dipoles sandwiched between dielectric slabs under arbitrary incidence. *IEEE transactions on antennas and propagation*, 60(10):4637–4649, 2012.

[127] Zhipeng Li, Xi Tian, Cheng-Wei Qiu, and John S Ho. Metasurfaces for bioelectronics and healthcare. *Nature Electronics*, 4(6):382–391, 2021.

[128] Amirhossein Hajiaghajani, Amir Hosein Afandizadeh Zargari, Manik Dautta, Abel Jimenez, Fadi Kurdahi, and Peter Tseng. Textile-integrated metamaterials for near-field multibody area networks. *Nature Electronics*, 4(11):808–817, 2021.

[129] Ali Lalbakhsh, Muhammad U Afzal, Touseef Hayat, Karu P Esselle, and Kaushik Mandal. All-metal wideband metasurface for near-field transformation of medium-to-high gain electromagnetic sources. *Scientific Reports*, 11(1):9421, 2021.

[130] He Li, Yun Bo Li, Gang Chen, Shu Yue Dong, Jia Lin Shen, Chao Yue Gong, Shi Yu Wang, Hai Peng Wang, and Tie Jun Cui. High-resolution near-field imaging and far-field sensing using a transmissive programmable metasurface. *Advanced Materials Technologies*, 7(5):2101067, 2022.

[131] Simone Genovesi, Ian Richard Butterworth, José Enrique Cruz Serrallés, and Luca Daniel. Metasurface matching layers for enhanced electric field penetration into the human body. *IEEE Access*, 8:197745–197756, 2020.

[132] Mohammad Alibakhshikenari, Esraa Mousa Ali, Mohammad Soruri, Mariana Dalarsson, Mohammad Naser-Moghadasi, Bal S Virdee, Caslav Stefanovic, Anna Pietrenko-Dabrowska, Slawomir Koziel, Stanislaw Szczepanski, et al. A comprehensive survey on antennas on-chip based on metamaterial, metasurface, and substrate integrated waveguide principles for millimeter-waves and terahertz integrated circuits and systems. *IEEE Access*, 10:3668–3692, 2022.

[133] Mohammad Alibakhshikenari, Bal S Virdee, Panchamkumar Shukla, Naser Ojaroudi Parchin, Leyre Azpilicueta, Chan Hwang See, Raed A Abd-Alhameed, Francisco Falcone, Isabelle Huynen, Tayeb A Denidni, et al. Metamaterial-inspired antenna array for application in microwave breast imaging systems for tumor detection. *IEEE Access*, 8:174667–174678, 2020.

[134] Rui Pei, Mark Paul Leach, Eng Gee Lim, Zhao Wang, Chaoyun Song, Jingchen Wang, Wenzhang Zhang, Zhenzhen Jiang, and Yi Huang. Wearable ebg-backed belt antenna

for smart on-body applications. *IEEE Transactions on Industrial Informatics*, 16(11): 7177–7189, 2020.

[135] Maged A Aldhaeebi, Khawla Alzoubi, Thamer S Almoneef, Saeed M Bamatraf, Hussein Attia, and Omar M Ramahi. Review of microwaves techniques for breast cancer detection. *Sensors*, 20(8):2390, 2020.

[136] Kai Zhang, Guy AE Vandenbosch, and Sen Yan. A novel design approach for compact wearable antennas based on metasurfaces. *IEEE Transactions on biomedical circuits and systems*, 14(4):918–927, 2020.

[137] Okan Yurduseven, David R Smith, and Thomas Fromenteze. Design of a reconfigurable metasurface antenna for dynamic near-field focusing. In *2018 IEEE International Symposium on Antennas and Propagation & USNC/URSI National Radio Science Meeting*, pages 1707–1708. IEEE, 2018.

[138] Shi Lin Liu and Xian Qi Lin. Ka-band near-field focusing lens antenna with frequency scanning focal spots. In *2019 IEEE Asia-Pacific Microwave Conference (APMC)*, pages 1491–1493. IEEE, 2019.

[139] Mohammad Omid Bagheri, Ali Gharamohammadi, Serene Abu-Sardanah, Omar M Ramahi, and George Shaker. Radar near-field sensing using metasurface for biomedical applications. 2023.

[140] Hamid Akbari-Chelaresi, Dawood Alsaedi, Seyed Hossein Mirjahanmardi, Mohamed El Badawe, Ali M Albishi, Vahid Nayyeri, and Omar M Ramahi. Mammography using low-frequency electromagnetic fields with deep learning. *Scientific Reports*, 13 (1):13253, 2023.

[141] Mohammad Omid Bagheri, Omar M Ramahi, and George Shaker. Near-field sensing improvement of a radar antenna-on-chip using a transmissive superstrate. In *2023 URSI International Symposium on Electromag. Theory (EMTS)*. IEEE, 2023.

[142] ShiLin Liu, XianQi Lin, XiaoCui Jia, and Pang Ping. A near field focused lens antenna for wireless power transmission systems. In *2018 IEEE Asia-Pacific Conference on Antennas and Propagation (APCAP)*, pages 313–315. IEEE, 2018.

[143] Farhan A Ghaffar, Muhammad Umair Khalid, Khaled N Salama, and Atif Shamim. 24-ghz ltcc fractal antenna array sop with integrated fresnel lens. *IEEE Antennas and Wireless Propagation Letters*, 10:705–708, 2011.

[144] Hong Hong, Li Zhang, Heng Zhao, Hui Chu, Chen Gu, Michael Brown, Xiaohua Zhu, and Changzhi Li. Microwave sensing and sleep: Noncontact sleep-monitoring technology with microwave biomedical radar. *IEEE Microwave Magazine*, 20(8): 18–29, 2019.

[145] Timo Lauteslager, Mathias Tømmer, Tor S Lande, and Timothy G Constandinou. Dynamic microwave imaging of the cardiovascular system using ultra-wideband radar-on-chip devices. *IEEE Transactions on Biomedical Engineering*, 69(9):2935–2946, 2022.

[146] Qian Zhai, Xiangyu Han, Yi Han, Jingang Yi, Shuoyu Wang, and Tao Liu. A contactless on-bed radar system for human respiration monitoring. *IEEE Transactions on Instrumentation and Measurement*, 71:1–10, 2022.

[147] Qimeng Li, Jikui Liu, Raffaele Gravina, Weilin Zang, Ye Li, and Giancarlo Fortino. A uwb radar-based adaptive method for in-home monitoring of elderly. *IEEE Internet of Things Journal*, 2023.

[148] Ann-Kathrin Seifert, Moeness G Amin, and Abdelhak M Zoubir. Toward unobtrusive in-home gait analysis based on radar micro-doppler signatures. *IEEE Transactions on Biomedical Engineering*, 66(9):2629–2640, 2019.

[149] Piyali Goswami, Sandeep Rao, Sachin Bharadwaj, and Amanda Nguyen. Real-time multi-gesture recognition using 77 ghz fmcw mimo single chip radar. In *2019 IEEE International Conference on Consumer Electronics (ICCE)*, pages 1–4. IEEE, 2019.

[150] Sergio Saponara, Maria Sabrina Greco, and Fulvio Gini. Radar-on-chip/in-package in autonomous driving vehicles and intelligent transport systems: Opportunities and challenges. *IEEE Signal Processing Magazine*, 36(5):71–84, 2019.

[151] Emanuele Tavanti, Ali Rizik, Alessandro Fedeli, Daniele D Caviglia, and Andrea Randazzo. A short-range fmcw radar-based approach for multi-target human-vehicle detection. *IEEE Transactions on Geoscience and Remote Sensing*, 60:1–16, 2021.

[152] Siew Bee Yeap, Xianming Qing, and Zhi Ning Chen. 77-ghz dual-layer transmit-array for automotive radar applications. *IEEE Transactions on Antennas and Propagation*, 63(6):2833–2837, 2015.

[153] Andrea Wrabel, Roland Graef, and Tobias Brosch. A survey of artificial intelligence approaches for target surveillance with radar sensors. *IEEE Aerospace and Electronic Systems Magazine*, 36(7):26–43, 2021.

[154] Paul Hallbjorner, Zhongxia He, Staffan Bruce, and Shi Cheng. Low-profile 77-ghz lens antenna with array feeder. *IEEE Antennas and wireless propagation letters*, 11: 205–207, 2012.

[155] Nicolas Scheiner, Ole Schumann, Florian Kraus, Nils Appenrodt, Jürgen Dickmann, and Bernhard Sick. Off-the-shelf sensor vs. experimental radar-how much resolution is necessary in automotive radar classification? In *2020 IEEE 23rd International Conference on Information Fusion (FUSION)*, pages 1–8. IEEE, 2020.

[156] Junho Yeo and Jong-Ig Lee. Gain enhancement of microstrip patch array antennas using two metallic plates for 24 ghz radar applications. *Electronics*, 12(7):1512, 2023.

[157] Jianqiang Zhang, Haokun Lan, Maliang Liu, and Yintang Yang. A handheld nano through-wall radar locating with the gain-enhanced vivaldi antenna. *IEEE Sensors Journal*, 20(8):4420–4429, 2019.

[158] Marco Faenzi, David González-Ovejero, Giovanni Petraglia, Giuliana D'Alterio, Fabio Pascariello, Roberto Vitiello, and Stefano Maci. A metasurface radar monopulse antenna. *IEEE Transactions on Antennas and Propagation*, 70(4):2571–2579, 2021.

[159] Rahul Umesh Kale and Manish Dhananjay Sawale. A systematic review of design and performance enhancement techniques for the reduction of radar cross section in multiple input multiple output antennas. *Computers and Electrical Engineering*, 120:109697, 2024.

[160] Deepak Gangwar, Shamsher Singh, Ankit Sharma, Satya P Singh, Aimé Lay-Ekuakille, et al. Design of polarization conversion metasurface for rcs reduction and gain improvement of patch antenna for ku-band radar sensing applications. *Sensors and Actuators A: Physical*, 333:113273, 2022.

[161] Hajar Abedi, Ala Eldin Omer, John Hanna, Ahmad Ansariyan, Steven Ding, Andrei Felipe Perez, Tom Paraschuk, Plinio P Morita, Jennifer Boger, Alexander Wong, et al. On the use of an in-package dielectric lens antenna for radar-based applications. *IEEE Transactions on Components, Packaging and Manufacturing Technology*, 2024.

[162] Hongming Wu, Feng Qi, Yelong Wang, and Jinkuan Wang. Refractive ice lens for millimeter wave radar imaging. *IEEE Geoscience and Remote Sensing Lett.*, 2023.

[163] Wei Lu, Bin Deng, Qiqing Fang, Xiaoqiao Wen, and Shixin Peng. Intelligent reflecting surface-enhanced target detection in mimo radar. *IEEE Sensors Letters*, 5(2):1–4, 2021.

[164] Halim Boutayeb and Tayeb A Denidni. Gain enhancement of a microstrip patch antenna using a cylindrical electromagnetic crystal substrate. *IEEE transactions on antennas and propagation*, 55(11):3140–3145, 2007.

[165] Sarawuth Chaimool, Kwok L Chung, and Prayoot Akkaraekthalin. Bandwidth and gain enhancement of microstrip patch antennas using reflective metasurface. *IEICE transactions on communications*, 93(10):2496–2503, 2010.

[166] Warren L Stutzman and Gary A Thiele. *Antenna theory and design*. John Wiley & Sons, 2012.

[167] Hajar Abedi and George Shaker. Low-cost 3d printed dielectric hyperbolic lens antenna for beam focusing and steering of a 79ghz mimo radar. In *2020 IEEE International Symposium on Antennas and Propagation and North American Radio Science Meeting*, pages 1543–1544. IEEE, 2020.

[168] Christoph Kohlberger, Richard Hüttner, Christoph Wagner, and Andreas Stelzer. Metamaterial lenses for monostatic and bistatic 77 ghz radar systems. *International journal of microwave and wireless technologies*, 15(6):1021–1026, 2023.

[169] Ayse Ecem Bezer, Mehmet Abbak, Tugrul Gursoy, and Umut Aydin. Comparison of 122 ghz lens antennas for system-on-chip fmcw radar with minimum back reflection and high gain. *IEEE Antennas and Wireless Propagation Letters*, 19(12):2329–2333, 2020.

[170] A Yaghjian and E Kornhauser. A modal analysis of the dielectric rod antenna excited by the he 11 mode. *IEEE Transactions on Antennas and Propagation*, 20(2):122–128, 1972.

[171] Kao-Cheng Huang and Zhaocheng Wang. V-band patch-fed rod antennas for high data-rate wireless communications. *IEEE transactions on antennas and propagation*, 54(1):297–300, 2006.

[172] N Fhafhiem and P Krachodnok. A high gain omnidirectional antenna using metamaterial rods. In *2014 11th International Conference on Electrical Engineering/Electronics, Computer, Telecommunications and Information Technology (ECTI-CON)*, pages 1–4. IEEE, 2014.

[173] Young Ju Lee, Wee Sang Park, Junho Yeo, and Raj Mittra. Directivity enhancement of printed antennas using a class of metamaterial superstrates. *Electromagnetics*, 26 (3-4):203–218, 2006.

[174] Mehmet A Belen and Peyman Mahouti. Design of nonuniform substrate dielectric lens antennas using 3d printing technology. *Microwave and Optical Technology Letters*, 62(2):756–762, 2020.

[175] Mohammad Omid Bagheri, Hajar Abedi, and George Shaker. 3d-printed dielectric rods for radar range enhancement. *Electronics*, 12(19):4016, 2023.

[176] Arthur A Oliner, David R Jackson, and JL Volakis. Leaky-wave antennas. *Antenna engineering handbook*, 4:12, 2007.

[177] Astrid Algaba-Brazález, Philip Arnberg, Oskar Zetterstrom, Freysteinn Viar Viarsson, Lars Manholm, Martin Johansson, and Oscar Quevedo-Teruel. Crossover level improvement between beams in a geodesic lens antenna based on a generalized luneburg lens. In *IEEE 16th European Conf. on Antennas and Propag. (EuCAP)*, pages 1–5, 2022.

[178] Omar Orgeira, Germán León, Nelson JG Fonseca, Pedro Mongelos, and Oscar Quevedo-Teruel. Near-field focusing multibeam geodesic lens antenna for stable aggregate gain in far-field. *IEEE Trans. on Antennas and Propag.*, 70(5):3320–3328, 2022.

[179] Dan Jia, Yingran He, Ning Ding, Jianzhai Zhou, Biao Du, and Wenjing Zhang. Beam-steering flat lens antenna based on multilayer gradient index metamaterials. *IEEE Antennas and Wireless Propag. Lett.*, 17(8):1510–1514, 2018.

[180] Shiyu Zhang, Yiannis Vardaxoglou, Will Whittow, and Raj Mittra. 3d-printed graded index lens for rf applications. In *2016 International Symposium on Antennas and Propagation (ISAP)*, pages 90–91. IEEE, 2016.

[181] Na Zhang, Wei Xiang Jiang, Hui Feng Ma, Wen Xuan Tang, and Tie Jun Cui. Compact high-performance lens antenna based on impedance-matching gradient-index metamaterials. *IEEE Trans. on Antennas and Propag.*, 67(2):1323–1328, 2018.

[182] Min Liang, Wei-Ren Ng, Kihun Chang, Kokou Gbele, Michael E Gehm, and Hao Xin. A 3-d luneburg lens antenna fabricated by polymer jetting rapid prototyping. *IEEE Transactions on Antennas and Propagation*, 62(4):1799–1807, 2014.

[183] Maral Ansari, Bevan Jones, and Y Jay Guo. Spherical luneburg lens of layered structure with low anisotropy and low cost. *IEEE Transactions on Antennas and Propagation*, 70(6):4307–4318, 2022.

[184] Andrey Sayanskiy, Stanislav Glybovski, Valeri Petrovich Akimov, Dmitry Filonov, Pavel Belov, and Igor Meshkovskiy. Broadband 3-d luneburg lenses based on metamaterials of radially diverging dielectric rods. *IEEE Antennas and Wireless Propagation Letters*, 16:1520–1523, 2017.

[185] Mohammad Omid Bagheri, Erik Yann Harmgarth, Henrik Ramberg, Omar M Ramahi, Yahia M. M. Antar, and George Shaker. Dielectric grin luneburg lens for enhanced radar sensing in communication systems. *IEEE Transactions on Microwave Theory and Techniques*, 2025.

[186] Guangjun Guo, Yulong Xia, Cun Wang, Muhammad Nasir, and Qi Zhu. Optimal radiation pattern of feed of luneburg lens for high-gain application. *IEEE Trans. on Antennas and Propag.*, 68(12):8139–8143, 2020.

[187] Jeffrey R von Loesecke, Henrik Ramberg, and Philip Lambert. Volume manufacturing of 3d printed grin lenses. In *2024 IEEE International Symposium on Antennas and Propagation and INC/USNC-URSI Radio Science Meeting (AP-S/INC-USNC-URSI)*, pages 533–534. IEEE, 2024.

[188] C Hobart. Novel 3d-printed flat, cylindrical lens for beam focusing and higher gain of horn antenna. In *2023 IEEE International Symposium on Antennas and Propagation and USNC-URSI Radio Science Meeting (USNC-URSI)*, pages 1693–1694. IEEE, 2023.

[189] Philip M Lambert and Trevor Polidore. 3d-printed e-band gradient dielectric lens for automotive and industrial applications. In *2022 IEEE International Symposium on Antennas and Propagation and USNC-URSI Radio Science Meeting (AP-S/URSI)*, pages 2074–2075. IEEE, 2022.

[190] Wei Wang, Philip Lambert, and Jonathan Chisum. High-frequency limits for 3d-printed gradient-index (grin) lens antennas. In *2023 IEEE International Symposium on Antennas and Propagation and USNC-URSI Radio Science Meeting (USNC-URSI)*, pages 1695–1696. IEEE, 2023.

[191] Mohammad Omid Bagheri, Hajar Abedi, and George Shaker. Radar antenna gain improvement using an integrated in-package dielectric rod superstrate. In *2021 IEEE*

International Symposium on Antennas and Propagation and USNC-URSI Radio Science Meeting (APS/URSI), pages 1793–1794. IEEE, 2021.

[192] M Grimm and D Manteuffel. On-body antenna parameters. *IEEE Transactions on Antennas and Propagation*, 63(12):5812–5821, 2015.

[193] Ashok Yadav, Vinod Kumar Singh, Akash Kumar Bhoi, Gonçalo Marques, Begonya Garcia-Zapirain, and Isabel de la Torre Díez. Wireless body area networks: Uwb wearable textile antenna for telemedicine and mobile health systems. *Micromachines*, 11(6):558, 2020.

[194] Mohammad Omid Bagheri, Ali Gharamohammadi, Serene Abu-Sardanah, Omar M Ramahi, and George Shaker. Radar near-field sensing using metasurface for biomedical applications. *Communications Engineering*, 3(1):51, 2024.

[195] Luyin Xiao, Yongjun Xie, Shida Gao, Junbao Li, and Peiyu Wu. Generalized radar range equation applied to the whole field region. *Sensors*, 22(12):4608, 2022.

[196] Hans Gregory Schantz. Near field propagation law & a novel fundamental limit to antenna gain versus size. In *2005 IEEE Antennas and Propagation Society International Symposium*, volume 3, pages 237–240. IEEE, 2005.

[197] Hassan Umair, Tarik Bin Abdul Latef, Yoshihide Yamada, Wan Nor Liza Binti Wan Mahadi, Mohamadariff Othman, Kamilia Kamardin, Mousa I Hussein, and Ali Imran Najam. Tilted beam fabry–perot antenna with enhanced gain and broadband low backscattering. *Electronics*, 10(3):267, 2021.

[198] Xianjun Sheng, Xiaolong Lu, Ning Liu, and Yunhong Liu. Design of broadband high-gain fabry–pérot antenna using frequency-selective surface. *Sensors*, 22(24): 9698, 2022.

[199] Luyin Xiao, Yongjun Xie, Peiyu Wu, and Junbao Li. Near-field gain expression for aperture antenna and its application. *IEEE Antennas and Wireless Propagation Letters*, 20(7):1225–1229, 2021.

[200] Eric A Richards, Hans G Schantz, John A Unden, Kurt A von Laven, Drew Compston, and Christian Weil. Electrically small antenna design for low frequency systems. *Notice and Signature Page*, 315, 2010.

[201] Stanislav Stefanov Zhekov, Ondrej Franek, and Gert Frølund Pedersen. Dielectric properties of human hand tissue for handheld devices testing. *Ieee Access*, 7:61949–61959, 2019.

[202] Wei Zhuang, Zhenhong Fan, Da-Zhi Ding, and Yuyuan An. Fast analysis and design of frequency selective surface using the gmresr-fft method. *Progress In Electromagnetics Research B*, 12:63–80, 2009.

[203] Xin Liu, Yuehe Ge, Xuxiang Chen, and Lvwei Chen. Design of folded reflectarray antennas using pancharatnam-berry phase reflectors. *IEEE Access*, 6:28818–28824, 2018.

[204] Mohammad Omid Bagheri, Hamid Reza Hassani, and Bahman Rahmati. Dual-band, dual-polarised metallic slot transmitarray antenna. *IET Microwaves, Antennas & Propagation*, 11(3):402–409, 2017.

[205] R Hansen. Focal region characteristics of focused array antennas. *IEEE transactions on antennas and propagation*, 33(12):1328–1337, 1985.

[206] B Rahmati and HR Hassani. High-efficient wideband slot transmitarray antenna. *IEEE Transactions on Antennas and Propagation*, 63(11):5149–5155, 2015.

[207] Ahmed H Abdelrahman, Atef Z Elsherbeni, and Fan Yang. Transmission phase limit of multilayer frequency-selective surfaces for transmitarray designs. *IEEE Transactions on Antennas and Propagation*, 62(2):690–697, 2013.

[208] Yosef Pinhasi, Asher Yahalom, and Sergey Petnev. Propagation of ultra wide-band signals in lossy dispersive media. In *2008 IEEE International Conference on Microwaves, Communications, Antennas and Electronic Systems*, pages 1–10. IEEE, 2008.

[209] Hans J Liebe, George A Hufford, and Takeshi Manabe. A model for the complex permittivity of water at frequencies below 1 thz. *International Journal of Infrared and Millimeter Waves*, 12:659–675, 1991.

[210] John W Garrett. The adult human hand: some anthropometric and biomechanical considerations. *Human factors*, 13(2):117–131, 1971.

[211] Akhileswar Chowdary, Ahmad Bazzi, and Marwa Chafii. On hybrid radar fusion for integrated sensing and communication. *IEEE Transactions on Wireless Communications*, 2024.

[212] Shuai Wang, Luoyu Mei, Ruofeng Liu, Wenchao Jiang, Zhimeng Yin, Xianjun Deng, and Tian He. Multi-modal fusion sensing: A comprehensive review of millimeter-wave radar and its integration with other modalities. *IEEE Communications Surveys & Tutorials*, 2024.

[213] Zhiqing Wei, Fengkai Zhang, Shuo Chang, Yangyang Liu, Huici Wu, and Zhiyong Feng. Mmwave radar and vision fusion for object detection in autonomous driving: A review. *Sensors*, 22(7):2542, 2022.

[214] Baris Erol, Moeness G Amin, and Boualem Boashash. Range-doppler radar sensor fusion for fall detection. In *Radar Conf.*, pages 0819–0824. IEEE, 2017.

[215] Willemijn Groenendaal, Golo Von Basum, Kristiane A Schmidt, Peter AJ Hilbers, and Natal AW Van Riel. Quantifying the composition of human skin for glucose sensor development, 2010.

[216] Brian Bogue-Jimenez, Xiaolei Huang, Douglas Powell, and Ana Doblas. Selection of noninvasive features in wrist-based wearable sensors to predict blood glucose concentrations using machine learning algorithms. *Sensors*, 22(9):3534, 2022.

[217] H van Rostenberghe. Venipuncture versus heel prick for blood glucose monitoring in neonates. *Singapore Med J*, 50(10):1004–1007, 2009.

[218] Kirsten C Kempe, David Budd, Marc Stern, John M Ellison, Linda A Saari, Carol A Adiletto, Bryan Olin, David A Price, and David L Horwitz. Palm glucose readings compared with fingertip readings under steady and dynamic glycemic conditions, using the onetouch® ultra® blood glucose monitoring system. *Diabetes technology & therapeutics*, 7(6):916–926, 2005.

[219] Debra M Lee, Sandra E Weinert, and Earl E Miller. A study of forearm versus finger stick glucose monitoring. *Diabetes Technology & Therapeutics*, 4(1):13–23, 2002.

[220] Hoda Farhat, Joseph Costantine, Youssef Tawk, Rouwaida Kanj, Ali H Ramadan, Batoul Dia, Joanna Ghaddar, and Assaad A Eid. Wireless continuous glucose monitoring using v-band circularly polarized directive antenna arrays in a transmit/receive system. *IEEE Trans. on Antennas and Propag.*, 2024.

[221] Eugene Z. Szuts, J. Phillip Lock, Kwame J. Malomo, and Antonios Anagnostopoulos. Blood glucose concentrations of arm and finger during dynamic glucose conditions. *Diabetes Technology & Therapeutics*, 4(1):3–11, 2002. doi: 10.1089/15209150252924030. Discussion 45–47.

[222] Laurence B Katz, Lorna Stewart, Danielle King, and Hilary Cameron. Meeting the new fda standard for accuracy of self-monitoring blood glucose test systems intended for home use by lay users. *Journal of diabetes science and technology*, 14(5):912–916, 2020.

[223] Guido Freckmann, Christian Schmid, Andreas Baumstark, Stefan Pleus, Maren Link, and Christof Haug. System accuracy evaluation of 43 blood glucose monitoring systems for self-monitoring of blood glucose according to din en iso 15197. *Journal of Diabetes Science and Technology*, 6(5):1060–1075, September 2012. doi: 10.1177/193229681200600510.

[224] Mohammad Omid Bagheri, Omar M Ramahi, and George Shaker. Metasurface-enhanced bio-sensing radar for advanced health monitoring. In *2024 IEEE International Symposium on Antennas and Propagation and INC/USNC-URSI Radio Science Meeting (AP-S/INC-USNC-URSI)*, pages 2473–2474. IEEE, 2024.

[225] Mohammad Omid Bagheri, Justin Chow, Omar M Ramahi, and George Shaker. Multi-radar bio-sensor fusion for real-time, distributed sensing. *IEEE International Symposium on Antennas and Propagation and North American Radio Science Meeting*, 2025.

[226] Mohammad Omid Bagheri, Omar M Ramahi, and George Shaker. Near-field scanning system for enhanced bio-sensing at low frequencies. In *2024 IEEE International Symposium on Antennas and Propagation and INC/USNC-URSI Radio Science Meeting (AP-S/INC-USNC-URSI)*, pages 2785–2786. IEEE, 2024.

[227] J Andrew Zhang, Xiaojing Huang, Y Jay Guo, Jinhong Yuan, and Robert W Heath. Multibeam for joint communication and radar sensing using steerable analog antenna arrays. *IEEE Transactions on Vehicular Technology*, 68(1):671–685, 2018.

[228] Seong-Hee Jeong, Han-Yeol Yu, Jae-Eun Lee, Jun-Nam Oh, and Kwae-Hi Lee. A multi-beam and multi-range radar with fmcw and digital beam forming for automotive applications. *Progress In Electromagnetics Research*, 124:285–299, 2012.

[229] Yuanxi Cao, Sen Yan, Jianxing Li, and Juan Chen. A pillbox based dual circularly-polarized millimeter-wave multi-beam antenna for future vehicular radar applications. *IEEE Transactions on Vehicular Technology*, 71(7):7095–7103, 2022.

[230] Yubo Wen, Pei-Yuan Qin, Stefano Maci, and Y Jay Guo. Low-profile multibeam antenna based on modulated metasurface. *IEEE Transactions on Antennas and Propagation*, 71(8):6568–6578, 2023.

[231] Daniel Martinez-de Rioja, Rafael Florencio, Eduardo Martinez-de Rioja, Manuel Arrebola, Jose A Encinar, and Rafael R Boix. Dual-band reflectarray to generate two spaced beams in orthogonal circular polarization by variable rotation technique. *IEEE Transactions on Antennas and Propagation*, 68(6):4617–4626, 2020.

[232] Haoyu Lei, Ying Liu, Yongtao Jia, Zhenzhen Yue, and Xing Wang. A low-profile dual-band dual-circularly polarized folded transmitarray antenna with independent beam control. *IEEE Transactions on Antennas and Propagation*, 70(5):3852–3857, 2021.

[233] Changzhan Gu and Changzhi Li. Assessment of human respiration patterns via non-contact sensing using doppler multi-radar system. *Sensors*, 15(3):6383–6398, 2015.

[234] Ali Gharamohammadi, Mohammad Pirani, Amir Khajepour, and George Shaker. Multi-bin breathing pattern estimation by radar fusion for enhanced driver monitoring. *IEEE Trans. on Instrumentation and Measurement*, 2023.

[235] Mohammad Omid Bagheri, Omar M Ramahi, and George Shaker. Multi-radar near-field system employing multi-band non-interleaved metasurface for enhanced bio-sensing. *19th European Conference on Antennas and Propagation*, 2025.

[236] Simon Anger, Matthias Jirousek, Stephan Dill, Timo Kempf, and Markus Peichl. High-resolution inverse synthetic aperture radar imaging of satellites in space. *IET Radar, Sonar & Navigation*, 18(4):544–563, 2024.

[237] Federal Communications Commission. FCC Empowers Short-Range Radars in the 60 GHz Band, July 2023. Final rule published in the Federal Register, Volume 88, No. 140. ET Docket No. 21-363; FCC 23-35; FR ID 153948.

[238] Bahman Rahmati and Hamid R Hassani. Low-profile slot transmitarray antenna. *IEEE Transactions on Antennas and Propagation*, 63(1):174–181, 2014.

[239] Ali Gharamohammadi, Mohammad Omid Bagheri, Serene Abu-Sardanah, Michael MYR Riad, Hajar Abedi, Ahmad Ansariyan, Kang Wang, Ashish Saragadam, Dmytro Chumachenko, Shahabeddin Abhari, et al. Smart furniture using radar technology for cardiac health monitoring. *Scientific Reports*, 15(1):1392, 2025.

[240] Mohammad Omid Bagheri, Hajar Abedi, and George Shaker. Radar antenna gain improvement using 3d-printed dielectric lens and metamaterial-inspired superstrates. In *2021 IEEE 19th International Symposium on Antenna Technology and Applied Electromagnetics (ANTEM)*, pages 1–2. IEEE, 2021.

[241] Mohammad Omid Bagheri, Omar M Ramahi, and George Shaker. Metasurface design for millimeter-wave radar biomedical sensing. *IEEE International Symposium on Antennas and Propagation and North American Radio Science Meeting (AP-S/URSI)*, 2025.

[242] Veronica Leong, Mohammad Omid Bagheri, and George Shaker. Smart earring for glucose monitoring using fusion of mm-wave radar and optical spectroscopy. *IEEE International Symposium on Antennas and Propagation and North American Radio Science Meeting (AP-S/URSI)*, 2025.

[243] M. O. Bagheri and G. Shaker. Methods and systems using a metasurface to enhance radar sensing, 2025. US Patent, 2025.

[244] Ali Gharamohammadi, Mohammad Omid Bagheri, Amir Khajepour, and George Shaker. Radar fusion for enhanced driver monitoring. In *2023 URSI International Symposium on Electromagnetic Theory (EMTS)*, pages 266–268. IEEE, 2023.

[245] Mohammad Omid Bagheri, Omar M Ramahi, and George Shaker. Dual-band, dual independently-tunable near-field focus metasurface for advanced radar bio-sensor. In *2025 IEEE International Workshop on Antenna Technology (iWAT)*, pages 1–4. IEEE, 2025.

[246] Md Rokunuzzaman, Asif Ahmed, Thomas Baum, and Wayne ST Rowe. Microwave power penetration enhancement inside an inhomogeneous human head. *Scientific Reports*, 11(1):21793, 2021.

[247] Paul M Meaney, Colleen J Fox, Shireen D Geimer, and Keith D Paulsen. Electrical characterization of glycerin: Water mixtures: Implications for use as a coupling medium in microwave tomography. *IEEE transactions on microwave theory and techniques*, 65(5):1471–1478, 2017.

[248] Alice Buffi, AA Serra, Paolo Nepa, G Manara, et al. A focused planar microstrip array for 2.4 ghz rfid readers. *IEEE Transactions on Antennas and Propagation*, 58 (5):1536–1544, 2010.

[249] John Sherman. Properties of focused apertures in the fresnel region. *IRE Transactions on Antennas and Propagation*, 10(4):399–408, 1962.

[250] W Graham. Analysis and synthesis of axial field patterns of focused apertures. *IEEE transactions on antennas and propagation*, 31(4):665–668, 1983.

[251] David R Reid and Glenn S Smith. A comparison of the focusing properties of a fresnel zone plate with a doubly-hyperbolic lens for application in a free-space, focused-beam measurement system. *IEEE Transactions on Antennas and Propagation*, 57(2):499–507, 2009.

[252] I Ohtera. Focusing properties of a microwave radiator utilizing a slotted rectangular waveguide. *IEEE transactions on antennas and propagation*, 38(1):121–124, 1990.

[253] Alejandro Javier Martinez-Ros, José Luis Gómez-Tornero, Vicente Losada, Francisco Mesa, and Francisco Medina. Non-uniform sinusoidally modulated half-mode leaky-wave lines for near-field focusing pattern synthesis. *IEEE Transactions on Antennas and Propagation*, 63(3):1022–1031, 2014.

[254] Yasuaki Monnai and Hiroyuki Shinoda. Focus-scanning leaky-wave antenna with electronically pattern-tunable scatterers. *IEEE transactions on antennas and propagation*, 59(6):2070–2077, 2011.

[255] Takuya Okuyama, Yasuaki Monnai, and Hiroyuki Shinoda. 20-ghz focusing antennas based on corrugated waveguide scattering. *IEEE Antennas and Wireless Propagation Letters*, 12:1284–1286, 2013.

[256] Mirjana Bogosanovic and Allan G Williamson. Microstrip antenna array with a beam focused in the near-field zone for application in noncontact microwave industrial inspection. *IEEE Transactions on Instrumentation and Measurement*, 56(6):2186–2195, 2007.

[257] Aidin Razavi, Rob Maaskant, Jian Yang, and Mats Viberg. Optimal aperture distribution for near-field detection of foreign objects in lossy media. In *2014 IEEE-APS Topical Conference on Antennas and Propagation in Wireless Communications (APWC)*, pages 659–662. IEEE, 2014.

[258] J Musil. Properties of antennas focused in the fresnel zone. *Czechoslovak Journal of Physics B*, 17(10):874–888, 1967.

[259] R Van der Linden and HJ Visser. Analysis, design and realization of a near-field focused rf power transfer system. In *Journal of Physics: Conference Series*, volume 476, page 012118. IOP Publishing, 2013.

[260] Xiao-Yi Wang, Guo-Min Yang, and Wen Geyi. A new design of focused antenna arrays. *Microwave and optical technology letters*, 56(10):2464–2468, 2014.

[261] Yuhai Jiang, Wen Geyi, and Hucheng Sun. A new focused antenna array with circular polarization. *Microwave and Optical Technology Letters*, 57(12):2936–2939, 2015.

[262] HM Aumann and FG Willwerth. Synthesis of phased array far-field patterns by focusing in the near-field. In *Proceedings of the IEEE National Radar Conference*, pages 101–106. IEEE, 1989.

[263] Shaya Karimkashi and Ahmed A Kishk. Focused microstrip array antenna using a dolph-chebyshev near-field design. *IEEE Transactions on Antennas and Propagation*, 57(12):3813–3820, 2009.

[264] Amy Droitcour, Victor Lubecke, Jenshan Lin, and Olga Boric-Lubecke. A microwave radio for doppler radar sensing of vital signs. In *2001 IEEE MTT-S International Microwave Sympsoium Digest (Cat. No. 01CH37157)*, volume 1, pages 175–178. IEEE, 2001.

[265] Jenshan Lin and Changzhi Li. Wireless non-contact detection of heartbeat and respiration using low-power microwave radar sensor. In *2007 Asia-Pacific Microwave Conference*, pages 1–4. IEEE, 2007.

[266] Amy Diane Droitcour. *Non-contact measurement of heart and respiration rates with a single-chip microwave doppler radar*. Stanford University, 2006.

[267] Graham M Brooker et al. Understanding millimetre wave fmcw radars. In *1st international Conference on Sensing Technology*, volume 1, 2005.

[268] Shekh MM Islam, Naoyuki Motoyama, Sergio Pacheco, and Victor M Lubecke. Non-contact vital signs monitoring for multiple subjects using a millimeter wave fmcw automotive radar. In *2020 IEEE/MTT-S International Microwave Symposium (IMS)*, pages 783–786. IEEE, 2020.

[269] George Vasilev Angelov, Dimitar Petrov Nikolakov, Ivelina Nikolaeva Ruskova, Elitsa Emilova Gieva, and Maria Liubomirova Spasova. Healthcare sensing and monitoring. In *Enhanced Living Environments: Algorithms, Architectures, Platforms, and Systems*, pages 226–262. Springer, 2019.

[270] Syed Aziz Shah and Francesco Fioranelli. Rf sensing technologies for assisted daily living in healthcare: A comprehensive review. *IEEE Aerospace and Electronic Systems Magazine*, 34(11):26–44, 2019.

[271] Hsi-Tseng Chou, Ming-Yu Lee, and Chia-Te Yu. Subsystem of phased array antennas with adaptive beam steering in the near-field rfid applications. *IEEE Antennas and Wireless Propagation Letters*, 14:1746–1749, 2015.

[272] Yuhai Jiang, Wen Geyi, Lingsheng Yang, and Hucheng Sun. Circularly-polarized focused microstrip antenna arrays. *IEEE antennas and wireless propagation letters*, 15:52–55, 2015.

[273] H-T Chou and Paolo Nepa. Multi-facet focused microwave antennas. In *2016 IEEE-APS Topical Conference on Antennas and Propagation in Wireless Communications (APWC)*, pages 294–297. IEEE, 2016.

[274] Hsi-Tseng Chou and Polao Nepa. Near-field focused radiation by two edge-coupled microstrip antenna arrays. In *2016 URSI International Symposium on Electromagnetic Theory (EMTS)*, pages 709–712. IEEE, 2016.

[275] Peng-Fa Li, Shi-Wei Qu, Shiwen Yang, and Zai-Ping Nie. Focused array antenna based on subarrays. *IEEE Antennas and Wireless Propagation Letters*, 16:888–891, 2016.

[276] Guilin Sun and Qi Zhu. The design of a focused sparse microstrip antenna array. In *2016 IEEE International Symposium on Antennas and Propagation (APSURSI)*, pages 515–516. IEEE, 2016.

[277] Romain Siragusa, Pierre Lemaître-Auger, and Smail Tedjini. Tunable near-field focused circular phase-array antenna for 5.8-ghz rfid applications. *IEEE Antennas and Wireless Propagation Letters*, 10:33–36, 2011.

[278] Ashwani Sharma, Ignacio J Garcia Zuazola, Ramon Martinez, John C Batchelor, Asier Perallos, and Leandro de-Haro Ariet. Optimal e-field vector combination for a highly focused antenna-array. *IEEE Antennas and Wireless Propagation Letters*, 13: 392–395, 2014.

[279] Lei Wang, Yu Jian Cheng, and Fei Xue. Design of a near-field-focused substrate integrated planar array antenna. In *2014 9th European Microwave Integrated Circuit Conference*, pages 568–571. IEEE, 2014.

[280] RC Hansen and J Brown. Minimum spot size of focused apertures. *Electromagnetic Wave Theory, Part*, 2:661–668, 1965.

[281] Hsi-Tseng Chou, Tso-Ming Hung, Nan-Nan Wang, Hsi-Hsir Chou, and Paolo Nepa. Characteristic comparisons between array, reflectarray and elliptic reflector antennas in rfid near-field focused communications. In *2010 IEEE International Conference on Wireless Information Technology and Systems*, pages 1–4. IEEE, 2010.

[282] Payam Nayeri, Atef Z Elsherbeni, Randy L Haupt, and Fan Yang. Near-field scanning characteristics of focused reflectarray antennas. In *2015 31st International Review of Progress in Applied Computational Electromagnetics (ACES)*, pages 1–2. IEEE, 2015.

[283] Xing Yun, Elise C Fear, and Ronald H Johnston. Compact antenna for radar-based breast cancer detection. *IEEE Transactions on Antennas and Propagation*, 53(8): 2374–2380, 2005.

[284] Paolo Nepa, Alice Buffi, and H-T Chou. Near-field focused antennas: from optics to microwaves. In *2016 IEEE-APS Topical Conference on Antennas and Propagation in Wireless Communications (APWC)*, pages 154–157. IEEE, 2016.

[285] Gurveer Kaur, Amandeep Kaur, Gurpreet Kaur Toor, Balwinder S Dhaliwal, and Shyam Sundar Pattnaik. Antennas for biomedical applications. *Biomedical Engineering Letters*, 5:203–212, 2015.

[286] Shaya Karimkashi and Ahmed A Kishk. Focusing properties of fresnel zone plate lens antennas in the near-field region. *IEEE Transactions on Antennas and Propagation*, 59(5):1481–1487, 2011.

[287] Amir Mirbeik-Sabzevari and Negar Tavassolian. Tumor detection using millimeter-wave technology: Differentiating between benign lesions and cancer tissues. *IEEE Microwave Magazine*, 20(8):30–43, 2019.

[288] Sven Thomas, Christian Bredendiek, and Nils Pohl. A sige-based 240-ghz fmcw radar system for high-resolution measurements. *IEEE Transactions on Microwave Theory and Techniques*, 67(11):4599–4609, 2019.

[289] Duncan Platt, Lars Pettersson, Darius Jakonis, Michael Salter, and Joacim Haglund. Integrated 79 ghz uwb automotive radar front-end based on hi-mission mcm-d silicon platform. *International Journal of Microwave and Wireless Technologies*, 2(3-4):325–332, 2010.

[290] Yukinobu Tokieda, Hiroki Sugawara, Shigeyuki Niimura, and Tatsuji Fujise. High precision waterlevel gauge with an fmcw radar under limited bandwidth. In *European Radar Conference, 2005. EURAD 2005.*, pages 339–342. IEEE, 2005.

[291] Jacques A Arnaud and FA Pelow. Resonant-grid quasi-optical diplexers. *Bell System Technical Journal*, 54(2):263–283, 1975.

[292] M Kamran Saleem, Hamsakutty Vettikaladi, Majeed AS Alkanhal, and Mohamed Himdi. Lens antenna for wide angle beam scanning at 79 ghz for automotive short range radar applications. *IEEE Transactions on Antennas and Propagation*, 65(4): 2041–2046, 2017.

[293] Xinghe Bao, Yunlong Zhan, Chang Xu, Kelu Hu, Chunlei Zheng, and Yingguan Wang. A novel dual microwave doppler radar based vehicle detection sensor for parking lot occupancy detection. *IEICE Electronics Express*, 14(1):20161087–20161087, 2017.

[294] May Zin Tun and Kay Thwe Zin. Implementation of doppler radar-based vehicle speed detection system. *Int. J. Trend Sci. Res. Dev.-IJTSRD*, 3:1708–1713, 2019.

[295] Young Ju Lee, Junho Yeo, Raj Mittra, and Wee Sang Park. Design of a high-directivity electromagnetic band gap (ebg) resonator antenna using a frequency-selective surface (fss) superstrate. *Microwave and Optical Technology Letters*, 43 (6):462–467, 2004.

[296] Hussein Attia, Omar F Siddiqui, Na'el Suwan, and Omar M Ramahi. Analytical and experimental study of gain enhancement in antenna arrays covered with high index metamaterial superstrate. *Microwave and Optical Technology Letters*, 55(1):215–218, 2013.

[297] Bradley G Porter, Leonard L Rauth, John R Mura, and Steven S Gearhart. Dual-polarized slot-coupled patch antennas on duroid with teflon lenses for 76.5-ghz automotive radar systems. *IEEE Transactions on Antennas and Propagation*, 47(12): 1836–1842, 1999.

[298] Jian Wang, Junping Duan, Xinxin Shen, Yongsheng Wang, and Binzhen Zhang. Miniaturized lens antenna with enhanced gain and dual-focusing for millimeter-wave radar system. *Micromachines*, 15(3):335, 2024.

[299] José-Manuel Poyanco, Francisco Pizarro, and Eva Rajo-Iglesias. 3d-printed integrated grin lens-polarizer using anisotropic materials. *IEEE Transactions on Antennas and Propagation*, 2023.

[300] Yongduk Oh, Neal Kordsmeier, Hussain Askari, and Jacob J Adams. Low profile grin lenses with integrated matching using 3-d printed ceramic. *IEEE Open Journal of Antennas and Propagation*, 4:12–22, 2022.

[301] Hind Reggad, Xiaonan Jiang, Xiaohu Wu, Rajeevan Amirtharajah, Dennis Matthews, and Xiaoguang Liu. A single-chip single-antenna radar for remote vital sign monitoring. *IEEE Transactions on Microwave Theory and Techniques*, 71 (10):4519–4532, 2023.

[302] Marco Mercuri, Ping Jack Soh, Pouya Mehrjouseresht, Felice Crupi, and Dominique Schreurs. Biomedical radar system for real-time contactless fall detection and indoor localization. *IEEE Journal of Electromagnetics, RF and Microwaves in Medicine and Biology*, 7(4):303–312, 2023.

APPENDICES

Appendix A

Radar Signal Processing

A.1 Radar Signal Processing

FMCW radar systems broadcast an amplified and frequency-modulated electromagnetic signal produced by a signal generator into the environment and then receive the reflected signals from various objects which carry the properties such as range and radar cross-section.

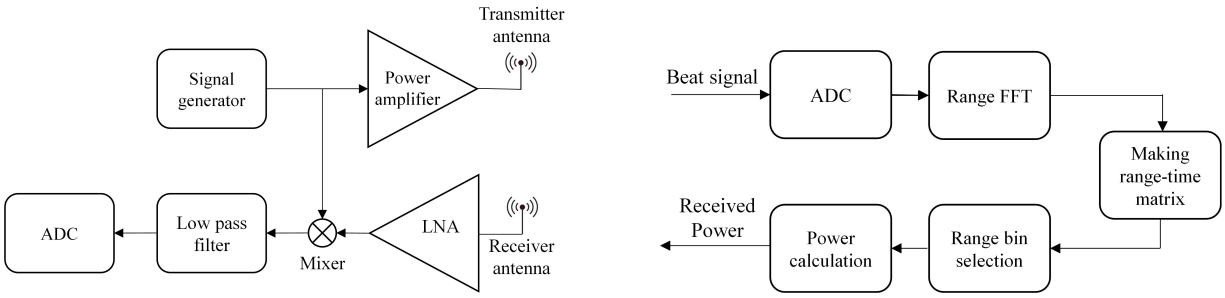


Figure A.1: (a) A simple block diagram of radar before signal processing where both transmitter and receiver are at the same place. (b) The signal processing chain for power calculation

Fig. A.1a shows a common block diagram of the current off-the-shelf FMCW radar modules where both transmitter and receiver are at the same place. As shown, after

amplification of the received signal by a low noise amplifier (LNA), the mixer correlates the transmitted and received signals leading to produce low frequency and high-frequency signals. The low-pass filter is added to the diagram to filter low-frequency signals in the next block, and then an analog-to-digital converter (ADC) is used to convert it to a digital signal which can be processed based on the given information of the designed signal, especially frequency bandwidth.

The signal generator in FMCW radar sweeps in a range of frequency (f_{min} to f_{max}) linearly with a positive slope of K and a time duration of T and prepares the output signal which is called chirp. The resulted frequency bandwidth, BW, for a chirp is as follows,

$$BW = f_{\max} - f_{\min} = K\,T \tag{A.1}$$

The frequency bandwidth presented in (A.1) determines the range resolution of the radar. The relationship between range resolution and frequency bandwidth as presented in (A.2) shows that the radar with higher frequency bandwidth provides better range resolution.

$$\Delta R = \frac{C}{2\,BW} \tag{A.2}$$

where ΔR is range resolution and C is light velocity in the free space. The range resolution in (A.2) discretizes the range of the FMCW radar such that better range resolution provides accurate range estimation and better discrimination between two close reflections. The range in FMCW radar can be estimated from the peak frequency of the reflected chirp signal in the frequency domain by taking Fast Fourier Transform (FFT) of the chirp signal in the time domain that is assumed as (A.3) [30]. Suppose that a single reflection with a delay of t_d from the environment, results in (A.4) at the output of mixer shown in Fig. A.1a.

$$x(t) = A\ \cos\left(2\pi f_{\min} t + \pi K t^2\right), \quad 0 < t < T \tag{A.3}$$

$$x(t) = A\ \cos\left(2\pi f_{\min} t + \pi K t^2\right) \times A\ \alpha \cos\left(2\pi f_{\min}(t - t_d) + \pi K (t - t_d)^2\right) \tag{A.4}$$

where α corresponds to the effect of environment and target on the transmitted signal amplitude. By passing through the low pass filter shown in Fig. A.1a, the resulting signal

which is called the beat signal is as (A.5). Considering the low range of the target, t_d is much less than t in (A.5) and the beat signal can be simplified as (A.6). Replacing $t_d = 2R/C$, the relationship between the beat and the range of the target, R, can be obtained as (A.7). By taking the Fast Fourier Transform from the signal presented in (A.7), the range of the target can be determined.

$$x(t) = A^2\,\alpha \cos\left(2\pi f_{\min} t_d + 2\pi K(t\,t_d - {t_d}^2)\right) \tag{A.5}$$

$$x(t) \simeq A^2\,\alpha \cos\left(2\pi f_{\min} t_d + 2\pi K\,t\,t_d\right) \tag{A.6}$$

$$x(t) \simeq A^2\,\alpha \cos\left(\frac{4\pi R}{C}(f_{\min} + Kt)\right) \tag{A.7}$$

In FMCW radar, the range resolution along with chirp length determines the maximum range of the system. The chirp length can be optimized to remove environmental clutter. Although the near-field measurement requires monitoring the low ranges, more samples benefit from clutter reflection removal. The extra range samples receive the close clutter effects up to the maximum range of the system and then these samples can be removed. In addition, the finer range resolution provides more accurate details of the environment. In this study, the best achievable range resolution of the employed system, 3 cm, is applied for signal design. By considering this range resolution and the maximum range of the system equal to 1 m, the chirp length, M, can be determined using (A.8) as equal to 64.

$$M = \frac{R_{\max}}{2\,\Delta R} \tag{A.8}$$

Using (A.1) to (A.8), the designed signal parameters are summarized in Table A.1 which are used in the signal processing chain. By considering the Pulse Repetition Frequency (PRF) equal to 20 and the sampling frequency of the beat signal equal to 1 MHz, the chirp slope, CS, is obtained as 78.128 MHz/µs which can be supported by the employed system.

Fig. A.1b depicts the signal processing chain for power calculation in a specific range bin. After ADC, the spectrum of the beat signal, which has peaks determining the targets at various ranges, is obtained by applying an FFT. This FFT can also be considered as range FFT since it reveals a range of reflections. Each range FFT bin corresponds to a range interval discretized by range resolution. For instance, if the range resolution is 3 cm and a target range is 20 cm, this target will appear in the 7th range bin. By collecting

Table A.1: The designed signal parameters

Parameter	Quantity	Value
PRF	pulse repetition frequency	20
BW	signal chirp bandwidth	5 GHz
ΔR	radar range resolution	3 cm
Rmax	maximum range of system	96 cm
M	chirp length	64
fs	beat signal sampling frequency	1 MHz
CS	chirp slope	78.128 MHz/µs

Algorithm 3 Power Calculation Algorithm

Input: Range-time Matrix in the Frequency Domain and Selected Range Bin
Output: Power Calculation
counter = 0
Sum = 0
for i in range (1, N): **do**
    counter = counter + 1
    selected sample = Beat signals in the frequency domain (selected range bin)
    sum = sum + selected sample
    Power = sum / counter
    Return Power

N consecutive chirps over time and putting them into a matrix, the range-time matrix is created. This matrix has M rows corresponding to all numbers of range bins and N columns corresponding to the number of chirps. Then, the desired range based on the experiment is selected and the power is calculated for that range bin. Algorithm 3 calculates power for a range-time matrix in a determined range.

A.2 Synchronized Multi-Radar System

The multi-radar fusion system is designed with two primary objectives: to synchronize radar operations for simultaneous execution without latency, thereby improving measurement accuracy, and to support real-time visualization for immediate monitoring.

To achieve parallel data acquisition from multiple radars, a Python-based multiprocessing framework is implemented using the `ifxradarsdk` API to interface with BGT60TR13C

radar modules. The software includes three functional modes—live visualization, data logging, and signal averaging—that can be flexibly combined. Each radar is handled by a separate subprocess, ensuring efficient parallel execution and optimal use of computational resources. Based on the selected operational mode, each process performs dedicated tasks, allowing for seamless and scalable multi-radar operation.

In live visualization mode, the system displays data streams from each radar module in separate windows. Each window presents real-time plots of the received signal amplitude and phase over time and is uniquely identified by a UUID automatically assigned by the operating system upon device connection.

The main process, after handling user-provided arguments, scans for connected radars. Upon detecting at least one radar, it initiates a dedicated child process for each device. These child processes are managed by the main process and are terminated under two conditions: either when the main process itself terminates or when a new radar is connected. In the latter case, the main process terminates all existing child processes and re-executes the radar detection routine to ensure synchronized operation across all radars within the same time frame.

In live capture mode, the program plots real-time amplitude and phase data for each connected radar. Each child process independently manages data acquisition for its assigned radar, while synchronization across all plots is achieved using Python's `Barrier` synchronization primitive. This mechanism ensures that all child processes wait until the required number of processes are ready before proceeding, maintaining synchronized data collection across all radars.

In data collection mode, the program functions similarly to live capture mode but with two key differences: no real-time plots are displayed, and the acquired data is written to disk. Since disk operations are slower compared to in-memory storage, writing data to disk can introduce a potential bottleneck. To address this issue, each child process spawns a dedicated worker thread to handle data writing. The worker thread utilizes a write queue, where newly acquired data is added before being written to disk. To prevent race conditions during queue interactions, a mutex can be used to ensure that only one thread writes at a time. However, to simplify the implementation and avoid potential conflicts, each worker thread writes data to a unique file path, allowing parallel writing without contention. This approach not only enhances efficiency but also facilitates easy retrieval of data from individual radars. The block diagram detailing the operations of both the main process and child processes in the non-averaging mode is presented in Fig. A.2a.

In averaging mode, the program calculates the average amplitude and phase across all connected radars and presents the results in a single consolidated plot. Each radar is still

managed by a dedicated child process, while the main process is responsible for computing and displaying the averaged data. A key limitation of this design is the lack of support for dynamic radar reconnection. To address this limitation, an alternative approach involves delegating the averaging and plotting tasks to a child process. This modification would enable the program to detect and integrate newly connected radars in a manner similar to live capture mode. The block diagram illustrating the operations of both the main and child processes in non-averaging mode is provided in Fig. A.2b.

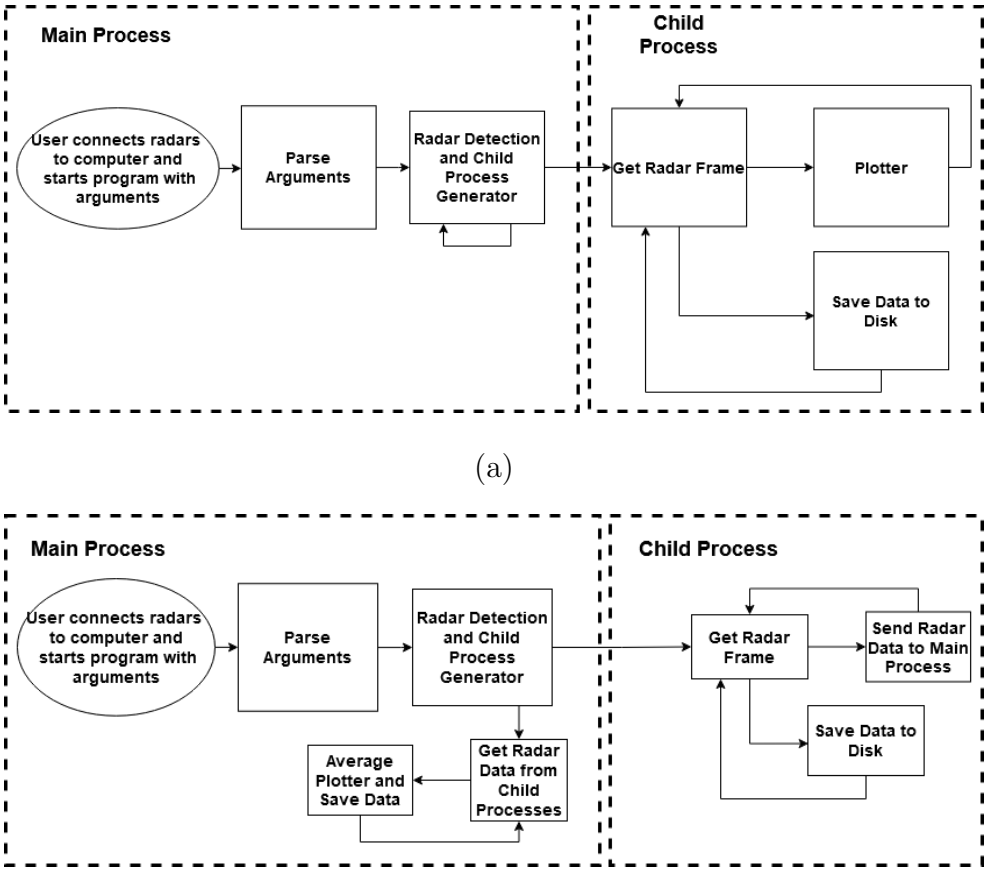


Figure A.2: Block diagram of radar signal processing: (a) non-averaging fusion mode, (b) averaging fusion mode.